DISSERTATION FOR THE DEGREE OF DOCTOR OF PHILOSOPHY (PHD)

Integrating Metabolic, Neo-Angiogenic, and HER2-Targeted Imaging to Characterize Breast Cancer in Preclinical Models

by Ngo Minh Toan

UNIVERSITY OF DEBRECEN
GYULA PETRÁNYI DOCTORAL SCHOOL OF ALLERGY AND CLINICAL IMMUNOLOGY

DEBRECEN, 2025

DISSERTATION FOR THE DEGREE OF DOCTOR OF PHILOSOPHY (PHD)

Integrating Metabolic, Neo-Angiogenic, and HER2-Targeted Imaging to Characterize Breast Cancer in Preclinical Models

by Ngo Minh Toan

Supervisor: Ildikó Garai PhD

UNIVERSITY OF DEBRECEN
GYULA PETRÁNYI DOCTORAL SCHOOL OF ALLERGY AND CLINICAL IMMUNOLOGY

DEBRECEN, 2025

Table of Contents

List of Abbreviations

TNBC	Triple-negative breast cancer
ER	Estrogen receptor
PR	Progesterone receptor
ADC	Antibody-drug conjugate
T-DXd	Trastuzumab-deruxtecan
NAC	Neo-adjuvant chemotherapy
IHC	Immunohistochemistry
FISH	Fluorescence in situ hybridization
CSF	Cerebrospinal fluid
ctDNA	Circulating tumour DNA
MRI	Magnetic resonance imaging
CT	Computed tomography
SPECT	Single photon emission computed tomography
PET	Positron emission tomography
[^{18}F]FDG	2-deoxy-2-[^{18}F]fluoro-D-glucose
FLT	[^{18}F]-3'-Fluoro-3'-deoxythymidine
FAP	Fibroblast activation protein
RGD	Arginine-glycine-aspartic acid
T-DM1	Trastuzumab emtansine
PPV	Positive predictive values
NPV	Negative predictive values
TBR	Tumour-to-background ratio
PEG	Polyethylene glycol
ABD	Albumin binding domain
DARPins	Designed ankyrin repeat proteins
GMP	Good manufacturing practice
FBS	Fetal bovine serum
FOV	Field of view

OSEM	Ordered subset expectation maximization
VOI	Volume-of-interests
SUV	Standardized Uptake Value
ROI	Regions of interest
MLEM	Maximum-likelihood expectation-maximization
H&E	Haematoxylin and eosin
RCP	Radiochemical purity
SD	Standard deviation
ANOVA	Analysis of variance
HPLC	High performance liquid chromatography
MS	Mass spectrometry
NMR	Nuclear magnetic resonance
SEFT	Spin-Echo Fourier transform
TLC	Thin-layer chromatography
iTLC-SG	Instant Thin-Layer chromatography silica gel
BFC	Bi-functional chelator
TFA	Trifluoroacetic acid
VDCC	Voltage-dependent calcium channel

I. Introduction

1. Breast Cancer Statistics

Breast cancer remains one of the most prevalent and deadly cancers worldwide. In 2022 alone, an estimated 2.3 million women were diagnosed with the disease, accounting for 11.6% of all cancer cases globally, and among this population more than 660,000 deaths, representing nearly 7% of total cancer deaths [1]. Moreover, approximately 13% of the female population is expected to be diagnosed with breast cancer during their lifetime, and 2.3% will die from it [2]. Consequently, among all cancers, breast cancer ranks as the second most common in incidence after lung cancer and the fourth in mortality across both sexes. However, it holds the highest incidence and mortality rates within the female population [1].

The incidence of breast cancer experienced a significant rise during the 1980s and 1990s, largely due to the widespread adoption of mammography screening. While the rate of increase has since slowed to approximately 1% annually [2], disparities in outcomes persist. Advances in early detection and treatment have led to improvements in mortality rates in high-income countries, yet mortality continues to rise in low-income countries and among specific racial groups, such as Asians and Pacific Islanders [1, 2]. Despite of these improvements, the global burden of breast cancer is predicted to escalate, with new cases expected to reach 3 million annually, a 40% increase, and deaths rising to 1 million annually, a 50% increase in 2040 [3].

With such predicted increase in cases and deaths, breast cancer remains not only one of the most common but also one of the deadliest cancers, requiring global attention and innovation to reduce its burden. Therefore, these statistics highlight the need for better diagnostics, classification, and therapies to address breast cancer's growing burden and reduce its global impact.

2. Breast Cancer Heterogeneity

Breast cancer incidence and progression exhibit significant variations across different ages and racial groups. Generally, the risk of breast cancer increases with age, peaking between 60 and 69 years [2]. However, younger patients often face poorer prognoses, with women aged 40-49 years particularly vulnerable, with the highest risk of breast cancer among younger age groups. Furthermore, white and Asian Pacific Islander women are more likely to be diagnosed at earlier stages, whereas Black women exhibit the highest rates of high-grade tumours [4].

Therefore, breast cancer is not a uniform disease but rather a spectrum with diverse biological behaviours and outcomes. This diversity requires the need to classify breast cancer into specific subtypes, allowing for more precise diagnosis, personalized treatment, and improved prognostic accuracy. Molecular subtypes were first described in 2000, till now at least four distinct breast cancer subtypes have been identified [5]: Luminal subtypes (luminal A and luminal B) with hormone receptor positivity which expresses genes characteristic of physiological epithelial cells lining the lumen; HER2-positive subtype; and triple-negative breast cancer (TNBC), a basal subtype which is triple-negative of estrogen receptor (ER)-negative, progesterone receptor (PR)-negative, and HER2-negative.

2.1. Molecular Classification of Breast Cancer Subtypes

Based on receptor positivities and Ki-67 protein levels, breast cancer is classified into specific molecular subtypes, providing critical insights into their molecular mechanisms and enabling potential targeted treatment strategies.

Luminal A breast cancer subtype is ER-positive, PR-positive (>20%), HER2-negative, and has a Ki-67 < 14%. It represents the most frequent subtype with more than 60% of breast cancer cases [5]. The estrogen receptor activation translocates the receptor into nucleus, regulating the transcription of specific genes responsible for cell growth and differentiation. When localized to the membrane, the receptor can stimulate the PI3K/AKT or Ras/MAPK pathways via non-genomic mechanisms, driving cell proliferation and survival. Additionally, progesterone contributes to carcinogenesis by triggering RANK-ligand expression, which in turn enhances proliferation in adjacent cells [6].

Luminal B breast cancer subtype is observed in more than 10% of the cases [5]. This subtype is hormone receptor-positive and fulfils one of the following criteria: ER-positive, Ki-67 ≥ 14% or/and PR < 20%, HER2-negative; or ER-positive, HER2-positive, with any Ki-67 or PR levels. Ki67 protein is active during the G1, S, G2, and M phases of the cell cycle but is not expressed in G0, anaphase, or telophase [7]. This makes Ki67 a key proliferation marker, particularly useful for differentiating HER2-negative luminal subtypes.

HER2-positive breast cancer subtype has the lowest prevalence, representing less than 10% of cases [5]. It is characterized by ER-negative, PR-negative, and HER2-positive status. The HER2 receptor is part of the epidermal growth factor (EGF) family and is defined by ErbB2 or neu oncogene mutation, amplification, or protein overexpression. Unlike other receptors, HER2 does not require a ligand for activation. Upon dimerization, it becomes the most potent member of its family, activating the PI3K/AKT, MAPK, and phospholipase Cγ (PLCγ) pathways, which regulate proliferation and cell survival [8].

TNBC subtype is traditionally defined by the absence of expression of the conventional receptors (ER, PR, and HER2). However, it is a highly complex and heterogeneous subtype, characterized by variable expression of additional biomarkers and signalling pathways. These may include tumour immunological status, the presence of androgen receptors, as well as markers indicative of mesenchymal features and angiogenesis [9].

2.2. Risk Factors Differences Across Subtypes

Patients with a family history of breast cancer are at an increased risk of developing breast cancer with the same ER status as their relatives. A family history of both prostate and breast cancer elevates the risk of ER-positive breast cancer, while a family history of cervical cancer increases the risk of ER-negative breast cancer and TNBC [10]. The BRCA1 mutation is particularly associated with an increased risk of TNBC, while the BRCA2 mutation is linked to a higher risk of Luminal B subtype [11].

Obstetric and gynaecological history risk factors vary across breast cancer subtypes. Later age at menarche is protective against breast cancer across all subtypes, although this effect is less pronounced in HER2-positive breast cancer. Delayed menopause and the use of hormone replacement therapy increase the risk of Luminal subtypes. In contrast, a later age at first pregnancy and a higher number of pregnancies reduce the risk of Luminal subtypes, while longer breastfeeding duration lowers the risk of TNBC. The use of oral contraceptives is associated with an increased risk of most subtypes, especially TNBC [12, 13].

Demographic profiles are also different among subtypes. Caucasian is more likely to develop luminal A, whereas African has higher risk of TNBC [2]. Although Luminal subtypes are more common overall, younger patients are more likely to develop TNBC, while older patients tend to develop Luminal A subtype [14].

Additionally, features of breast tissue can influence the risk of developing different breast cancer subtypes. For example, high mammographic density is associated with an increased risk of HER2-positive breast cancer [15].

2.3. Histology and Radiological Characteristics Among Subtypes

Luminal A cancers tend to present with lower-grade tumours, and features such as tubular and cribriform carcinoma. Luminal B tumours are more commonly higher grade, typically grade 2, and are more often associated with micropapillary carcinoma. In contrast, TNBC exhibits heterogeneous expression, with variations based on the morphology of basal epithelial cells and normal myoepithelial cells [16].

Imaging patterns also differ among subtypes. Luminal A tumours exhibit the highest stiffness, indicating a low grade and desmoplastic reaction [17], and demonstrates speculated margin allowing earlier detection [18]. Both TNBC and luminal B tends to appear more oedematous [19]. TNBC tumours often have a necrotic core, despite the presence of hyper-vascularization at the tumour rim, HER2-positive tumours also demonstrate increased vascularization with an internal blood supply [20].

2.4. Therapeutic Approach Differences Across Subtypes

Due to their hormone receptor positivity, Luminal subtypes of breast cancer can be effectively treated with endocrine therapies. These include aromatase inhibitors or anti-estrogenic drugs like tamoxifen and fulvestrant, which help block the hormones that promote tumour growth [21].

HER2-positive breast cancers are treated with therapies that specifically target the HER2 receptor. These treatments include monoclonal antibodies like trastuzumab and pertuzumab, as well as antibody-drug conjugates (ADCs) such as trastuzumab-deruxtecan (T-DXd), which deliver chemotherapy directly to the cancer cells [21, 22].

TNBC primarily relies on cytotoxic agents for treatment. In recent years, the use of immune checkpoint inhibitors has shown promise as a new therapeutic approach, offering additional options for patients with this aggressive subtype [21, 22].

2.5. Prognosis Differences Across Subtypes

Luminal subtypes generally have a better prognosis compared to non-luminal subtypes, with the highest breast-specific survival rates [23]. However, they also carry the highest risk of bone metastasis, particularly when HER2-positive [24].

HER2-positive breast cancer is associated with the highest rate of metastasis [24, 25] with a strong predilection for the liver. Additionally, this subtype shows a higher incidence of brain and lung metastases compared to other subtypes [24-26]. Therefore, prior to the introduction of trastuzumab in treatment regimens, HER2-positive breast cancer had the worst survival rates [27, 28]. The use of trastuzumab has significantly improved survival outcomes for this subtype [29]. Despite this advancement, HER2-positive breast cancer remains the second deadliest subtype [30], and carries the highest medical care costs due to the reliance on HER2-targeted therapies [31].

TNBC has a lower rate of metastasis compared to HER2-positive cancer [25], but it is associated with the worst outcomes, including the lowest rate of breast-specific survival [23], regardless of the cancer stage [30].

2.6. Levels of Breast Cancer Heterogeneity

Breast cancer is a highly heterogeneous disease, with variations not only between patients but also within tumours and over time. This heterogeneity significantly impacts tumour progression, therapeutic responses, and clinical outcomes.

Intertumour heterogeneity refers to the presence of different subtypes of breast cancer between the primary tumour and metastatic sites, as well as among various metastatic sites [32]. Differences in receptor status between lesions are commonly observed, particularly in therapy-resistant metastatic cases.

Intratumour heterogeneity describes the existence of distinct cell subpopulations with varying subtypes within the same tumour [32]. As the results, different cell populations may respond differently to therapies, potentially leading to incomplete eradication and disease recurrence.

The tumour microenvironment plays a critical role in breast cancer progression and therapy resistance. Factors such as metabolic rate differences, the presence of supporting stromal cells, immune cell composition, neovascularization, and perfusion variability can all influence tumour behaviour [33]. Therefore, tracking these microenvironmental biomarkers can provide valuable insights into cancer behaviour and progression.

Temporal heterogeneity refers to the development of cellular variations within the tumour over time, particularly during disease progression or after treatment [33]. Receptor conversion or downregulation is often observed following endocrine or targeted therapies, contributing to therapy resistance. For instance, up to 30% of primary tumours show receptor conversion after neoadjuvant chemotherapy (NAC), with loss of HER2 or PR expression being most common [34]. Furthermore, breast cancer recurrence or metastasis may result in distinct subpopulations. Approximately 20% of molecular subtype conversion between primary and metastasis, with ER and PR showing the highest conversion rate (more than 20%), typically to a negative receptor status [35]. Whereas HER2 conversion occurs in approximately 10% of cases, with gain in HER2 expression being more frequent, particularly in distant or multiple metastases [35, 36].

Other biomarkers or intermediate subtypes: other biomarkers can also affect tumour progression and therapy approach including HER3, EGFR, VEGF, androgen receptor, PD-L1, particular in aggressive and heterogeneous subtype like TNBC [37]. Additionally, emerging intermediate subtypes such as HER2-low (IHC +1 or IHC +2 with negative FISH) [38], and estrogen receptor-low (ER+ in 1–10% of cancer cells) [39] require adjusted chemotherapy regimens to optimize treatment efficacy while minimizing side effects.

Therefore, dedicated, systematic, and temporal approaches to assessing breast cancer biomarkers are essential for selecting effective therapies, monitoring treatment responses, predicting outcomes, and making timely adjustments to treatment strategies.

3. Biomarkers Assessment in Breast Cancer

Biomarkers are defined as objective, quantifiable indicators of biological processes and are considered surrogate endpoints for disease detection and progression [40]. Their abilities to assess and characterize the heterogeneity of breast cancer at different levels make them crucial for understanding tumour behaviour and personalizing treatment strategies.

3.1. Types of Biomarker

There are numerous biomarkers currently used or under investigation to classify breast cancer subtypes or assess protein expression levels in breast cancer cells:

Biofluid biomarkers include substances found in urine, saliva, blood, and cerebrospinal fluid (CSF). Various modalities, such as genomics, proteomics, and lipidomics, are employed to detect these biomarkers. Recently, circulating tumour DNA (ctDNA), cell-free DNA, and hypermethylated DNA fragments have been identified as potential indicators of early breast cancer metastasis. These biofluid biomarkers are non-invasive, easy to collect in serial samples, and capable of assessing tumour heterogeneity, making them useful for monitoring tumour progression. However, they require high sensitivity, as tumour-derived material can be diluted in blood; moreover, the techniques cannot provide localization information [41].

Tissue samples are obtained through surgical biopsies, endoscopic biopsies, needle biopsies, or aspirates from nipple fluid or pleural effusions. These samples are analysed using techniques like immunohistochemistry (IHC) or fluorescence in situ hybridization (FISH) to identify specific genes, such as HER2 gene amplification. These modalities are currently gold standard for obtaining essential pathological data, but it is invasive, time-consuming, and uncomfortable for patients. The processing and staining of samples can delay results, and some locations within the body are challenging to access. Additionally, tissue sampling does not provide spatial information or capture the full extent of tumour mass or metastasis, as its results are highly dependent on the specific location and timing of the sample collection, potentially overlooking tumour heterogeneity and dynamic changes in disease progression [41].

Imaging biomarkers, such as Magnetic Resonance Imaging (MRI), Computed Tomography (CT), especially molecular imaging with Single Photon Emission Computed Tomography (SPECT) or Positron Emission Tomography (PET) are used to visualize specific radiopharmaceuticals within the body. These imaging modalities offer non-invasive, real-time information with detailed spatial data, allowing for the detection of metastasis, the morphology and dimensions of lesions, and tumour heterogeneity. Thus, they can be essential tools for staging and follow-up tumour progression especially for targeted therapies.

II. A Literature Review of PET Molecular Imaging in Breast Cancer: Metabolic, Microenvironmental, and HER2 Imaging for Tumour Stratification

1. PET Imaging of Metabolic, Proliferative and Microenvironmental in Breast Cancer Subtyping

1.1. [^{18}F]FDG

Given the distinct differences between subtypes, metabolic biomarkers assessed through 2-deoxy-2-[^{18}F]fluoro-D-glucose (FDG) imaging can reveal valuable insights into their unique characteristics. A meta-analysis study on FDG uptake variation among subtypes has shown that higher FDG uptake is typically observed in tumours with hormone receptor negativity, HER2 positivity, and high Ki67 levels, which are associated with more aggressive cancer behaviour [42].

However, the differences in FDG uptake between HER2-positive and TNBC subtypes are not statistically significant [42, 43]. Furthermore, the correlation between FDG uptake and HER2 status is not evident [44], rather stronger correlations have been observed between FDG uptake and tumour grade, size, stage [44, 45] as well as additional marker such as p53, EGFR [44].

Nevertheless, FDG uptake does show a correlation with Ki67 expression [43, 44]. A meta-analysis reported an overall correlation coefficient of $r = 0.44$ across various cancers and a similar correlation ($r = 0.44$) specifically in breast cancer [46].

Overall, while [^{18}F]FDG is routinely available and can differentiate several markers, it remains nonspecific and is not able to identify any single biomarker with high specificity.

1.2. [^{18}F]FLT

[^{18}F]-3'-Fluoro-3'-deoxythymidine (FLT) is a biomarker for in vivo imaging of cell proliferation, targeting thymidine kinase 1 protein. a meta-analysis revealed a strong overall correlation between FLT uptake and Ki-67 ($r = 0.7$), with particularly strong correlations observed in lung, brain, and breast cancers [47]. Further analysis comparing these two tracers specifically in breast cancer found that FLT had a higher correlation with Ki-67 ($r = 0.54$) compared to FDG ($r = 0.4$) [48]. Nevertheless, the tracer is mostly studied for predicting responses to chemotherapy [49] rather than classify breast cancer subtypes.

1.3. FAPI

^{68}Ga-labelled Inhibitor of fibroblast activation protein (FAP), a serine protease from the dipeptidyl peptidase-4 (DPP-4), has emerged as an attractive tracer in recent studies. Research comparing [^{68}Ga]Ga-FAPI uptake across different breast cancer subtypes showed that higher uptake was observed in HER2 positive tumours [50]. While this tracer cannot directly classify breast cancer subtypes, the tracer demonstrated its superiority over FDG in detecting lesions [50, 51], suggesting that [^{68}Ga]Ga-FAPI could offer a valuable alternative to FDG, potentially improving the detection of certain tumour characteristics and guiding treatment strategies.

1.4. Angiogenesis imaging

Angiogenesis is a crucial component of tumour microenvironment, plays main roles in cancer cell survival, promoting growth and metastasis. The angiogenesis is a complex process involving many pathways stimulate pro-angiogenic factors and inhibit anti-angiogenic factors. Thus, angiogenesis imaging tracers have been studied directly targeting various markers such as VEGF, integrins, aminopeptidase N (CD13) [52].

VEGF is commonly expressed in breast cancer with highest prevalence in HER2-positive subtypes. There are many studies using tracer targeting VEGF and VEGFR in breast cancer ([^{89}Zr]Zr-DFO-bevacizumab, [^{89}Zr]Zr-DFO-aflibercept, [^{64}Cu]Cu-DOTA-VEGFDEE). However, renal physiology VEGFR1 expression, and many conditions involving neovascularization, such as atherosclerosis, stroke, and osteoarthritis, can provide a false positive when imaging tumour VEGFR, especially in the brain and bones, which are frequent sites of breast cancer metastasis. Thus, VEGF imaging in breast cancer is currently suboptimal [37].

Aminopeptidase N (CD13) is another promising target in angiogenesis imaging. The labelled NGR (Asn-Gly-Arg) peptide (such as [^{68}Ga]-NOTA-c(NGR)) were proven to have high affinity for the protein and looks promising in mouse models [52]. Nevertheless, there is limited research on the application of NGR-based peptides in breast cancer.

Intergins also participate in the neo-angiogenesis process, particularly the integrin $\alpha v\beta 3$. The over-expression of this heterodimeric integrin on the surface of tumour endothelial cells make this an attractive target for anti-angiogenic therapy and angiogenic imaging. While many peptide-based agents targeting $\alpha v\beta 3$ have shown limited effectiveness due to partial agonist effects and changes in affinity of the receptors, various alternative strategies including allosteric modulators or pure antagonists have been developed to enhance the efficacy of $\alpha v\beta 3$-targeted treatments [53].

Arginine-glycine-aspartic acid (RGD)-based radiopharmaceuticals, particularly cyclic pentapeptides like RGDfK, have demonstrated high specificity for visualizing αvβ3. Polymerizing these peptides, especially in a dimeric form, has yielded promising and consistent results [54].

Studies using RGD-based imaging have attempted to classify breast cancer subtypes based on integrin expression. For example, [^{68}Ga]Ga-RGD uptake was higher in tumour with HER2 positivity, and lower in TNBC [55]. In other clinical study, using [^{18}F]Alfatide II (a dimeric version of RGD labelled with ^{18}F via NOTA chelating with AlF) showed similar results, *i.e.* TNBC had lowest RGD uptake, but the highest uptake were observed in luminal B (with HER2 negativity) subtype [56]. Both studies used the FDG-to-RGD uptake ratio to further classify breast cancer subtypes and showed greater confidence in subtype identification. Specifically, the ratio was lowest for luminal B and highest for TNBC [55, 56].

2. HER2 PET Imaging in Breast Cancer

HER2 imaging is crucial in the diagnosis and treatment of breast cancer and has been extensively researched in recent years. Advances in HER2-targeted molecular imaging, particularly with PET, have shown promising potential. Recent developments, particularly in breast cancer preclinical and clinical studies (Table 1), highlight significant implications for improving breast cancer detection, treatment planning, and monitoring. However, despite extensive research on HER2-targeted PET tracers, only a limited number have progressed to human studies, and none have yet achieved widespread acceptance in routine clinical diagnostics. This translational gap highlights the importance of ongoing research in this field, which aims to further advance HER2-targeted imaging strategies and support their integration into clinical practice in the future.

2.1. Trastuzumab Labelled with ^{89}Zr

The use of the radiolabelled isotope ^{89}Zr, with an extended half-life of approximately 78 hours, is effective for labelling antibodies (also with long biological half-life). Trastuzumab labelled with ^{89}Zr using the chelator DFO has been extensively evaluated in clinical settings. In most trials, it is common practice to administer a "cold" dose of trastuzumab, typically around 50 mg, prior to the tracer injection to reduce background signal. Scanning is usually performed 4 to 5 days after tracer administration [57, 58]. However, studies suggest a lower cold dose may be more appropriate for patients already undergoing trastuzumab treatment [59]. The [^{89}Zr]Zr-DFO-trastuzumab tracer has demonstrated its ability to detect or monitor HER2 status in metastatic lesions in the liver, bone, and lymph nodes regardless of the HER2 status of the primary tumour [57-59]. Notably, it can also detect brain metastases, likely due to tracer uptake facilitated by the disruption of the blood-brain barrier [60].

Despite these promising results, there is a recognized risk of discordance between the tracer uptake and IHC results, particularly in bone, liver, and lymph node lesions [61]. This discrepancy may lead to false positives, primarily attributed to the instability of DFO as a chelator for ^{89}Zr. The free zirconium that is released tends to accumulate in bone tissue. Moreover, Fc-mediated uptake in active lymph nodes and the liver, key sites of antibody metabolism, can also result in false positives.

The tracer's potential in following up therapy responses was demonstrated by Linders *et al.*, using different parameters and ΔSUV_R (the difference between SUV ratios of before and after therapy). However, the study included a small number of patients (n = 6) and reported some false-negative cases (2 cases) likely due to HER2 downregulation following high-dose trastuzumab [62]. In larger clinical trials (*e.g.*, the ZEPHIR trial), combining [^{89}Zr]Zr-DFO-trastuzumab imaging with conventional FDG PET/CT significantly improved the ability to predict treatment response to trastuzumab emtansine (T-DM1), achieving positive predictive values (PPV) and negative predictive values (NPV) exceeding 90%, up to 100% [63, 64]. Furthermore, a clinical trial by Gaykema *et al.* showed that [^{89}Zr]Zr-DFO-trastuzumab imaging can help predict treatment responses when used alongside heat shock protein 90 (HSP90) inhibitors in patients. The results showed significant correlations between the ΔSUV_{max} and decrease in tumour size ($r^2 = 0.69$) [65]. Additionally, in a preclinical study by McKnight *et al.* involving breast cancer tumour-bearing mice, the tracer was able to assess the effectiveness of tyrosine kinase inhibitors. There were significant correlations between tumour uptake and the decreases in HER2 expression (*r* around 0.6) and in tumour volume (*r* around 0.8) [66]. These findings underscore the potential of [^{89}Zr]-DFO-trastuzumab not only in monitoring HER2 status but also in evaluating the efficacy of different therapeutic approaches. Nevertheless, larger studies with standardized assessment methods are required, whether using the SUV_{max} lesion-to-background ratio, blood, liver, or contralateral side.

To address the *in vivo* instability of DFO, alternative chelators for [^{89}Zr]Zr-DFO-trastuzumab have been developed and tested in preclinical models. For example, Deri *et al.* showed that HOPO improved stability with lower bone uptake but presented challenges in synthesis and lower tumour uptake [67]. DFO* (DFOstar) was demonstrated by Chomet *et al.* to significantly improve thermodynamic stability while maintain similar tumour-to-background ratios (TBRs). This resulted in lower bone uptake and greater accuracy in detecting breast cancer bone metastases [68].

Site-specific conjugation produces a more homogeneous tracer, leading to more predictable specificity and pharmacokinetics. In a study by Vivier *et al.* involving humanized mice with breast cancer, both fully (by PNGaseF) and partially (by EndoS) deglycosylated antibodies were conjugated to DFO specifically at the heavy chain glycan site ([^{89}Zr]Zr-DFO-^{ss}trastuzumab-EndoS) or non-specifically ([^{89}Zr]Zr-DFO-^{nss}trastuzumab-PNGaseF). Both strategies showed significantly higher tumour uptake and an improved tumour contrast with significantly lower liver and spleen uptake compared to [^{89}Zr]Zr-DFO-trastuzumab [69]. This improvement is attributed to the attenuation of FcγR interactions while maintaining high HER2 binding affinity, requires additional but facile enzymatic deglycosylation step.

2.2. Trastuzumab Labelled with ^{64}Cu

In addition to [^{89}Zr]Zr-DFO-trastuzumab, the use of [^{64}Cu]Cu-DOTA-trastuzumab has also been investigated in patients due to its comparable long half-life of 12.7 hours and better resolution due to lower positron energy (0.656 MeV vs 0.897 MeV) [70]. Studies suggest that administering a cold dose of 50 mg trastuzumab, followed by a 48-hour incubation period would optimize the TBR [71]; however, the tracer's tumour visualization was limited in patients undergoing trastuzumab therapy [72]. Like [^{89}Zr]Zr-DFO-trastuzumab, [^{64}Cu]Cu-DOTA-trastuzumab has proven effective in visualizing known brain metastases larger than 1 cm with high confidence and HER2 specificity (validated with IHC and autoradiography) [73]. There is some discordance between FDG PET imaging and [^{64}Cu]Cu-DOTA-trastuzumab, with certain lesions showing positivity with one tracer but not the other [71], suggesting the potential supplementary role of the tracer to the conventional FDG.

Moreover, [^{64}Cu]Cu-DOTA-trastuzumab has demonstrated potential in predicting therapy response in HER2-positive patients. Mortimer *et al.* showed that patients who responded to treatment exhibited significantly higher baseline uptake at 2 days post-injection compared to non-responders. Although the study's small sample size (n = 10) limits the generalizability of these findings [74].

One challenge with ^{64}Cu is its tendency to transchelate with serum compounds, highlighting the need for a more stable chelator. A preclinical study by Woo *et al.* showed that [^{64}Cu]Cu-NOTA-trastuzumab offers high specificity (significant tumour uptake decrease when blocked *in vivo* with cold trastuzumab) and a lower uptake and absorbed dose to organs compared to DOTA, indirectly indicating greater stability [75]. A clinical pilot study using the same tracer by Lee *et al.* also reported a reduced organ dose while maintaining higher uptake in HER2-positive lesions compared to negative ones [76]. Recently, the NODAGA chelator has emerged as a promising alternative, [^{64}Cu]Cu-NODAGA-trastuzumab offers easier labelling and enhanced stability while retaining high specificity in vitro [77].

2.3. Pertuzumab Labelled with ^{89}Zr

Imaging the HER2 receptor with a trastuzumab-based tracer during trastuzumab therapy can be challenging due to the saturation of the receptor's binding sites. An alternative approach using pertuzumab, which binds to a distinct epitope on HER2, offers a potential solution. In a preclinical study by Marquez *et al.* using breast cancer xenografts, the [^{89}Zr]Zr-DFO-pertuzumab tracer demonstrated high specificity, with significant tracer uptake observed during trastuzumab therapy [78]. Building on these findings, a patient study ($n = 6$) by Ulaner *et al.* revealed that optimal imaging was achieved 5-8 days post-injection with a cold dose of pertuzumab administered beforehand to enhance the TBR. The approach resulted in a slightly higher absorbed dose compared to [^{89}Zr]Zr-DFO-trastuzumab. Nevertheless, the tracer proved effective in investigating HER2 heterogeneity and was able to detect brain HER2 metastases in some patients [79].

Beyond differentiating HER2 positivity, this tracer has been explored in preclinical models for its ability to follow up and predict therapy response. For instance, after T-DM1 treatment, the tracer visualized changes in HER2-positive tumour size more effectively than FDG. Specifically, the tumour's tracer uptake did not significantly changed, which is hypothesized to correspond to the unchanged HER2 concentration post-therapy [80]. In contrast, a study by Kang *et al.* with HSP90 inhibitor therapy showed decreased HER2 expression and a significant reduction in tumour uptake after treatment [81]. Another study by Lu *et al.* demonstrated the tracer's predictive ability following paclitaxel treatment, where tumours with higher tracer uptake responded better, exhibiting reduced size and decreased FDG uptake ($r = -0.59$), correlating with lower HER2 expression post-therapy [82]. These findings highlight the tracer's potential not only for characterizing HER2 expression but also for predicting and monitoring dynamic changes in HER2 status.

Similar to [^{89}Zr]Zr-DFO-trastuzumab, a site-specific version, [^{89}Zr]Zr-^{ss}DFO-pertuzumab developed by Vivier et al., showed improved tumour-to-spleen and liver ratios in preclinical models [83]. In a clinical study ($n = 6$) by Yeh *et al.*, the site-specific tracer exhibited a similar total absorbed dose compared to non-specific [^{89}Zr]Zr-DFO-pertuzumab, but with the kidney identified as the critical organ instead of the liver. Nevertheless, the site-specific tracer provided better lesion visualization in some HER2-positive patients than the non-specific version [84].

2.4. Trastuzumab Emtansine Labelled with ^{89}Zr

Trastuzumab emtansine (T-DM1) is an antibody-drug conjugate effective for some patients with trastuzumab-resistant cancers, but many either fail to respond or develop resistance over time. To improve therapy selection, [^{89}Zr]Zr-DFO-T-DM1 can be employed over [^{89}Zr]Zr-DFO-trastuzumab. In preclinical breast cancer models with varying HER2 expression, Al-Saden *et al.* demonstrated that this tracer shows high HER2 specificity, comparable to [^{89}Zr]Zr-DFO-trastuzumab, and is particularly effective at stratifying HER2 status at 4 days post-injection [85]. A subsequent study, also in preclinical models using tumour-to-blood ratios, showed that the tracer could classify HER2 expression levels, with very strong correlations with HER2 expression (r^2 = 0.94) and, importantly, with tumour response to T-DM1 [86].

2.5. Labelled Trastuzumab Fragments

Antibody fragments lacking the Fc region could offer superior alternatives due to their faster pharmacokinetics compared to full-length antibodies. In a study by Suman *et al.* using F(ab') and F(ab')2 fragments labelled with ^{68}Ga via the NOTA chelator, the fragments retained their affinity, and the labelling process was gentler than with the conventional DOTA chelator, which can damage heat-labile fragments. As expected when using antibody fragments, the F(ab') was primarily eliminated through the kidneys, exhibiting a faster clearance rate and consequently achieving higher tumour-to-organ ratios than F(ab')2, except for the tumour-to-kidney ratios [87].

A study by Moreau *et al.* on breast cancer tumour-bearing mice, investigating the optimal chelator for the ^{64}Cu labelling of trastuzumab's Fab fragment found that MANOTA provided better stability and superior tumour-to-blood and tumour-to-liver ratios (around twofold higher) compared to DOTA, DOTAGA, and even the previously mentioned NODAGA, which already had shown some improvements [88].

Various methods for the site-specific labelling of trastuzumab fragments have been explored. For instance, a modified Fab with a mutated light chain containing methionine - a rare amino acid typically hidden within protein pockets, enables easy and specific conjugation, enhancing labelling precision. Implementing the techniques in preclinical models, Yue *et al.* demonstrated that [^{68}Ga]Ga-DFO-M74 trastuzumab's Fab demonstrated higher affinity and stability, leading to faster clearance from organs and higher tumour uptake, resulting in an approximately 2-fold higher tumour-to-background than the wild-type tracer [89].

However, their small size makes antibody fragments rapidly cleared from the body, which may limit tumour uptake. Strategies such as adding polyethylene glycol (PEG) can extend their half-life, although this requires chemical conjugation. An alternative approach, PASylation, the addition of Pro, Ala, and Ser sequences, has been tested in pilot mice models by Mendler *et al.* [90] and in a human study (n = 1) with HER2-positive breast cancer by Richter *et al.* [91]. This technique showed prolonged plasma retention and successfully visualized primary tumours and metastases.

2.6. HER2 Nanobody

Nanobodies, which are heavy-chain antibodies found in camelids, are even smaller than antibody fragments. HER2-targeting nanobodies, such as 2Rs15d and 5F7, are particularly well-suited for imaging with ^{18}F due to the complementary short half-lives.

Zhou *et al.* utilized these two nanobodies with the novel fluorine prosthetic TFPFN for HER2-positive breast cancer xenograft imaging. In vitro results showed that [^{18}F]TFPFN-5F7 exhibited a better binding affinity and a higher internalization rate than [^{18}F]TFPFN-2Rs15d. However, 2Rs15d binds to a different domain (domain I) than trastuzumab (domain IV) and pertuzumab (domain II), making it a suitable imaging agent for patients undergoing HER2-targeting antibody therapies, whereas 5F7 binds to domain IV. Nevertheless, *in vivo*, both tracers showed high specificity for HER2 tumours and lower kidney uptake compared to other available ^{18}F prosthetics. This reduced the radiation dose to the kidneys and improved tumour contrast, achieving tumour visualization comparable to residualizing labels [92]. Due to the similarly short physical half-life, [^{68}Ga]Ga-NOTA-2Rs15d was studied by Gondry *et al.* and Keyaerts *et al.* in breast cancer patients, demonstrating good reproducibility, safety, and effectiveness in detecting tumour heterogeneity [93, 94]. In a preclinical study by Ducharme *et al.* involving breast cancer xenografts with varying HER2 expression levels, [^{89}Zr]Zr-DFO-2Rs15d was used to investigate the biodistribution of the nanobody at later time points. The tracer demonstrated high specificity for HER2 and was only partially blocked by trastuzumab in vitro, likely due to the induced internalization after binding. However, while small tracers like nanobodies are primarily cleared through the kidneys, the consistent and prominent kidney uptake observed up to day 3 poses a challenge for dosimetry [95].

2.7. HER2 Affibody

Affibody molecules, which are protein scaffolds based on the Z domain of Staphylococcus Protein A, have an even smaller molecular size than nanobodies (just a few kDa) and exhibit exceptionally high affinity for the HER2 receptor (in the pM KD range). $ZHER_{2:342}$ (ABY-002) was the first affibody tested in humans; however, it showed high liver uptake, which could impede the detection of hepatic metastases and necessitate modifications for optimal labelling, potentially altering the tracer's *in vivo* behaviour [96]. To address this, $ZHER_{2:2395}$ was developed with an added cysteine at the C-terminus, increasing labelling possibilities [97]. Further refinement led to $ZHER_{2:2891}$, which includes amino acid substitutions near the C-terminus to improve stability and increase hydrophilicity while retaining high affinity for HER2 [98], adding a cysteine residue along with a DOTA chelator produces ABY-025.

[^{68}Ga]Ga-ABY-025 has been clinically tested, demonstrating a lower absorbed dose compared to FDG [99] and effectively differentiating HER2 positivity, particularly through the TBR (optimally tumour-to-spleen ratio) [100]. It was also able to detect HER2 heterogeneity [101], which is especially beneficial in HER2-low patients [102]. While the correlation with IHC was not significant [102], the tracer did show a significant correlation with metabolic response to HER2-targeted therapy [103].

To reduce the hepatic uptake of $ZHER_{2:342}$ tracers, Xu *et al.* developed $MZHER_{2:342}$ by adding a hydrophilic linker and labelling the affibody with different isotopes. In preclinical models, [^{18}F]F-Al-MAL-NOTA-Cys-$MZHER_{2:342}$ successfully demonstrated HER2 specificity and showed a significant correlation with HER2 IHC scores (r^2 = 0.99). This labelling strategy also further decreased liver uptake, along with low bone uptake, indicating enhanced tracer stability; however, kidney uptake remained high [104]. Similarly, [^{68}Ga]Ga-MAL-NOTA-Cys-$MZHER_{2:342}$ was able to differentiate HER2 positivity in patients and showed lower liver uptake compared to ABY-025 [105]. [^{89}Zr]Zr-DFO-MAL-NOTA-Cys-$MZHER_{2:342}$ in tumour-bearing mice also exhibited HER2 specificity, with reduced liver and osseous uptake, further suggesting the tracer's stability [106]. Consequently, this highlights the flexibility and reproducibility of labelling $MZHER_{2:342}$ and its potential for future studies.

Affibody molecules represent a promising approach for HER2 breast cancer imaging, and ongoing developments aim to enhance their performance. Recently, $ZHER_{2:2891}$ was modified to ABY-027 (including an albumin-binding domain) to reduce kidney uptake and tested in preclinical models with [^{177}Lu]Lu-ABY-027 for targeted radionuclide therapy [107].

Additionally, the newer affibody $ZHER_{2:41071}$ features improved stability and hydrophilicity and is currently being evaluated in clinical studies using SPECT imaging with the ^{99m}Tc-$ZHER_{2:41071}$ tracer [108].

2.8. Other Scaffolds and Peptides

Similar to affibodies, ADAPT6 (ABD-Derived Affinity ProTein), a scaffold derived from the albumin binding domain (ABD) of streptococcal protein G, can target HER2 with high affinity and rapid clearance. A study using (HE)3DANS-ADAPT6-GSSC labelled with ^{68}Ga by different chelators showed high affinity for HER2-positive breast and ovarian cancer cell lines in vitro. *In vivo* testing on ovarian cancer-bearing mice revealed that [^{68}Ga]Ga-(HE)3DANS-ADAPT6-GSSC- NODAGA achieved the best TBR (compared to DOTA, DOTAGA, and NOTA variants), highlighting its potential as a promising small molecule for HER2 targeting [109].

Another promising candidate is DARPins (designed ankyrin repeat proteins), small peptides with a high affinity for HER2. [^{89}Zr]Zr-DFO-G3-DARPin, produced by Fay *et al.* through sortase enzyme site-specific conjugation, despite the slow conjugation process, demonstrated high affinity and specificity with excellent tumour contrast in breast cancer xenograft preclinical models [110].

Protein scaffolds of bacterial origin, or to a lesser extent from camelid, may trigger immunogenic responses [111]. Small synthetic peptides are a promising class of candidates for HER2 imaging due to their ease of modification and reduced immunogenicity. However, these peptides can be degraded by enzymes *in vivo*, so strategies like D- or beta-amino acid substitution, cyclization, and PEGylation are often employed to enhance their stability [112]. Among the studied peptides, two are particularly notable: KCCYSL, which has a high affinity with a Kd of 295 nM and binds to a different site than trastuzumab, and LTVSPWY, which, while having a lower affinity, binds to the same site as trastuzumab [113]. A study by Biabani *et al.* using [^{68}Ga]Ga-DOTA-$(Ser)_3$-LTVSPWY to assess HER2-positive breast cancer xenografts in mice showed high tumour affinity, with a significant decrease in uptake when blocked both in vitro and *in vivo* with an unlabelled peptide. The tracer demonstrated serum and *in vivo* stability, with rapid renal clearance due to increased hydrophilicity from serine residues. Despite high initial renal activity, uptake decreased rapidly after 1 hour, maintaining an adequate tumour-to-blood ratio of 1.7 at 2 h post-injection [114]. Another study by Ducharme *et al.* compared [^{68}Ga]Ga-DOTA-PEG_2-DTFPYLGWWNPNEYRY and [^{68}Ga]Ga-DOTA-PEG_2-GSGKCCYSL, using phosphoramidon to protect against degradation. Although both tracers demonstrated significant differences between HER2-positive and HER2-negative tumours. The differences were inconsistent across time points (1h versus 2h post-injection) and did not show significant uptake decreases in the *in vivo* PET blocking study. Nonetheless, [^{68}Ga]Ga-DOTA-PEG$_2$-DTFPYLGWWNPNEYRY appeared more promising, with higher tumour uptake at 1 h post-injection and greater stability in human serum [115].

In conclusion, small molecules (nanobodies, affibodies, *etc*.) targeting HER2 offer significant advantages, including high affinity and rapid clearance, leading to high tumour contrast and lower absorbed doses. However, they commonly suffer from high kidney uptake, prompting various strategies to address this issue, such as administering Gelofusine, adding linkers like PEG or PAS, using non-residualizing chelators or prosthetics, and improving tracer stability [116]. However, these modifications can potentially alter the peptide's function and biodistribution, underscoring the need for further research to develop optimal HER2 imaging agents.

Table 1. *Summary of radiopharmaceuticals assessing conventional biomarkers in breast cancer across preclinical and clinical studies*

Radiopharmaceuticals		**Clinical/ Preclinical phase**	**Key features**	**References**
Trastuzumab labelled ^{89}Zr	[^{89}Zr]Zr-DFO-trastuzumab	Clinical	Effective in detecting HER2+ metastases, including brain lesions Helped predict and follow-up therapy response, especially when combined with FDG PET/CT Challenges include false positives in liver and bone possibly due to instability.	[57-66]
	[^{89}Zr]Zr-HOPO-trastuzumab	Preclinical	Improved stability but lower tumour uptake compared to [^{89}Zr]Zr-DFO-trastuzumab	[67]
	[^{89}Zr]Zr-DFO*-trastuzumab	Preclinical	Improved stability, retained high tumour contrast compared to [^{89}Zr]Zr-DFO-trastuzumab, and was able to visualize HER2+ metastasis in bone	[68]
	[^{89}Zr]Zr-DFO-^{ss}trastuzumab-EndoS, [^{89}Zr]Zr-DFO-^{nss}trastuzumab-PNGaseF	Preclinical	Higher tumour uptake and higher tumour contrast (especially against liver and spleen) compared to [^{89}Zr]Zr-DFO-trastuzumab Required enzymatic deglycolysating step	[69]
Trastuzumab labelled ^{64}Cu	[^{64}Cu]Cu-DOTA-trastuzumab	Clinical	Successful for imaging HER2+ metastasis, including brain metastases Potential in predicting therapy responses Noted transchelation with serum compounds.	[71-74]

	[^{64}Cu]Cu-NOTA-trastuzumab	Clinical	Higher tumour contrast and lower off-target uptake and absorbed compared to [^{64}Cu]Cu-DOTA-trastuzumab	[75, 76]
Pertuzumab labelled ^{89}Zr	[^{89}Zr]Zr-DFO-pertuzumab	Clinical	Was able to detect HER2+ metastasis, including brain metastasis Showed potential in predict and follow-up therapy responses (even during trastuzumab treatment) Has slightly higher absorbed dose compared to [^{89}Zr]Zr-DFO-trastuzumab	[78-82]
	[^{89}Zr]Zr-^{ss}DFO-pertuzumab	Clinical	Improved tumour-to-liver and –spleen ratios, but increased renal absorbed dose compared to [^{89}Zr]Zr-DFO-pertuzumab	[83, 84]
Trastuzumab emtansine labelled ^{89}Zr	[^{89}Zr]Zr-DFO-T-DM1	Preclinical	Higher HER2+ tumour uptake than [^{89}Zr]Zr-DFO-trastuzumab Potential in predict T-DM1 responses	[85, 86]
Labelled trastuzumab fragments	[^{68}Ga]Ga-NOTA-F(ab')-trastuzumab, [^{68}Ga]Ga-NOTA-F(ab')$_2$-trastuzumab	Preclinical	Faster clearance than trastuzumab while retain affinity F(ab') tracer showed faster clearance and higher tumour-to-background ratios than F(ab')$_2$, except for tumour-to-kidney ratios	[87]
	[^{64}Cu]Cu-MANOTA-Fab-trastuzumab	Preclinical	Better stability and tumour contrast than using other chelators (DOTA, DOTAGA, NODAGA) Clear visualization of the HER2+ tumour from 4h p.i.	[88]
	[^{68}Ga]Ga-DFO-M74 trastuzumab's Fab	Preclinical	Better stability and higher tumour contrast compared to non-specific wild type Fab tracer	[89]
	[^{89}Zr]·DFO-HER2-Fab-PAS$_{200}$	Clinical	Extend biological half-life and improved tumour visualization including metastasis	[90, 91]
HER2 nanobody	[^{18}F]TFPFN-5F7, [^{18}F]TFPFN-2Rs15d	Preclinical	Lower kidney uptake, improved tumour contrast compared to tracers using other ^{18}F prosthetics	[92]
	[^{68}Ga]Ga-NOTA-2Rs15d	Clinical	Confirmed safety and reproducibility, able to detect inter-lesion heterogeneity Discordance with IHC results posed challenges	[93, 94]
	[^{89}Zr]Zr-DFO-2Rs15d	Preclinical	Explored the biodistribution of the tracer at later time points, kidney uptake remained a dosimetry challenge	[95]
HER2 affibody	[^{68}Ga]Ga-ABY-025	Clinical	Detected HER2 heterogeneity and was able to follow HER2 targeting therapy Tumour uptake correlation with IHC was not significant	[99-103]
	[^{18}F]F-Al-MAL-NOTA-Cys-MZHER$_{2:342}$	Preclinical	Good HER2 specificity with lower liver uptake than ZHER$_{2:342}$ tracers. Low bone uptake indicated tracer stability	[104]

	[^{68}Ga]Ga-MAL-NOTA-Cys-MZHER$_{2:342}$	Clinical	Able to differentiate HER2 positivity Lower liver uptake compared to ABY-025 tracer	[105]
	[^{89}Zr]Zr-DFO-MAL-NOTA-Cys-MZHER$_{2:342}$	Preclinical	Good HER2 specificity with low liver and bone uptake, indirectly indicated tracer’s stability	[106]
Other HER2 scaffolds and peptides	[^{89}Zr]Zr-DFO-G3-DARPin	Preclinical	High HER2 affinity and specificity but prominent kidney uptake, and slow site-specific conjugation step	[110]
	[^{68}Ga]Ga-DOTA-(Ser)$_3$-LTVSPWY	Preclinical	Good HER2+ tumour visualization, and tracer’s stability despite prominent kidney uptake	[114]
	[^{68}Ga]Ga-DOTA-PEG$_2$-DTFPYLGWWNPNEYRY, [^{68}Ga]Ga-DOTA-PEG$_2$-GSGKCCYSL	Preclinical	[^{68}Ga]Ga-DOTA-PEG$_2$-DTFPYLGWWNPNEYRY showed better human serum stability and significant differentiate HER2-positivty 1h p.i. than [^{68}Ga]Ga-DOTA-PEG$_2$-GSGKCCYSL	[115]

III. Aims of the Studies

1. Evaluation of Metabolic Activity & αvβ3 Expression in Aggressive Breast Cancer

Angiogenesis process involves the upregulation of pro-angiogenic factors and the inhibition of anti-angiogenic factors. Given the significant energy requirements of intercellular interactions within the cancer microenvironment, exploring the potential relationship between angiogenesis and glucose metabolism is essential to understanding their interplay.

[^{68}Ga]Ga-NODAGA-c(RGDfK)$_2$, a dimeric cyclic penta-peptide RGD-based radiopharmaceutical was used for angiogenesis imaging. Thanks to the relatively short biological and physical half-lives of [^{18}F]FDG and [^{68}Ga]-c(RGDfK)$_2$ ($T_{1/2}$^{18}F = 109.7 minutes, $T_{1/2}$^{68}Ga = 68 minutes), we were able to perform a longitudinal preliminary study using dual radiopharmaceuticals to closely monitor tumour progression. The study evaluated the correlation between tumour-to-muscle ratios of the two tracers and tumour growth in xenograft models. Two cell lines were investigated: the fast-growing 4T1 (triple-negative murine breast cancer) and the slower-growing MDA-MB-HER2+ (HER2-positive human breast cancer), representing the two most aggressive breast cancer subtypes. Additionally, tumour heterogeneity was analysed in the 4T1 model.

2. Preclinical Evaluation of ^{52}Mn-Trastuzumab for Biodistribution, HER2 Imaging, and Biological Characterization

In comparison with other prolonged half-live radiometals for antibody labelling, ^{52}Mn is a promising candidate. ^{52}Mn can be produced from natural chromium by conventional medical cyclotron using 16–6 MeV bombardment energy [117]. With a similar extended half-life of 5.6 days, ^{52}Mn, imaging, offers an attractive radiation profile compared to ^{89}Zr and ^{64}Cu. Its 29% positron emission with low maximum and average energy results in enhanced resolution (Table 2) comparable to ^{18}F. However, dosimetry calculations should be approached with caution due to the higher energy γ-photons [118, 119].

***Table 2**. Decay properties, production methods for potential trastuzumab-radiometals* [118, 119]

Radionuclide	$T_{1/2}$	Max β^+Energy (MeV)	Average β^+Energy/ I_{β^+} (%)	Principle γ Emissions / I_γ (%)	Target Material and Natural Abundance
^{89}Zr	3.27 d	0.900	396 keV/ 23%	909 keV/ 99%	^{89}Y (100%)
^{64}Cu	12.8 h	0.656	278 keV/ 18%	-	^{64}Ni (0.9%)
^{52}Mn	5.6 d	0.575	242 keV/ 29%	1434 keV/ 100% 935 keV/95% 744 keV/90%	^{52}Cr (82%)

Manganese in the +2 oxidation state typically exhibits a coordination number of 6 or 7, making it well-suited for complexation with oxygen and nitrogen atoms [120]. Macrocyclic chelators often demonstrate greater inertness compared to acyclic chelators, which are prone to dissociation when exposed to excess Cu^{2+} ions [121, 122]. Thus, selecting suitable chelator for the labelling with ^{52}Mn process is required.

2.1. [^{52}Mn]Mn-DOTAGA(anhydride)-trastuzumab

DOTA, a macrocyclic chelator, is recognized for forming highly stable complexes with Mn^{2+}, boasting one of the highest binding affinities among studied chelators (stability constant log $K_{ML} > 19$) [123], and can be complexed with room temperature, which is crucial in labelling heat-labile trastuzumab [120].

In our first ^{52}Mn-trastuzumab study, our team chose DOTAGA-anhydride (a derivative of DOTA chelator) as a bifunctional chelator owing to its high reactivity, regioselective anhydride-opening reaction, and the ability to conjugate without needing protection for other chelating ligands or producing unwanted side products [124]. Therefore, using [^{52}Mn]Mn-DOTAGA(anhydride)-trastuzumab we assessed the tumour uptake of HER2-positive and HER2-negative xenografts in preclinical models, melanoma xenografts were included as specificity control. Additionally, we investigated the tumour uptake differences between orthotopic and ectopic HER2-positive tumours.

2.2. [^{52}Mn]Mn-BPPA-trastuzumab

In our second ^{52}Mn-trastuzumab study, we designed a Mn(II)-specific chelator capable of providing satisfactory labelling yields, meanwhile showing sufficient stability and inertness. A novel bispyclen-based bifuncional chelator possessing a picolinate pendant arm, BPPA, was developed, synthesized, characterized, conjugated with trastuzumab, and labelled with

[^{52}Mn]Mn. The biological behaviour of the novel conjugate was investigated in different HER2-expressing breast tumour xenograft mouse models at both orthotopic and ectopic inoculation sites using PET/MRI imaging in comparison to a reference [^{52}Mn]Mn-DOTAGA(pSCN-Bn)-trastuzumab.

IV. Materials and Methods

1. Research 1: Temporal Assessment of Metabolic Activity and αvβ3 Expression in Aggressive Breast Cancer Models

1.1. Radiopharmaceuticals

NODAGA-c(RGDfK)$_2$ was obtained from ABX (Radeberg, Germany). Ultrapure HCl, NH4OAc buffer and water were purchased from Merck KGaA (Darmstadt, Germany). Oasis HLB 1 cc cartridge was the product of Waters Corporation (Milford, MA, USA). All other reagents and solvents were obtained from Sigma-Aldrich Ltd. (Budapest, Hungary) and were of analytical grade. They were used without further purification in all cases.

[^{18}F]FDG was produced following the Good Manufacturing Practice (GMP) standards for its clinical use in PET imaging. [^{18}F]FDG production was performed in the radiochemical laboratory of the Division of Nuclear Medicine and Translational Imaging, Department of Medical Imaging, Faculty of Medicine, University of Debrecen (Debrecen, Hungary).

Cyclotron produced ^{68}Ga (Division of Nuclear Medicine and Translational Imaging, Department of Medical Imaging, University of Debrecen, Hungary) was used for radiolabelling NODAGA-c(RGDfK)$_2$. After fractional elution, 0.5 ml eluate was buffered with 0.5 ml (3 mol/dm^3) ultrapure ammonium acetate to adjust the pH of the reaction mixture to 4–4.1 for each compound. A 10 µl (3 mmol/dm^3) NODAGA-RGD dimer acetate aq. solution was added, and the reaction solution was incubated for 15 min at 95°C. Then, solid-phase extraction (SPE – Waters Oasis HLB cartridge; 30 mg) was required to trap the radiopeptide. The radiolabelled peptide ([^{68}Ga]Ga-NODAGA-c(RGDfK)$_2$) was elutable from the HLB column with 0.1 ml of isotonic NaCl solution/EtOH 1:1 mixture. [^{68}Ga]Ga-NODAGA-c(RGDfK)$_2$ was produced with a high specific activity (15.7 ± 0.17 GBq/µmol) and a good radiochemical purity (>95%), in all cases. Quality control of the radiolabelled NODAGA-c(RGDfK)$_2$ was performed with thin-layer chromatography (TLC) and citrate buffer was used as an eluent (0.1 mol/dm^3; pH = 5.5).

1.2. Cell Lines and Preclinical Models

Cell lines were generously provided by Dr. György Vereb (Department of Biophysics and Cell Biology, University of Debrecen). They were cultured at 37°C with 5% CO$_2$ in Dulbecco's Modified Eagle Medium (DMEM, GIBCO, Life Technologies Magyarország Ltd., Budapest, Hungary), supplemented with 10% fetal bovine serum (FBS) (10%, heat-inactivated FBS from GIBCO, Life technologies) and 1% antibiotic-antimycotic solution (1%, Sigma-

Aldrich, Merck KGaA, Darmstadt, Germany). Monolayer cultures were passaged three times a week.

Female CB17 SCID mice, weighing 21.68 ± 2.74 g and between ages of 12 to 16 weeks, were divided into two groups: one group of mice ($n = 3$, initially but one mouse died during the protocol) was inoculated into mammillary fat pad with a fast-growing cell line (4T1), whereas the other group ($n = 3$) received a slow-growing tumour cell line (MDA-MB-HER2+). The animal research was registered by the University of Debrecen Committee of Animal Welfare (registration No: 8/2016/DEMÁB). Compliance with all relevant Hungarian laws and European Union animal welfare guidelines, following the "4R" principles (reduce, refine, replace, and responsibility), was ensured in animal handling.

4T1 cells and MDA-MB-HER2+ cells were injected into the fat pad of the inguinal breast at a concentration of 5×10^6 cells in saline (150 µl 0.9% NaCl) to achieve optimal xenograft growth [125]. For a complete xenograft establishment, imaging was started two days after tumour onset (when tumours were first detected and palpable): 7 days and 20 days after inoculation of 4T1 [126] and MDA-MB-HER2+ cell lines, respectively (Figure 1).

1.3. In Vivo Experimental Protocol

Both the groups received FDG and RGD four times on separate days. In the 4T1 group, mice were scanned four times in two weeks with both tracers, whereas the HER2-positive group underwent weekly scans for four weeks (Figure 1).

Administration of the radiopharmaceuticals into the lateral tail veins was carried out under inhalational anaesthesia. The acquisition occurred after an incubation period, allowing sufficient time for urinary excretion to minimize urinary bladder uptake. The exact injected radioactivity was determined by measuring the syringe volume and calculating the activity using a dose calibrator before and after every injection.

The administered dose of $[^{18}F]FDG$ was 14.83 ± 2.91 MBq. Prior to scanning, mice were subjected to overnight fasting, lasting for at least 12 h, to minimize background uptake in the blood pool and myocardium. The incubation time before scanning was 80.45 ± 2.47 min.

The administered dose of $[^{68}Ga]Ga\text{-}NODAGA\text{-}c(RGDfK)_2$ was 14.45 ± 3.83 MBq. All mice were provided with a sterile semi-synthetic rodent diet and sterile tap water before the scan. The incubation time before scanning was 82.95 ± 5.27 min.

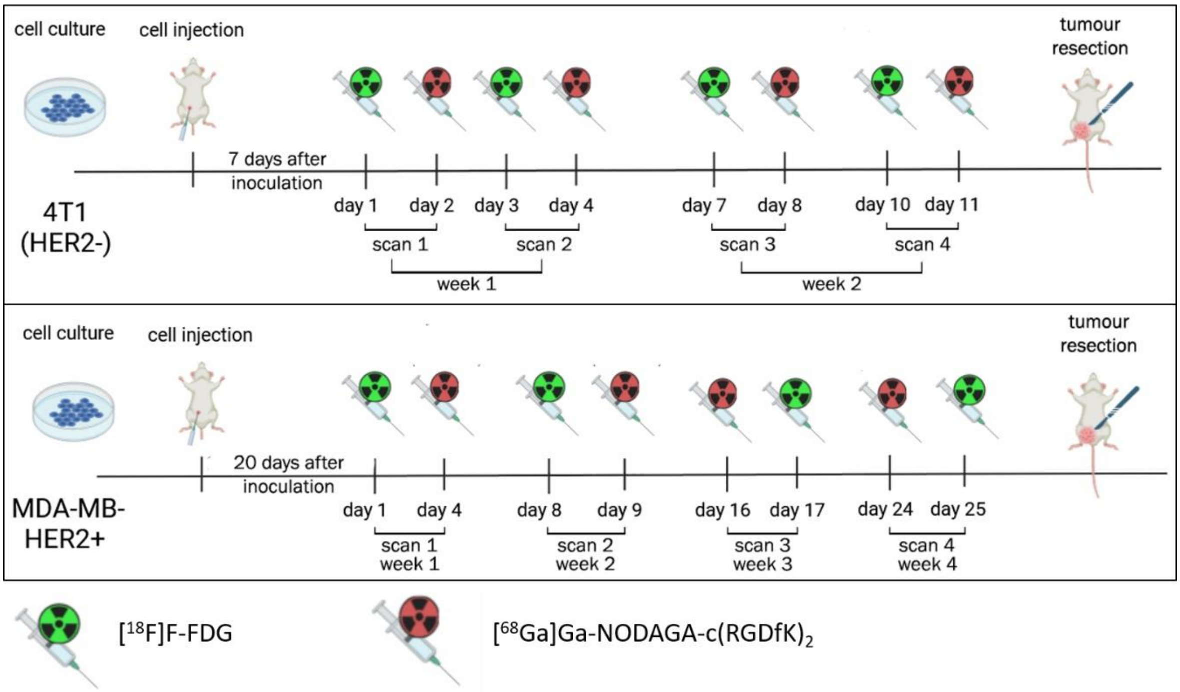

Figure 1. *Timeline of the study including cell culturing, tumour inoculation, and scanning time of the fast-growing cell line 4T1 (upper) and of the slow-growing cell line MDA-MB-HER2+ (lower).*

1.4. In Vivo Imaging Protocol

PET/MRI images were conducted using the nanoScan® PET/MRI 1T (Mediso Ltd., Budapest, Hungary) while ensuring the animals remained under inhalational anaesthesia with isoflurane (Forane, AbbVie, Budapest, Hungary) (3% for initiation and 2% for maintenance) with a continuous supply of 0.4 l/min oxygen (Linde Healthcare, Budapest, Hungary) and 1.2 l/min nitrous oxide gas (Linde Healthcare). The animals were securely positioned on a scanning bed to maintain a constant body temperature of 37°C throughout the procedure.

PET acquisitions lasted for 20 min with a field of view (FOV) of 98.5 mm. Following the PET scan, MRI acquisition was performed with specific parameters: flip angle of 20 degrees, repetition time of 15 ms, echo time of 2 ms, FOV of 60 mm, and number of excitations was set to 2, for approximately 18 min.

Reconstruction of the acquired raw data was carried out using Nucline software (Mediso Ltd., Budapest, Hungary) and employed the 3D-OSEM (Ordered Subset Expectation Maximization) algorithm with attenuation correction and random correction. When reconstructing [^{18}F]FDG images, the voxel size was set at 0.4 mm^3 with 6 iterations and low regularization. In contrast, the reconstruction of [^{68}Ga]Ga-NODAGA-c(RGDfK)$_2$ images utilized a smaller voxel size of 0.3 mm^3, 12 iterations, and high regularization to enhance resolution and minimize partial volume effects, which is more pronounced when imaging with ^{68}Ga due to its higher positron energy of 1.9 MeV [127].

1.5. In Vivo PET Measurements

Measurements were done with InterView™ FUSION software (Mediso Ltd., Budapest, Hungary). Volume-of-interests (VOIs) were delineated on both tumour and muscle reference areas using Muscle-Spacing Correction Method, *i.e.,* using muscle reference with an equal distance from the urinary bladder to correct its spillover effect (Figure 2).

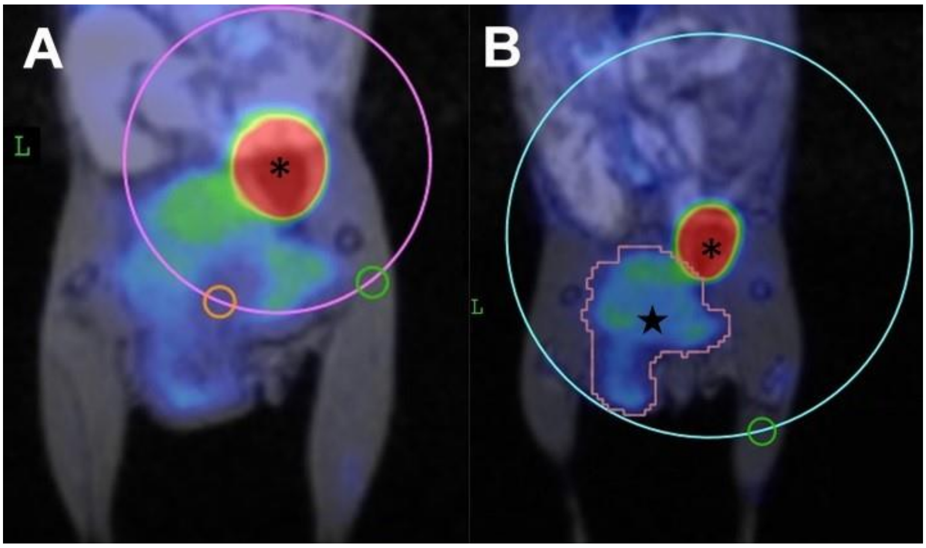

Figure 2. *Muscle-Spacing Correction Method: To guarantee the equal distance from the urinary bladder to each measured volume of interest (VOI), a large VOI is drawn over the centre of the urinary bladder. This bladder VOI intersects with both the central point of the tumour's avid/non-avid area VOI / the furthest point of the whole tumour VOI from the bladder and the centre of the reference muscle VOI. (**A**) Evaluating tumour heterogeneity, pink circle denotes the urinary bladder VOI, orange circle indicates the non-avid area VOI, green circle represents the muscle reference VOI, and the asterisk sign indicates the urinary bladder. (**B**) Accessing the whole tumour uptake; light blue circle indicates the urinary bladder VOI, the brown VOI indicates the whole tumour VOI, and the green circle represents the muscle reference VOI; the asterisk marks the urinary bladder.*

To assess tumour heterogeneity, VOIs with a diameter of 2 mm were drawn over the most avid and least avid regions within the tumour. These VOIs were positioned equidistant with the reference VOIs from the centre of the urinary bladder to minimize the partial volume effect of the bladder activity (Figure 2A).

Activity of the entire tumour was assessed by drawing VOIs manually around the tumour's contour. Muscle uptake was used as a reference, and the distance from the bladder to the reference muscle was adjusted to match the distance of the farthest point of the tumour from the bladder (Figure 2B).

To calculate the Standardized Uptake Value (SUV) the following formula was used: SUV = [VOI activity (MBq/ml)] / [injected activity (MBq) / animal weight (g)]. Evaluation of tumour uptake was performed by calculating the ratio of tumour SUV_{mean} to muscle SUV_{mean}.

Regions of interest (ROIs) were drawn around the tumour contours in each axial slice of the MRI images. Tumour volumes were calculated by summing the areas of these ROIs and multiplying the result by the slice thickness (0.5 mm).

1.6. Histopathology and Immunohistochemistry

After the last scan, the mice were euthanized by cervical dislocation under anaesthesia, and the tumours were resected, fixed in 10% formalin and frozen at a fixed temperature of -20°C. The tumours were then sent for histopathologic and immunohistochemistry examinations. In addition to the conventional haematoxylin and eosin (H&E) staining, immunohistochemistry staining was performed to visualize the expression of GLUT1 transporter (GLUT1 Recombinant Rabbit Monoclonal Antibody, SA0377, Thermo Fisher Scientific, Dreieich, Germany) and avb3 integrin (Anti-Integrin αVβ3 Antibody, clone EM22703 ZooMAb® Rabbit Monoclonal, Merck KGaA, Darmstadt, Germany) proteins. Texas-red (Goat anti-Rabbit IgG (H+L) Cross-Adsorbed Secondary Antibody, Texas Red, Thermo Fisher Scientific) was used as the secondary antibody, and cell nuclei were counterstained with DAPI (DAPI ready-made solution, MBD0015, Merck KGaA, Darmstadt, Germany).

1.7. Data Presentation

Due to the small sample size, resulting in a non-normal distribution, data were presented as median and interquartile range: median (lower quartile to upper quartile). All the graphs were created using GraphPad Prism 9.4.1 software (GraphPad Software, Boston, MA, USA).

2. Research 2: HER2 Expression in Different Cell Lines and Inoculation Sites Assessed by [^{52}Mn]Mn-DOTAGA(anhydride)-trastuzumab

2.1. Chemicals

HPLC-MS grade ACN was from Scharlau. Rotipuran Ultra H2O (up H2O), Rotipuran Ultra HCl 34% (up HCl), Rotimetic 99.995% anhydrous sodium acetate (NaOAc), and Cellpure HEPES were purchased from Carl Roth. Lyophilized Seronorm Human (5 mL) was bought from Sero. Amicon Ultra (Ultracel – 30K, 0.5 mL) Centrigal Filters produced by Merck Millipore. 450 Å, 2.7 µm Bioresolve RP mAb Polyphenyl 2.1 x 50 mm column was used for analytical examinations. Instant Thin-Layer Chromatography Silica Gel (iTLC-SG) was supplied by Agilent Technologies.

2.2. ^{52}Mn Production

The ^{52}Mn isotope was produced by proton irradiation with a 14 MeV beam on a natural Cr target via a ^{52}Cr(p,n)^{52}Mn reaction. The purification of the radionuclide from $CrCl_3$ was performed on AG1-X8 anion-exchange resin using 3% (v/v) HCl in absolute ethanol and 0.1 M HCl solvents. A post-purification was carried out using DGA resin to remove other metal contaminants (*e.g.* Fe, Cu).

2.3. Synthesis of DOTAGA(anhydride)-trastuzumab

Trastuzumab (Ontruzant®, Samsung Bioepis) was purified on a 30 kDa centrifugal filter. Conjugation of pure antibody with DOTAGA-anhydride was carried out at pH 8 in 0.1 M $NaHCO_3$ with 20-fold chelator excess. The conjugation efficiency and DOTAGA substitution level were calculated by a UPLC-RA-MS (Waters) system (chelator/antibody ratio: 2.067). DOTAGA-trastuzumab was purified and concentrated to 37 ± 14 mg/ml in up. H_2O by ultrafiltration.

2.4. Preparation of [^{52}Mn]Mn-DOTAGA(anhydride)-trastuzumab

50 µL of 37 ± 14 mg/ml DOTAGA-trastuzumab solution was added to a mixture of [^{52}Mn]$MnCl_2$ solution in 0.1 M HCl (29 ± 17 MBq, 100 µL), 0.1 M NaOAc (140 µL) and 0.5 M NaOH (22.5 µL). The reaction mixture was incubated at room temperature for 15 min. Radiochemical purity (RCP) was determined on iTLC-SG by TLC chromatography, using 0.1 M citric acid solution. Each product had an RCP higher than 95%. The reaction mixture was divided into aliquots and diluted to 200 µL portions with 0.9 % NaCl solution (molar activity: 12.43 ± 10.85 MBq/mg).

2.5. In Vitro Comparative Cell Binding Study

Human breast cancer cell lines MDA-MB-HER2+ (HER2 expressing cell line) and MDA-MB-468 (HER2-negative cell line) (all from Department of Biophysics and Cell Biology, University of Debrecen), were cultured for 24 hours at 36°C in RPMI medium supplemented with 10% FBS at a concentration of 0.66×10^6 cells/mL for MDA-MB-HER2+ and 0.52×10^6 cells/mL for MDA-MB-468. The radiopharmaceutical [^{52}Mn]Mn-DOTAGA(anhydride)-trastuzumab, with an activity of 1.00 mCi (37 MBq), was added to the cell suspensions, and they were incubated at 36°C for 30, 60, 120, and 180 minutes. After each incubation period, radioactivity in the cells was measured using a gamma counter. Each cell line was performed in duplicate (n = 2)

2.6. Preclinical Model

MDA-MB-HER2+, MDA-MB-468, and murine melanoma cell line B16F10 were used for the in vivo study. The cells were cultured at 37°C with 5% CO2 in DMEM media (from GIBCO) that was supplemented with 10% FBS and a 1% antibiotic-antimycotic solution (from Merck). The monolayer cell cultures were passaged three times per week.

The study used female mice aged 16 – 24 weeks, weighing 22.90 ± 4.28 grams: CB17 SCID mice used for breast cancer xenograft study (n = 5), and C57BL/6 mice used for melanoma xenograft study (n = 3). All mice (Animalab Ltd., Hungary) were provided with a sterile semi-synthetic diet (VRF1, Akronom Ltd., Hungary) and sterile drinking water. The animal research was registered by the University of Debrecen Committee of Animal Welfare (registration No: 16/2020/DEMÁB). Animal handling followed all applicable Hungarian laws, and European Union animal welfare regulations taking into account the “4R” principle (based on the principles of reduction, replacement, refinement, and responsibility).

CB17 SCID mice were divided into 2 groups: HER2 positive group (n = 3) and HER2 negative group (n = 2, originally n = 3, one excluded due to death during scanning). The HER2 positive group was injected with 4 x 10^6 MDA-MB-HER2+ cells mixed thoroughly in 100 μL of saline solution before each injection. This group received two injections: one into the inguinal mammary fat pad and another subcutaneously into the subscapular area then the tumours were inoculated for 2 weeks after the injection. The HER2 negative group was inoculated subcutaneously under the scapula with 4 x 10^6 MDA-MB-468 cells suspended in 100 μL of saline solution for the duration of 4 weeks. C57BL/6 mice (n = 3) were injected with 2 x 10^6 B16F10 suspended in 100 μL of saline into the subscapular area and were inoculated for 2 weeks.

2.7. In Vivo PET Imaging

All mice were injected with 3.50 ± 0.59 MBq of [^{52}Mn]Mn-DOTAGA(anhydride)-trastuzumab intravenously into the lateral tail veins. Under inhalation anaesthesia (induction: 3% isoflurane, maintenance: 2% isoflurane combined with 1 – 2 l/min O_2 and 0.8 – 1 l/min N_2O) using anaesthesia device (IsoFlo, EICKEMEYER®), the HER2 positive groups scanned with hybrid cameras nanoScan® PET/CT (Mediso Ltd., Hungary), while the HER2 negative and melanoma bearing mice underwent scans with nanoScan® PET/MRI 1T (Mediso Ltd., Hungary). The scans were conducted using a scanning bed to minimize model movements, while closely monitoring temperature, heart rate, and respiratory rate throughout the procedure. The PET static scans with a duration of 20 minutes each scan were performed at 4 h, 24h, 48h, 72h, and 120h post-injection. The anatomical images for localization and attenuation correction maps were obtained by either MRI T1 gradient echo with 0.5 mm slice thickness, 20 ms repetition time, 2.6 ms echo time, and 20° flip angle; or CT with 180 projections, 55 kVp X-ray source.

The image reconstruction was done by Nucline software (Mediso Ltd., Hungary) using Tera-Tomo™ 3D maximum-likelihood expectation-maximization (MLEM) method with attenuation correction, random correction, and scatter correction. Using the InterView™ FUSION software (Mediso Ltd., Hungary), VOIs and ROIs were delineated on the reconstructed images. The VOIs and ROIs were drawn with a 3 mm diameter over the following areas: tumours, mediastinal blood pool, liver lobe, kidney cortex, spleen, lung lobe, pancreas, submandibular salivary gland, knee joint, ovary, lacrimal gland, intestine, urinary bladder, and quadriceps muscle. The measurements were done using the SUV was calculated by the software with the formula: SUV = [ROI or VOI activity concentration (MBq/mL)]/[injected activity (MBq)/mouse body weight (gram)]. The measured organs' and tumour' SUV means to muscle SUV mean ratios were used for investigation. Tumour sizes were assessed using the formula: tumour volume (mm^3) = 0.5 x length (mm) x width (mm) x height (mm) [128].

2.8. Histopathological Examination

After the *in vivo* measurements were completed, the mice were humanely euthanized by cervical dislocation under general anaesthesia. The tumours were then resected and fixed in 10% neutral buffered formalin. The fixed tumour samples were subsequently sent for histopathological analysis, including staining with H&E, and immunohistochemistry, to determine HER2 status.

2.9. Statistical Analysis

The experimental data were expressed as mean ± standard deviation (SD). Two-way analysis of variance (ANOVA) with post-hoc Tukey's test was used to analyse the data. A *p*-value less than 0.05 was considered statistically significant. Data analysis and presentation were performed using GraphPad Prism 9.4.1 software and Microsoft Excel.

3. Research 3: Evaluation of [^{52}Mn]Mn-BPPA-trastuzumab for Highly Specific HER2 PET Imaging

3.1. Synthesis and Characterization of BPPA and New Compounds

Starting commercial reagents/solvents were purchased from Sigma-Aldrich (St. Louis, MO, USA), Tokyo Chemical Industry (Tokyo, Japan) and Fluorochem (Hadfield, Glossop, UK) and were used without further purification unless otherwise stated. The syntheses requiring microwave irradiation were performed in a CEM Discover microwave synthesis reactor (CEM Corp., Matthews, NC, USA), using dynamic (constant temperature) mode and strong stirring during the reactions. Deionized Milli-Q® water and gradient/LC-MS grade acetonitrile was used for the preparation of all eluents and samples for High Performance Liquid Chromatography (HPLC) and Mass Spectrometry (MS) measurements, and preparative HPLC separations. Analytical HPLC was performed with a Waters Alliance 2690/5 HPLC (Waters Corp., Milford, MA, USA) system equipped with a Waters 996 or Waters 2996 photodiode array detector with an Alliance series column heater at 25°C temperature. Eluent composition and other parameters are specified separately for each chromatogram. Small molecules were analysed with a Luna C18(2) column (150 mm × 4.6 mm, 100 Å, 3 µm or 5 µm, Phenomenex Inc., Torrance, CA, USA) or an XBridge Shield RP18 C18 column (75 mm × 4.6 mm, 100 Å 2.5 µm, Waters Corp., Milford, MA, USA). Results were evaluated with Waters Empower software. Preparative reverse-phase HPLC was performed using a YL9100 (YoungIn Chromass, Anyang-si Korea) system equipped with a YL91110s quaternary pump and a YL9120s UV/Vis detector. Small molecules were purified on a Luna C18(2) Prep column (250 mm × 21.2 mm, 100 Å, 5 µm, Phenomenex Inc., Torrance, CA, USA). Eluent composition and other parameters are specified separately for each compound.

Nuclear magnetic resonance (NMR) spectra (^{1}H and ^{13}C-JMOD) were recorded at 298.0 K using a Bruker Avance DRX 360 MHz (360.13 MHz - ^{1}H, 90.55 MHz - ^{13}C) or Avance I 400 MHz (400.13 MHz - ^{1}H, 100.62 MHz - ^{13}C) or Bruker Avance II 500 MHz spectrometer. The chemical shifts (δ) were calibrated against reference solvent peaks (^{1}H, $\delta = 7.26$ ppm and ^{13}C, $\delta = 77.16$ ppm for $CDCl_3$; ^{1}H, $\delta = 4.79$ ppm for D_2O; ^{1}H, $\delta = 3.31$ ppm and ^{13}C, $\delta = 49.00$ ppm for CD_3OD, ^{1}H, $\delta = 1.32$ ppm and ^{13}C, $\delta = 118.26$ ppm for CD_3CN, ^{1}H, $\delta = 2.50$ ppm and ^{13}C, $\delta = 39.52$ ppm for DMSO-d_6) [129]. In ^{13}C-JMOD (J-modulated) spectrum the multiplicity of the ^{13}C signals (methyl: quartet, methylene: triplet, methine: doublet, quaternary: singlet) is reflected in the phase of the fully ^{1}H decoupled ^{13}C spectrum using the SEFT (Spin-Echo Fourier Transform) technique. In the spectrum, the methyl and methine signals (odd number of hydrogen atoms) give signals with positive phase, while the methylene and quaternary carbon atoms (even number and lacking hydrogen atoms) give negative phase signals.

High resolution (ESI) mass spectra were measured on a Bruker maXis II UHR ESI-QTOF mass spectrometer (Bruker, Bremen, Germany) using a capillary electrophoresis - electrospray ionization (CE-ESI) Sprayer interface (G1607B, Agilent). Sample introduction was carried out with an Agilent 7100 model capillary electrophoresis (CE) instrument (Agilent, Waldbronn, Germany) using a 70 cm x 75 µm id. capillary (Polymicro, Phoenix, AZ, USA). The MS instrument was controlled by otofControl version 4.1 (build: 3.5, Bruker), obtained mass spectra were processed by Compass DataAnalysis version 4.4 (build: 200.55.2969, Bruker). MS measurements were performed in positive ionization mode with the following instrument settings: 0.8 bar nebulizer pressure, 200°C dry gas temperature, 4.5 L/min dry gas flow rate, 3500 V capillary voltage, 500 V end plate offset, 1 Hz spectra rate, 100-1400 m/z mass range were applied. Sodium formate was used for internal m/z calibration.

3.2. Equilibrium, Kinetic and Relaxometric Characterization of the [Mn(BPPA)] Complex

Equilibrium studies

$MnCl_2$ stock solution was prepared from the highest analytical grade chemical, and its concentration was determined by complexometric titration with standardized Na_2H_2EDTA and eriochrome black T indicator in the presence of ascorbic acid and potassium hydrogen tartrate. The concentration of the ligand stock solution was determined by pH-potentiometric titration. For determining the protonation constants of the ligand, pH potentiometric titration was carried out with 0.15 M NaOH, using 0.0026 M ligand solution. The ionic strength was set to 0.15 M by using NaCl. The titrated samples (starting volume of 6.00 mL) were stirred mechanically and thermostated at 25°C by a circulating water bath (±0.1°C). The protonation constants of the ligand (log K_i^H) are defined as follows:

$$K_i^{\mathrm{H}} = \frac{[\mathrm{H}_i\mathrm{L}]}{[\mathrm{H}_{i-1}\mathrm{L}][\mathrm{H}^+]} \qquad \text{(eq. 1)}$$

where i = 1, 2, …, 5 and $[H_{i-1}L]$ and $[H^+]$ are the equilibrium concentrations of the ligand (i = 1), its protonated forms (i = 2, …, 5) and hydrogen ion, respectively. The stability constant of the MnL complexes is defined as follows:

$$K_{\mathrm{ML}} = \frac{[\mathrm{ML}]}{[\mathrm{M}][\mathrm{L}]} \qquad \text{(eq. 2)}$$

To avoid the effect of CO_2, N_2 gas was bubbled through the solutions during the titrations process. The pH-potentiometric titrations were performed with a Metrohm 785 DMP Titrino titration workstation with the use of a Metrohm 6.0234.100 combined electrode in the pH range of 1.75-11.85. For the calibration of the pH meter, KH-phtalate (pH = 4.005) and borax (pH = 9.177) buffers were used, and the $[H^+]$ concentrations were calculated from the measured pH values by applying the method proposed by Irving *et al.* [130]. A solution of approximately 0.01 M HCl was titrated with a 0.15 M NaOH solution (I = 0.15 M NaCl), and the differences between the measured and calculated pH values (for the points with pH < 2.2) were used to calculate the $[H^+]$ from the pH values measured in the titration experiments. The measured points with pH > 11.0 of the acid-base titration were used to calculate the ionic product of water which was found to be 13.882 under our experimental conditions.

The stability of $[Mn(BPPA)]^+$ was determined using standard pH-potentiometric approach by titrating a sample containing the $MnCl_2$ and the ligand 2.60 mM concentration, and accessed by ^1H relaxometric titration by applying an out-of-cell technique. Longitudinal (T_1) and transverse (T_2) relaxation times were recorded for samples at 20 and 60 MHz proton Larmor frequency containing 1.48 mM complex in the acid concentration range of 2.45 – 251 mM (a total 14 samples). Fitting of the equilibrium data was performed by PSEQUAD computer program [131] by fixing the molar relaxivity of the Mn(II) ion (determined previously) [132].

Relaxometric measurements

The ^1H longitudinal (T_1) and transverse (T_2) relaxation times were measured by using Bruker Minispec MQ-20 and MQ-60 NMR Analyzers. The temperature of the sample holder was set 25.0 (±0.2)°C and controlled with a circulating water bath thermostat. The r_{1p} values for the investigated complexes were determined by means of inversion recovery method (180° – τ – 90°), averaging 4-6 data points obtained at 12 different τ delay times, while r_{2p} data were collected by using Carl-Purcell-Meiboom-Gill (CPMG) spin-echo pulse sequence. Relaxivities were determined following published protocols using samples of 0.3-0.4 mL volume. pH was either set by using a 0.05 M 4-(2-hydroxyethyl)-1-piperazine-ethanesulfonic acid (HEPES) buffer (pH = 7.4) while the ionic strength in the samples was set to 0.15 M NaCl.

Dissociation kinetics

The inertness of the $[Mn(BPPA)]^+$ complex was assessed by following the transmetallation reaction provoked by the large excess of the essential Zn(II) ions. The curse of the reaction was monitored by measuring the T_2 relaxation times as a function of time at pH = 6.0, set by 50 mM 2-(*N*-morpholino)ethanesulfonic acid (MES) buffer in the presence of 25 equivalents of Zn(II) ions at 25 and 37 °C. These conditions were used recently by P. Caravan *et al.* [133].

3.3. Chemicals and Synthesis of BPPA-trastuzumab and DOTAGA(pSCN-Bn)-trastuzumab

Rotipuran Ultra H_2O (u.p. H_2O), 34% Rotipuran Ultra HCl (u.p. HCl), Rotimetic 99.995% anhydrous sodium acetate (NaOAc) and Pufferan ≥ 99.5%, Cellpure HEPES were purchased from Carl Roth. HPLC-MS grade ACN was provided by Scharlau. Lyophilized Seronorm Human (5 mL) was bought from Sero.

Amicon Ultra (Ultracel – 30K, 0.5 mL) Centrigal Filters was provided by Merck Millipore. Bioresolve RP mAb Polyphenyl (450 Å, 2.7 µm) 2.1 x 50 mm column was purchased from Waters. Glass macrofiber chromatography paper impregnated with silica gel (iTLC-SG) was supplied by Agilent Technologies. The conjugation of trastuzumab with BPPA-Bn^{pMMA} and serum stability of [^{52}Mn]Mn-BPPA-trastuzumab was followed by a Waters Acquity UPLC I Class system with a Bertold FlowStar LB 513 radioactivity detector (RA) connected to a Xevo G2 Q-TOF mass spectrometer (UPLC-RA-MS). RCP of [^{52}Mn]Mn-BPPA and [^{52}Mn]Mn-BPPA-trastuzumab was determined by a Raytest miniGita Star thin layer chromatography scanner (TLC scanner).

Trastuzumab (Ontruzant®, Samsung Bioepis) was purified on a 30 kDa centrifugal filter. Antibody was conjugated with BPPA-Bn-pMMA and pSCN-Bn-DOTAGA was carried out at pH 8 – 8.2 in 0.1 M $NaHCO_3$ using 20 and 5 fold chelator excess, respectively. The conjugation efficiency and BPPA/DOTAGA substitution level was calculated by a UPLC-RA-MS system. BPPA-trastuzumab and DOTAGA-trastuzumab was purified and concentrated to 21 mg/ml in up. H_2O by ultrafiltration.

3.4. Optimization of Radiolabelling Conditions of [^{52}Mn]Mn-BPPA

RCP of [^{52}Mn]Mn-BPPA was examined in the presence of 0.03, 0.1, 0.3, 1, 3, 10, 30 and 100 µM ligand, in the pH range of 4 - 8. A 10 µL [^{52}Mn]$MnCl_2$ solution (~200 kBq), 80 µL buffer solution and 10 µl of 0.3, 1, 3, 10, 30, 100 or 300 µM ligand solutions were mixed in order to reach the required concentration of ligands. 0.5 M u.p. NaOAc was applied as buffer in the pH range of 4 - 6 and 0.5 M HEPES was used at pH 7 and 8. Reactions were carried out in Eppendorf tubes with 5 min reaction time at 25°C and 95°C in a dry bath. Labelling of BPPA with [^{52}Mn]$MnCl_2$ was followed by TLC scanner. 3 µL of the reaction mixture was dropped to an iTLC-SG strip and developed in 3% NH_3 solution. ^{52}Mn(II) was remained near the start point (Rf = 0.1 – 0.2), whereas [^{52}Mn]Mn-BPPA was eluted with the solvent front (Rf = 0.7 - 0.9).

3.5. Preparation of [^{52}Mn]Mncl$_2$, [^{52}Mn]Mn-BPPA-Bn^{pCOOH} and [^{52}Mn]Mn-DOTAGA for In Vivo Imaging

[^{52}Mn]MnCl$_2$

35 µL of [^{52}Mn]MnCl$_2$ solution in 0.1 M HCl (12 MBq) was diluted with 65 µL 0.1 M NaOAc and 5.2 µL 0.5 M NaOH. Reaction mixture was incubated at room temperature for 10 min. 3 x 4 MBq of reaction mixture was diluted to 200 µL portions with saline and their pH was checked by pH paper (pH 6.0 – 6.5).

[^{52}Mn]Mn-BPPA-Bn^{pCOOH}

30 µL of 1 mg/ml BPPA-Bn^{pCOOH} (59 nmol) solution was added to a mixture of [^{52}Mn]MnCl$_2$ solution in 0.1 M HCl (50 µL; 30 MBq), 0.1 M pH 7 HEPES (43.5 µL) and 0.5 M NaOH (10 µL). Reaction mixture was incubated at room temperature for 10 min. RCP was determined by TLC chromatography. 3 x 4.5 MBq of reaction mixture was diluted to 200 µL portions with saline.

[^{52}Mn]Mn-DOTAGA

15 µL of 1 mg/ml DOTAGA (63 nmol) solution was added to a mixture of [^{52}Mn]MnCl$_2$ solution in 0.1 M HCl (40 µL; 22 MBq), 0.1 M NaOAc (65 µL) and 0.5 M NaOH (6 µL). Reaction mixture was incubated at room temperature for 10 min. RCP was determined on iTLC-SG by TLC chromatography, using 3% NH_3 eluent. 3 x 3.5 MBq of reaction mixture was diluted to 200 µL portions with saline.

3.6. Preparation of [^{52}Mn]Mn-BPPA-Trastuzumab and [^{52}Mn]Mn-DOTAGA(pSCN-Bn)-Trastuzumab for In Vivo Imaging

[^{52}Mn]Mn-BPPA-trastuzumab

10 - 15 µL of 21 mg/ml BPPA-trastuzumab solution was added to a mixture of [^{52}Mn]MnCl$_2$ solution in 0.1 M HCl (50 µL; 16 – 26 MBq), 0.1 M pH 7 HEPES (43.5 µL) and 0.5 M NaOH (10 µL). Reaction mixture was incubated at room temperature for 15 min. RCP was determined on iTLC-SG by TLC chromatography, using 0.1 M citric acid. The reaction mixture was divided into three aliquots and diluted to 200 µL portions with saline.

[^{52}Mn]Mn-DOTAGA(pSCN-Bn)-trastuzumab:

35 - 40 µL of 21 mg/ml DOTAGA-trastuzumab solution was added to a mixture of [^{52}Mn]MnCl$_2$ solution in 0.1 M HCl (32 – 36 MBq), 0.1 M NaOAc (65 µL) and 0.5 M NaOH (7 - 10 µL). Reaction mixture was incubated at room temperature for 15 min. RCP was

determined on iTLC-SG by TLC chromatography, using 0.1 M citric acid. The reaction mixture was divided into three aliquots and diluted to 200 µL portions with saline.

3.7. Determination of Serum Stability of [^{52}Mn]Mn-BPPA-trastuzumab and [^{52}Mn]Mn-DOTAGA(pSCN-Bn)-trastuzumab

[^{52}Mn]Mn-BPPA-trastuzumab and [^{52}Mn]Mn-DOTAGA(pSCN-Bn)-trastuzumab solution were diluted to five times its volume with human plasma (Seronorm), then placed into a closed syringe (sealed off from air) and incubated for 10 day at 37°C. The solutions were analysed at the following time points: 10 min, 2 h, 23 h, 2 d, 5 d, 7 d and 10 d. RCP values were determined on a polyphenyl column (Bioresolve RP mAb) by UPLC-RA-MS.

3.8. Experimental Animals

At least 16 weeks old, 23.02 ± 2.92 g weighted female CB17 SCID and BALB/c mice (n = 20; Animalab Ltd, Budapest, Hungary) were used for the experiments. The sterile semi-synthetic diet (VRF1; Akronom Ltd., Budapest, Hungary) and sterile drinking water were available ad libitum to all animals. The animal research was registered by the University of Debrecen Committee of Animal Welfare (registration No: 16/2020/DEMÁB). Laboratory animals were kept and treated in compliance with all applicable sections of the Hungarian Laws and animal welfare directions and regulations of the European Union.

3.9. Xenograft Inoculation

All cell lines were kindly gifted by Dr. Vereb György (Department of Biophysics and Cell Biology, University of Debrecen) and was grown at 37°C and 5% CO2 in DMEM media (GIBCO) supplemented with 10% FBS and 1% antibiotic-antimycotic solution (Merck), the monolayer cultures were passaged 3 times a week. CB17 SCID mice (n = 12) were anaesthetized with 3% isoflurane (Forane) applying an anaesthesia device (IsoFlo, EICKEMEYER®) and divided into 2 groups. Group 1 (n = 6) was inoculated at 2 sites with 5 x 10^6 4T1 (HER2−, triple negative mouse breast cancer) cells in 100 µL saline subcutaneously at the shoulder area and intramammarily at the orthotopic site to inguinal breast fat pad. Group 2 (n = 6) was inoculated also at 2 sites with 5 x 10^6 MDA-MB-HER2+ (a human breast cancer cell line expressing a high level of HER2 receptor, originally developed by Dr. György Vereb for HER2 studies) cells in 100 µL saline subcutaneously at the shoulder area and intramammarily at the orthotopic site to inguinal breast fat pad.

3.10. PET/MRI Imaging and In Vivo Measurements

Healthy BALB/c (n = 8) and MDA-MB-HER2+ (n = 6) and 4T1 (n = 6) tumour bearing CB17 SCID mice were examined. After 1-3 weeks of inoculating, as the tumours had reached 5–7 mm in maximum diameter the mice were anaesthetized (induction: 3% isoflurane, maintenance: 2% isoflurane combined with 1 – 2 l/min O_2 and 0.8 – 1 l/min N_2O) with anaesthesia device and injected at the lateral tail vein with 2.61 ± 0.36 MBq in 200 µl of $[^{52}Mn]MnCl_2$ or $[^{52}$Mn]Mn-DOTAGA or $[^{52}$Mn]Mn-BPPA (healthy mice), 2.52 ± 0.24 MBq in 200 µl $[^{52}$Mn]Mn-DOTAGA(pSCN-Bn)-trastuzumab or $[^{52}$Mn]Mn BPPA-trastuzumab (tumour bearing mice).

Throughout the scanning process mice were put on scanning bed (MultiCell Imaging Chamber, Mediso Ltd., Hungary) to maintain body temperature and to prevent movement. Right after injection 90 min dynamic whole-body PET/MRI (nanoScan PET/MRI 1T, Mediso Ltd., Hungary) scans were performed then 20 min static whole-body PET/MRI scans (98.5 mm FOV; 400 – 600 keV energy window) were carried out 4 h, 24 h, 72 h, 120 h, 156 h and 240 h post injection. Dynamic PET acquisitions were reconstructed with the time frame of 4 x 15 s, 4 x 60 s, 11 x 300 s and 3 x 600 s. For anatomical references, the mice were scanned by MRI T1 gradient echo with 0.5 mm slice thickness, 50 slices, and 20° flip angle.

After the scans, maximum-likelihood expectation-maximization (MLEM) reconstruction was completed by Nucline software (Mediso Ltd., Hungary) using Tera-Tomo 3D method, 0.4 mm^3 voxel size, 4 iterations, with attenuation correction, random correction and scatter correction. From the reconstructed images (InterView FUSION software, Mediso, Hungary), VOIs were drawn with a diameter of 3 mm over tumours and blood pool (over mediastinum), liver, lungs and muscle; ROIs with area of 7.065 mm^2 (corresponding to volume of a circle with a diameter of 3 mm) were drawn over kidney cortex, pancreas, and salivary gland. SUV was calculated using the following formula: SUV = [ROI activity (MBq/mL)]/[injected activity (MBq)/animal weight (g)].

3.11. Immunohistochemistry and Histopathology

Following the *in vivo* measurements, the mice were euthanized by cervical dislocation under general anaesthesia, the xenografts were resected and fixed with 10% formalin then sent for HER2 status immunohistochemistry analysis and histopathological examination.

3.12. Statistical Analysis

Experimental data was presented as mean with standard deviation (mean ± SD). Data were analysed using two-way ANOVA and student's t-test, $p \leq 0.05$ was considered to be statistically significant. All the computation was done by GraphPad software (GraphPad Prism 9.4.1) or Microsoft Office Excel.

V. Results

1. Research 1: Temporal Assessment of Metabolic Activity and αvβ3 Expression in Aggressive Breast Cancer Models

1.1. 4T1 Tumour Heterogeneity

During our two-week longitudinal study, there was significant heterogeneity in the tracer uptake in different areas within the 4T1 tumours. We monitored the changes in the activities of both high-uptake areas (avid areas) and low-uptake areas (non-avid areas) throughout the study (Figure 3). Based on SUV measurements, there were fluctuations in tumour/muscle ratios in both radiopharmaceuticals. As the tumours grew, the heterogeneity became more prominent (on days 7-8 and days 10-11). These differences were more pronounced when using [^{18}F]FDG compared to [^{68}Ga]Ga-NODAGA-c(RGDfK)$_2$. Specifically, the ratios of [^{18}F]FDG uptakes on days 10-11 were: avid areas 18.62 (14.99 to 22.25) *vs*. non-avid areas 7.06 (6.19 to 7.93); whereas with [^{68}Ga]Ga-NODAGA-c(RGDfK)$_2$ the ratios were: avid areas 13.98 (10.58 to 17.38) *vs*. non-avid areas 6.85 (6.74 to 6.97) (Figure 4A).

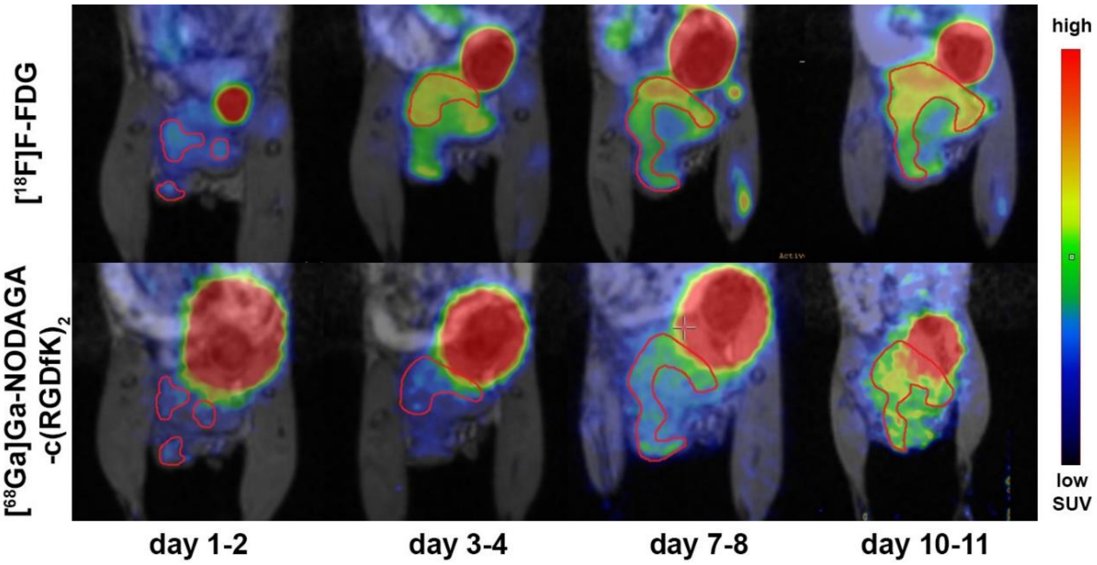

Figure 3*. PET/MRI hybrid images on different scanning days using [^{18}F]FDG (upper row) and [^{68}Ga]Ga-NODAGA-c(RGDfK)$_2$ (lower row) on 4T1 tumour-bearing mouse. Red contours highlight the avid areas within the tumour. The SUV scale is displayed at the right.*

Tracking the changes of the two tracers over time in both avid and non-avid areas revealed a synchronized pattern (Figure 4B).

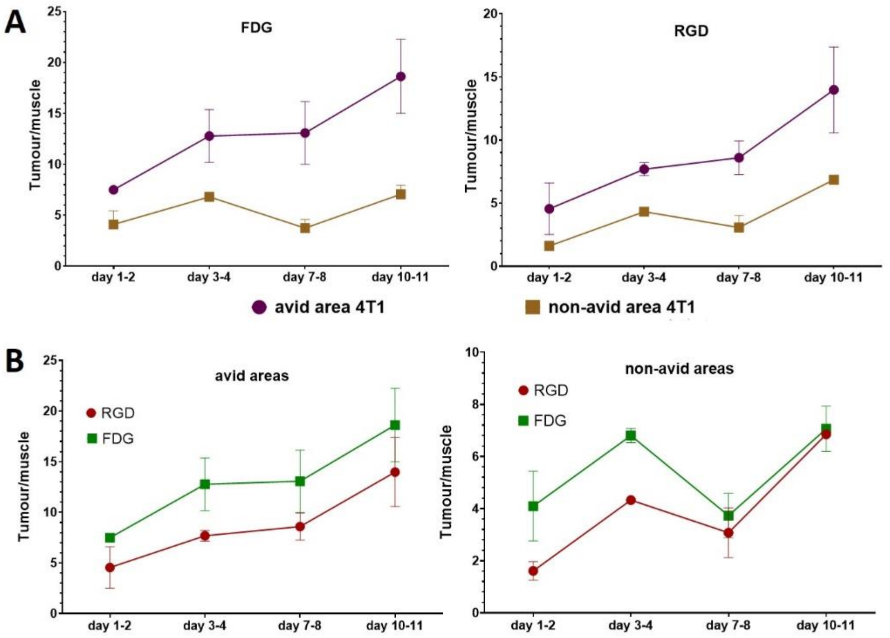

*Figure 4. Line graphs presenting tumour/muscle ratios using [^{18}F]FDG (FDG) and [^{68}Ga]Ga-NODAGA-c(RGDfK)$_2$ (RGD) in avid areas and non-avid areas of 4T1 tumours (**A, B**).*

1.2. 4T1 and MDA-MB-HER2+ Whole Tumour Assessment

Due to the noticeable trends between FDG and RGD in both avid and non-avid areas of fast-growing 4T1 tumours, we investigated the correlation across the entire tumour. Based on the line graphs following the two tracers over time, it was evident that the two ratios were comparable and their changes follow a similar direction. The scatter plot further confirmed this observation, revealing a relatively remarkable positive correlation between the two tracers, which both increased from the 1st scan [FDG: 7.22 (7.00 to 7.43), RGD: 9.05 (6.13 to 11.96)] to the 3rd scan [FDG: 9.05 (9.03 to 9.06), RGD: 12.63 (10.48 to 14.79)] (Figure 5A). Furthermore, HER2-positive graph also revealed a relative correlation in this slow-growing group, even though the correlation seemed weaker. Specifically, there was a slight increase in FDG from week 1: 2.04 (1.50 to 2.39) to week 2: 2.04 (1.74 to 2.015), and week 3: 2.45 (1.32 to 4.21), whereas the RGD decreased from week 1: 8.70 (7.76 to 9.93) to week 2: 7.50 (4.98 to 10.37), and week 3: 5.35 (5.26 to 25.88). Nevertheless, scatter plots revealed a noticeable correlation between the two tracers in both groups (Figure 5A).

However, there was a noticeable difference in the trend of whole tumour FDG ratios over RGD ratios between 4T1 and MDA-MB-HER2+ xenografts. The MDA-MB-HER2+ tumours exhibited higher tumour-to-muscle ratios for RGD compared to FDG, resulting in notably lower FDG-to-RGD ratios in this group, as demonstrated in the scatter plot (Figure 5A).

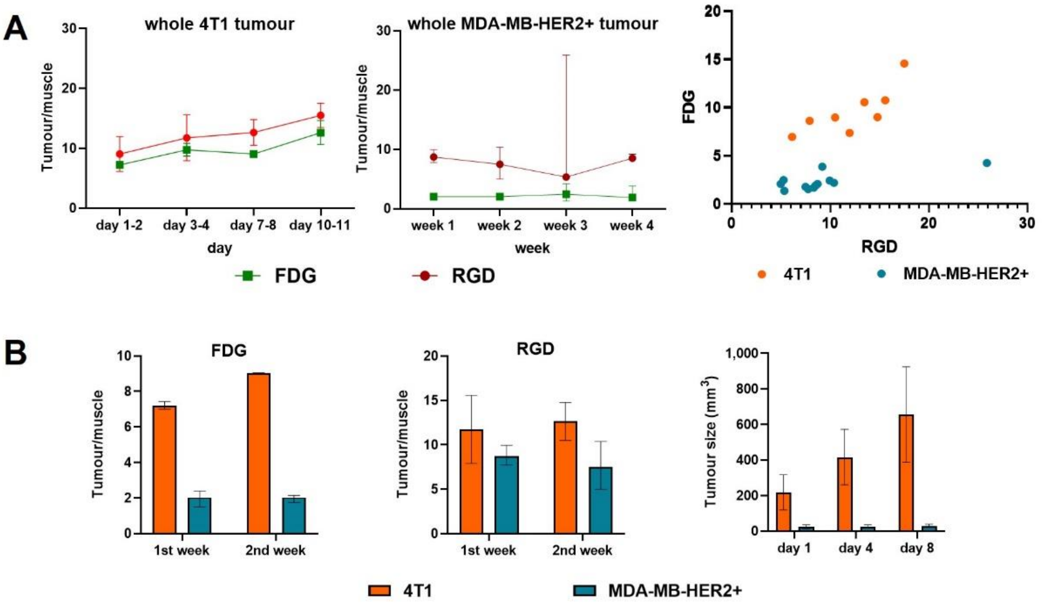

Figure 5. *Line graphs and scatter plots of whole tumour/muscle ratios using [^{18}F]FDG and [^{68}Ga]Ga-NODAGA-c(RGDfK)$_2$ in MDA-MB-HER2+ tumours and 4T1 tumours (**A**). Bar graphs demonstrate the tumour/muscle ratios using [^{18}F]FDG (left), [^{68}Ga]Ga-NODAGA-c(RGDfK)$_2$ (middle) in the 1st (day 1: FDG, day 4: RGD) and 2nd (day 7-8: FDG, day 8-9: RGD) scanning week on MDA-MB-HER2+ and 4T1 tumours, right bar graph compares tumour sizes of the two groups (**B**).*

There were notable differences in tumour sizes within the two groups, *i.e.*, on day 8: MDA-MB-HER2+ tumour size was 28.84 (27.97 to 39.98) mm^3, whereas 4T1 tumour size was 656.24 (387.81 to 924.66) mm^3 (Figure 5B). When comparing the FDG SUV$_{mean}$ ratios between the two groups on corresponding scanning days, consistently higher ratios were observed in the fast-growing 4T1 group. For instance, in the second week, the FDG ratio for 4T1 tumours was 9.05 (9.03 to 9.06), while for MDA-MB-HER2+ tumours, it was 2.04 (1.74 to 2.15). The difference was less pronounced for the RGD tracer [the ratios of 4T1 tumour *vs*. MDA-MB-HER2+ tumour on the second week were 12.63 (10.48 to 14.79) *vs*. 7.50 (4.98 to 10.37), respectively] (Figure 5B).

There were notable correlations between FDG ratios and RGD ratios with the tumour sizes in the 4T1 group. Both line graphs (Figure 6A) and scatter plots (Figure 6B) demonstrated comparable positive correlations between 4T1 tumour sizes and 4T1 tumour-to-muscle ratios using the two radiopharmaceuticals. However, these positive correlations were not as visible in the slow-growing group (Figure 7).

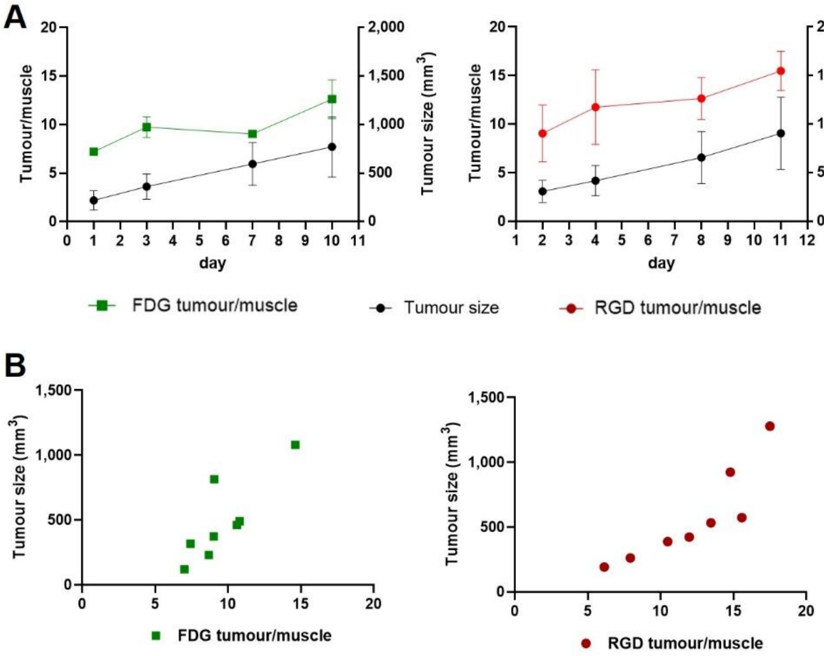

Figure 6. Line graphs (**A**) and scatter plots (**B**) showing changes over time and correlation between tumour sizes and whole tumour/muscle SUV$_{mean}$ ratios using [^{18}F]FDG (left) and [^{68}Ga]Ga-NODAGA-c(RGDfK)$_2$ (right) in 4T1 tumours.

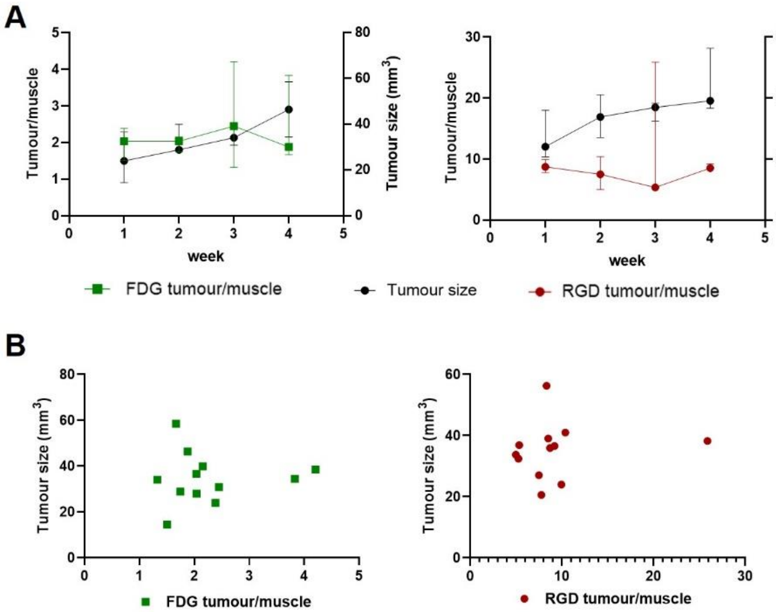

Figure 7. Line graphs (**A**) and scatter plots (**B**) showing changes over time and correlation between tumour sizes and whole tumour/muscle SUV$_{mean}$ ratios using [^{18}F]FDG (left) and [^{68}Ga]Ga-NODAGA-c(RGDfK)$_2$ (right) in MDA-MB-HER2+ tumours.

1.3. Histopathology and Immunohistochemistry Examination

H&E staining revealed that the triple-negative tumour group was stroma-rich, while the HER2-positive group showed prominent necrosis. GLUT1 transporter staining in the 4T1 xenografts showed strong, widespread staining, particularly in the stromal areas. HER2-positive tumours had less intense GLUT1 transporter staining, which showed a rather heterogeneous cellular distribution. The two tumour types displayed similar αvβ3 integrin staining intensities, with HER2-positive tumours showing slightly weaker stromal staining and a more uniform distribution (Figure 8).

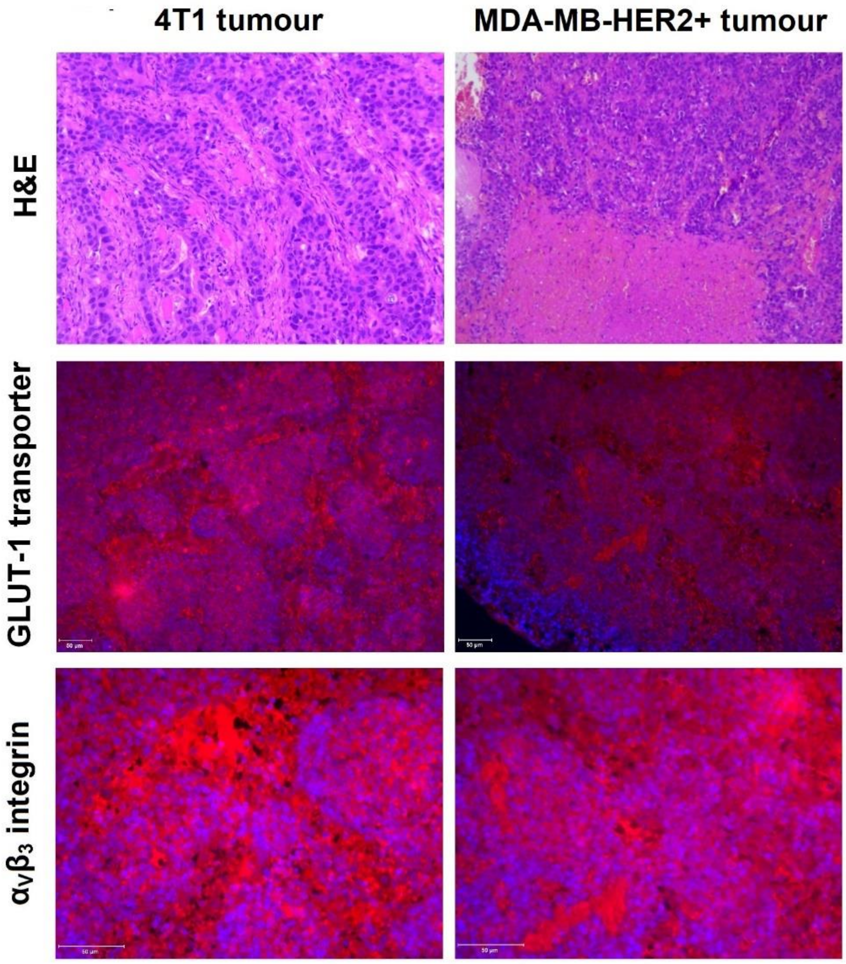

Figure 8. *Histopathology and immunohistochemistry results of triple-negative (4T1) and HER2 positive (MDA-MB-HER2+) xenografts. Upper row shows hematoxylin and eosin (H&E) staining, middle row and bottom row display GLUT-1 transporter and αvβ3 integrin staining, respectively.*

2. Research 2: HER2 Expression in Different Cell Lines and Inoculation Sites Assessed by [^{52}Mn]Mn-DOTAGA(anhydride)-trastuzumab

2.1. In Vitro Comparative Cell Binding Study

The cell binding study demonstrated significant time-dependent uptake of [^{52}Mn]Mn-DOTAGA(anhydride)-trastuzumab in both MDA-MB-HER2+ and MDA-MB-468 cell lines. MDA-MB-HER2+ cells consistently exhibited higher counts per minute (cpm) compared to MDA-MB-468 cells, with values increasing from 544.8 ± 161.4 to 671.5 ± 16.4 cpm/10^6 cells over 180 minutes, while MDA-MB-468 cells showed a more modest rise, from 156.8 ± 10.8 to 355.4 ± 81.8 cpm/10^6 cells (Figure 9).

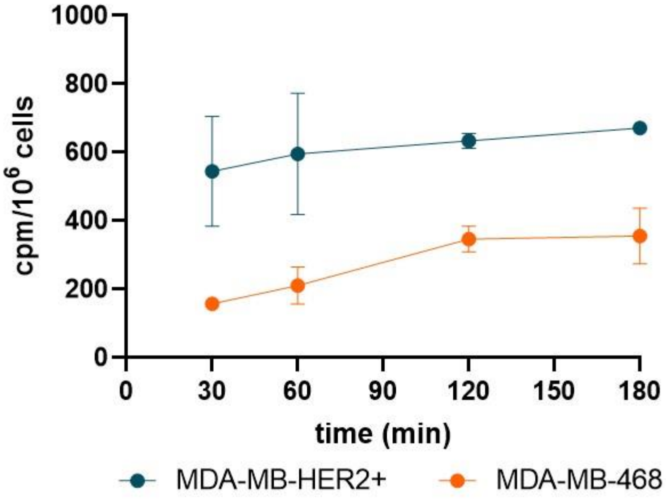

Figure 9. *Line graph shows that in vitro MDA-MB-HER2+ cells exhibited higher of [^{52}Mn]Mn-DOTAGA(anhydride)-trastuzumab uptake (counts per minute, cpm) across all time points compared to MDA-MB-468 cells.*

2.2. In vivo Temporal Biodistribution

In vivo biodistribution consistently showed the highest uptake in the blood pool at all time points. Liver, spleen, kidney, and lung all display comparable uptake with similar clearance rate. Low activity was noted in the pancreas, joints, and salivary glands. Initially, elevated activity was observed in the lacrimal glands and ovaries, which gradually cleared in subsequent scans (Figure 10).

In the MDA-MB-HER2+ groups, uptake in HER2-positive tumours was notably higher than in major organs at most time points, particularly evident in breast tumours. Specifically, starting at 24 hours post-injection, the activity ratio in breast tumours (SUV_{mean}: 1.67 ± 0.19) was significantly higher than that in the blood pool (SUV_{mean}: 1.16 ± 0.18), and other major

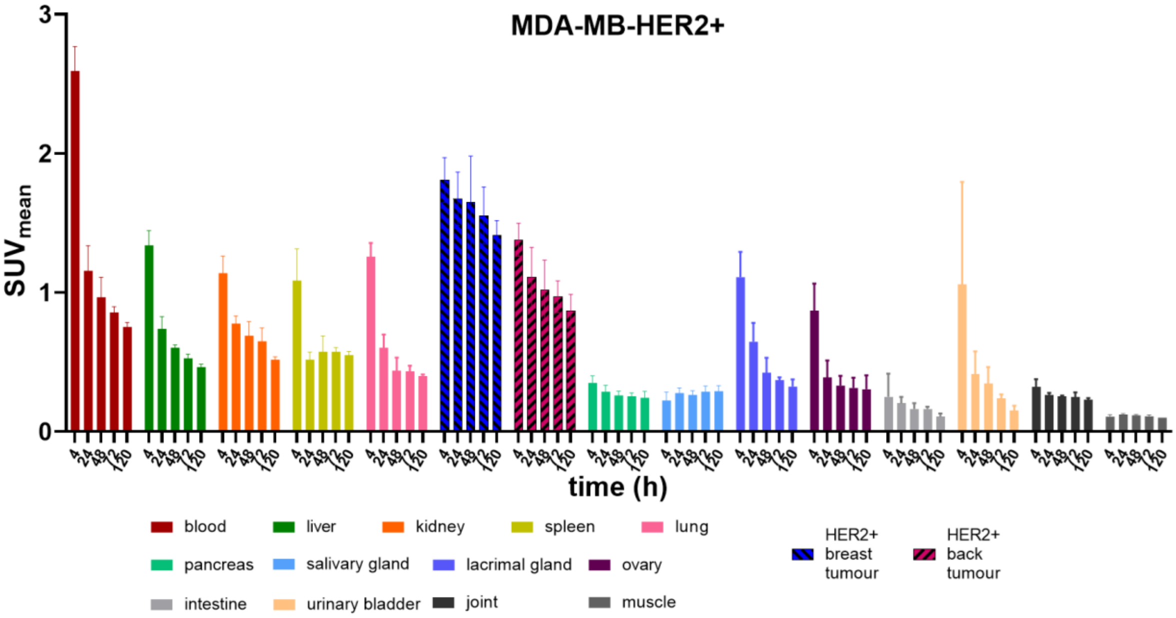

Figure 10. *Bar graphs show mean and standard deviation of the 20-minute static PET measurements were taken at 4, 24, 48, 72, and 120 hours post-injection with [^{52}Mn]Mn-DOTAGA(anhydride)-trastuzumab into MDA-MB-HER2+ tumour- bearing mice (n = 3) scanned with PET/CT.*

organs (liver, kidney, spleen, lung) ($p < 0.01$). Conversely, starting from 48 hours post-injection, the ectopic tumours uptake (SUV$_{mean}$: 1.11 ± 0.22) was only significantly higher than that of the liver (SUV$_{mean}$: 0.74 ± 0.09) and lung (SUV$_{mean}$: 0.60 ± 0.10) ($p < 0.05$), and only slightly higher than that of the spleen and kidney in subsequent scans (Figure 10).

Table 3*. Biodistribuion of [^{52}Mn]Mn-DOTAGA(anhydride)-trastuzumab on MDA-MB-HER2+ tumour bearing mice (n = 3) using hybrid PET/CT cameras. The data is presented as SUV mean (standard deviation).*

	4 h	**24h**	**36 h**	**72 h**	**120 h**
Blood	2.59 (0.18)	1.16 (0.18)	0.97 (0.14)	0.86 (0.04)	0.75 (0.03)
Liver	1.34 (0.10)	0.74 (0.09)	0.60 (0.02)	0.53 (0.03)	0.46 (0.02)
Kidney	1.14 (0.12)	0.78 (0.06)	0.69 (0.10)	0.65 (0.10)	0.52 (0.02)
Spleen	1.09 (0.23)	0.52 (0.06)	0.57 (0.12)	0.57 (0.03)	0.55 (0.03)
Lung	1.26 (0.10)	0.60 (0.10)	0.44 (0.09)	0.43 (0.04)	0.40 (0.01)
Pancreas	0.35 (0.05)	0.29 (0.05)	0.26 (0.03)	0.25 (0.03)	0.24 (0.05)
Salivary gland	0.22 (0.06)	0.28 (0.04)	0.26 (0.03)	0.29 (0.04)	0.29 (0.04)
Ovary	0.87 (0.19)	0.39 (0.12)	0.33 (0.07)	0.31 (0.07)	0.30 (0.10)

Lacrimal gland	1.11 (0.18)	0.65 (0.14)	0.42 (0.11)	0.37 (0.02)	0.32 (0.05)
Joint	0.32 (0.06)	0.26 (0.02)	0.25 (0.01)	0.25 (0.04)	0.23 (0.01)
Tumour back	1.38 (0.12)	1.11 (0.22)	1.02 (0.21)	0.97 (0.11)	0.87 (0.12)
Tumour breast	1.81 (0.16)	1.67 (0.19)	1.65 (0.33)	1.55 (0.21)	1.41 (0.11)
Intestine	0.25 (0.17)	0.20 (0.05)	0.16 (0.04)	0.16 (0.02)	0.11 (0.02)
Urinary bladder	1.06 (0.74)	0.41 (0.16)	0.34 (0.12)	0.24 (0.03)	0.15 (0.03)
Muscle	0.11 (0.02)	0.12 (0.01)	0.12 (0.01)	0.11 (0.01)	0.10 (0.00)

Table 4. *Biodistribuion of [^{52}Mn]Mn-DOTAGA(anhydride)-trastuzumab on MDA-MB-468 tumour bearing mice (n = 2) using hybrid PET/MRI cameras. The data is presented as SUV mean (standard deviation).*

	4 h	**24h**	**36 h**	**72 h**	**120 h**
Blood	4.37 (0.21)	2.53 (0.83)	2.27 (0.53)	2.08 (0.29)	2.03 (0.50)
Liver	2.13 (0.48)	1.22 (0.24)	1.19 (0.14)	1.16 (0.18)	0.88 (0.12)
Kidney	1.80 (0.30)	1.31 (0.15)	1.23 (0.06)	1.23 (0.04)	0.97 (0.05)
Spleen	2.33 (0.08)	1.81 (0.01)	1.69 (0.01)	1.54 (0.14)	1.38 (0.04)
Lung	1.91 (0.61)	1.24 (0.42)	0.96 (0.06)	0.76 (0.25)	0.80 (0.10)
Pancreas	0.95 (0.45)	0.57 (0.13)	0.52 (0.07)	0.54 (0.02)	0.55 (0.13)
Salivary gland	0.58 (0.04)	0.70 (0.06)	0.61 (0.10)	0.60 (0.06)	0.60 (0.13)
Ovary	1.44 (0.16)	1.18 (0.37)	0.89 (0.04)	0.93 (0.30)	0.74 (0.46)
Lacrimal gland	1.68 (0.12)	1.25 (0.06)	1.18 (0.15)	0.85 (0.14)	0.89 (0.23)
Joint	0.64 (0.08)	0.61 (0.04)	0.56 (0.06)	0.54 (0.03)	0.52 (0.08)
Tumour back	0.46 (0.09)	1.04 (0.02)	1.69 (0.15)	2.05 (0.22)	2.53 (0.06)
Instestine	0.71 (0.06)	0.57 (0.06)	0.49 (0.15)	0.39 (0.01)	0.39 (0.03)
Urinary bladder	0.68 (0.21)	0.47 (0.09)	0.39 (0.12)	0.27 (0.06)	0.43 (0.06)
Muscle	0.23 (0.04)	0.35 (0.06)	0.27 (0.00)	0.28 (0.06)	0.35 (0.16)

Table 5. *Major organs uptake of [^{52}Mn]Mn-DOTAGA(anhydride)-trastuzumab on B16F10 tumour bearing C57BL/6 mice (n = 3) using hybrid PET/MRI cameras. The data is presented as SUV mean (standard deviation).*

	4 h	**24h**	**36 h**	**72 h**	**120 h**
Blood	6.37 (0.67)	2.64 (0.65)	1.93 (0.38)	1.37 (0.44)	1.03 (0.39)
Liver	2.21 (0.20)	1.68 (0.12)	1.57 (0.16)	1.41 (0.08)	0.92 (0.13)
Kidney	1.89 (0.17)	1.24 (0.16)	0.98 (0.17)	0.79 (0.09)	0.57 (0.18)
Spleen	2.64 (0.14)	1.43 (0.23)	1.23 (0.28)	1.09 (0.23)	0.90 (0.32)
Lung	1.87 (0.41)	1.08 (0.23)	0.75 (0.15)	0.67 (0.15)	0.53 (0.14)
Tumour back	1.40 (0.68)	1.54 (0.26)	1.09 (0.22)	1.00 (0.22)	0.61 (0.16)
Muscle	0.17 (0.04)	0.24 (0.09)	0.16 (0.06)	0.14 (0.04)	0.08 (0.02)

2.3. Tumour uptake in HER2-positive orthotopic and ectopic breast xenograft

Given the prominent tumour-to-background ratios observed in HER2-positive breast xenografts compared to HER2-positive ectopic tumours based on biodistribution, we investigated the SUV differences between tumour uptake in HER2-positive cell lines inoculated at orthotopic versus ectopic sites. The orthotopic tumours consistently exhibited significantly greater tracer activity than the ectopic tumours at all time points ($p < 0.01$). This difference increased over time and peaked around day 3, with breast tumour SUV_{mean}: 1.55 ± 0.21 versus back tumour SUV_{mean}: 0.97 ± 0.11 ($p < 0.0001$). Similarly, on imaging, the orthotopic tumours showed significantly higher tumour-to-background contrast, becoming clearly visible from the first time point, whereas the ectopic tumours showed lower contrast, with only peripheral areas being highlighted at most of time points (Figure 11).

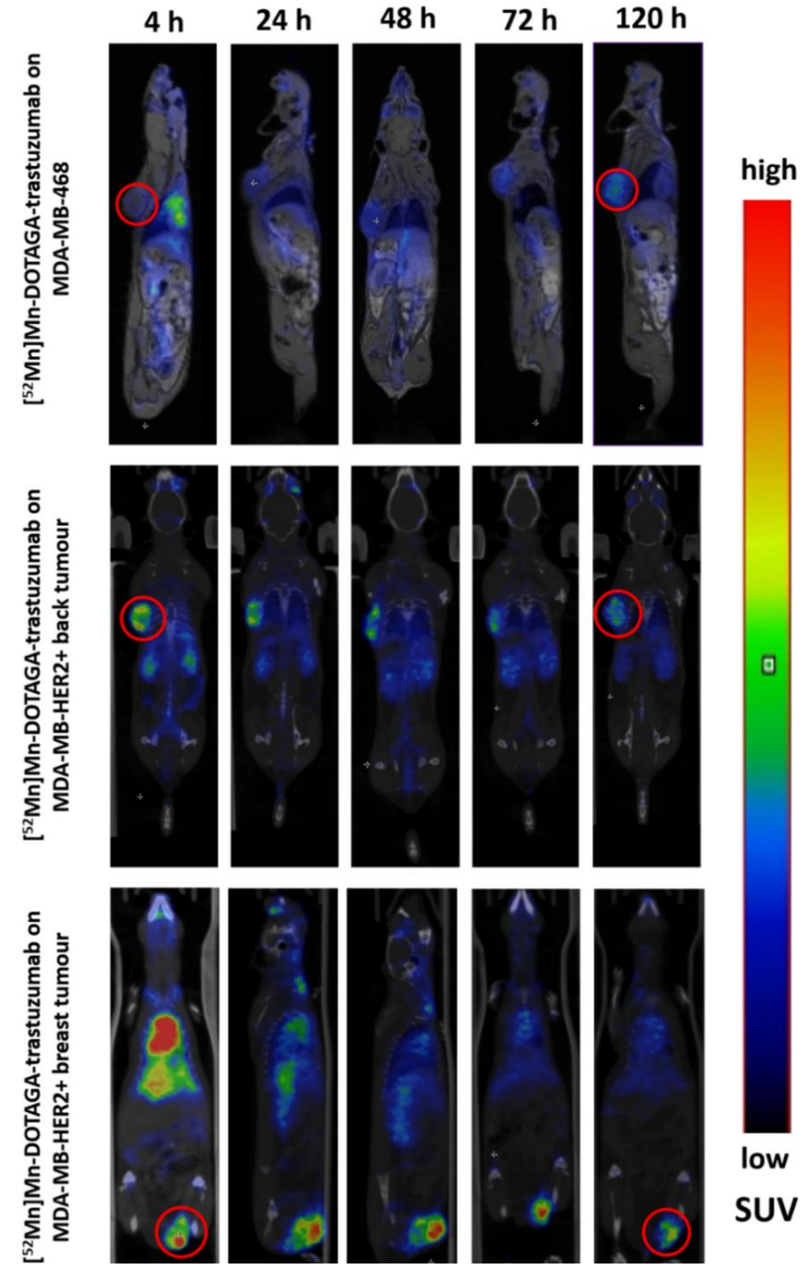

Figure 11. *Images of PET/MRI and PET/CT scans were obtained at different time points (4, 24, 48, 72, 120 hours) following injection of [^{52}Mn]Mn-DOTAGA(anhydride)-trastuzumab into MDA-MB-468 tumour-bearing mice (upper row) and into the MDA-MB-HER2+ tumour-bearing mice (middle and bottom rows displaying the back and breast tumours, respectively). Red circles were used to highlight the MDA-MB-468 back tumour (upper row), the MDA-MB-HER2+ back tumour (middle row), the MDA-MB-HER2+ breast tumour (bottom row) at 4 h and 120 h time points. A prominent high uptake in the HER2-positive orthotopic xenografts, characterised by a particularly good tumour-to-background. Tumour contrast was also visible in the ectopic HER2-positive xenografts but less markedly, both HER2-positive tumours showing a stronger peripheral uptake compared to the less avid core. In contrast, the HER2-negative xenografts exhibited less pronounced tumour contrast, but this contrast increased at later time points with relatively homogeneous uptake even in the core of the xenografts.*

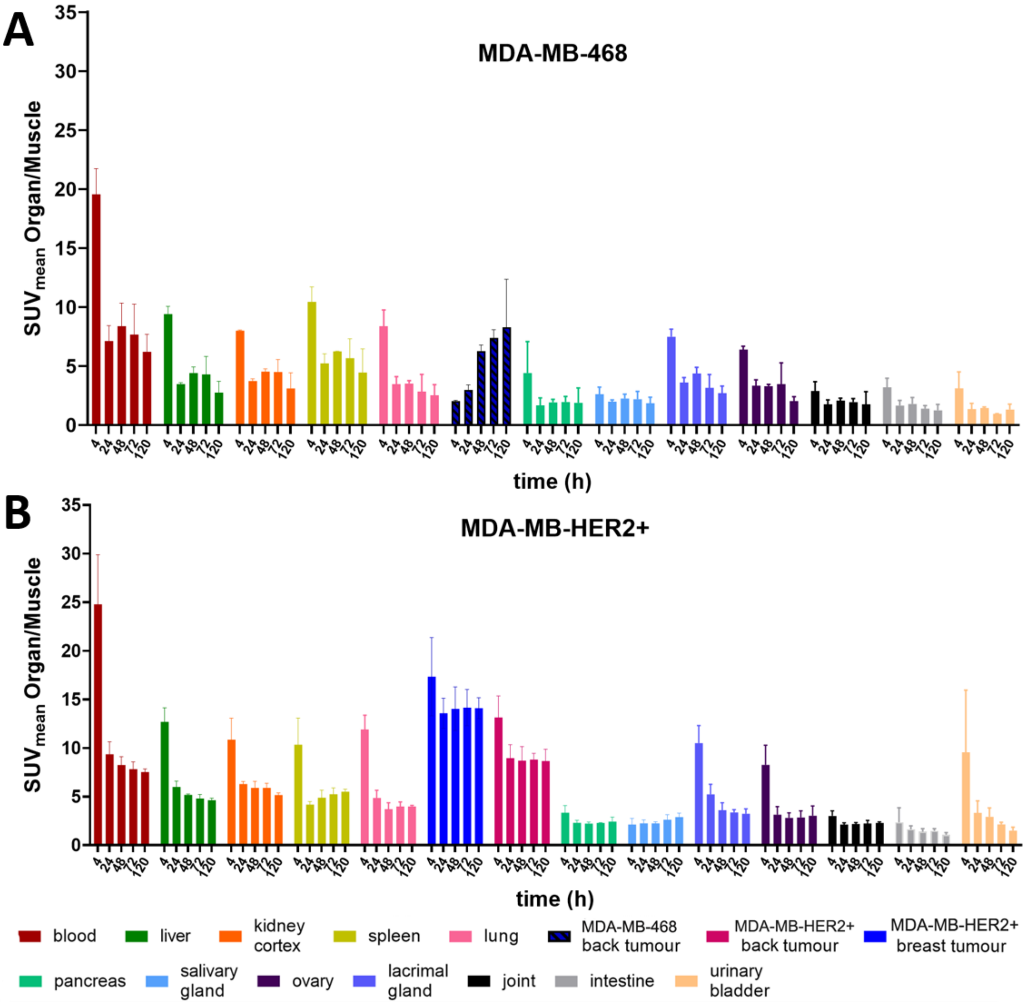

Figure 12. *Bar graphs show mean and standard deviation of the 20-minute static PET measurements were taken at 4, 24, 48, 72, 120 hours post-injection with [52Mn]Mn-DOTAGA(anhydride)-trastuzumab into (**A**) MDA-MB-468 tumour bearing mice (n = 2) scanned with PET/MRI and (**B**) MDA-MB-HER2+ tumour bearing mice (n = 3) scanned with PET/CT. Using SUVmean Organ/Muscle, comparable biodistribution was seen in both groups, despite scanning with different attenuation maps (PET/CT vs PET/MRI).*

2.4. Tumour uptake in cell lines with different HER2 expressions

In contrast, it was evident that the orthotopic HER2-positive tumours consistently exhibited dominance throughout all time points, although an increase in the ratios of the MDA-MB-468 xenografts was observed in the later scans. Specifically, the tumour-to-background ratios of the orthotopic HER2-positive tumours were significantly higher than those of the melanoma at all scan time points, and notably higher than those of the HER2-negative xenografts throughout the study duration (two-way ANOVA, $p < 0.05$) (Figure 13)

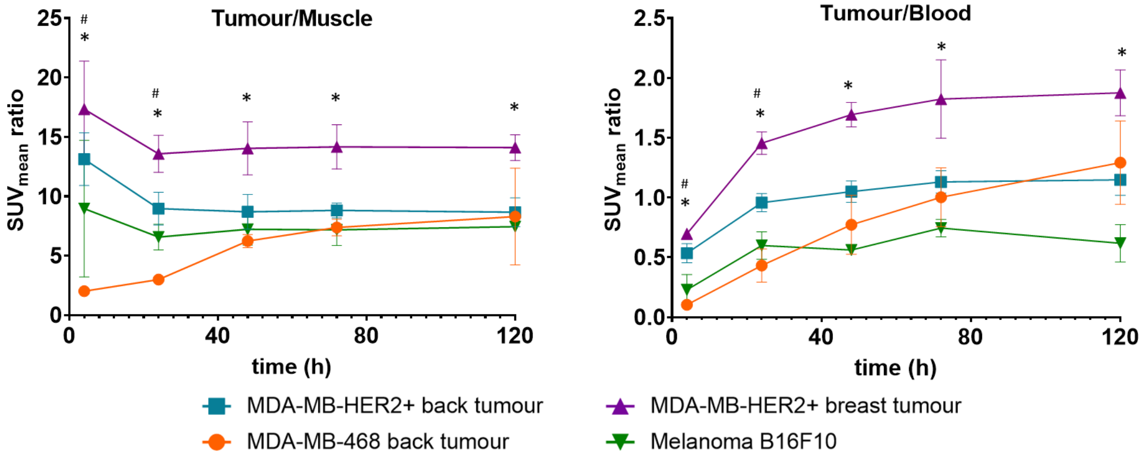

Figure 13. *Line graphs represent the mean and standard deviation of the tumour/background ratios of MDA-MB-HER2+ breast (orthotopic) tumours (purple lines), MDA-MB-HER2+ back (ectopic) tumours (blue lines), MDA-MB-468 back tumours (orange lines) in the CB17 SCID mice, and B16F10 tumours (green lines) in the C57BL/6 mice after injection of with [^{52}Mn]Mn-DOTAGA(anhydride)-trastuzumab. * indicates significantly higher ratios of breast HER2-positive tumours than all other tumours, # indicates significantly higher ratios of HER2-positive back tumours than HER2-negative tumours.*

2.5. Histopathological examination

Histopathological findings revealed distinct characteristics between the samples. The MDA-MB-HER2+ and B16F10 samples exhibited pronounced necrotic features, particularly in the B16F10 sample. In contrast, the MDA-MB-468 sample demonstrated a complex intertwining of stromal components without necrotic activity (Figure 14).

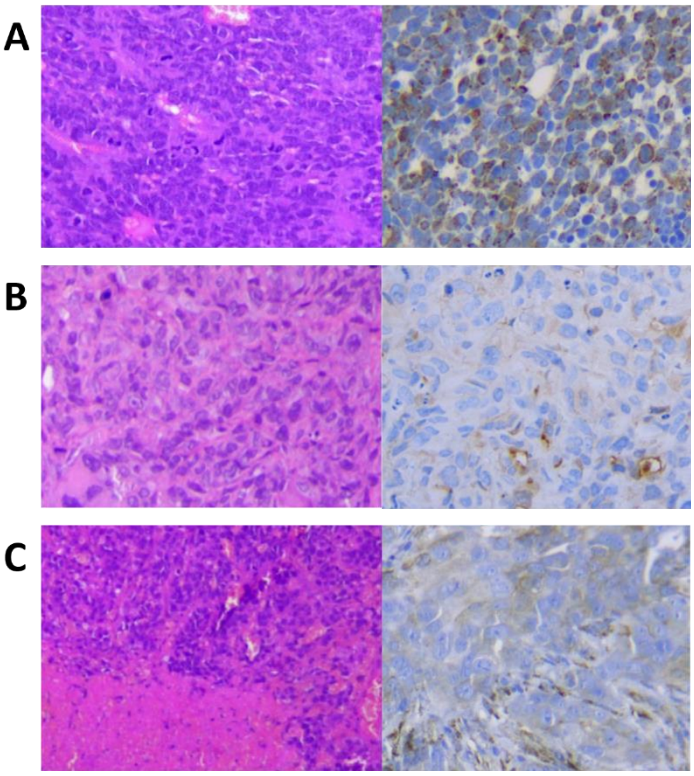

***Figure 14**. Histopathological and the HER2 staining images of the (**A**) MDA-MB-HER2+, the (**B**) MDA-MB-468, and the (**C**) B16F10 after the tumours being resected and fixed with 10% formalin.*

Our HER2 staining results on the MDA-MB-HER2+ xenografts showed HER2 positivity with varying levels of staining due to necrosis or hypoxia. In contrast, the MDA-MB-468 and B16F10 samples exhibited minimal HER2 staining, perfectly representing HER2-negative tumours (Figure 14).

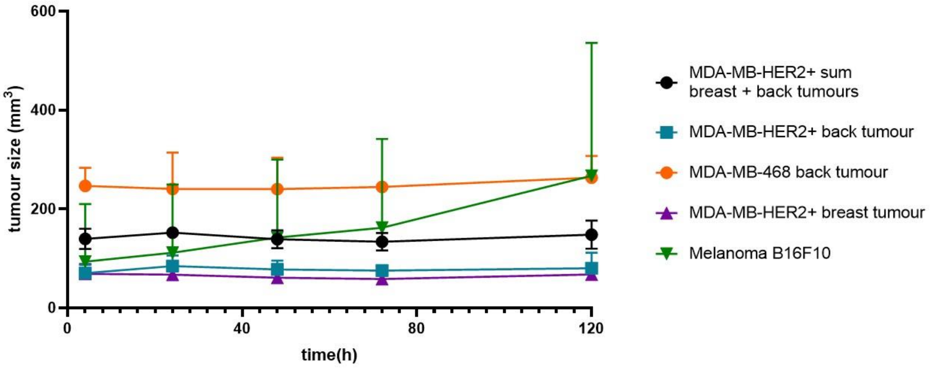

***Figure 15**. The line graph shows progression of tumour size for each tumour group and for the sum of the breast and back HER2+ tumours, data are shown as mean + standard deviation. The larger size of HER2-negative tumours compared to the sum of ectopic and orthotopic HER2-positive tumours can be seen. There was a rapid growth of melanoma tumours that were larger than the sum of HER2-positive tumours on later days.*

3. Research 3: Evaluation of [^{52}Mn]Mn-BPPA-trastuzumab for Highly Specific HER2 PET Imaging

3.1. Synthesis of the BPPA, BPPA-Bn^{pCOOH} and BPPA-Bn^{pMMA} chelators

The synthesis of the BPPA, BPPA-Bnp^{COOH} and BPPA-Bnp^{MMA} (Scheme 1) ligands was started from the bispyclen (3,7-diaza-1,5(2,6)-dipyridinacyclooctaphane, BP) (**1**) macrocycle, whose synthesis was recently optimized [134]. N-alkylation of the given macrocycle with methyl 6-(chloromethyl)picolinate obtained following literature protocols [135] in the presence of K_2CO_3 as base and catalytic amounts of KI in anhydrous acetonitrile under argon atmosphere afforded the BPPA methyl ester. The ester protecting group was removed from (**2**) by acid hydrolysis with 6 mol/L hydrochloric acid to give BPPA chelator. For the synthesis of the bi-functional chelators (BFCs), bispyclen (**1**) was first N-alkylated with tert-butyl 4-(bromomethyl)benzoate in the presence of K_2CO_3 in acetonitrile to form the platform with non-coordinating benzyl spacer. The tert-butyl ester protecting group was then removed from (**3**) with trifluoroacetic acid (TFA) in dichloromethane affording the compound (**4**). Picolinate pendant arm (PA) required for the metal ion coordination was introduced to the remaining secondary amine group with tert-butyl 6-(bromomethyl)picolinate prepared following literature methods in the presence of Hünig’s base (N,N-diisopropylethylamine) in N,N-dimethylformamide (**5**). The maleimide derivative of (**5**) was obtained by coupling the para-benzoic acid pendant of (**5**) to 1-(2-aminoethyl)-1H-pyrrole-2,5-dione hydrochloride using 1-hydroxybenzotriazole (HOBt) and 2-(1H-benzotriazole-1-yl)-1,1,3,3-tetramethyluronoium hexafluorophosphate (HBTU) reagents in the presence of N,N-diisopropylethylamine (DIPEA) in dichloromethane (**6**). Tert-butyl ester protective groups of (**5**) and (**6**) were then cleaved in the same way as described earlier for (**3**) to receive BPPA-Bn^{pCOOH} and BPPA-Bn^{pMMA} BFCs. Details of the synthesis steps of each compounds and their HPLC, NMR spectra (1H and 13C-JMOD), high resolution (ESI) mass spectra result details are presented at the end of this section (Figure 31- Figure 62).

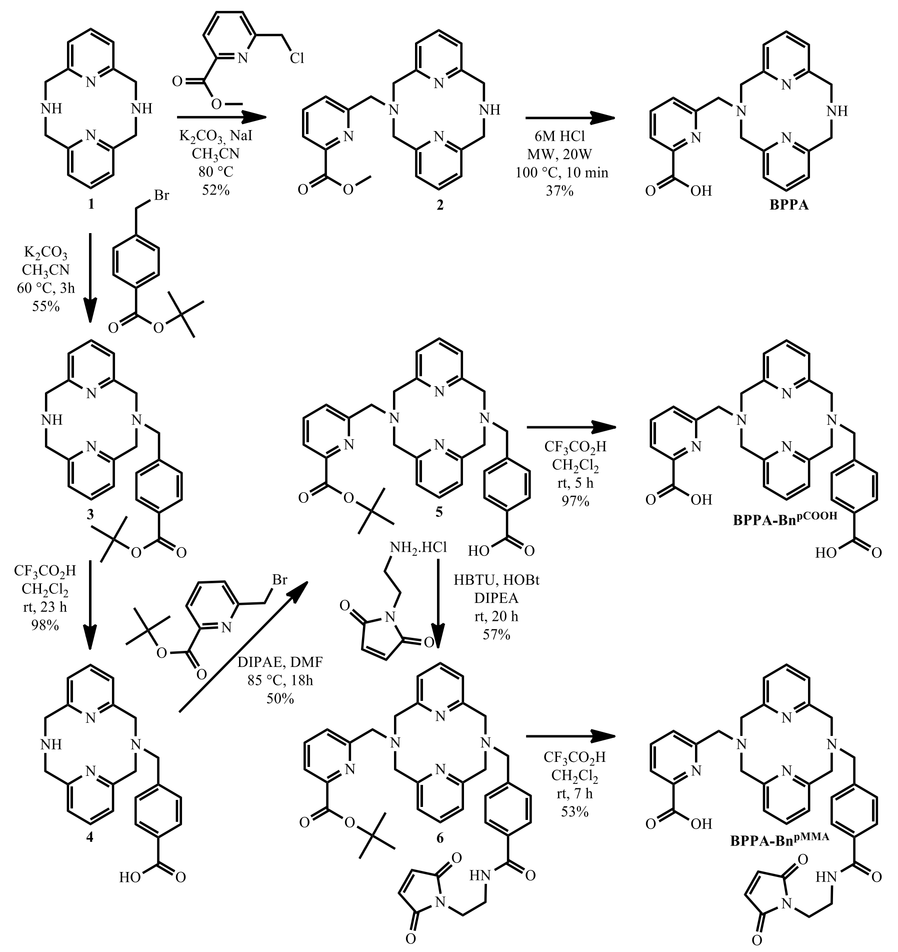

***Scheme 1**. Scheme of visualizing the synthesis of the BPPA, BPPA-Bn^{pCOOH} and BPPA-Bn^{pMMA} chelators.*

3.2. Equilibrium, kinetic and relaxometric characterization of the [Mn(BPPA)] complex

Protonation constants of the BPPA chelator were accessed by pH-potentiometric titration (25 °C and I = 0.15 M NaCl) (Figure 16). The first and the second protonation occurs at the secondary and tertiary amine groups whereas the last protonation can be assigned to the picolinate pendant arm. Comparing protonation constants with those of the parent 3,9-PC2A, it's evident that the BPPA ligand is less basic due to fewer basic macrocyclic N-atoms, as seen in the parent BP2A chelator (the first protonation constant of BPPA is being ca. 3-5 log units lower than that of the 3,9-PC2A) [132, 136, 137]. Stability of the [Mn(BPPA)] complex was attempted to be determined by pH-potentiometirc titration, however the fitting of the data acquired indicated the quantitative formation of the complex at the beginning of the titration (pH = 1.80) (Figure 16).

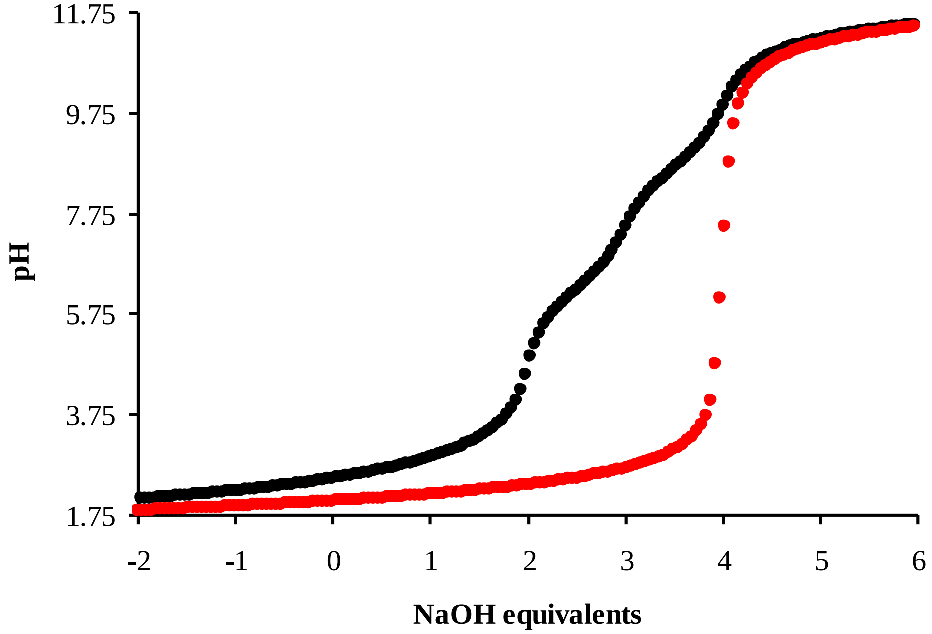

Figure 16. *Potentiometric titration curves for BPPA in the absence (black) and in the presence (red) of an equivalent* $MnCl_2$ *(*$c_{Mn(II)} = c_L = 2.6$ *mM; 0.15 M NaCl, 25°C)*

Therefore, an out-of-cell relaxometirc titration was performed with the use of samples containing equimolar amounts of Mn(II) and BPPA ligand in the acid concentration range of 2.42-252 mM. The relaxation rate data was measured and fitted simultaneously with the titration data obtained pH-potentiometrically (Figure 17). The model used for the data fitting appeared to be simple as the formation of only MnL and MnL(OH) species were detected (the later complex forms when the water molecule (the existence of which was confirmed by the relaxivity measurements) deprotonates under very basic conditions ($pK_a = 12.19(2)$). The

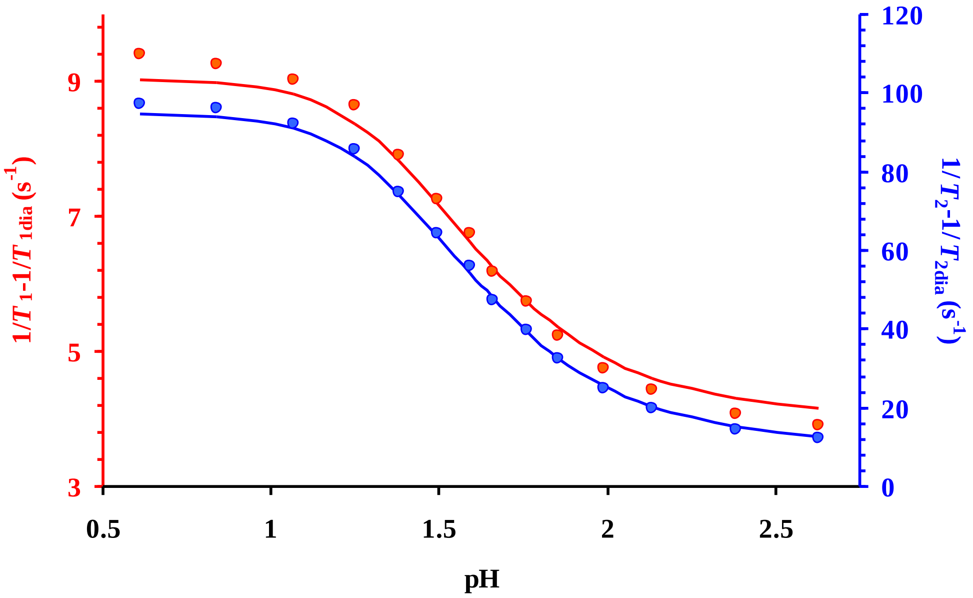

Figure 17. *Relaxation rates (red: R_{1p} and blue: R_{2p}) as function of total acid concentration recorded for the samples containing equimolar amounts of $MnCl_2$ and BPPA ligand (T = 25°C and I=0.15 M NaCl).*

stability constant of the [Mn(BPPA)] complex is nearly as high (log K_{MnL} = 16.14(1)), as it was observed for the parent [Mn(3,9-PC2A)] (log K_{MnL}=17.09) which in the light of reduced basicity of BPPA predicts the high apparent stability of the chelate. Indeed, the calculated pMn values (pMn = -log[Mn_{free}]; at pH 7.4 and 10^{-5} M total ligand and metal concentrations) allowing for the comparison of complex stabilities of ligands with different basicity (Table 6), was found to be higher (pMn = 10.98) than those calculated for the Mn(II) complexes formed with DOTA (9.02) or PCTA (9.74) ligands [123, 138]. Only two systems are known to the literature with higher pMn values reported (12.73 and 12.59) [139]. However, these Mn(II) complexes formed with bispidine derivative chelators were found to form slowly (taking 6-72 h for the complexation depending upon acid concentration of the sample) [139] whereas in our case the complex formation was instantaneous which fits the radiochemical applications.

Prior to the radiochemical studies, information on the inertness of chelate was accessed by studying the rate of metal exchange reaction occurring Zn(II) (pH = 6.0, 25 equivalents of Zn(II), T_2 relaxometry at 25 °C and 37 °C). Such study does not provide detailed information on the dissociation (contribution of different reaction pathways), yet the pseudo-first order rate constants (and the half-lives calculated with their use) determined allows to set an order of inertness of the complexes under the conditions applied. The dissociation kinetics studies results showed that the [Mn(BPPA)] chelate had improved inertness (k_{obs} at 37 °C is 8.29 x 10^{-5} s-1 which translates into a half-life of 2.32 h) (Figure 18) as compared to that of the parent

[Mn(3,9-PC2A)] complex (an improvement of almost an order of magnitude). However, the inertness of the chelate does not reach the half-lives observed for the pH or Zn(II) responsive Mn(II) probes designed recently [140, 141]. On this basis, it is expected that the inertness of the chelate will be further improved during the derivatization. Furthermore, the ^{1}H longitudinal (T1) and transverse (T2) relaxation times results (Figure 19), the complex's potential as an MRI contrast agent (Table 6).

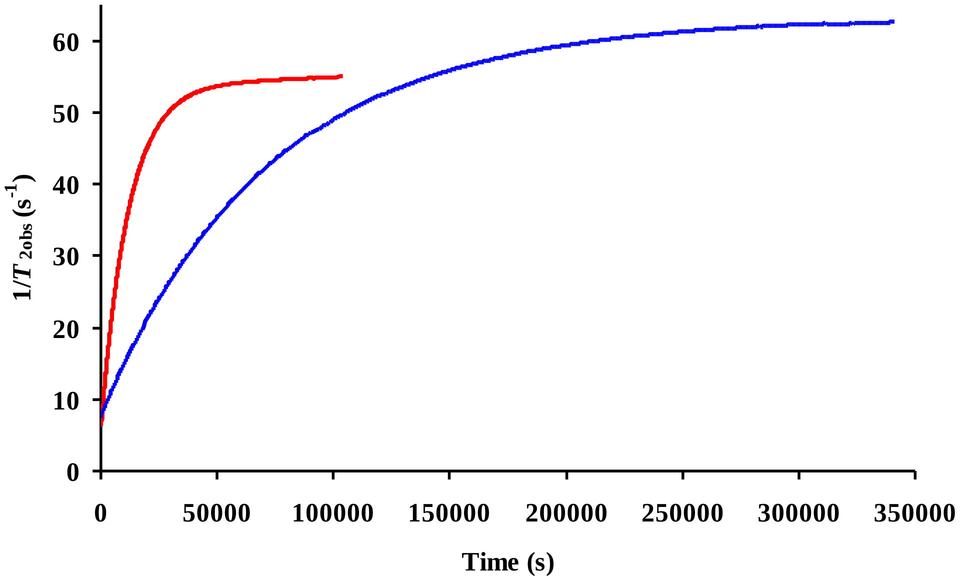

Figure 18. *Dissociation of the [Mn(BPPA)]$^+$ complex in the presence of 25 equiv. of Zn(II) at pH = 6.0 as determined by T_2 relaxometry at 1,41 T filed strength at 25 (blue) and 37°C (red).*

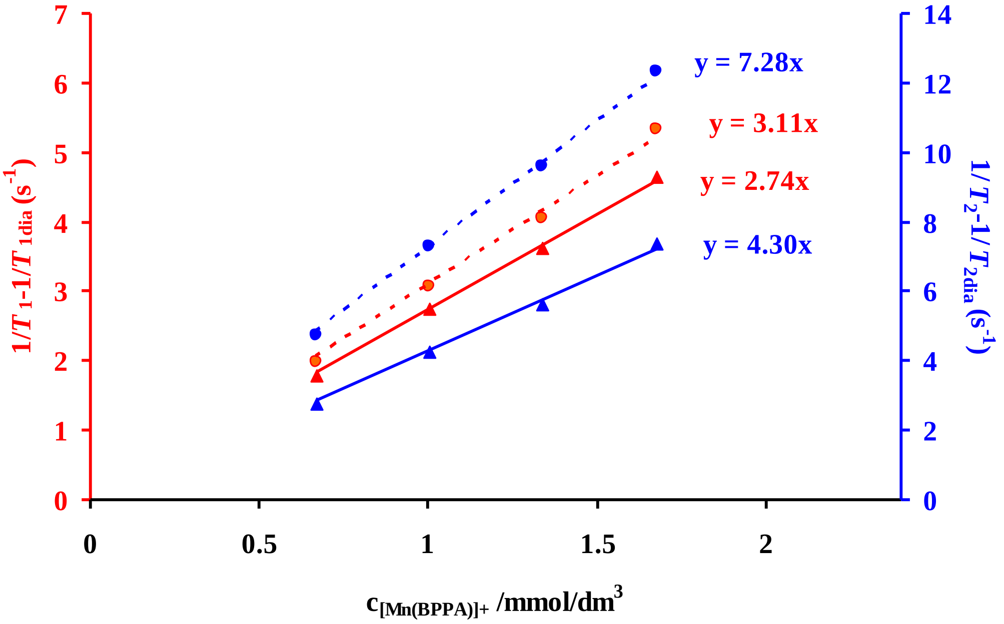

Figure 19. *Determination of r_{1p} (red) and r_{2p} (blue) relaxivities for [Mn(BPPA)]$^+$ at 0.49 T (triangles) and 1.41 T (circles) field strengths at 25°C.*

Table 6. *Summary of physicochemical data (protonation constants, stability, pMn values, dissociation rates, half-lives of dissociation and relaxivities) obtained for the [Mn(BPPA)]$^+$ as compared to the complexes formed with model ligands (I = 0.15 M, NaCl and t = 25 °C).*

	BPPA	BP2A	3,9-PC2A[c]	3,9-PC2A Bn$^{p\text{COOH}}$ [d]	PyC3A[e]	L^1 [f]
log K_1^{H}	**8.65(1)**	9.57; 8.18[b]	12.25	10.28	10.16	>11.05
log K_2^{H}	**6.26(1)**	5.99; 5.77[b]	5.97	6.88	6.39	6.73
log K_3^{H}	**2.92(1)**	2.59; –[b]	3.47	3.98	3.13	5.62
log K_4^{H}	–	2.22; –[b]	1.99	1.89	–	5.27
log K_5^{H}	–	–	–	1.66	–	2.30
$\sum_{i=1}^{2} log\,K_i^H$	**14.91**	15.56; 14.95[b]	18.22	17.16	16.55	>17.78
log K_{MnL}	**16.14(1)**	–	17.09	14.76	14.11	24,20
log K_{MnHL}	–	–	–	4.04	2.43	3.04
log $K_{\mathrm{MnH\text{-}1L}}$	**12.19(2)**	–	–	–	–	–
*p*Mn[g]	**10.98**	–	8.64	8.37	8.17	12.73
k_{obs} (s^{-1})[h]	**8.29×10^{-5}**	–	5.43×10^{-4}	4.28×10^{-5}	6.76×10^{-4}	–
$t_{1/2}$ (h)[i]	**2.32**	–	0.35	4.50	0.28	2400
$r_{1\mathrm{p}}$ (mM^{-1}s^{-1})[j]	**2.74(2)**	–	2.40	4.95	2.10[k]	5.04[l]

[a] from [136]; [b] from [137]; [c] from [132]; [d] from [142]; [e] from [133]; [f] from [139]; [g] calculated by using c_{Mn2+} = 0.01 mM, c_L = 0.01 mM at pH = 7.4 as suggested by É. Tóth and co-workers [143]; [h] the rate of transmetallation kinetics measured at pH = 6.0 in the presence of 25 fold Zn(II) excess under conditions suggested by P. Caravan and co-workers from [133]; [i] $t_{1/2}$ = ln2/k_{obs} (h); [j] measured at 1.41 T and 25°C; [k] measured at 1.41 T and 37°C; [l] measured at 0.49 T and 25°C

3.3. Radiolabelling of [^{52}Mn]Mn-BPPA-trastuzumab

To optimize the radiolabelling of BPPA-trastuzumab with [^{52}Mn]Mn(II), the effect of pH, temperature, reaction time and ligand concentration on labelling efficiency were investigated. Radiochemical purity of [^{52}Mn]Mn-BPPA was examined by using 5 min reaction time at 25°C and 95°C (Figure 20) with a BPPA concentration of 0.1 µM - 100 µM, in the pH range of 4 - 8. HEPES buffer was applied at pH 7 and 8, whereas NaOAc was used between of pH 4 - 6.

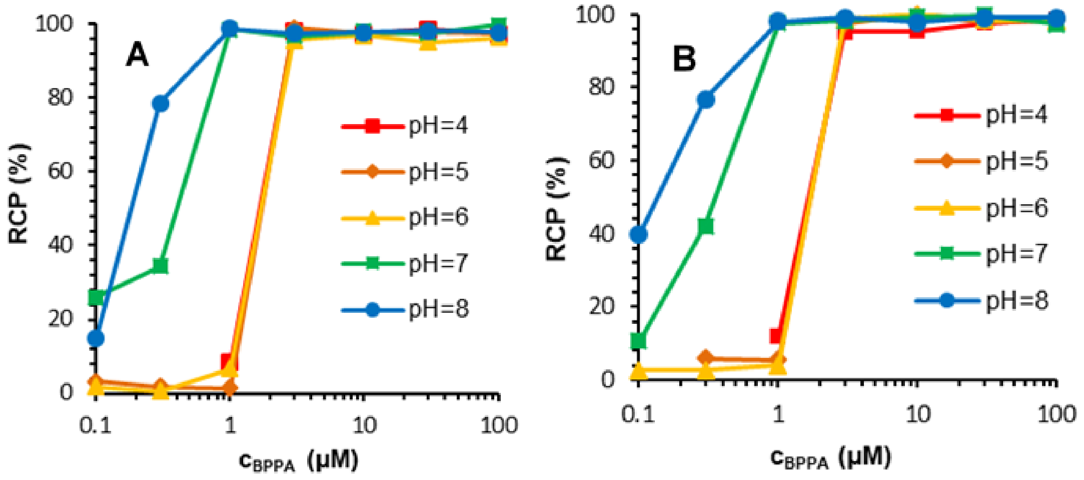

Figure 20. *Radiochemical purity (RCP) of [^{52}Mn]Mn-BPPA as a function of chelator concentration in the pH range of 4 – 8 at 25°C (**A**) and 95°C (**B**) with 5 min reaction time.*

The rate of change (slope) of the curves is consistent at both 25°C and 95°C. Efficiency of BPPA labelling with [^{52}Mn]Mn(II) was enhanced with increasing pH, > 95% RCP was obtained using a ligand concentration of 1 μM above pH 7, while one order of magnitude higher ligand concentration was required below pH 6 for the same yield. The impact of reaction time was also studied on the inflection point of the ligand concentration curves for each pH, whereby no effect was observed toward the prolonged reaction times.

Based on the optimization, BPPA-trastuzumab labelling with [^{52}Mn]Mn(II) was ideally performed at room temperature using pH 7 HEPES buffer for 15 min. Molar activity and RCP of [^{52}Mn]Mn BPPA-trastuzumab was higher (0.085 ± 0.033 MBq/μg; 99.93 ± 0.07%) than that of [^{52}Mn]Mn DOTAGA trastuzumab (0.0200 ± 0.002 MBq/μg; 88.37 ± 8.37%).

3.4. Determination of Serum Stability of [^{52}Mn]Mn-BPPA-trastuzumab and [^{52}Mn]Mn-DOTAGA(pSCN-Bn)-trastuzumab

Preliminary kinetic measurements of cold Mn(II)-BPPA complex showed that the complex stable against transchelation with CDTA, however [^{52}Mn]Mn-BPPA-trastuzumab provided reduced stability results in serum. Its RCP decreased to 71% by day 10, while the RCP of [^{52}Mn]Mn-DOTAGA(pSCN-Bn)-trastuzumab did not fall below 90%, even after 10 days (Figure 21).

3.5. Biodistribution of [^{52}Mn]MnCl$_2$, [^{52}Mn]Mn-BPPA, [^{52}Mn]Mn-DOTAGA

Biodistribution of [^{52}Mn]MnCl$_2$, [^{52}Mn]Mn-BPPA and [^{52}Mn]Mn-DOTAGA was investigated on healthy mice by dynamic and static PET/MRI imaging. [^{52}Mn]MnCl$_2$ showed high kidney and liver uptake which reduced over time, notably there was a plateau clearance

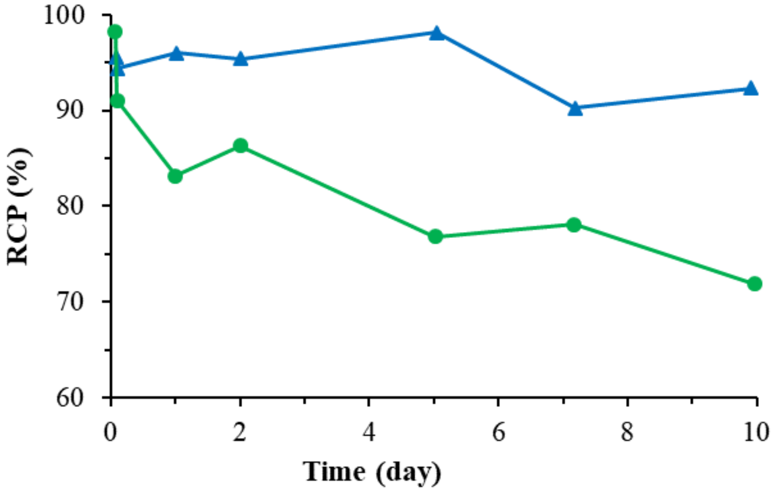

Figure 21. *Serum stability of [^{52}Mn]Mn-BPPA-trastuzumab (●) and [^{52}Mn]Mn-DOTAGA(pSCN-Bn)-trastuzumab (▲) at 37°C*

pattern observed in the case of pancreas and salivary gland (Figure 22A, Figure 23C). Unlike [^{52}Mn]MnCl$_2$, the chelated [^{52}Mn]Mn exhibited rapid clearance. Most of [^{52}Mn]Mn-DOTAGA was excreted by urine in the first hour (Figure 22B, Figure 24A), while [^{52}Mn]Mn-BPPA showed some faecal excretion in addition to kidneys (Figure 22C, Figure 24B). At later time point, [^{52}Mn]Mn-DOTAGA showed dominant lung and liver uptake (Figure 23A), whereas [^{52}Mn]Mn-BPPA presented a similar distribution pattern with [^{52}Mn]MnCl$_2$ (Figure 23B).

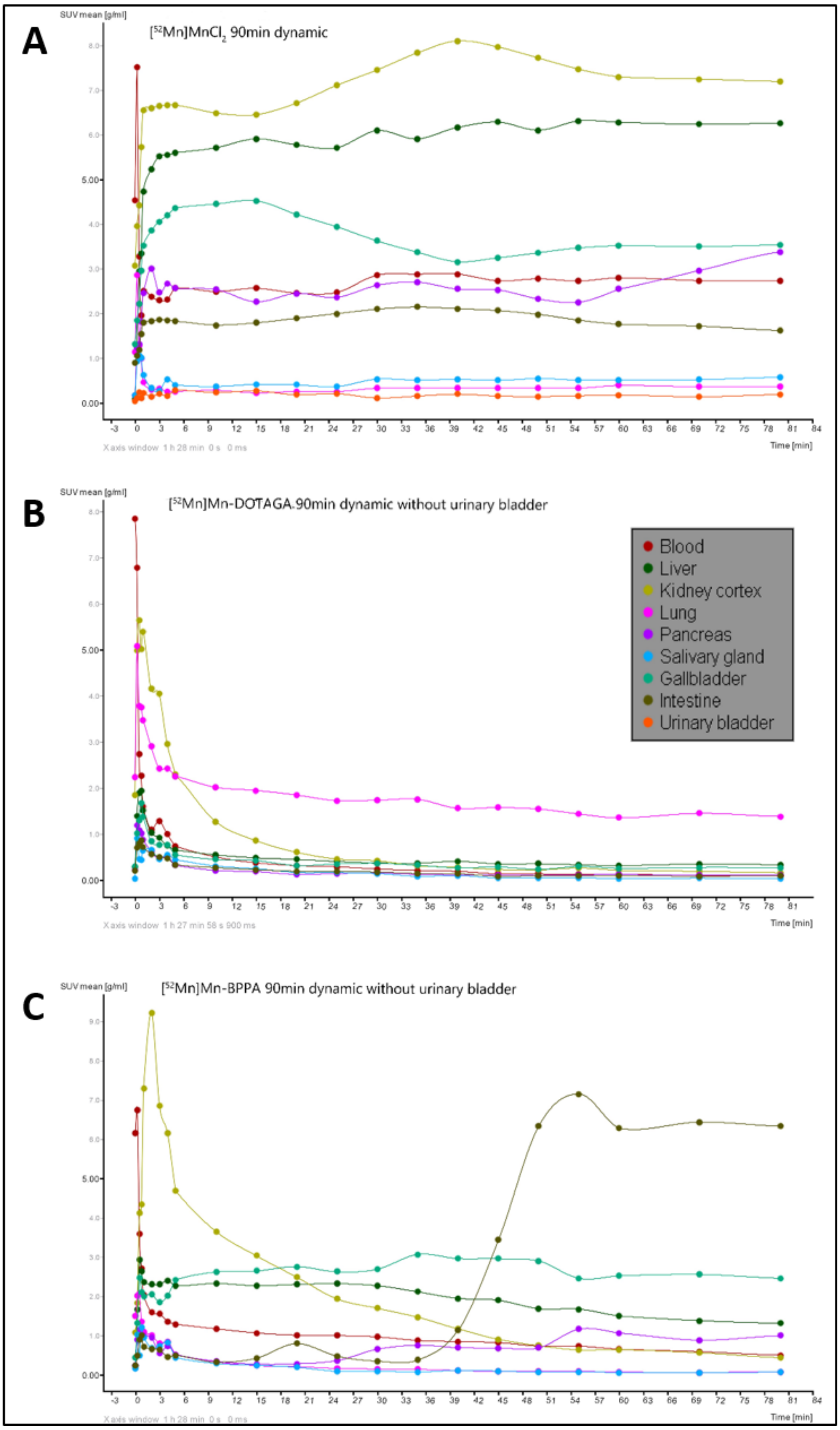

Figure 22. *90-minute dynamic PET time activity curves of (**A**) healthy BALB/c mouse received i.v 2.37 MBq [^{52}Mn]MnCl$_2$, (**B**) healthy mouse injected with 2.20 MBq [^{52}Mn]Mn-DOTAGA without urinary bladder, (**C**) healthy mouse injected with 3.09 MBq [^{52}Mn]Mn-BPPA without urinary bladder. Curves were created by using curve viewer tool in InterView FUSION software (Mediso Ltd) ROI were drawn over abdominal aorta, liver, kidney cortex, lung, pancreas, salivary gland, gallbladder, intestine and urinary bladder.*

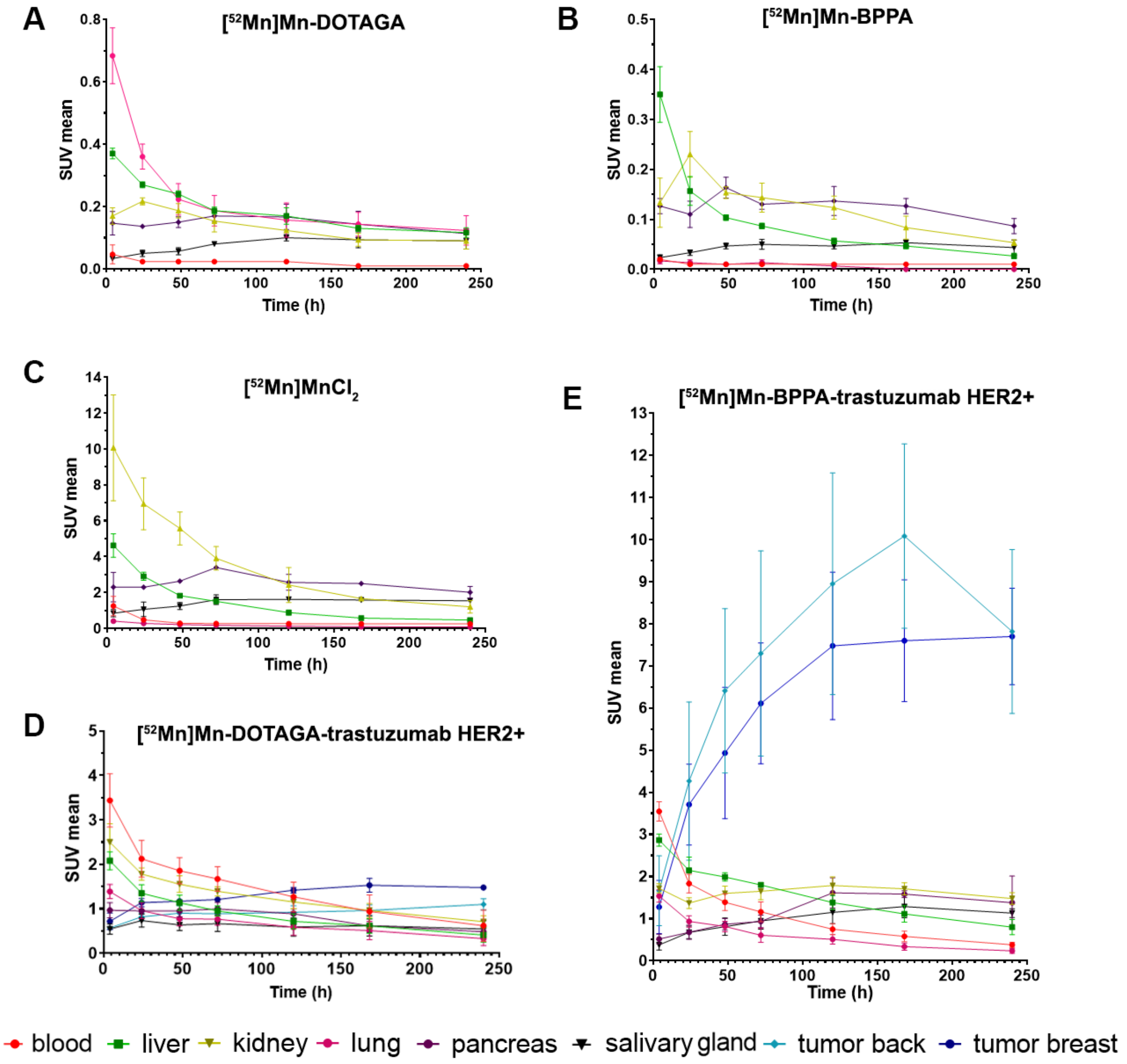

Figure 23. *20-minute static PET measurements on 4 hours, 1 day, 2 days, 3 days, 5 days, 7 days, 10 days post injection of (**A**) [^{52}Mn]Mn-DOTAGA (n = 3), (**B**) [^{52}Mn]Mn-BPPA (n = 3), (**C**) [^{52}Mn]MnCl$_2$ (n = 2) on healthy BALB/c mice, and (**D**) [^{52}Mn]Mn-DOTAGA(pSCN-Bn)-trastuzumab (n=3), (**E**) 52Mn-BPPA-trastuzumab (n = 3) on HER2+ tumour bearing SCID mice. ROI were drawn over mediastinum, liver, kidney, lung, pancreas, salivary gland and tumours.*

3.6. In Vivo Investigation of [^{52}Mn]Mn-DOTAGA(pSCN-Bn)-trastuzumab and [^{52}Mn]Mn-BPPA-trastuzumab

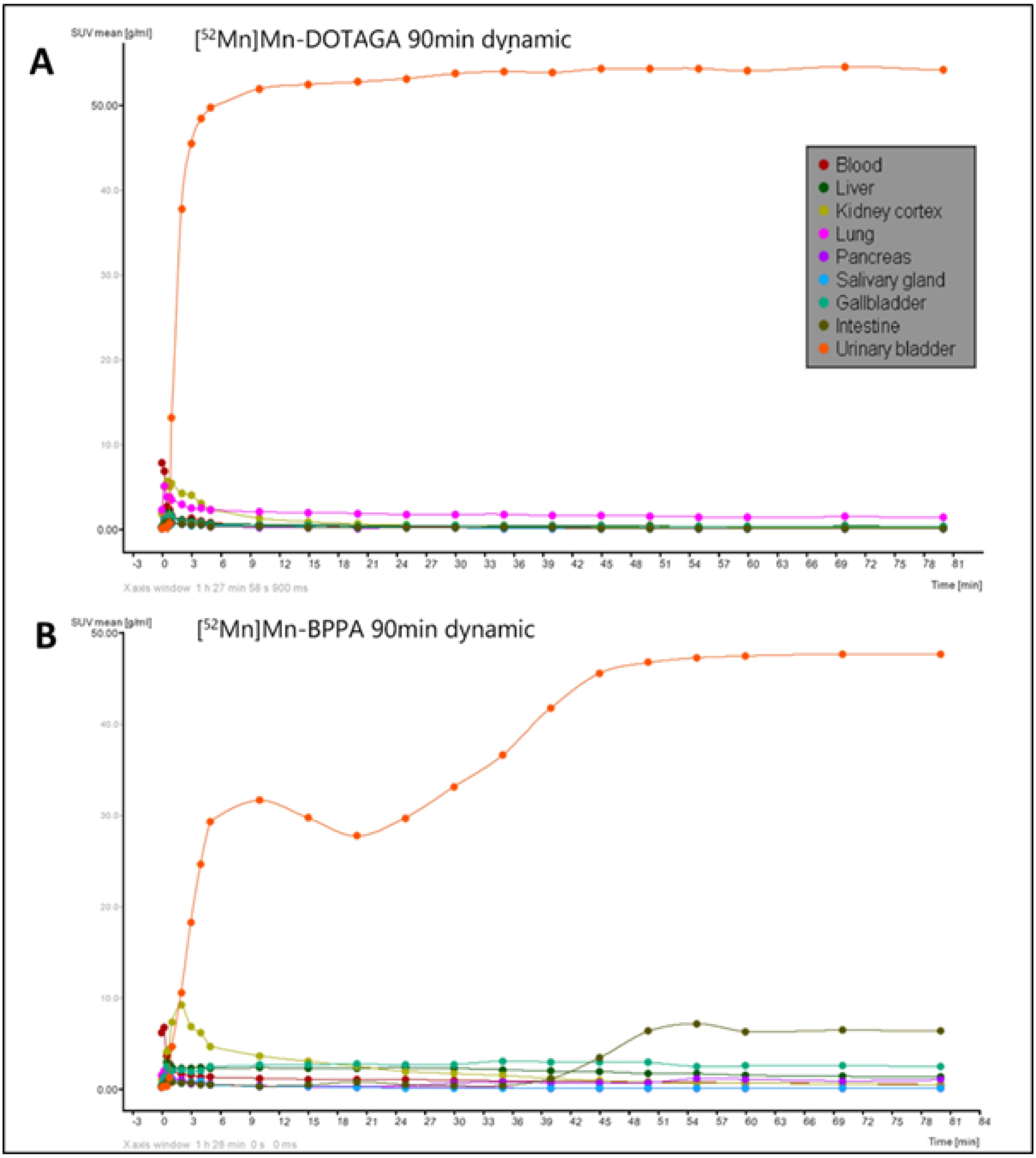

Figure 24. *90-minute dynamic PET time activity curves with urinary bladder of (a) healthy mouse injected with 2.20 MBq [^{52}Mn]Mn-DOTAGA, (**B**) healthy mouse injected with 3.09 MBq [^{52}Mn]Mn-BPPA. Curves were created by using curve viewer tool in InterView FUSION software (Mediso Ltd). ROI were draw over abdominal aorta, liver, kidney cortex, lung, pancreas, salivary gland, gallbladder, intestine and urinary bladder.*

It is demonstrated that [^{52}Mn]Mn-BPPA-trastuzumab provides HER2 specificity and higher uptake values from 24 h than [^{52}Mn]Mn-DOTAGA(pSCN-Bn)-trastuzumab (Figure 25). Using [^{52}Mn]Mn-DOTAGA(pSCN-Bn)-trastuzumab most of the organs showed a gradual decline in uptake over time (Figure 23D). Tumour uptake increased steadily overtime, with the back xenograft reaching the maximum uptake at 240 h (SUV 1.10 ± 0.12), while the breast tumour peaked at 168 h (SUV 1.53 ± 0.16). The difference of uptake between orthotopic HER2+ and HER2− tumours was observable only from 168 h, however the difference was not statistically significant (Figure 26A). By examining tumour/liver and tumour/muscle ratios, it

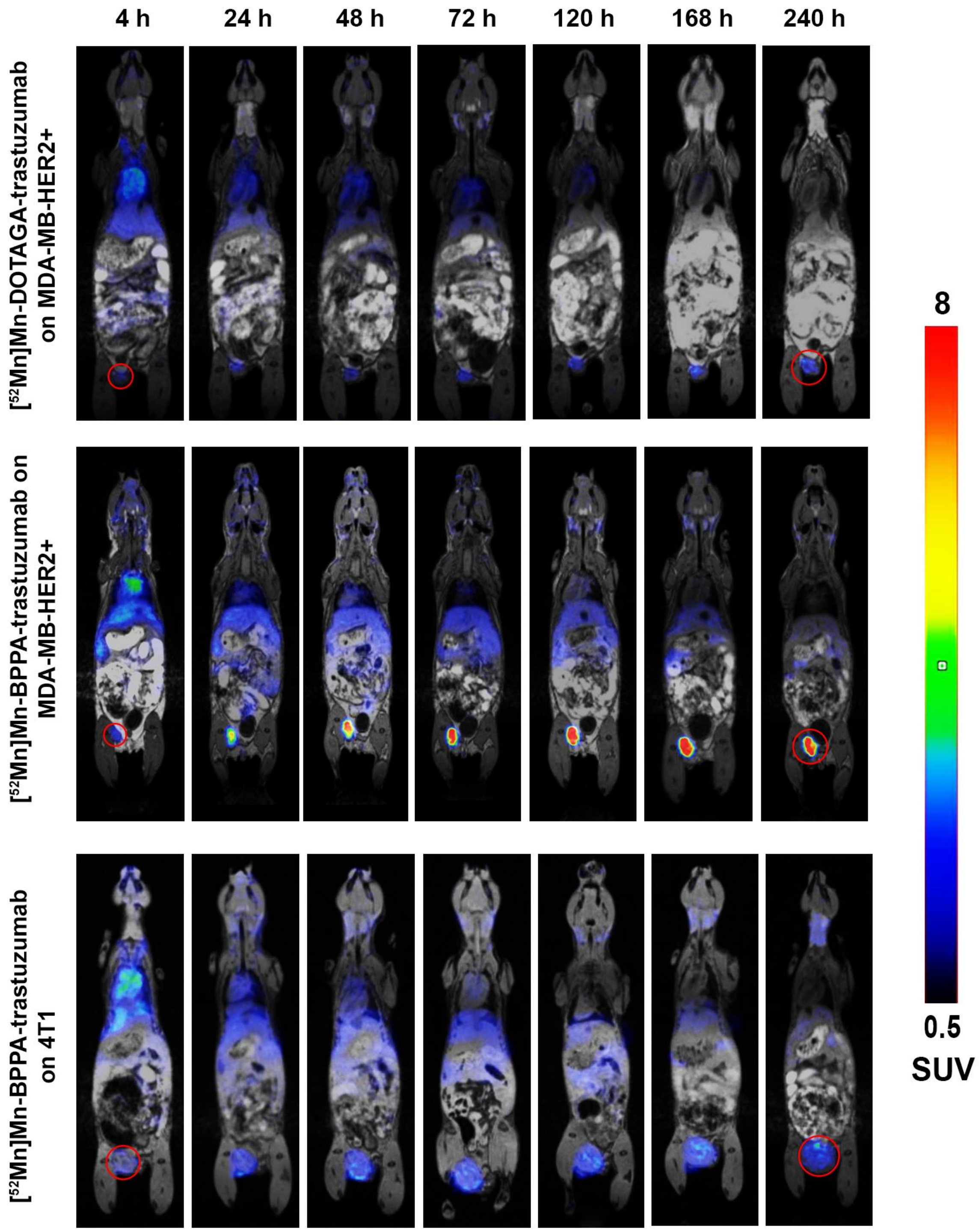

Figure 25. *PET/MRI hybrid images results on different time points after injecting [^{52}Mn]Mn-DOTAGA(pSCN-Bn)-trastuzumab on HER2+ bearing mice (upper row), [^{52}Mn]Mn-BPPA-trastuzumab on HER2+ and HER2− bearing mice (middle and lower rows respectively). Red circles highlight the orthotopic breast tumours. The SUV scale is demonstrated at the right.*

can be seen that HER2+ breast tumour showed significant difference with 4T1 tumours, but only at the 240 h scan (ANOVA, $p \leq 0.001$) (Figure 26B).

The biodistribution of [^{52}Mn]Mn-BPPA-trastuzumab was different than that of [^{52}Mn]Mn-DOTAGA(pSCN-Bn)-trastuzumab (Figure 23E). On the first 48 h, liver uptake was significantly higher than kidney uptake thereafter, blood pool and liver showed much faster clearance rate than kidney, pancreas, and salivary glands. Uptake in both back and breast tumours was so pronounced that it was significantly higher than in the liver and other organs as early as 48 hours (ANOVA, $p \leq 0.001$). Their uptake increased steeply and peaked around 168 h (SUV 10.08 ± 2.18) and 240 h (SUV 7.7 ± 1.15) for back and breast tumour, respectively (Figure 27A). While the uptake of HER2+ breast tumours at 24 h was barely higher than that of 4T1 breast tumours (SUV: 3.71 ± 0.96 vs. SUV: 2.33 ± 0.30, $p \leq 0.05$), this difference

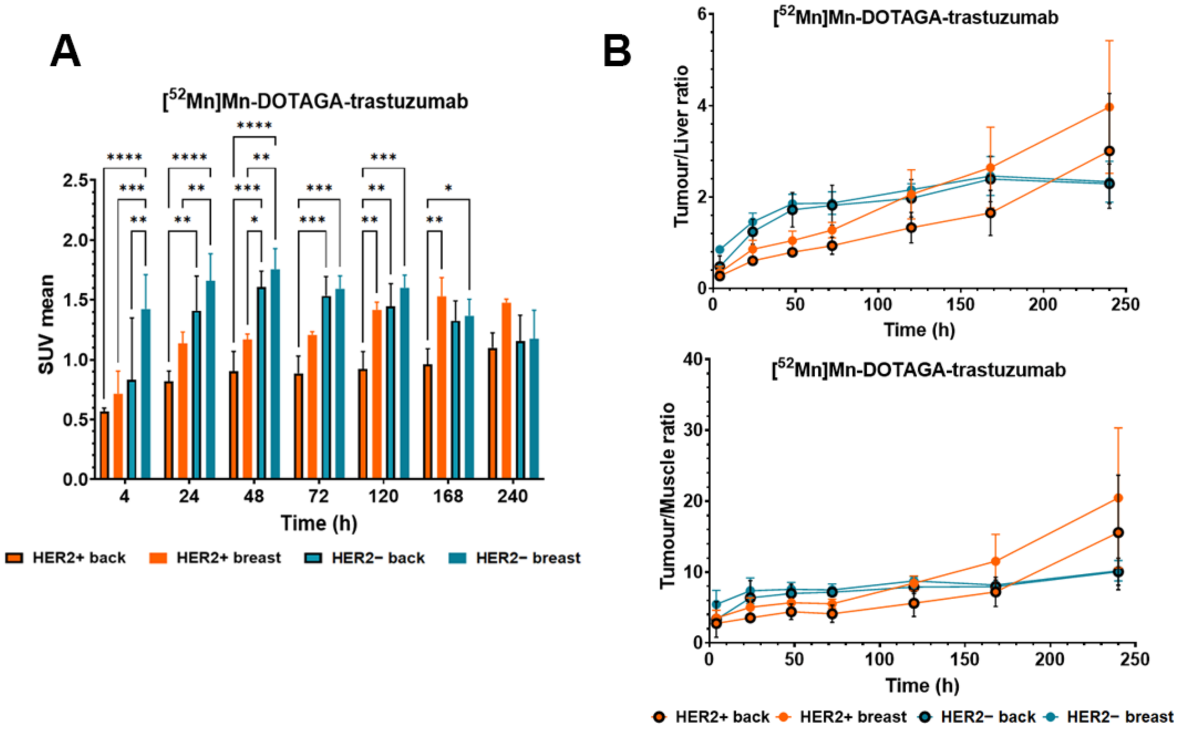

***Figure 26**. HER2 targeting ability of [^{52}Mn]Mn-DOTAGA(pSCN-Bn)-trastuzumab. Left bar graph (**A**) shows SUV mean values of HER2+ back, HER2+ breast, HER2− back, HER2− breast tumours. Upper and lower right line graphs (**B**) display tumour/liver and tumour/muscle uptake ratio, respectively, of each tumour after the injection of [^{52}Mn]Mn-DOTAGA(pSCN-Bn)-trastuzumab. ANOVA was used to compare tumour uptakes, asterisks indicate level of statistical significance: * $p \leq 0.05$, ** $p \leq 0.01$, ***$p \leq 0.001$, **** $p \leq 0.0001$.*

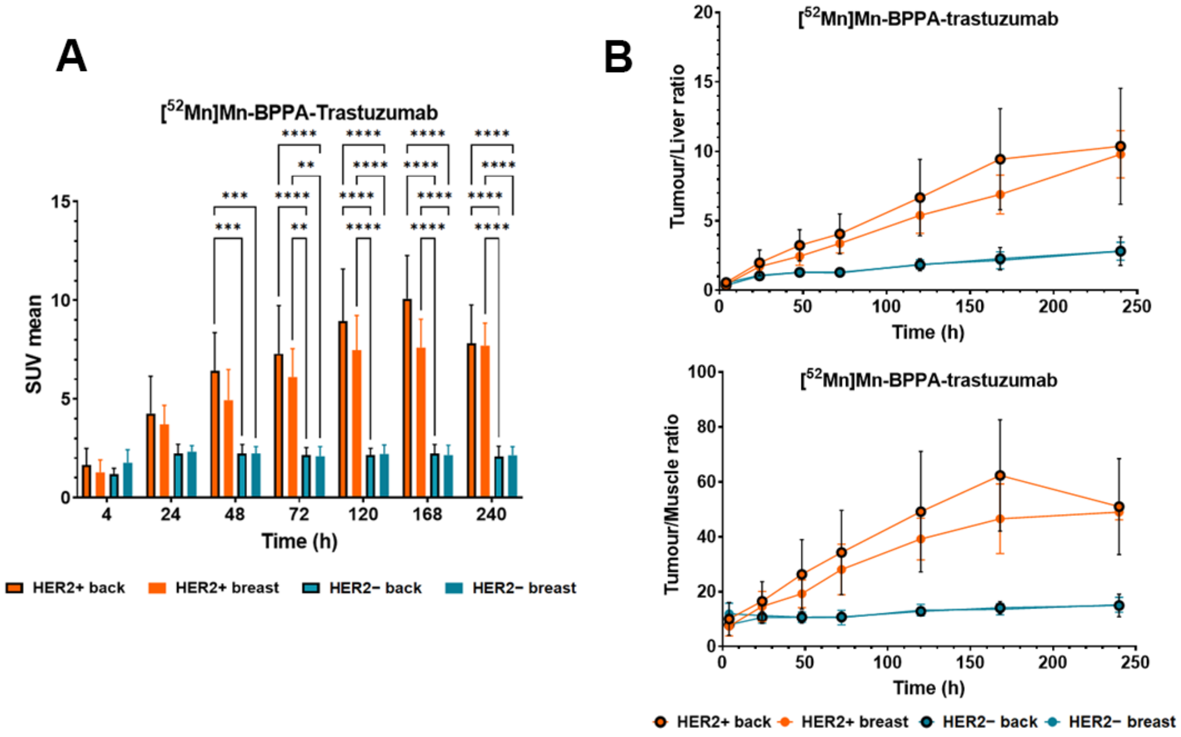

***Figure 27**. HER2 targeting ability of [^{52}Mn]Mn-BPPA-trastuzumab. Left bar graph (a) shows SUV mean values of HER2+ back, HER2+ breast, HER2− back, HER2− breast tumours. Upper and lower right line graphs (b) display tumour/liver and tumour/muscle uptake ratio, respectively, of each tumour after the injection of [^{52}Mn]Mn-BPPA-trastuzumab. ANOVA was used to compare tumour uptakes, asterisks indicate level of statistical significance:* * $p \leq 0.05$, ** $p \leq 0.01$, ***$p \leq 0.001$, **** $p \leq 0.0001$.

became more pronounced at later time points (breast: SUV 7.60 ± 1.45 vs. SUV 2.15 ± 0.51, $p \leq 0.01$ and back: SUV 10.08 ± 2.18 vs. SUV 2.22 ± 0.47, $p \leq 0.001$).

Comparing the HER2 specificity of the two labelled antibody on HER2+ tumours, accumulation of [^{52}Mn]Mn-BPPA-trastuzumab was significantly higher than that of [^{52}Mn]Mn-DOTAGA(pSCN-Bn)-trastuzumab from 48 h onwards (Figure 28).

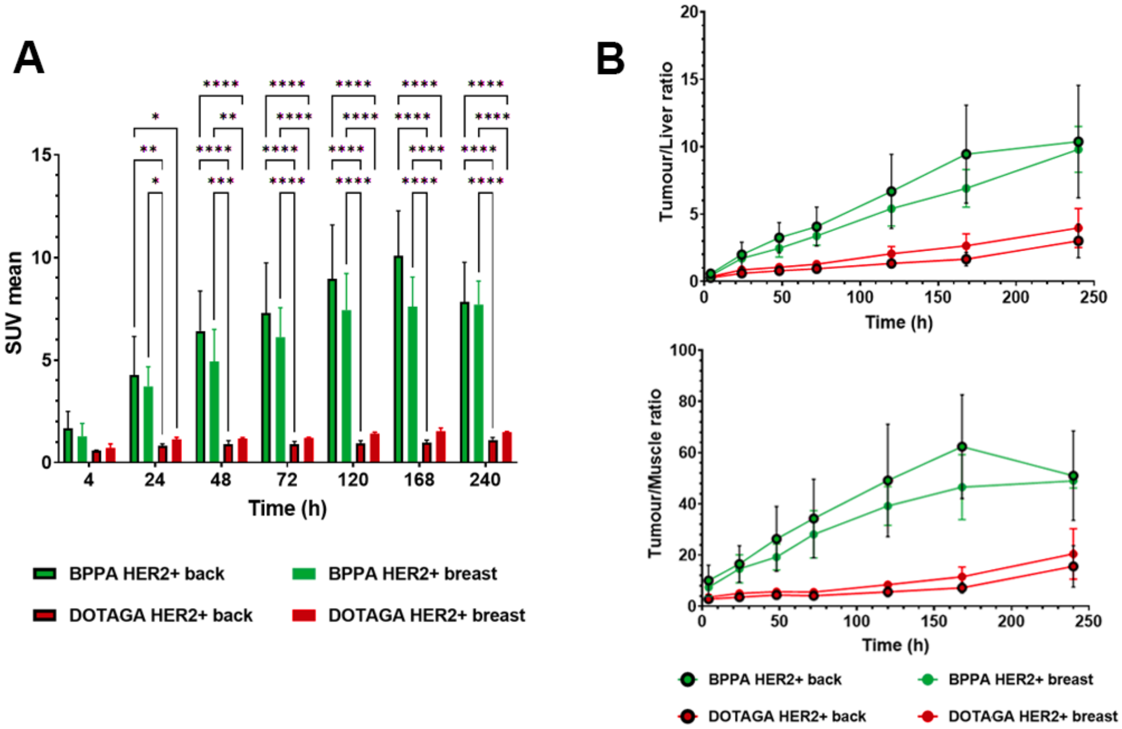

Figure 28. *The superior tumour specificity and tumour to background ratio of [^{52}Mn]Mn-BPPA-trastuzumab over [^{52}Mn]Mn-DOTAGA(pSCN-Bn)-trastuzumab on HER2+ tumour bearing mice. Left bar graph (**A**) shows tumour uptakes over time for both radiotracers, ANOVA was used to compare BPPA group with DOTAGA group, asterisks indicate level of statistical significance: * $p \leq 0.05$, ** $p \leq 0.01$, ***$p \leq 0.001$, **** $p \leq 0.0001$. Upper and lower right line graphs (**B**) display the tumour/liver and tumour/muscle of the two groups on HER2+ tumours.*

3.7. Histopathology and Immunohistochemistry

HER2 expression was confirmed by immunohistochemistry and based on this result the MDA-MB-HER2+ tumour showed a clear HER2 2+ morphology, whereas the 4T1 tumour showed minimal HER2 staining, indicating its HER2 negativity (Figure 29, Figure 30).

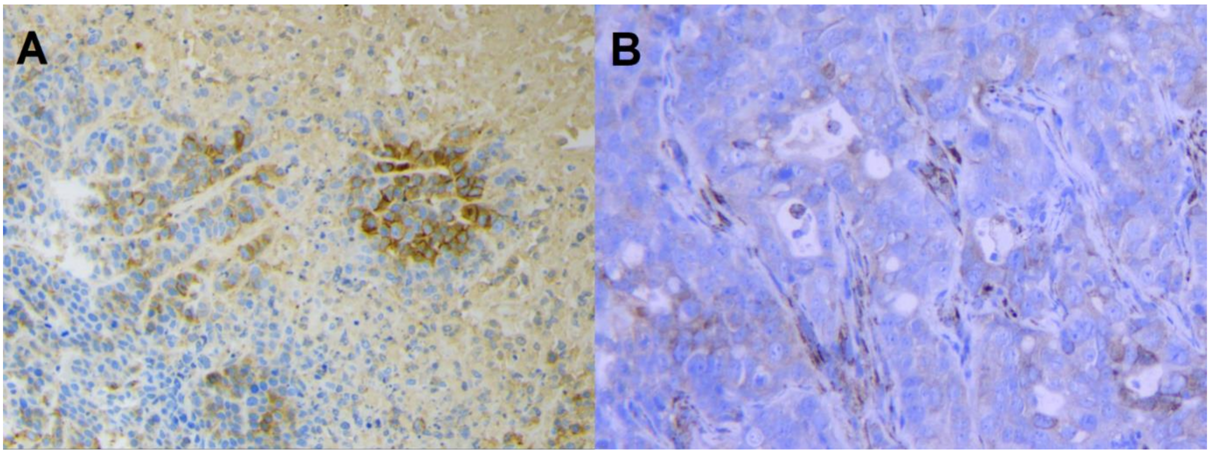

Figure 29. *Immunohistochemistry results on the MDA-MB-HER2+ tumour and 4T1 tumour. (**A**) MDA-MB-HER2+ tumour showed an IHC HER2 2+ pattern, and (**B**) 4T1 tumour demonstrated HER2 negative staining.*

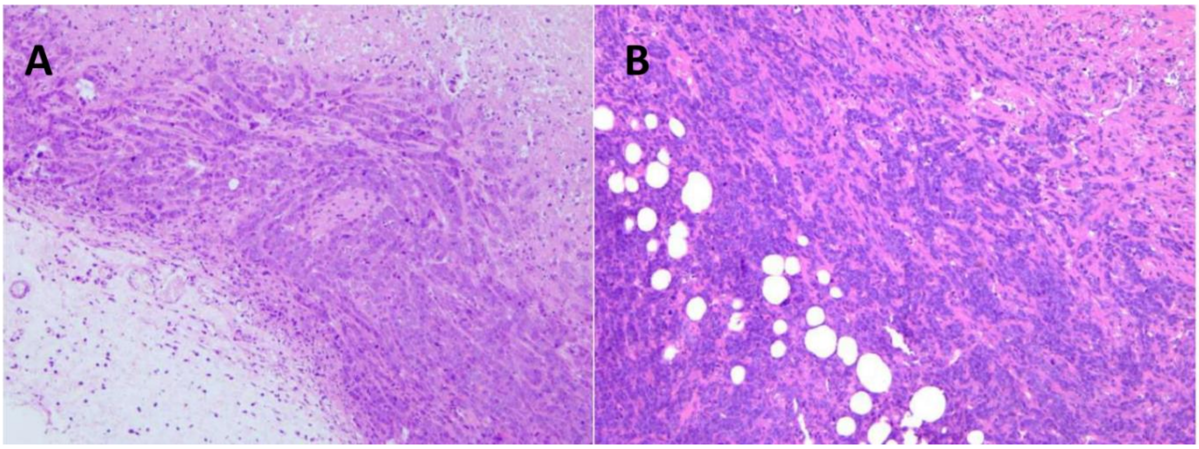

Figure 30. *Histopathological results on the MDA-MB-HER2+ tumour and 4T1 tumour. (**A**) MDA-MBHER2+ tumour showed necrotic pattern, and (**B**) 4T1 tumour demonstrated abundance of stromal component.*

3.8. High-performance Liquid Chromatography (HPLC), NMR Spectra (^{1}H and ^{13}C-JMOD), High Resolution (ESI) Mass Spectra Results

Methyl 6-(3,7-diaza-1,5(2,6)-dipyridinacyclooctaphane-3-ylmethyl)picolinate (2)

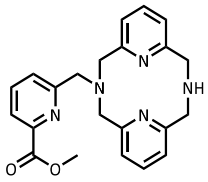

250 mg (1.04 mmol) of 3,7-diaza-1,5(2,6)-dipyridinacyclooctaphane (bispyclen, BP) macrocycle (1) was dissolved in 350 mL of anhydrous acetonitrile. Finely powdered anhydrous potassium carbonate (360 mg, 2.60 mmol) and sodium iodide (16.5 mg, 0.11 mmol) were added to the solution and the suspension was heated up to 80°C under Ar atmosphere while being stirred vigorously. Upon reaching the reflux dropwise addition of methyl 6-(chloromethyl)picolinate (195 mg, 1.04 mmol) dissolved in 50 mL of anhydrous acetonitrile has started. The course of the reaction was monitored using analytical HPLC technique. When the area of the monosubstituted product did not increase further (the optimal amount of 6-(chloromethyl)picolinate was found to be between 0.80-0.85 equivalent), the reaction suspension was cooled down to room temperature, filtered, and the filtrate was evaporated under reduced pressure. The resulting oil was redissolved in 1 mL of 50% (v/v%) acetonitrile and water and the product was purified using preparative HPLC. The collected fractions containing the product were unified and freeze-dried. The desired product (209 mg) is white fluffy powder (yield 52%).

Preparative HPLC: UV-Vis detection: 210 and 260 nm; retention time: 6.97 min; gradient: 0.00→7.00 min 8→13.6% B; eluent: mixture of 5 mM TFA in MQ-water (A) and acetonitrile (B); flow: 25.00 mL/min; column: Phenomenex Luna Prep C18(2) 100 Å, 5 µm, 250 × 21.20 mm; column ID: H18-268346

^{1}H NMR (400.13 MHz, CD_3CN-*d3*) δ; 8.05 (d, J = 7.7 Hz, 1H), 7.98 (t, J = 7.7 Hz, 1H), 7.81 (d, J = 7.7 Hz, 1H), 7.58 (t, J = 7.7 Hz, 2H), 7.12 (d, J = 7.7 Hz, 2H), 7.07 (d, J = 7.7 Hz, 2H), 4.87 (s, 2H), 4.64 (s, 4H), 4.47 (s, 4H), 3.94 (s, 3H) ppm; **^{13}C-JMOD NMR** (100.61 MHz, CD_3CN-*d3*) δ; 166.10, 154.26, 154.00, 152.89, 148.41, 140.17, 139.90, 128.51, 125.86, 124.03, 123.66, 62.60, 61.13, 53.51, 52.95 ppm. **UHRMS** (ESI+) *m/z* calculated for $C_{22}H_{23}N_5O_2$ $[M+H]^+$ 390.1925; found 390.1925; **HPLC** purity (260 nm): 98.43%; retention time: 6.186 min; gradient: 0.00→15.00 min 0→90% B; eluent: mixture of 5 mM TFA in MQ-water (A) and acetonitrile (B); flow: 1.00 mL/min; injection volume: 10.00 µL; sample: 1 mg/mL 50% ACN in H_2O; column: Phenomenex Luna C18(2) 100 Å, 5 µm, 150 × 4.60 mm; column ID: 345362.

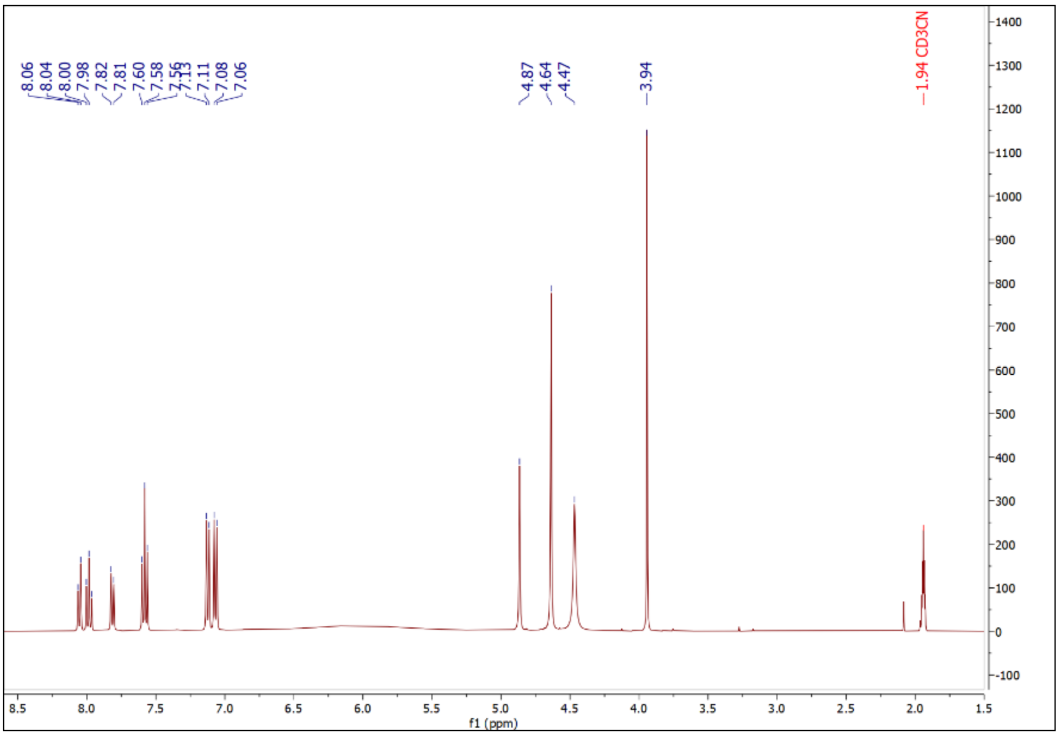

Figure 31. *^{1}H NMR (400.13 MHz, 298.0 K, CD_3CN-d3) spectra of compound* ***2***.

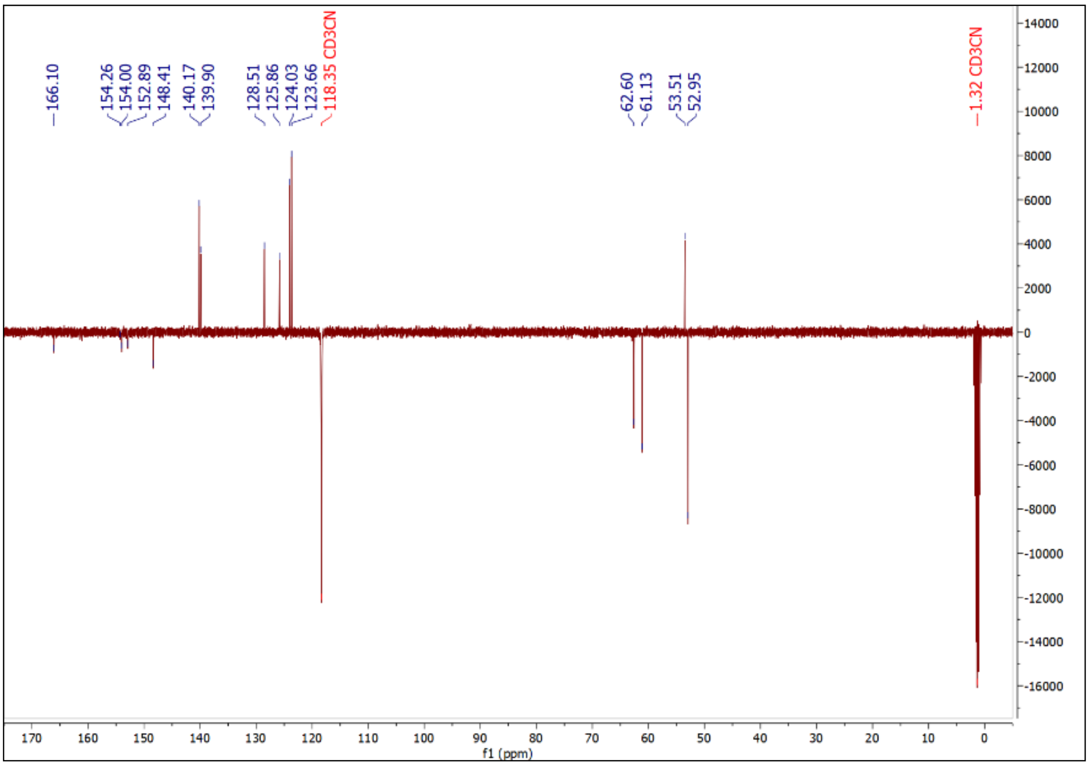

Figure 32. *^{13}C-JMOD NMR (100.62 MHz, 298.0 K, CD_3CN-d3) spectra of compound* ***2***.

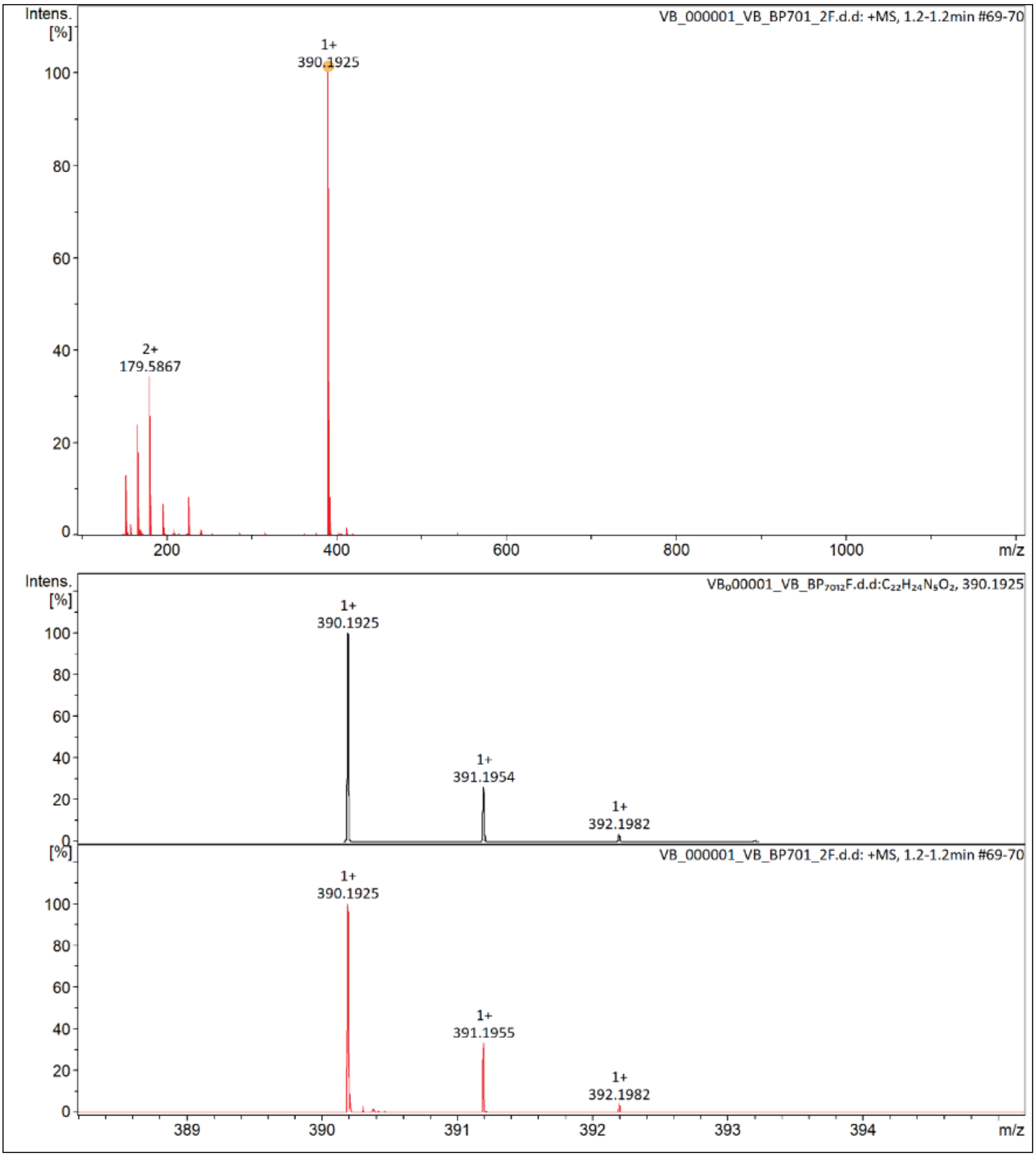

Figure 33. *UHRMS spectra (ESI+) of compound* ***2***.

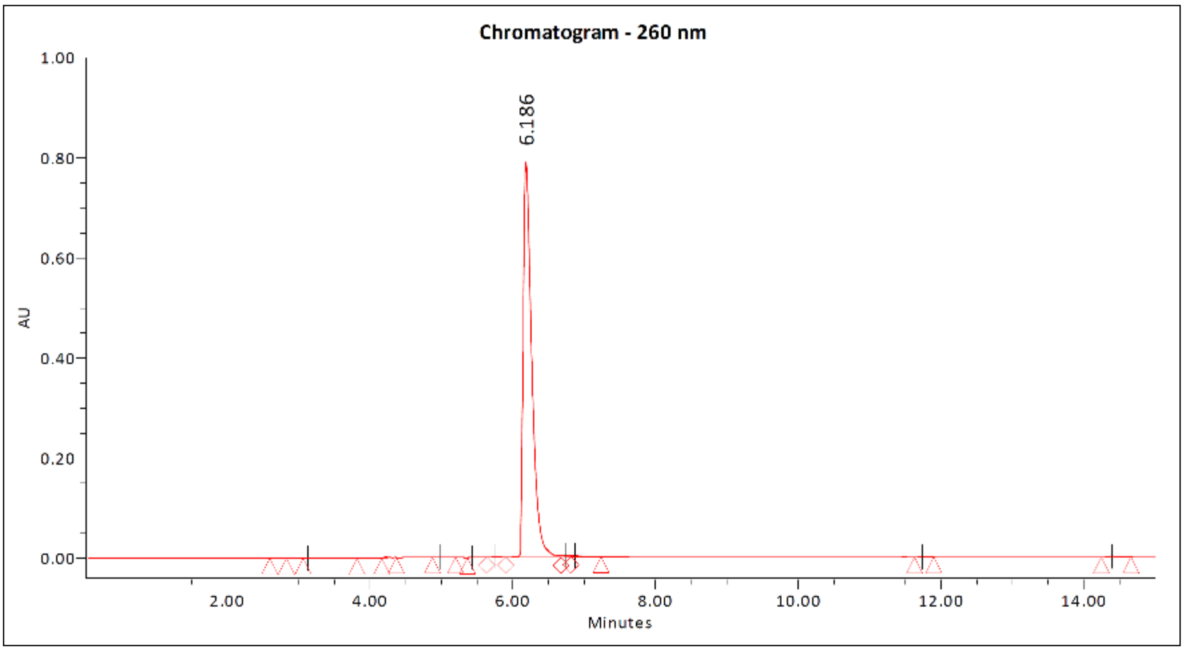

Figure 34. *Analytical HPLC chromatogram (260 nm) of compound **2**.*

6-(3,7-Diaza-1,5(2,6)-dipyridinacyclooctaphane-3-ylmethyl)picolinic acid (BPPA)

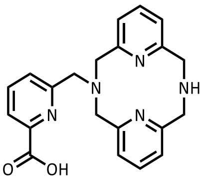

200 mg (0.51 mmol) of (**2**) was dissolved in 4.00 mL of 6 mol/L hydrochloric acid and the solution was sealed in a pressure tube and placed in a microwave reactor. The mixture was heated up to 100°C while being stirred strongly and kept at a given temperature for 10 minutes with an irradiation power of 20 W or less (dynamic mode). After the reaction was complete the solution was freeze-dried. The crude product was redissolved in 1 mL of water and purified using preparative HPLC. The fractions containing the pure product were unified and freeze-dried, yielding 71 mg (yield 37%) of the desired product as white fluffy powder.

Preparative HPLC: UV-Vis detection: 210 and 260 nm; retention time: 2.58 min; gradient: 0.00→8.00 min 8→10% B; eluent: mixture of 5 mM TFA in MQ-water (A) and acetonitrile (B); flow: 25.00 mL/min; column: Phenomenex Luna Prep C18(2) 100 Å, 5 µm, 250 × 21.20 mm; column ID: H18-268346.

^{1}H NMR (360.13 MHz, D_2O) δ; 8.15 (d, J = 7.8 Hz, 1H), 8.14 (t, J = 7.8 Hz, 1H), 7.87 (d, J = 7.8 Hz, 1H), 7.55 (t, J = 7.7 Hz, 2H), 7.13 (d, J = 7.8 Hz, 2H), 7.08 (d, J = 7.8 Hz, 2H), 5.12 (s, 2H), 4.63 (bs, 8H) ppm; **^{13}C-JMOD NMR** (100.61 MHz, D_2O:CD_3CN-*d3* 2:1) δ;

166.84, 151.04, 150.92, 150.20, 148.24, 141.00, 139.79, 128.92, 126.34, 124.96, 124.34, 61.86, 61.74, 52.95 ppm. **UHRMS** (ESI+) *m/z* calculated for $C_{21}H_{21}N_5O_2$ $[M+H]^+$ 376.1768; found 376.1768; **HPLC** purity (260 nm): 99.38%; retention time: 5.662 min; gradient: 0.00→15.00 min 0→90% B; eluent: mixture of 5 mM TFA in MQ-water (A) and acetonitrile (B); flow: 1.00 mL/min; injection volume: 10.00 µL; sample: 1 mg/mL 50% ACN in H_2O; column: Phenomenex Luna C18(2) 100 Å, 5 µm, 150 × 4.60 mm; column ID: 345362.

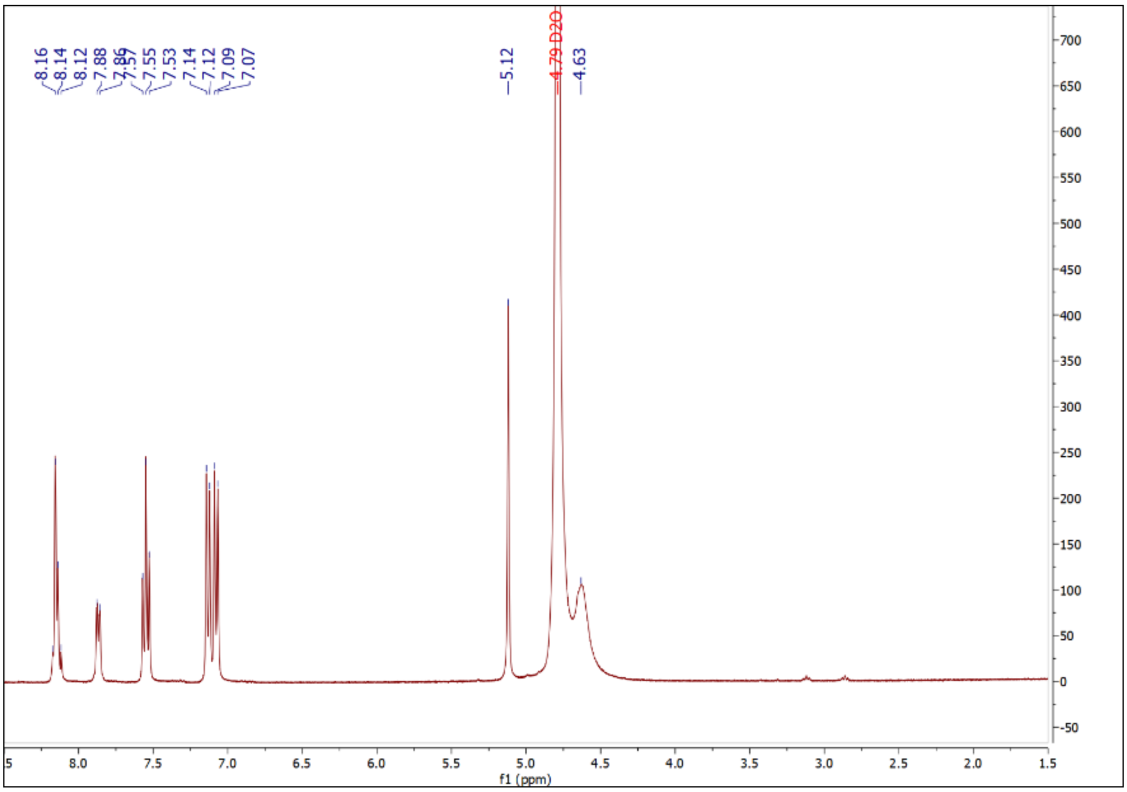

Figure 35. ^{1}H NMR (360.13 MHz, 298.0 K, D_2O) spectra of **BPPA**.

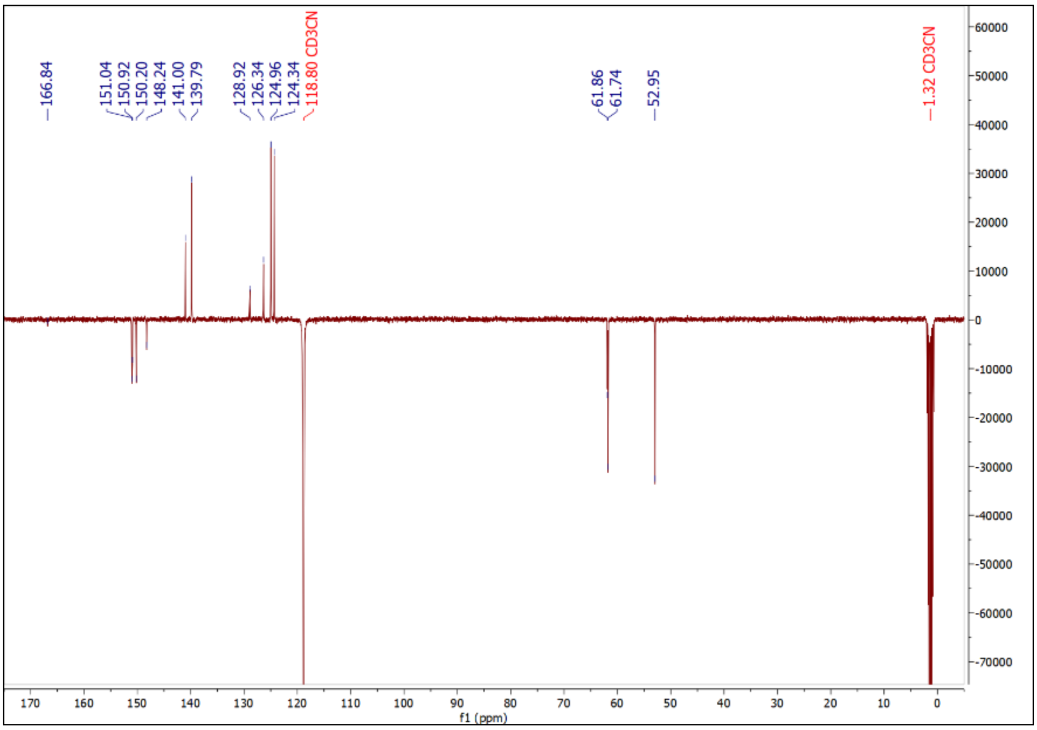

Figure 36. ^{13}C-JMOD NMR (100.62 MHz, 298.0 K, D_2O:CD_3CN-d3 2:1) spectra of **BPPA**.

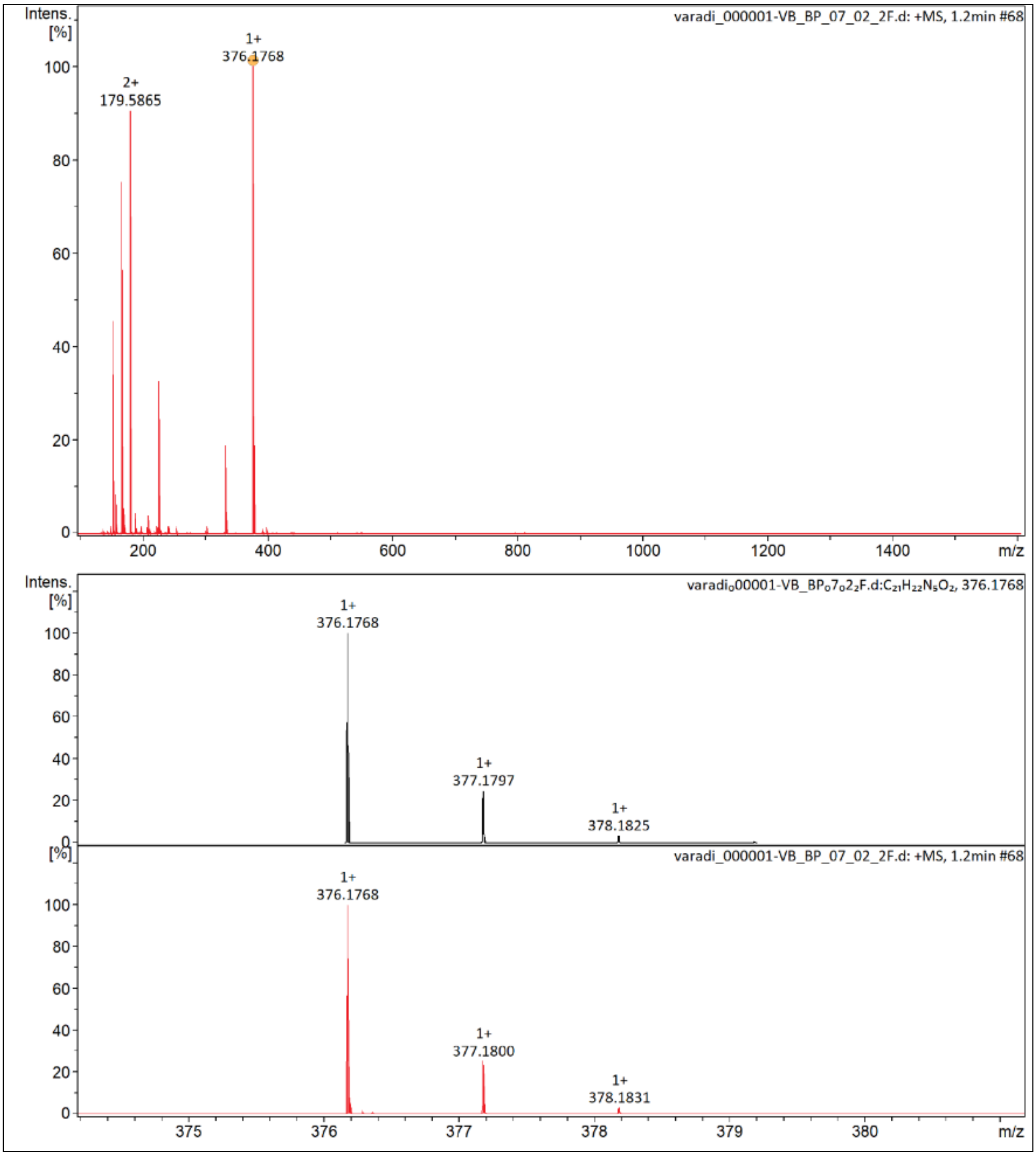

Figure 37. *UHRMS spectra (ESI+) of* ***BPPA****.*

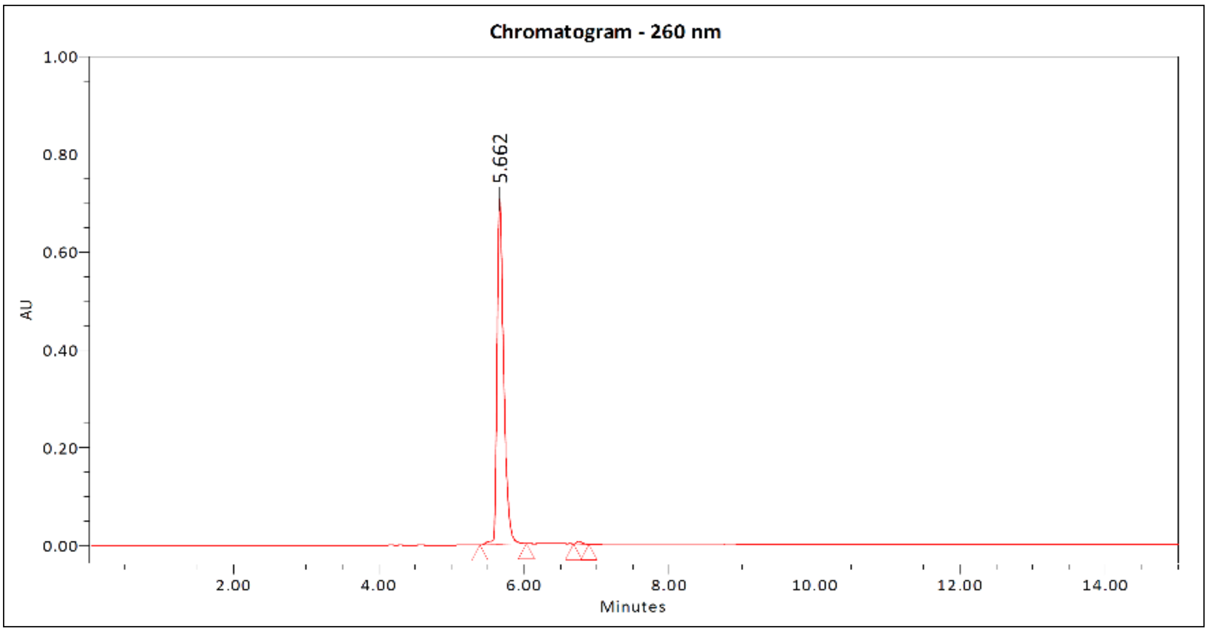

***Figure 38**. Analytical HPLC chromatogram (260 nm) of **BPPA**.*

***Tert*-butyl 4-(3,7-diaza-1,5(2,6)-dipyridinacyclooctaphane-3-ylmethyl)benzoate (3)**

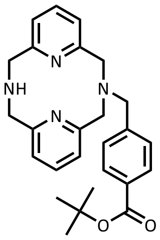

500 mg (2.08 mmol) of 3,7-diaza-1,5(2,6)-dipyridinacyclooctaphane (**1**) was dissolved in 400 mL of acetonitrile and 890 mg (6.44 mmol) potassium carbonate was added to the solution. The temperature of the reaction mixture was brought up to 60°C and stirred for 15 min. The solution of 170 mg (0.627 mmol) alkylating agent (*tert*-butyl 4-(bromomethyl)benzoate) in 60 mL acetonitrile was added to the reaction mixture dropwise. The mixture was stirred for an additional 3 hours at 60°C and the solvent was removed under reduced pressure to afford the crude product, which was purified by preparative HPLC. The fractions containing the pure product were combined and lyophilized. The product obtained is a white solid (150 mg, yield 55%).

Preparative HPLC: UV-Vis detection: 210 and 260 nm; retention time: 10.15 min; gradient: 0.00→11.00 min 10→32% B; eluent: mixture of 5 mM TFA in MQ-water (A) and acetonitrile (B); flow: 25.00 mL/min; column: Phenomenex Luna Prep C18(2) 100 Å, 5 µm, 250 × 21.20 mm; column ID: H18-268346

^{1}**H NMR** (360.13 MHz, MeOD-*d4*) δ; 8.11 (d, J = 8.3 Hz, 2H), 7.92 (d, J = 8.3 Hz, 2H), 7.52 (t, J = 7.7 Hz, 2H), 7.11 (d, J = 7.7 Hz, 2H), 7.04 (d, J = 7.7 Hz, 2H), 5.08 (s, 2H), 4.86 - 4.35 (m, 8H), 1.59 (s, 9H) ppm; ^{13}**C-JMOD NMR** (90.56 MHz, MeOD-*d4*) δ; 166.32, 151.82, 139.98, 135.01, 134.63, 132.56, 131.23, 124.84, 124.40, 82.84, 62.64, 61.28, 53.48, 28.32 ppm; **UHRMS** (ESI+) *m/z* calculated for $C_{26}H_{30}N_4O_2$ $[M+H]^+$ 431.2442; found 431.2442; **HPLC** purity (260 nm): 99.35%; retention time: 7.208 min; gradient: 0.00→15.00 min 5→95% B; eluent: mixture of 5 mM TFA in MQ-water (A) and acetonitrile (B); flow: 1.00 mL/min; injection volume: 10.00 µL; sample: 1.2 mg/mL 50% ACN in H_2O; column: Phenomenex Luna C18(2) 100 Å, 5 µm, 150 × 4.60 mm; column ID: H21-212012.

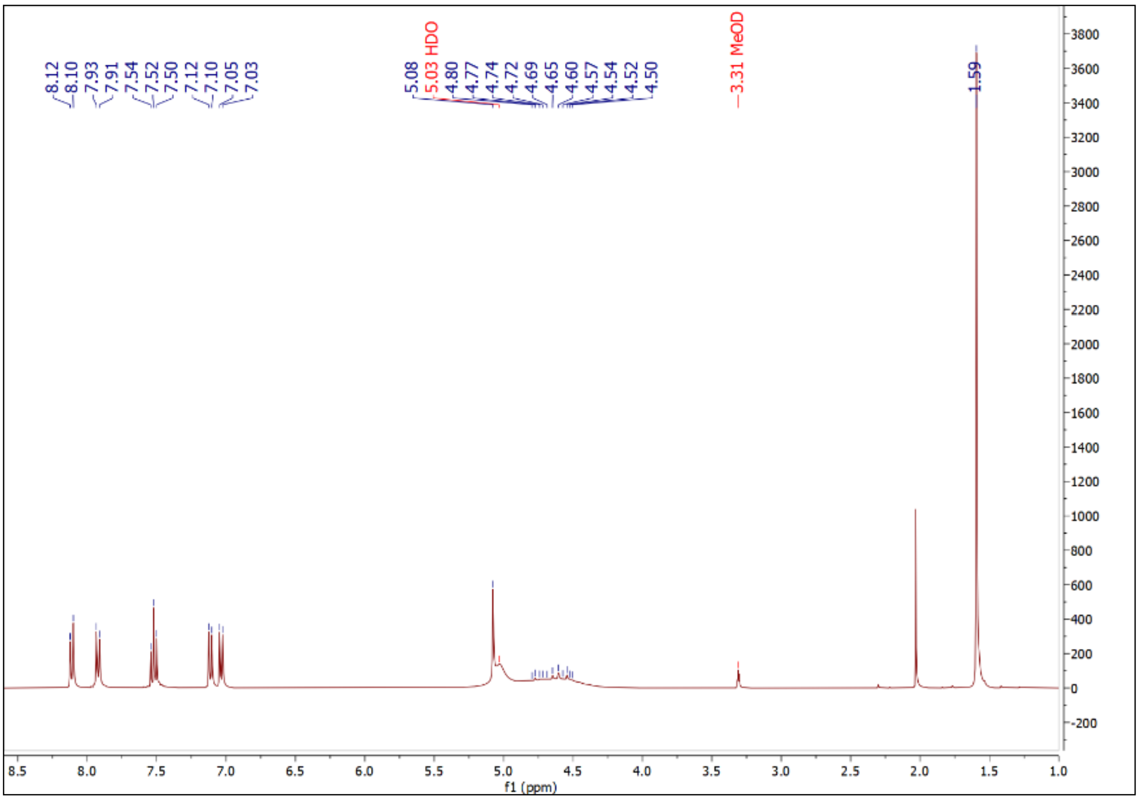

Figure 39**. ^{1}H NMR (360.13 MHz, 298.0 K, MeOD-d4) spectra of compound **3.

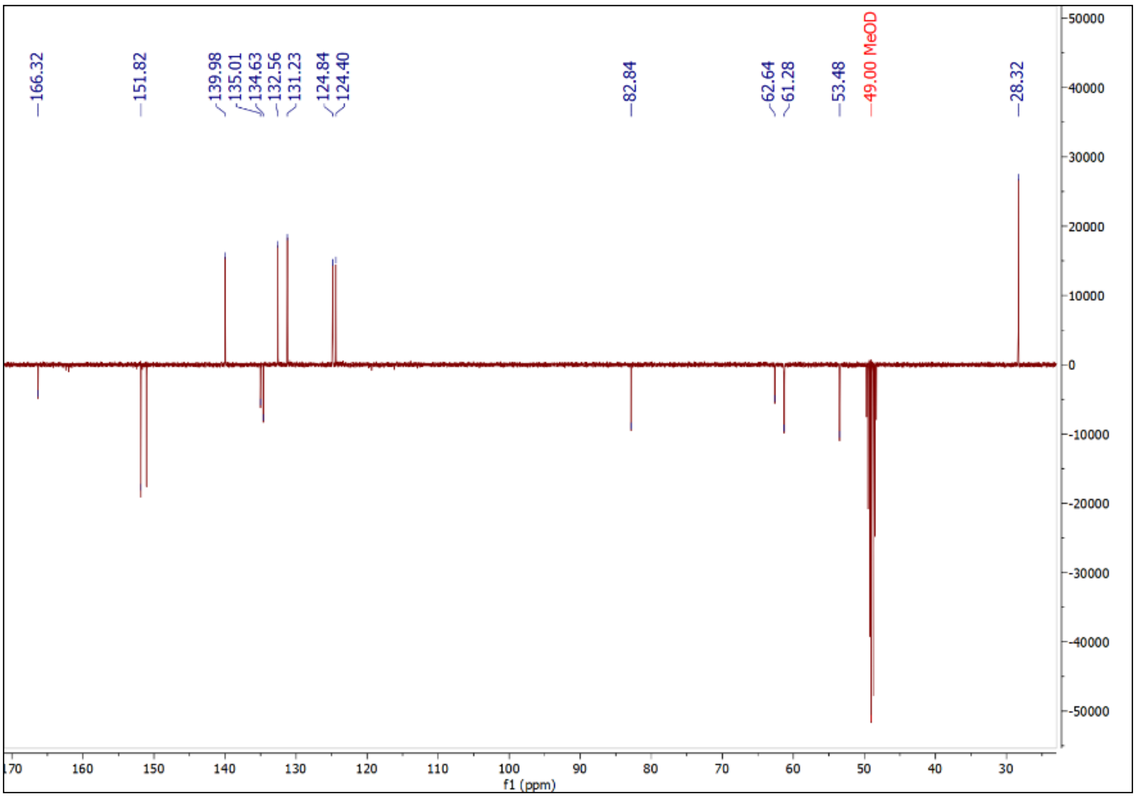

Figure 40. *^{13}C-JMOD NMR (90.56 MHz, 298.0 K, MeOD-d4) spectra of compound* ***3****.*

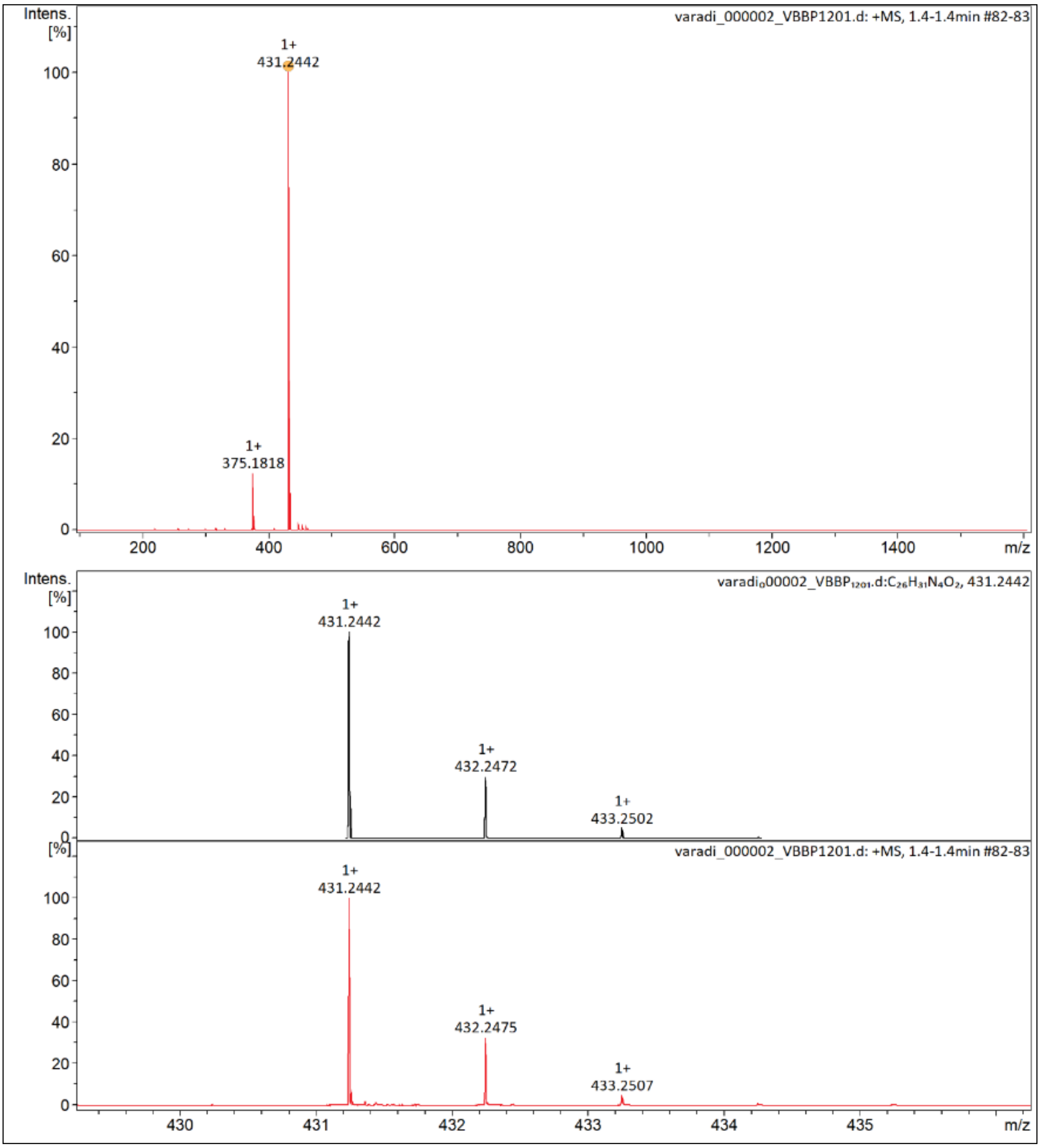

Figure 41. *UHRMS spectra (ESI+) of compound **3**.*

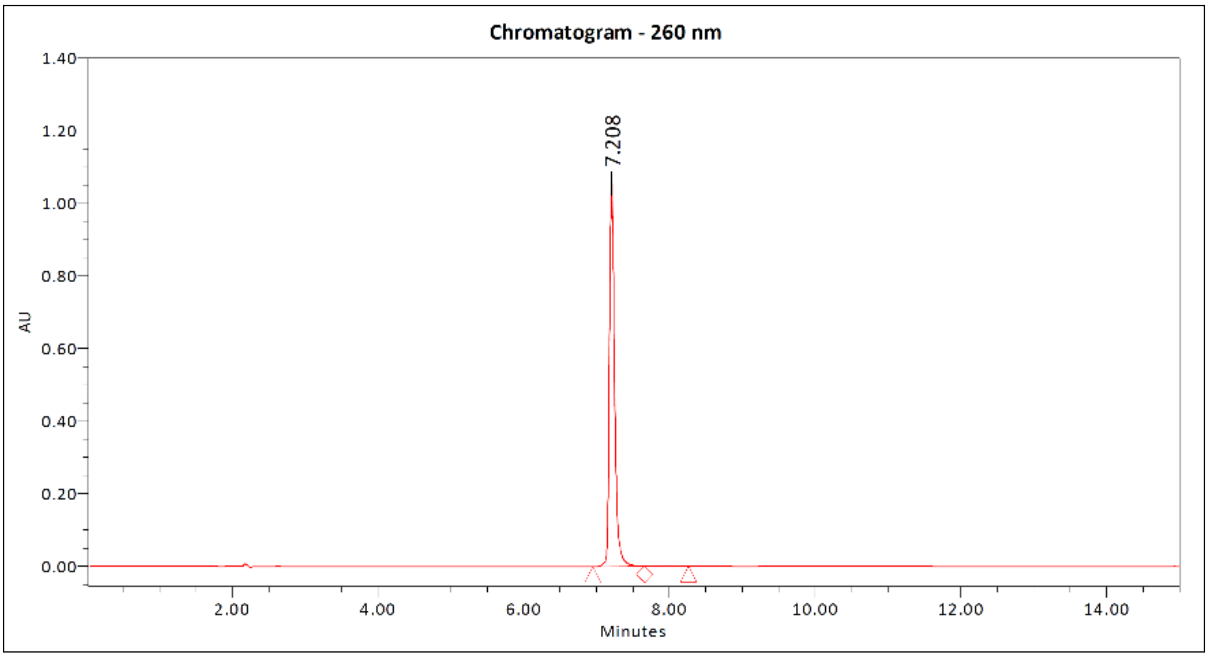

Figure 42. *Analytical HPLC chromatogram (260 nm) of compound **3**.*

4-(3,7-diaza-1,5(2,6)-dipyridinacyclooctaphane-3-ylmethyl)benzoic acid (4)

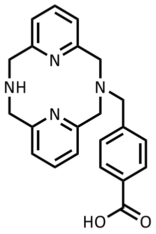

Tert-butyl-4-(3,7-diaza-1,5(2,6)-dipyridinacyclooctaphane-3-ylmethyl)benzoate (**3**) (140 mg, 0.325 mmol) was dissolved in 15.0 mL of dichloromethane and 7.0 mL trifluoroacetic acid was added dropwise to this solution at room temperature. The reaction mixture was stirred at room temperature for an additional 23 hours and concentrated under vacuum to afford **4** as a white solid (120 mg, yield 98%).

^{1}H NMR (360.13 MHz, MeOD-*d4*) δ; 8.17 (d, J = 8.2 Hz, 2H), 7.93 (d, J = 8.2 Hz, 2H), 7.50 (t, J = 7.7 Hz, 2H), 7.10 (d, J = 7.7 Hz, 2H), 7.03 (d, J = 7.8 Hz, 2H), 5.08 (s, 2H), 4.86 - 4.35 (m, 8H) ppm; **^{13}C-JMOD NMR** (90.56 MHz, MeOD-*d4*) δ; 168.87, 151.80, 151.02, 140.01, 134.78, 133.95, 132.63, 131.69, 124.87, 124.43, 62.73, 61.34, 53.53 ppm; **UHRMS** (ESI+) *m/z* calculated for $C_{22}H_{22}N_4O_2$ $[M+H]^+$ 375.1816 ; found 375.1816; **HPLC** purity (260 nm): 88.36%; retention time: 2.735 min; gradient: 0.00→7.50 min 5→95% B; eluent: mixture of 5 mM TFA in MQ-water (A) and acetonitrile (B); flow: 1.00 mL/min; injection volume:

5.00 µL; sample: 1 mg/mL H_2O; column: Waters XBridge Shield RP18 C18 100 Å 2.5µm 75 × 4.60 mm; column ID: 01193505914502.

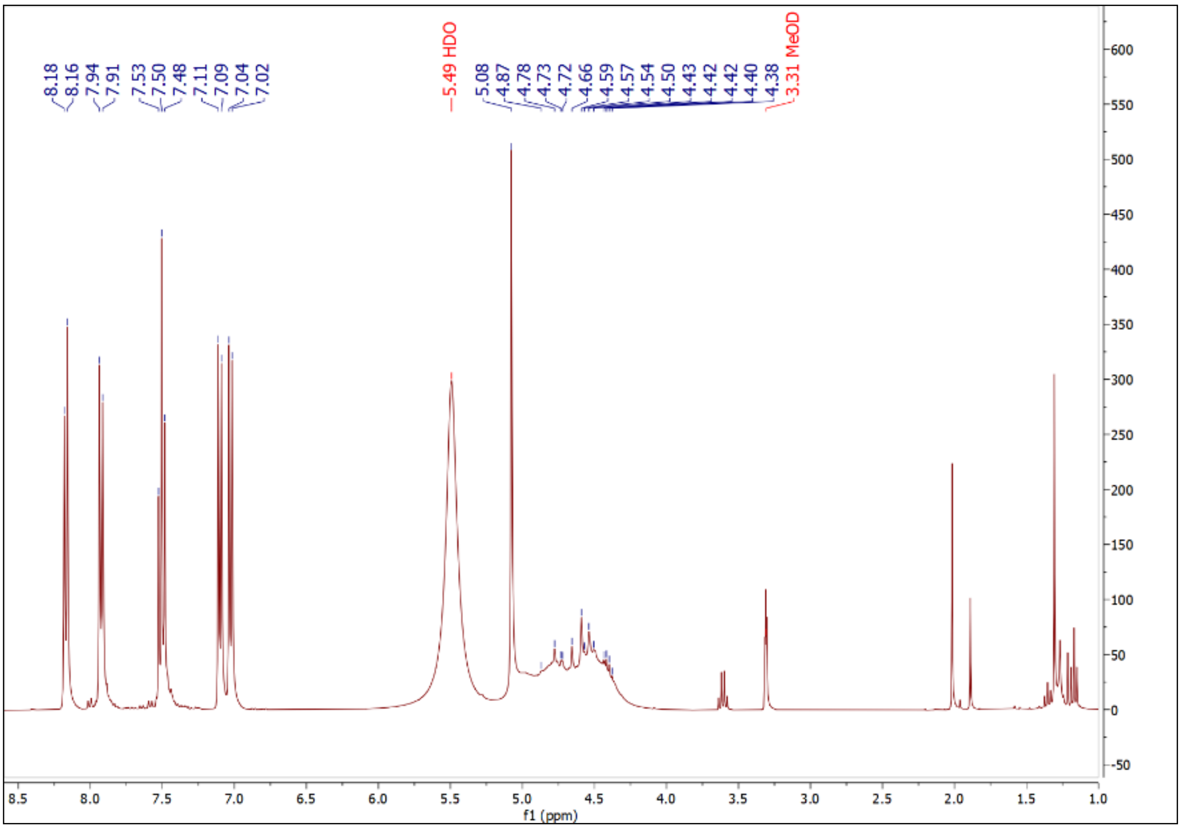

Figure 43. *^{1}H NMR (360.13 MHz, 298.0 K, MeOD-d4) spectra of compound* ***4****.*

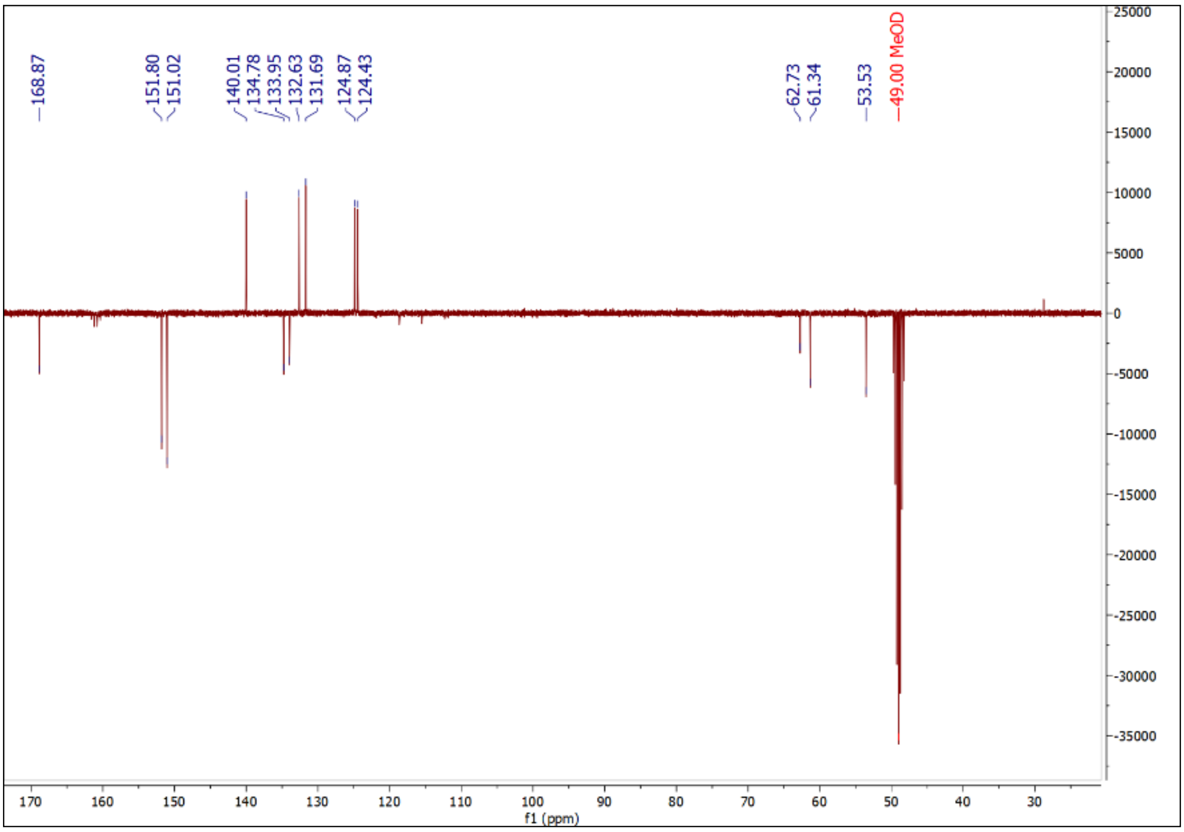

Figure 44. *^{13}C-JMOD NMR (90.56 MHz, 298.0 K, MeOD-d4) spectra of compound* ***4****.*

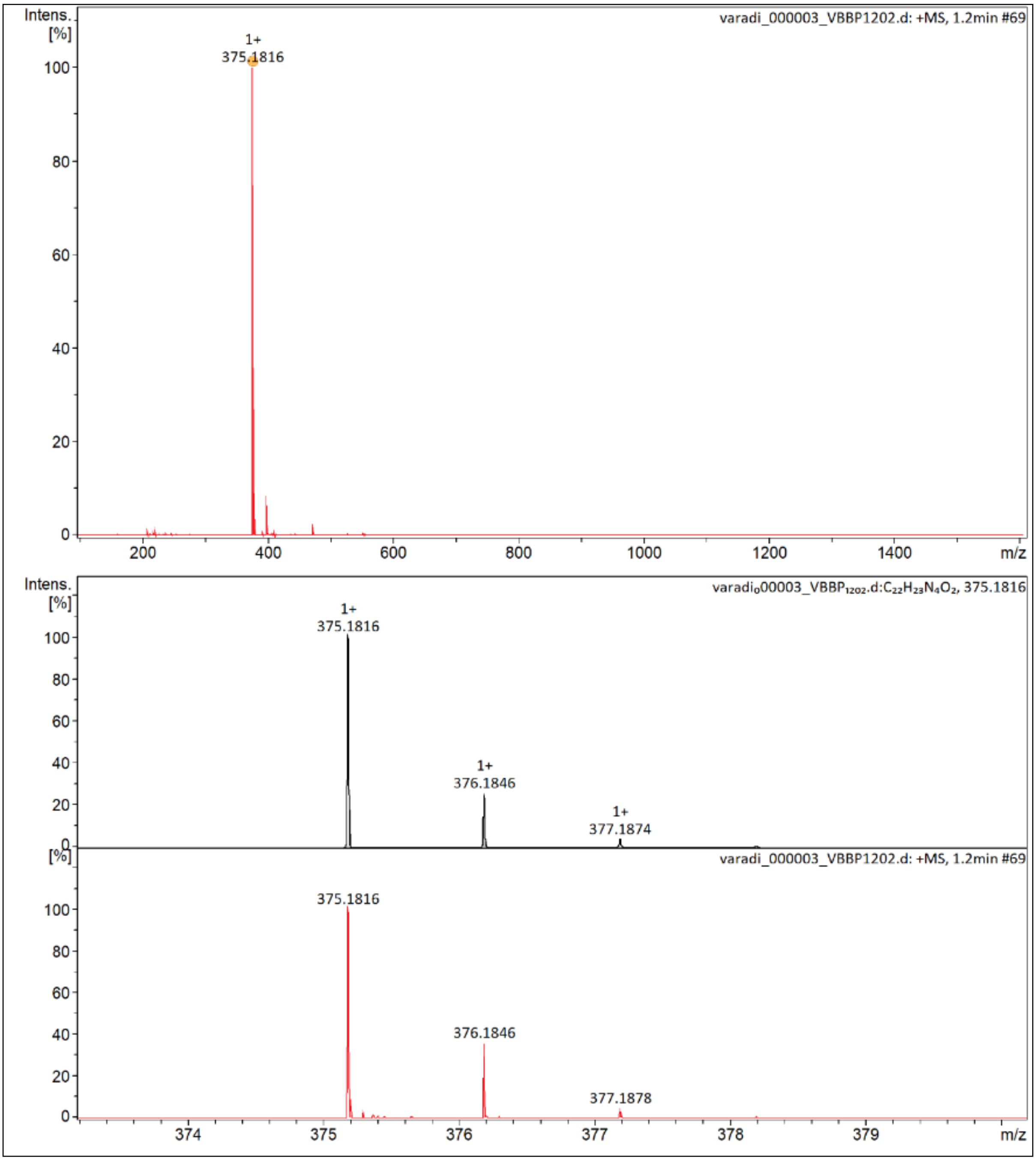

Figure 45. *UHRMS spectra (ESI+) of compound* ***4****.*

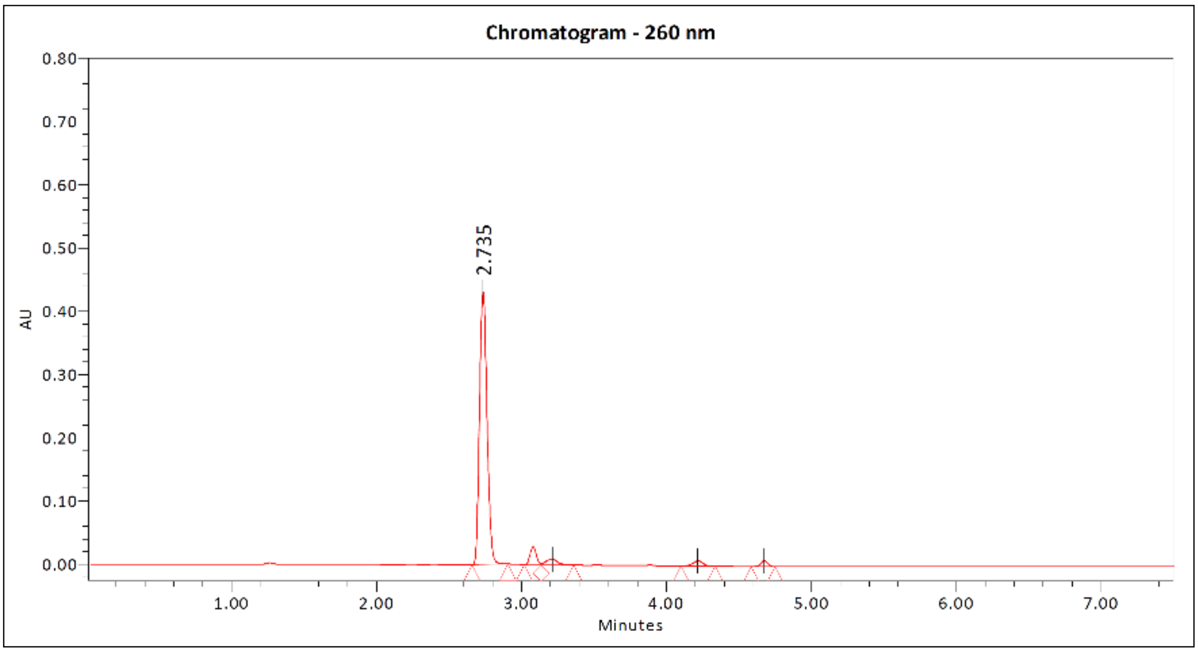

Figure 46. *Analytical HPLC chromatogram (260 nm) of compound **4**.*

4-((7-((6-(*tert*-butoxycarbonyl)pyridin-2-yl)methyl)-3,7-diaza-1,5(2,6)-dipyridinacyclooctaphane-3-yl)methyl)benzoic acid (5)

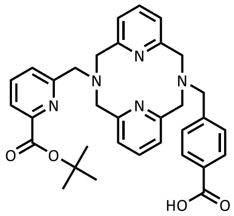

120 mg (0.320 mmol) of 4-(3,7-diaza-1,5(2,6)-dipyridinacyclooctaphane-3-ylmethyl) benzoic acid (**4**) was dissolved in 100 mL of *N*,*N*-dimethylformamide and 340 µL (1.95 mmol) *N*,*N*-diisopropylethylamine was added to the solution. The temperature of the reaction mixture was brought up to 85°C and stirred for 15 min. The solution of 50 mg (0.184 mmol) of the alkylating agent (*tert*-butyl 6-(bromomethyl)picolinate) dissolved in 25 mL *N*,*N*-dimethylformamide was added to the reaction mixture dropwise. The mixture was stirred for an additional 18 hours at 85°C and the solvent was then removed in vacuum to afford the crude product, which was purified by preparative HPLC. The combined fractions containing of the target substance were lyophilized. Freezer-drying returned 52 mg (yield 50%) of the product **5** as a white solid.

Preparative HPLC: UV-Vis detection: 210 and 260 nm; retention time: 9.60 min; gradient: 0.00→15.00 min 20→60% B; eluent: mixture of 5 mM TFA in MQ-water (A) and acetonitrile (B); flow: 25.00 mL/min; column: Phenomenex Luna Prep C18(2) 100 Å, 5 µm, 250 × 21.20 mm; column ID: H18-268346

^{1}H NMR (360.13 MHz, MeOD-*d4*) δ; 7.87 (d, J = 7.8 Hz, 1H), 7.86 (t, J = 7.8 Hz, 2H), 7.78 (d, J = 8.0 Hz, 2H), 7.77 (t, J = 7.8 Hz, 1H), 7.58 (d, J = 7.8 Hz, 1H), 7.39 (d, J = 8.0 Hz, 2H), 7.31 (d, J = 7.8 Hz, 2H), 7.26 (d, J = 7.8 Hz, 2H), 4.47 (bs, 4H), 4.39 (s, 2H), 4.34 (s, 4H), 4.23 (s, 2H), 1.59 (s, 9H) ppm; **^{13}C-JMOD NMR** (90.56 MHz, MeOD-*d4*) δ; 169.31, 165.25, 162.15, 159.70, 158.26, 149.71, 144.42, 142.44, 139.20, 131.25, 130.72, 130.38, 128.09, 124.82, 123.12, 123.09, 83.66, 61.84, 61.35, 58.88, 58.72, 28.29.ppm; **UHRMS** (ESI+) *m/z* calculated for $C_{33}H_{35}N_5O_4$ $[M+H]^+$ 566.2762; found 566.2762; **HPLC** purity (260 nm): 99.25%; retention time: 6.181 min; gradient: 0.00→15.00 min 5→95% B; eluent: mixture of 5 mM TFA in MQ-water (A) and acetonitrile (B); flow: 1.00 mL/min; injection volume: 10.00 µL; sample: 1 mg/mL 50% ACN in H_2O; column: Phenomenex Luna C18(2) 100 Å, 3 µm, 75 × 4.60 mm; column ID: 413959-7.

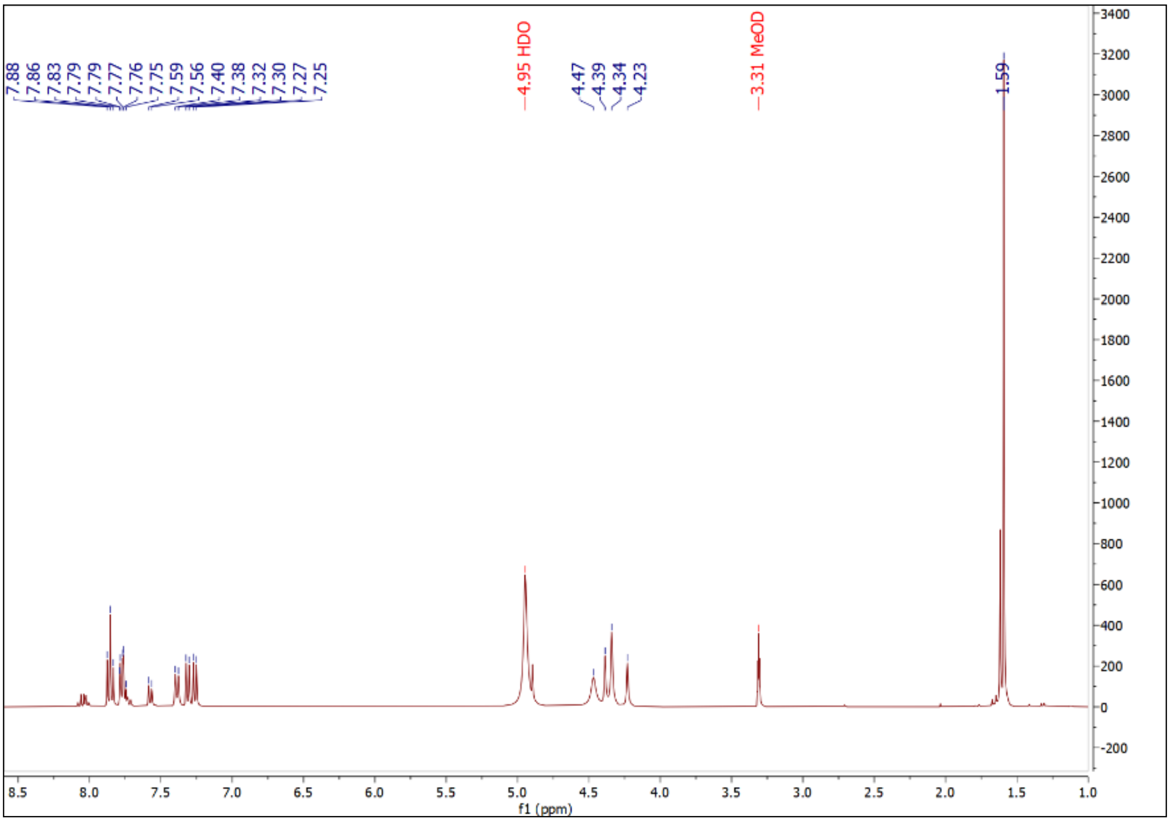

Figure 47. *^{1}H NMR (360.13 MHz, 298.0 K, MeOD-d4) spectra of compound* ***6****.*

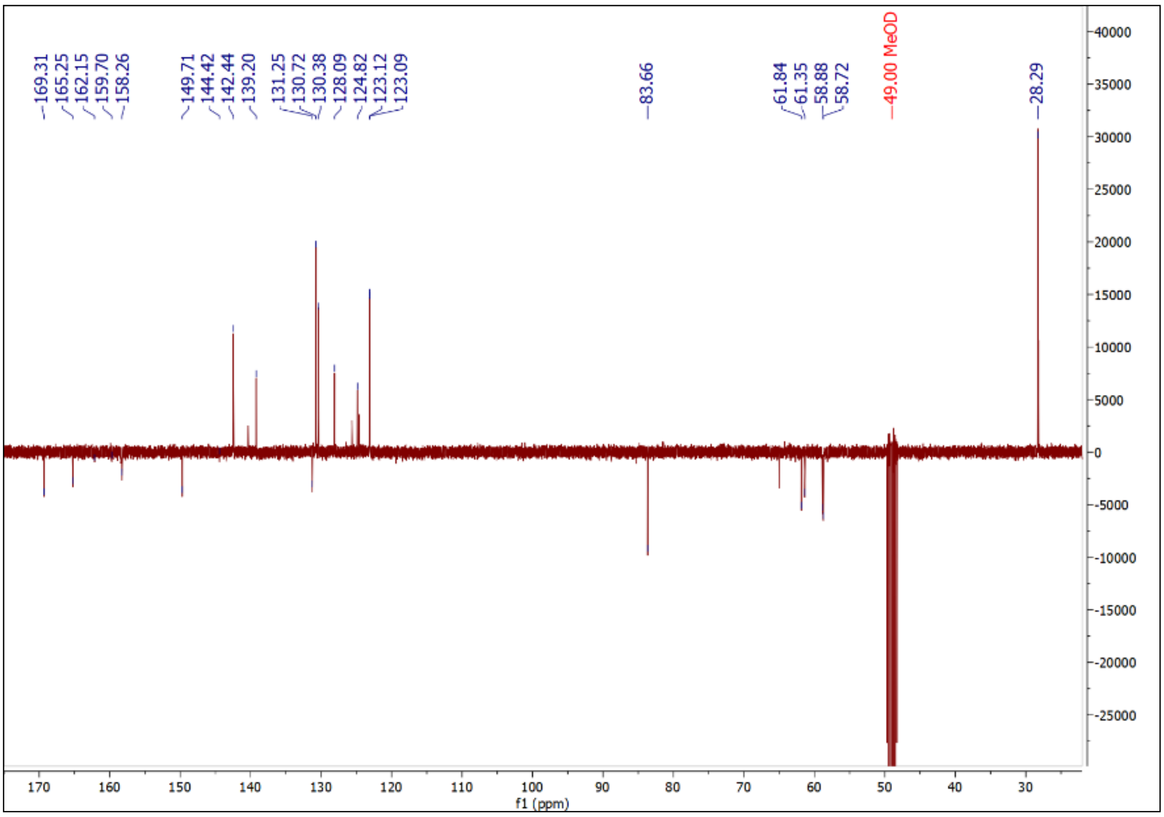

Figure 48. *^{13}C-JMOD NMR (90.56 MHz, 298.0 K, MeOD-d4) spectra of compound* ***6***.

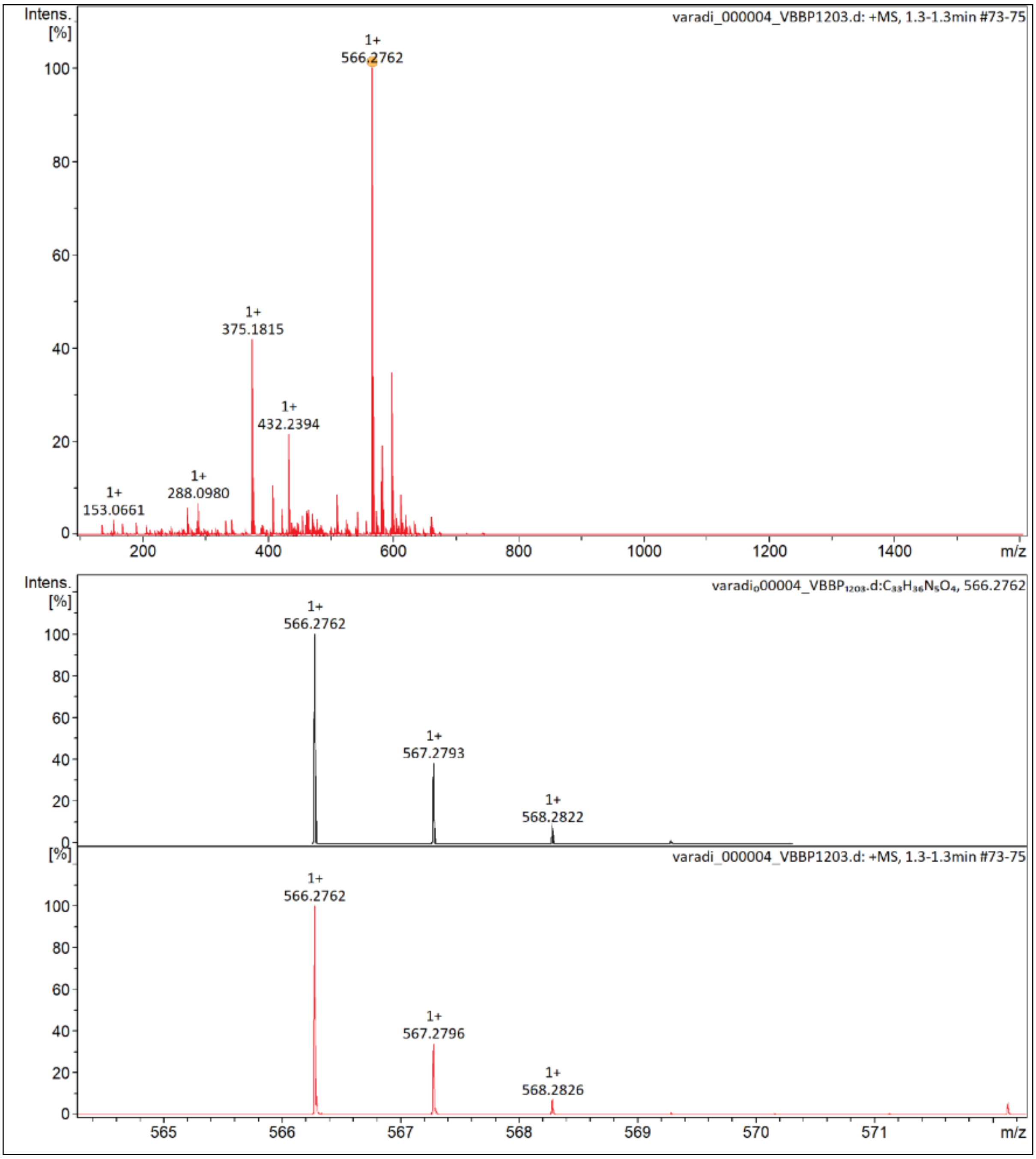

Figure 49. *UHRMS spectra (ESI+) of compound* ***6****.*

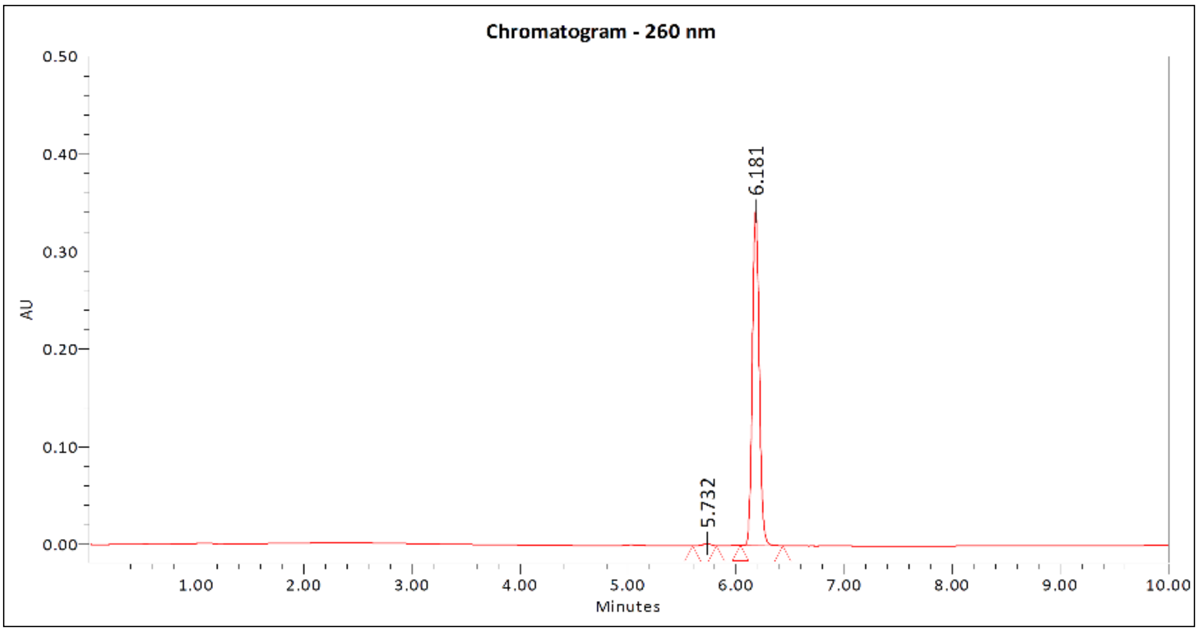

***Figure 50**. Analytical HPLC chromatogram (260 nm) of compound **6**.*

6-((7-(4-carboxybenzyl)-3,7-diaza-1,5(2,6)-dipyridinacyclooctaphane-3-yl)methyl)picolinic acid (BPPA-Bn^{pCOOH})

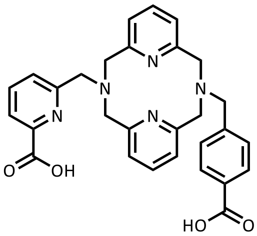

4-((7-((6-(*tert*-butoxycarbonyl)pyridin-2-yl)methyl)-3,7-diaza-1,5(2,6)-dipyridinacyclooctaphane-3-yl)methyl)benzoic acid (6) (7.0 mg, 0.0124 mmol) was dissolved in 1.0 mL of dichloromethane and 470 µL trifluoroacetic acid was added dropwise to this solution at room temperature. The reaction mixture was stirred at room temperature for 5 hours and concentrated under vacuum to afford the crude product, which was purified by preparative HPLC. The fractions of the pure product were combined, lyophilized to yield the **BPPA-Bn^{pCOOH}** ligand as a white solid (6.1 mg, yield 97%).

Preparative HPLC: UV-Vis detection: 210 and 260 nm; retention time: 6.60 min; gradient: 0.00→10.00 min 5→65% B; eluent: mixture of 5 mM TFA in MQ-water (A) and acetonitrile (B); flow: 25.00 mL/min; column: Phenomenex Luna Prep C18(2) 100 Å, 5 µm, 250 × 21.20 mm; column ID: H18-268346

^{1}H NMR (500.13 MHz, CD_3CN-*d3*) δ; 7.91 (d, J = 7.7 Hz, 1H), 7.81 (t, J = 7.8 Hz, 2H), 7.75 (d, J = 8.0 Hz, 2H), 7.74 (t, J = 7.7 Hz, 1H), 7.55 (d, J = 7.7 Hz, 1H), 7.32 (d, J = 8.0 Hz, 2H), 7.23 (d, J = 7.8 Hz, 2H), 7.19 (d, J = 7.8 Hz, 2H), 4.37 (bs, 4H), 4.30 (s, 2H), 4.22 (s, 4H), 4.12 (s, 2H) ppm; **^{13}C-JMOD NMR** (125.77 MHz, CD_3CN-*d3*) δ; 167.76, 165.66, 160.99, 159.13, 158.25, 147.15, 144.59, 142.26, 139.52, 130.69, 130.42, 130.07, 128.63, 123.56, 122.86, 122.78, 61.55, 60.89, 58.29, 58.17 ppm; **UHRMS** (ESI+) *m/z* calculated for $C_{29}H_{27}N_5O_4$ $[M+H]^+$ 510.2136; found 510.2133; **HPLC** purity (260 nm): 96.09%; retention time: 7.049 min; gradient: 0.00→15.00 min 5→95% B; eluent: mixture of 5 mM TFA in MQ-water (A) and acetonitrile (B); flow: 1.00 mL/min; injection volume: 10.00 µL; sample: 1 mg/mL H_2O; column: Phenomenex Luna C18(2) 100 Å, 5 µm, 150 × 4.60 mm; column ID: H21-212012.

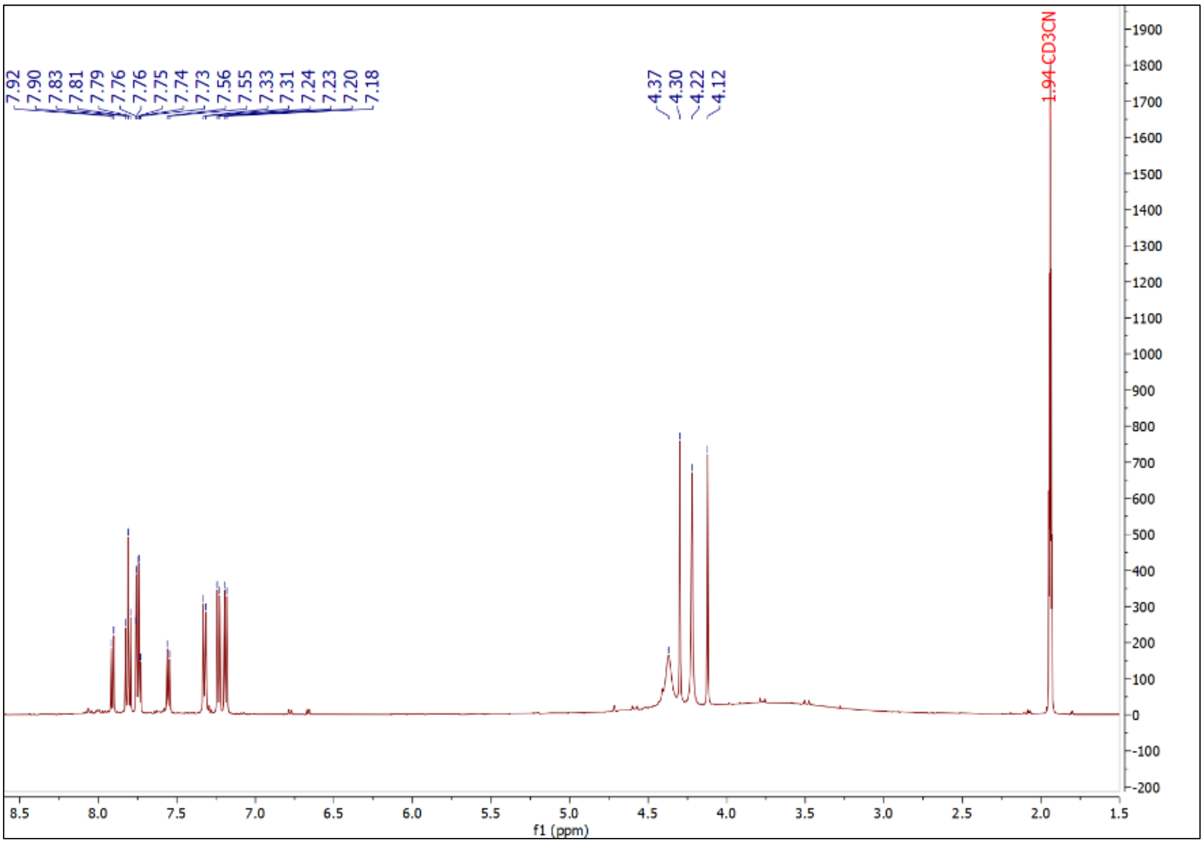

Figure 51. *^{1}H NMR (500.13 MHz, 298.0 K, CD_3CN-d3) spectra of* ***BPPA-Bn^{pCOOH}***.

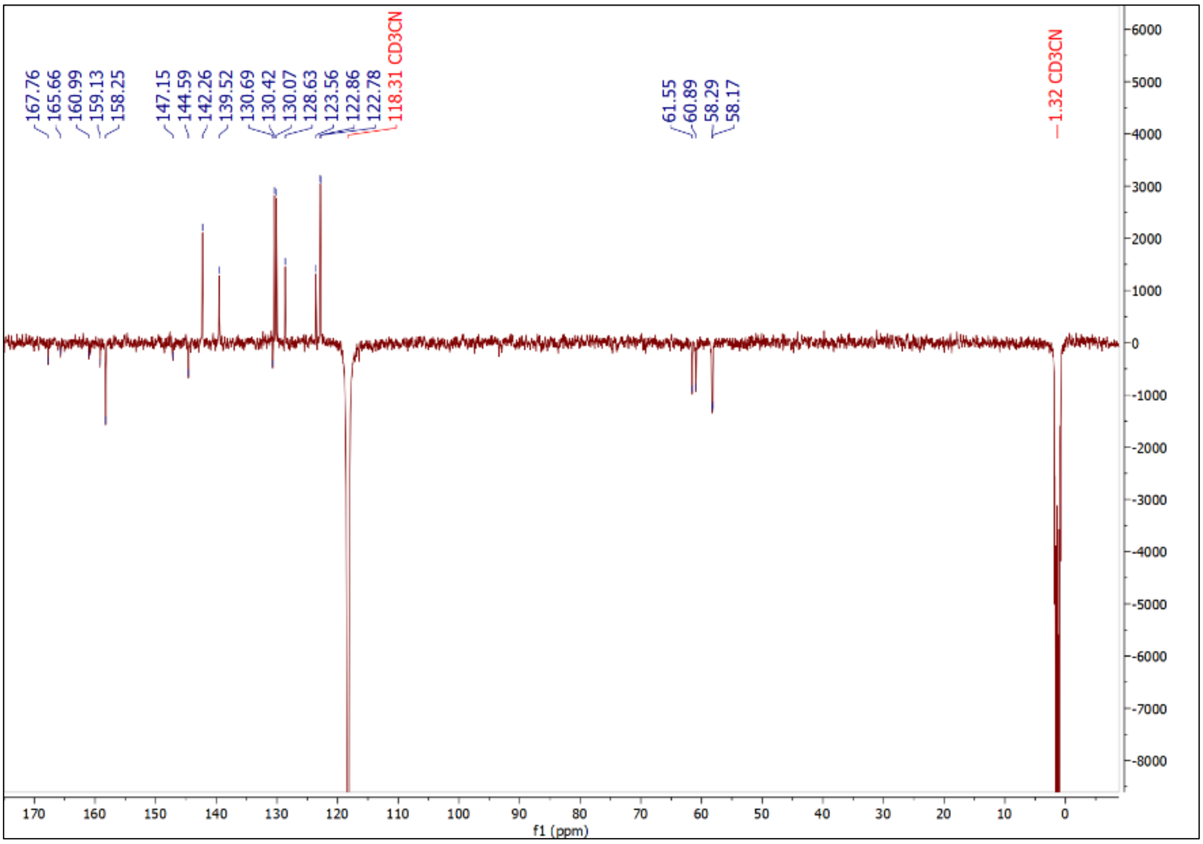

Figure 52. *^{13}C-JMOD NMR (125.77 MHz, 298.0 K, CD_3CN-d3) spectra of* ***BPPA-Bn^{pCOOH}***.

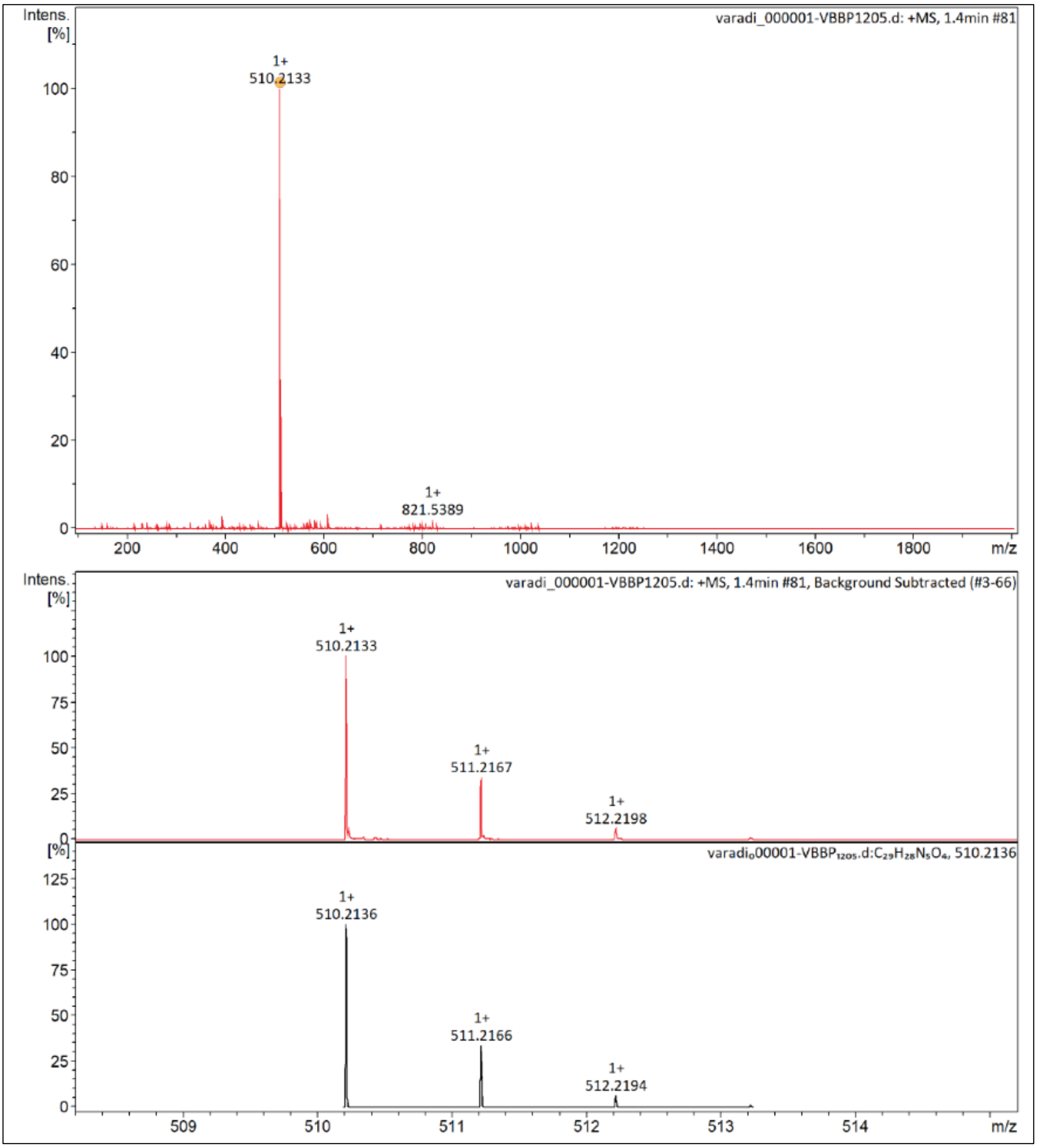

Figure 53. *UHRMS spectra (ESI+) of the* **BPPA-Bn**^{pCOOH}.

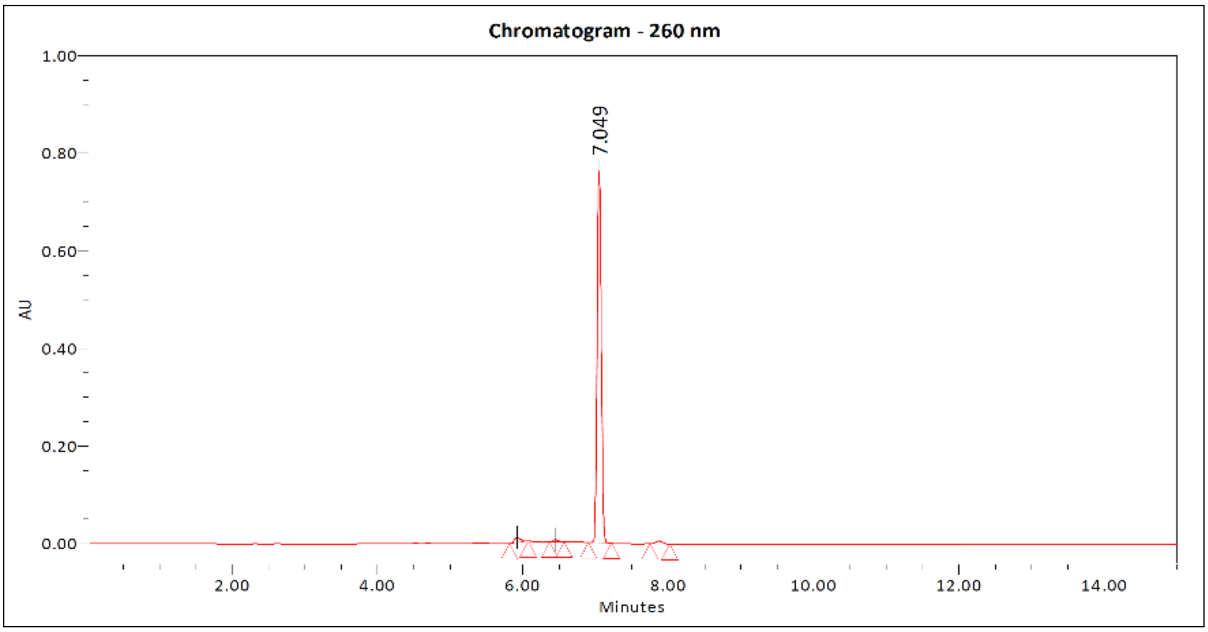

Figure 54. *Analytical HPLC chromatogram (260 nm) of the* ***BPPA-Bn^{pCOOH}***.

***Tert*-butyl 6-((7-(4-((2-(2,5-dioxo-2,5-dihydro-1*H*-pyrrol-1-yl)ethyl)carbamoyl)benzyl)-3,7-diaza-1,5(2,6)-dipyridinacyclooctaphane-3-yl)methyl)picolinate (7)**

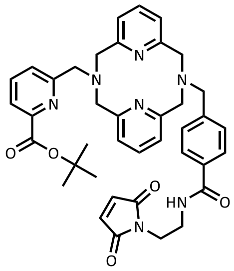

10.6 mg (0.0782 mmol) 1-hydroxybenzotriazole (HOBt), 22.1 mg (0.0583 mmol), 2-(1*H*-benzotriazole-1-yl)-1,1,3,3-tetramethyluronium hexafluorophosphate (HBTU) and 37.0 µL (0.212 mmol) diisopropylethylamine were added to the solution of 4-((7-((6-(*tert*-butoxycarbonyl)pyridin-2-yl)methyl)-3,7-diaza-1,5(2,6)-dipyridinacyclooctaphane-3-yl)methyl)benzoic acid (6) prepared by dissolving 30.0 mg (0.0530 mmol) in 20 mL of dichloromethane. The reaction mixture was stirred at room temperature for 30 min, and 10.1 mg (0.141 mmol) 1-(2-aminoethyl)-1*H*-pyrrole-2,5-dione hydrochloride was added to the reaction mixture under argon protected atmosphere. The reaction mixture was stirred for an additional 20 hours at room temperature and the solvent was removed in vacuum to afford the crude product, which was purified by preparative HPLC. Fractions containing the pure product were combined, lyophilized receive the product **7** as a white solid (20.5 mg, yield 57%).

Preparative HPLC: UV-Vis detection: 210 and 260 nm; retention time: 9.68 min; gradient: 0.00→15.00 min 20→60% B; eluent: mixture of 5 mM TFA in MQ-water (A) and acetonitrile (B); flow: 25.00 mL/min; column: Phenomenex Luna Prep C18(2) 100 Å, 5 µm, 250 × 21.20 mm; column ID: H18-268346

^{1}H NMR (360.13 MHz, MeOD-*d4*) δ; 7.87 (d, J = 7.8 Hz, 1H), 7.86 (t, J = 7.8 Hz, 2H), 7.77 (t, J = 7.8 Hz, 1H), 7.59 (d, J = 7.8 Hz, 1H), 7.50 (d, J = 8.0 Hz, 2H), 7.36 (d, J = 8.0 Hz, 2H), 7.32 (d, J = 7.8 Hz, 2H), 7.25 (d, J = 7.8 Hz, 2H), 6.78 (s, 2H), 4.46 (bs, 4H), 4.37 (s, 2H), 4.32 (s, 4H), 4.20 (s, 2H), 3.70 (m, 2H), 3.51 (m, 2H), 1.61 (s, 9H) ppm; **^{13}C-JMOD NMR** (90.56 MHz, MeOD-*d4*) δ; 172.54, 169.93, 165.32, 159.84, 158.37, 149.73, 143.06, 142.52, 139.25, 135.43, 134.87, 130.44, 128.29, 128.01, 124.84, 123.08, 83.68, 61.76, 61.37, 58.79, 58.70, 39.52, 38.43, 28.31 ppm; **UHRMS** (ESI+) *m/z* calculated for $C_{39}H_{41}N_7O_5$ $[M+H]^+$ 688.3242; found 688.3242; **HPLC** purity (260 nm): 99.37%; retention time: 10.181 min; gradient: 0.00→15.00 min 20→60% B; eluent: mixture of 5 mM TFA in MQ-water (A) and acetonitrile (B); flow: 1.00 mL/min; injection volume: 10.00 µL; sample: 0.2 mg/mL ACN; column: Phenomenex Luna C18(2) 100 Å, 5 µm, 150 × 4.60 mm; column ID: H21-212012.

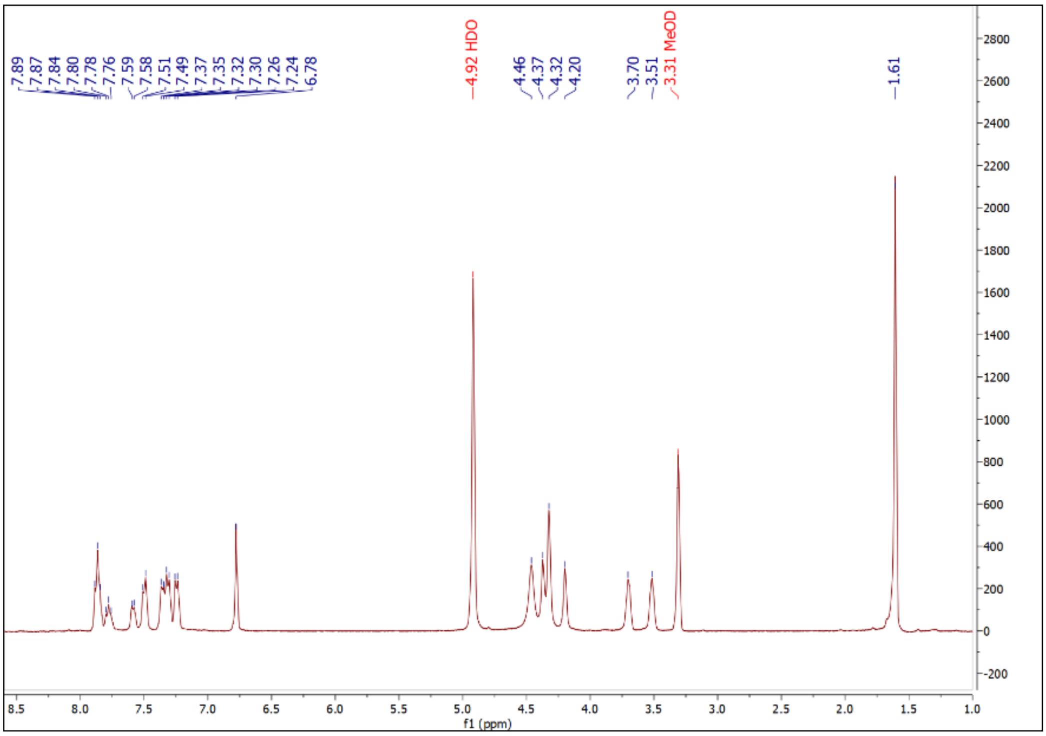

Figure 55. *^{1}H NMR (360.13 MHz, 298.0 K, MeOD-d4) spectra of compound* ***7****.*

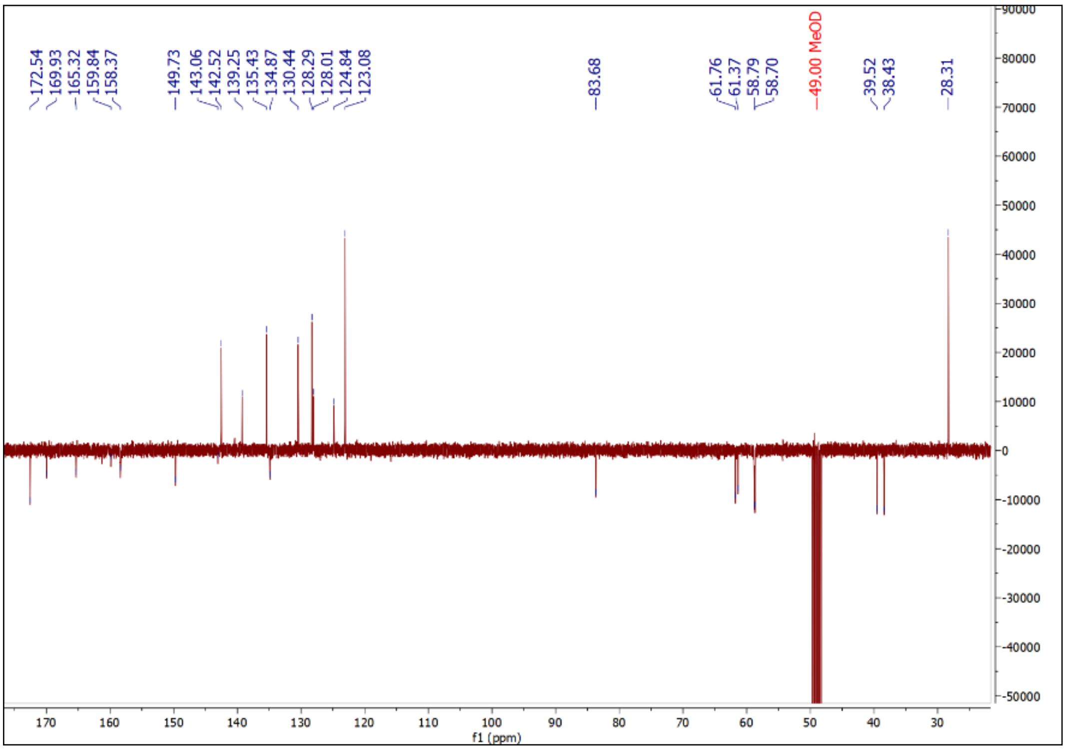

Figure 56. *^{13}C-JMOD NMR (90.56 MHz, 298.0 K, MeOD-d4) spectra of compound **7**.*

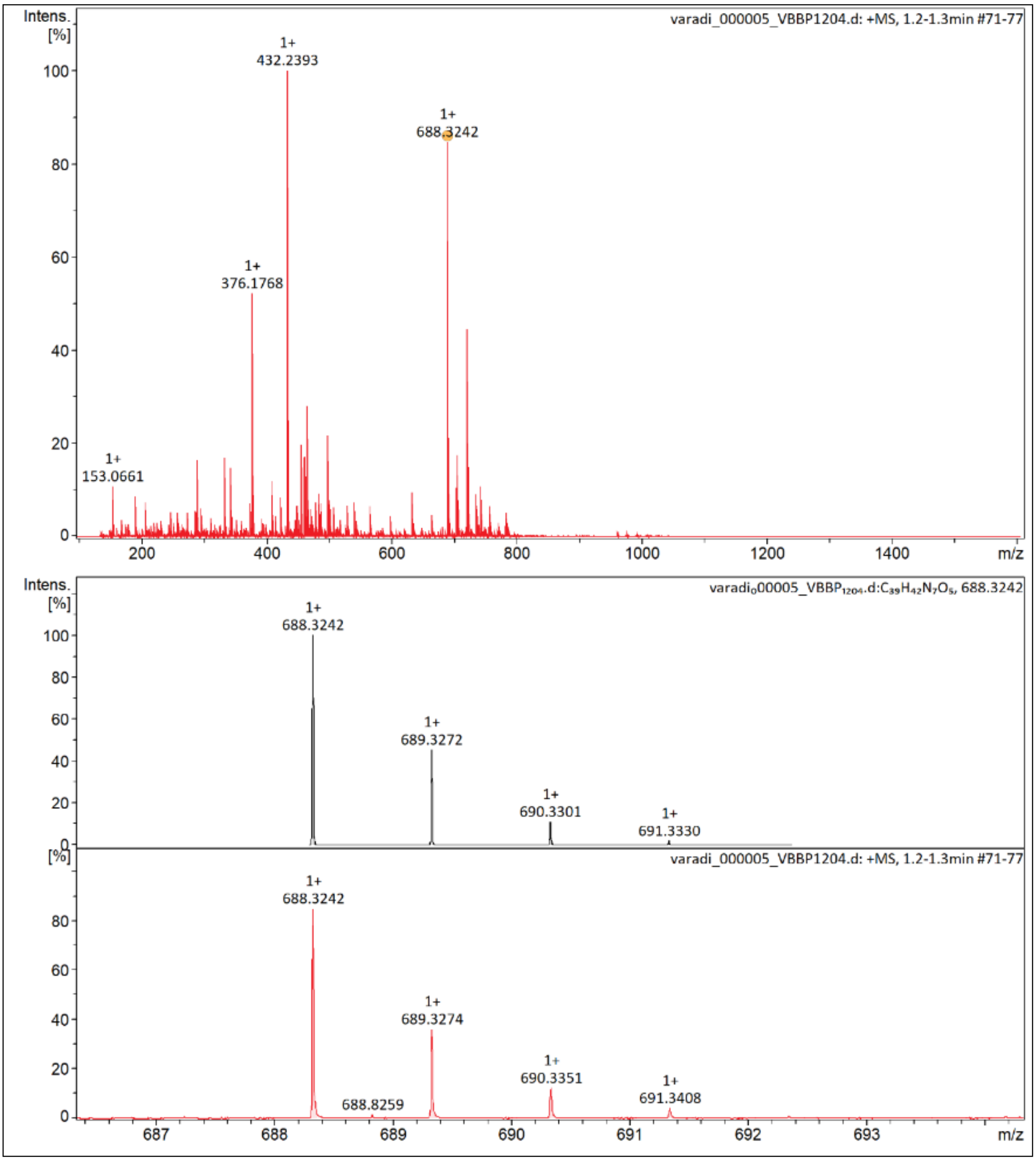

Figure 57. *UHRMS spectra (ESI+) of compound **7**.*

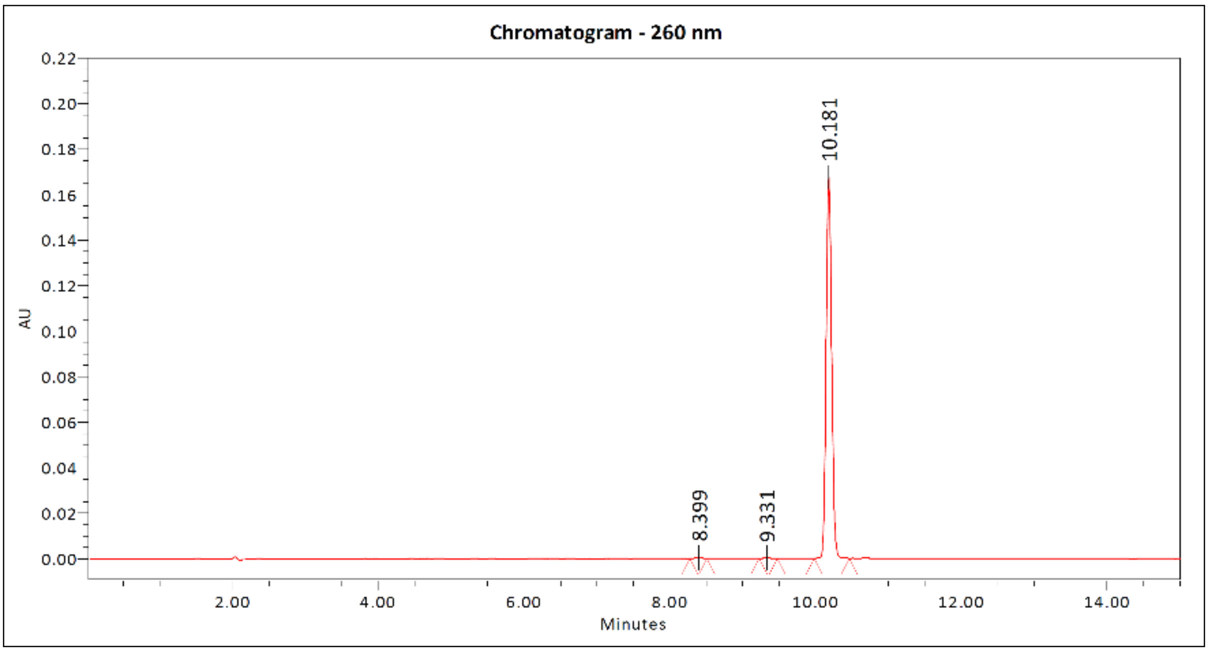

Figure 58. *Analytical HPLC chromatogram (260 nm) of compound **7**.*

6-((7-(4-((2-(2,5-dioxo-2,5-dihydro-1*H*-pyrrol-1-yl)ethyl)carbamoyl)benzyl)-3,7-diaza-1,5(2,6)-dipyridinacyclooctaphane-3-yl)methyl)picolinic acid (BPPA-Bn$^{p\mathrm{MMA}}$)

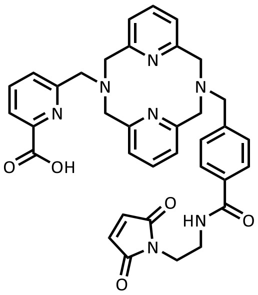

Tert-butyl 6-((7-(4-((2-(2,5-dioxo-2,5-dihydro-1*H*-pyrrol-1-yl)ethyl)carbamoyl)benzyl)-3,7-diaza-1,5(2,6)-dipyridinacyclooctaphane-3-yl)methyl)picolinate (7) (17.6 mg, 0.0256 mmol) was dissolved in 1.5 mL of dichloromethane and 700 µL trifluoroacetic acid was added dropwise to the given solution at room temperature. The reaction mixture was stirred at room temperature for 7 hours and concentrated under vacuum to afford the crude product, which was purified by preparative HPLC. Fractions containing the pure product were combined, freezed, lyophilized to furnish the **BPPA-Bn$^{p\mathrm{MMA}}$** ligand as a white solid (8.6 mg, yield 53%).

Preparative HPLC: UV-Vis detection: 210 and 260 nm; retention time: 6.67 min; gradient: 0.00→10.00 min 5→65% B; eluent: mixture of 5 mM TFA in MQ-water (A) and acetonitrile (B); flow: 25.00 mL/min; column: Phenomenex Luna Prep C18(2) 100 Å, 5 µm, 250 × 21.20 mm; column ID: H18-268346

^{1}**H NMR** (360.13 MHz, MeOD-*d4*) δ; 8.01 (d, J = 7.8 Hz, 1H), 7.86 (t, J = 7.8 Hz, 1H), 7.81 (t, J = 7.8 Hz, 2H), 7.66 (d, J = 7.8 Hz, 1H), 7.57 (d, J = 8.0 Hz, 2H), 7.45 (d, J = 8.0 Hz, 2H), 7.27 (d, J = 7.8 Hz, 2H), 7.21 (d, J = 7.8 Hz, 2H), 4.53 (bs, 8H), 4.39 (s, 2H), 4.34 (s, 2H), 3.71 (m, 2H), 3.53 (m, 2H) ppm; ^{13}**C-JMOD NMR** (90.56 MHz, MeOD-*d4*) δ; 172.57, 169.91, 167.48, 158.71, 157.44, 148.81, 144.10, 142.25, 139.71, 135.44, 135.24, 130.72, 128.51, 128.44, 125.32, 123.31, 61.95, 61.56, 59.22, 58.95, 39.56, 38.43 ppm; **UHRMS** (ESI+) *m/z* calculated for $C_{35}H_{33}N_{7}O_{5}$ $[M+H]^{+}$ 632.2616; found 632.2616; **HPLC** purity (260 nm): 95.21%; retention time: 6.991 min; gradient: 0.00→15.00 min 5→95% B; eluent: mixture of 5 mM TFA in MQ-water (A) and acetonitrile (B); flow: 1.00 mL/min; injection volume: 10.00 µL; sample: 1 mg/mL ACN; column: Phenomenex Luna C18(2) 100 Å, 5 µm, 150 × 4.60 mm; column ID: H21-212012.

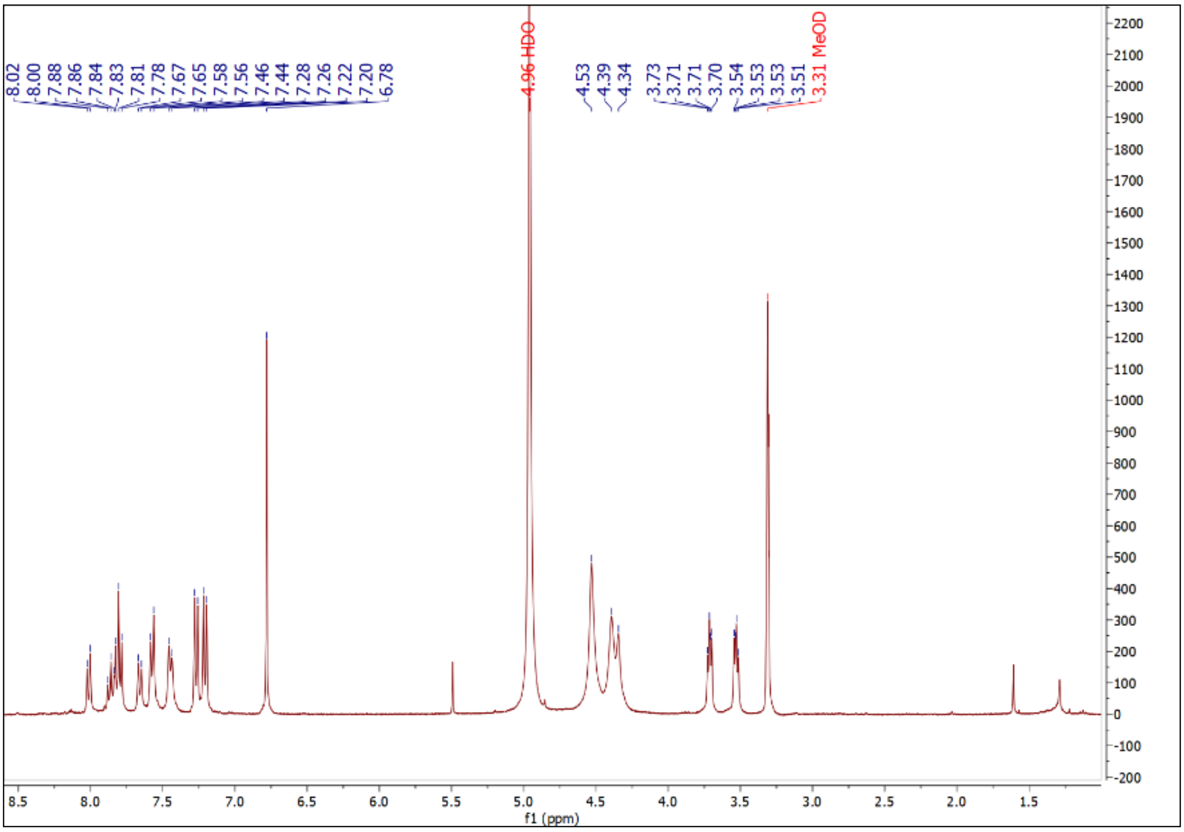

Figure 59. *^{1}H NMR (360.13 MHz, 298.0 K, MeOD-d4) spectra of* ***BPPA-Bn^{pMMA}***.

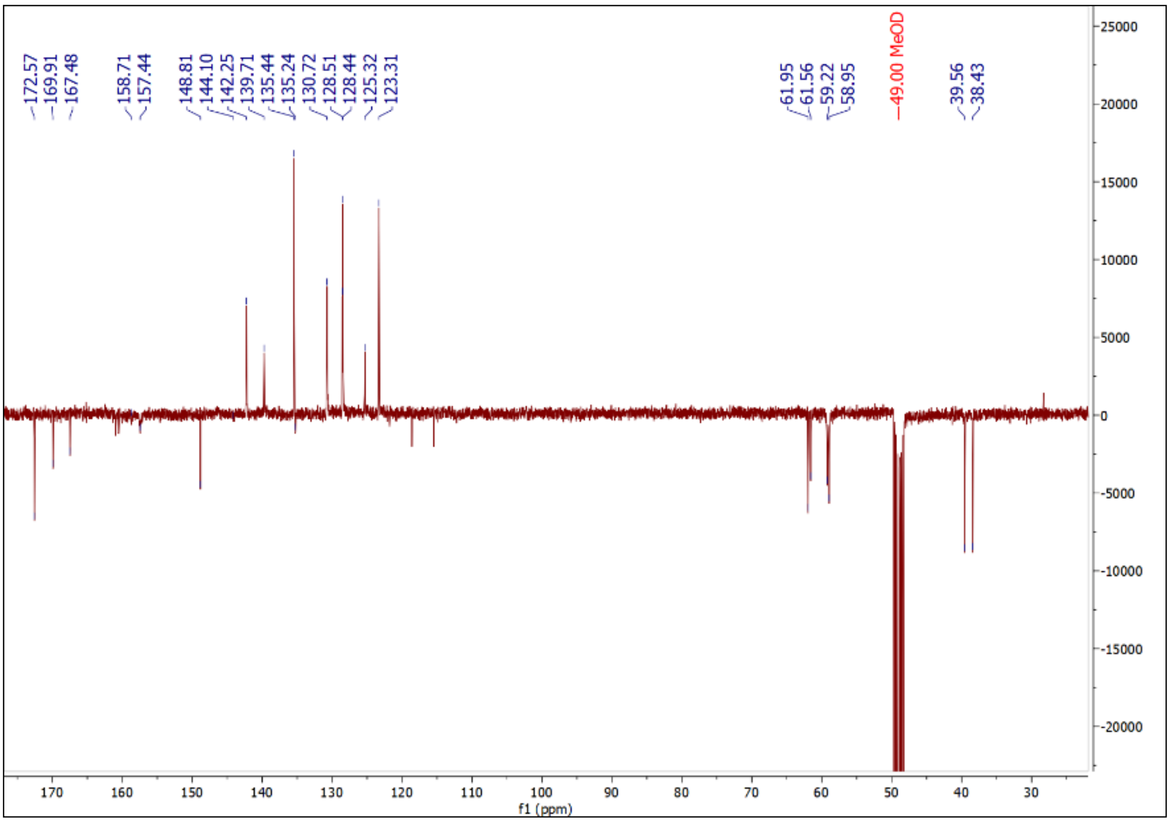

Figure 60. *^{13}C-JMOD NMR (90.56 MHz, 298.0 K, MeOD-d4) spectra of* ***BPPA-Bn^{pMMA}***.

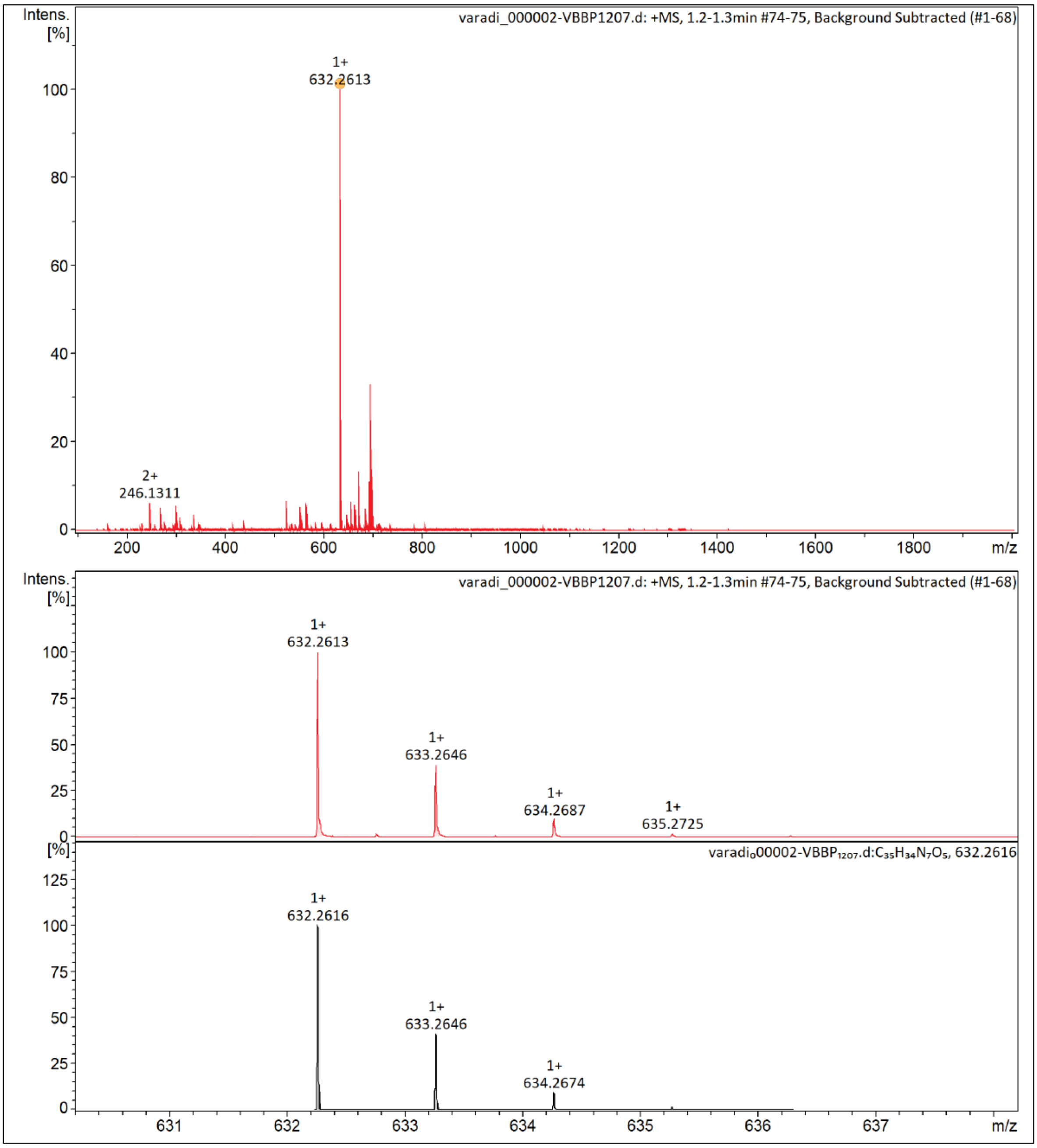

Figure 61. *UHRMS spectra (ESI+) of the compound* ***BPPA-Bn***^{pMMA}.

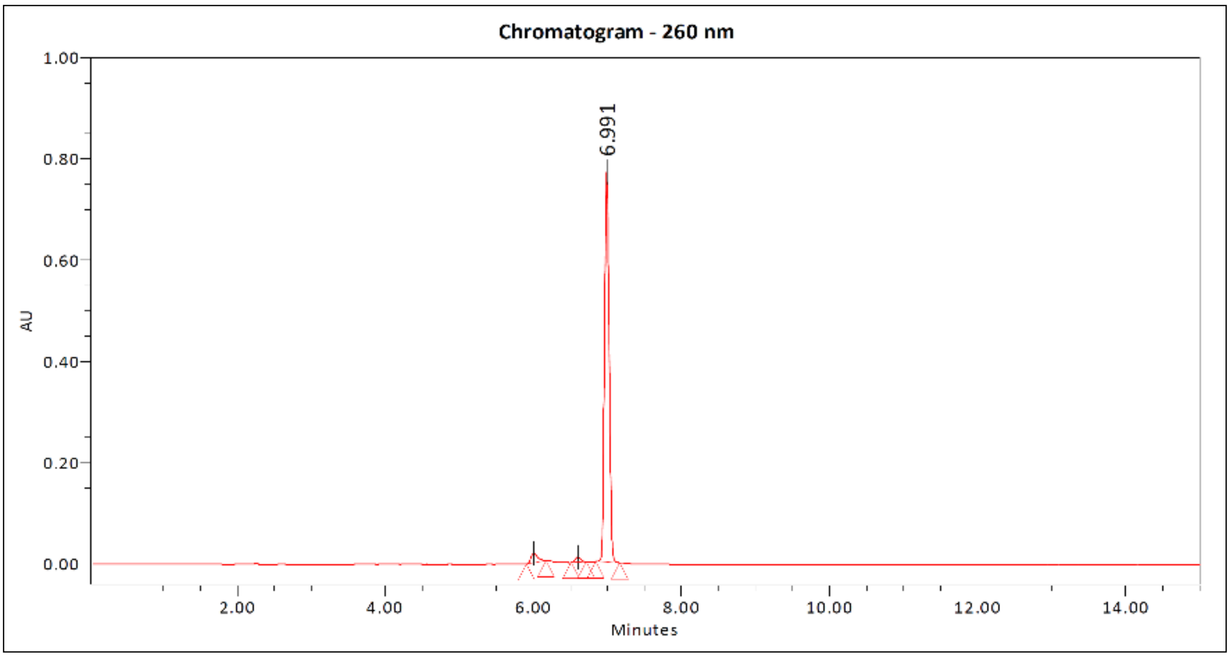

Figure 62. *Analytical HPLC chromatogram (260 nm) of the compound* ***BPPA-Bn***^{pMMA}.

VI. Discussions

Tumour imaging research continues to advance our understanding of breast cancer biology, particularly regarding the interplay between angiogenesis and glucose metabolism, the biodistribution and specificity of antibody-based radiotracers, and the development of novel chelators to enhance HER2-targeted imaging. However, despite substantial progress, the correlation between glucose metabolism and angiogenesis imaging in breast cancer subtypes still requires further investigation. Moreover, only a few HER2-targeted PET tracers have progressed to routine clinical application, highlighting the need for continued research to bridge these gaps. The following sections present findings from three interrelated experimental studies focused on tumour PET imaging and HER2-targeted PET tracers, contributing to our overall research aims.

1. Temporal Assessment of Metabolic Activity and αvβ3 Expression in Aggressive Breast Cancer Models

In our first study, the results show a noticeable positive correlation between glucose metabolism and angiogenesis imaging, indicating their possible significant interplay in tumour characterization. Moreover, both FDG and RGD correlate with tumour growth, particularly in the 4T1 tumour. Furthermore, there were variations in FDG over RGD ratios between the two groups, highlighting the different behaviours among breast cancer subtypes.

Angiogenesis relies on several biochemical processes, which include the expression of pro-angiogenetic factors, VEGF, bFGF, TGF, TNF, and other cytokines and growth factors, especially under hypoxic conditions mediated *via* the transcription factor HIF-1α. In addition, inhibiting negative regulatory processes, such as tissue inhibitor metalloprotease, angiotensin, and angiostatin, is also required for effective angiogenesis [144]. Therefore, considering the substantial energy demands of intercellular crosstalk within the cancer microenvironment, there may be a direct correlation between angiogenesis and glucose utilization.

Studies have indeed demonstrated a positive correlation of FDG uptake with different histologic angiogenesis markers, such as CD31 and CD105, in lung and breast cancers [145-147], prompting ongoing investigations into the relationship between FDG and RGD tracers. Wei *et al.* conducted a study on mice bearing lung cancer xenografts and found a very strong correlation between these two tracers with $r = 0.917$ [148]. Additionally, several clinical studies have reported a positive correlation across various tumour types, particularly in tumours with high FDG avidity (rectal, breast, non-small cell lung cancer, and head and neck cancer) [55, 149-

156]. The correlation between the two radiopharmaceuticals may become more evident when their values are corrected using a muscle reference [151, 156]. This adjustment is necessary due to the substantially lower uptake of RGD compared to FDG in general [151, 156-158] and the distinct differences in the biodistribution of these two radiopharmaceuticals [159].

In our study, relatively positive linear correlations were observed between RGD and FDG tumour/muscle ratios regardless of the growth rate of the tumour, indicating a potentially significant relationship between angiogenesis and glucose metabolism. It is assumed that several factors may contribute to these observations. Firstly, tumour endothelial cells were found to up-regulate glucose transporters GLUT1 and GLUT3 in response to high glucose transportation [160] leading to increased FDG uptake in regions of enhanced angiogenesis. Additionally, cancer cells exhibit an elevated FDG uptake due to the Warburg effect, particularly within hypoxic regions [161]. These hypoxic areas are closely associated with regions undergoing angiogenesis, further contributing to the strong correlation between FDG uptake and angiogenic regions [162]. Moreover, cancer-associated fibroblasts have a significant impact on tumour FDG uptake [163], and have an essential role in angiogenesis processes, particularly in cancers with substantial stromal components, such as breast cancers [164]. Furthermore, angiogenesis in cancer is characterized by abnormal vessel formation involving immature endothelial cells which tend to be leaky, and lack proper basement membrane and supporting pericytes [165]. This neo-vasculature is associated with increased permeability and perfusion within the tumour [166], further enhancing FDG uptake [167].

Utilizing the observed correlation between tumour sizes and tumour/muscle SUV ratios of the two tracers, coupled with the ability to assess tumour heterogeneity, provides a valuable means of precisely determining the target tumour volume for therapy. In our study, comparable correlations of the FDG and RGD with tumour size were observed, especially in the aggressive tumours. The correlations were not clearly seen in slow-growing tumours, likely due to the different behaviours between subtypes of the same cancer, as reported in a study on non-small cell lung cancer, where both adenocarcinoma and squamous cell carcinoma demonstrated positive correlations between FDG uptake and tumour size; however, the correlation coefficient and correlation pattern varied between the two subtypes [168]. Nevertheless, comparing the correlation of two tracers with tumour size, a previous larger study reported a superior correlation of RGD with the pathologic volume of the tumour [169], possibly because tumour growth heavily relies on angiogenesis more linearly, while glucose metabolism is more complex, encompassing elements like inflammation and stromal activity. RGD imaging can assist oncology surgeons to determine the possible resection margins or even delineate the gross tumour volume for radiotherapy by precise detection of the tumour extension. Therefore, it can serve as a specific predictive tool, minimizing false positives associated with inflammation, for evaluating tumour progression and monitoring responses to treatment, particularly in anti-angiogenic therapy [170, 171] used in metastatic colorectal cancer, non-small-cell lung cancer, glioblastoma, ovarian and cervical cancers [172].

Despite differences in growth rates, the breast cancer subtypes used in our study represent the most aggressive types reliant on angiogenesis, resulting in the highest expression of $\alpha v\beta 3$ among all breast cancer subtypes [173, 174]. While both cell lines exhibited correlations in tumour/muscle ratios between FDG and RGD, glucose metabolism was noticeably higher than angiogenesis in the 4T1 triple-negative cell line. This observation can be attributed to the aggressive nature of 4T1, given that the triple-negative breast cancer subtype is known to have the worst prognosis and the lowest survival rate of all breast cancer subtypes regardless of cancer stage [30, 175]. Consequently, this aggressive subtype, displaying a faster growth rate, has a higher FDG-to-RGD ratio when compared to other subtypes [55]. Furthermore, larger tumours are associated with denser microvascularity, which facilitates the penetration and uptake of FDG, thus increasing overall FDG tumour uptake [167]. Our histopathological examination revealed that 4T1 had an abundant tumour stroma, which has been reported in the literature [176]. The stroma-rich cancer environment has a significant impact on increased FDG uptake within the tumour, especially in cancers with high FDG that have a greater distribution of stroma [163]. In contrast, the HER2-positive subtype is known to have the highest rate of parenchymal organ metastases among all breast cancer subtypes [25], although recent advances in HER2-targeted therapies have improved the survival rates of this particular subtype. As a result, HER2-enriched tumours displayed an elevated RGD uptake, whereas triple-negative breast cancer exhibited lower RGD uptake relative to its high FDG uptake [55, 56]. Moreover, a study has associated HER2 positivity with an increased expression of HIF-1α [177], which may further promote neo-angiogenesis [162]. These explain the minimal differences observed between the HER2-positive xenograft and the aggressive triple-negative 4T1 xenograft when using RGD imaging and $\alpha v\beta 3$ integrin staining.

Tumours characterized by a higher FDG uptake [152] or higher FDG tumour-to-muscle ratio, like the triple-negative breast cancer subtype we used in our experiments, exhibited a more robust correlation between neo-angiogenesis and FDG-avidity in comparison to other tumours [55, 178]. Our study observed relatively more linear relationships in the group with higher

FDG tumour-to-muscle ratios; however, due to the small sample size no statistical analysis was performed to investigate the differences further, thus the results should be considered preliminary. Nevertheless, this observation emphasizes the significance of neo-angiogenesis in tumour growth, particularly in aggressive tumours, where rapid growth demands high levels of oxygen and nutrients.

Peptide-derived tracers like RGD are predominantly excreted *via* the kidneys, leading to high activity accumulation in the urinary bladder [179]. This can cause a partial volume effect, resulting in false increased activity measured in the surrounding organs. Invasive bladder continuous flushing [180] and non-invasive hydration plus furosemide [181] protocols have been proposed to minimize this artifact. Reconstructing with spatial resolution improvements, such as using the OSEM iterative reconstruction method [180], increasing the number of iterations, and reducing voxel size [182], have been attempted to reduce this unwanted effect. In this study, we further enhanced quantitative accuracy without *in vivo* intervention by implementing the Muscle-Spacing Correction Method. Taking advantage of the consistently minimal muscular uptake, along with the homogenous and relatively oval shape of the fully filled urinary bladder, the method uses a muscle VOI as the reference for background correction. In order to ensure equal distances from the reference VOI to the bladder centre and from the target VOI to the bladder centre, an additional VOI is drawn. Its centre aligns with the centre of the bladder and intersects with the centres of the target and reference VOIs. Utilizing this method, we can correct the partial volume effect not only when the target is near the bladder but also potentially in brain imaging, where a similar phenomenon frequently occurs.

One notable limitation of this study is the relatively small sample size, especially in the 4T1 group (n = 2), which may limit the statistical power and the generalizability of the findings. Additionally, the measuring method employed in the study has not been thoroughly validated, and therefore further investigation is needed to verify the reliability and reproducibility of the technique. Moreover, it is important to acknowledge that breast cancers are substantially complex and heterogeneous with various subtypes exhibiting distinct molecular profiles and clinical behaviours. Further research with larger sample sizes and various breast cancer subtypes is necessary to confirm the complex relationship between glucose metabolism, vascular formation, and tumour progression in this heterogeneous cancer type.

2. HER2 Expression in Different Cell Lines and Inoculation Sites Assessed by [^{52}Mn]Mn-DOTAGA(anhydride)-trastuzumab

Building upon the tumour biology insights from our FDG/RGD study, our second investigation explored HER2-targeted imaging using [^{52}Mn]Mn-DOTAGA(anhydride)-trastuzumab. The study demonstrates high tumour/non-tumour ratios, the relative stability of [^{52}Mn]Mn-DOTAGA(anhydride)-trastuzumab, and highlights the influence of inoculation sites, tumour characteristics, and the microenvironment on tumour tracer uptake. Despite its ease of production, the tracer exhibits noticeable non-specific binding and requires further improvement in immunoreactivity.

After intravenous injection, the tracer shows an initial high blood uptake due to FcRn-mediated antibody recycling, with moderate liver and spleen uptake driven by FcR-mediated uptake [183] facilitated by permeable sinusoidal capillaries [184, 185]. Lung uptake is attributed to the high vascularity [186] and low reflection coefficient of pulmonary tissue, allowing for enhanced tracer uptake [187]. Remarkably, renal activity exceeded typical liver activity for antibody-based tracers, due to the additional carboxylic arm of the tracer (compared to the conventional DOTA chelator), which increases the hydrophilicity of the tracer and consequently elevates the renal excretion [188].

Interestingly, moderate activity was also seen in the ovaries and the lacrimal glands. The physiological expression of HER2 in the ovaries is well-documented [189]. However, since trastuzumab does not cross-react with murine HER2 [190], the ovarian activity may be attributed to non-specific uptake. The lacrimal glands produce protective tears containing immunoglobulins [191], especially under the effect of anaesthesia with constant airflow from the breathing mask [192], which causes dry eyes and lens opacity [193], that also observed in our scans, resulting in the noticeable tracer uptake in the eyes and lacrimal glands, particularly in SCID mice that lack endogenous immunoglobulins. These findings underscore the advantages of PET imaging in providing a comprehensive whole-body assessment, enabling the detection of unexpected tracer accumulation.

Initial urinary activity in the bladder suggests the rapid excretion of a small portion of unconjugated tracer, as observed in our previous study using unconjugated [^{52}Mn]Mn-DOTAGA [194] and in our unconjugated study; nonetheless, low urinary bladder activity in subsequent scans indicates stable conjugation *in vivo*. The kidney, pancreas, salivary glands, and joints are frequently identified as the localised sites of free manganese, as demonstrated in our study with [^{52}Mn]MnCl$_2$ (Figure 23C), and in other related research [195, 196]. In this [^{52}Mn]Mn-DOTAGA(anhydride)-trastuzumab study, in addition to the stable conjugation, the complexation of the tracer seems to be stable *in vivo,* as suggested by the minimal uptake in the pancreas, salivary glands, and joints without renal reabsorption. Using a similar compound, [^{52}Mn]Mn-DOTAGA(pSCN-Bn)-trastuzumab, we reported a high stability (RCP maintained above 90% up to day 10) of the ^{52}Mn-labelled trastuzumab using the DOTAGA chelator (Figure 21).

Both HER2-positive tumours demonstrated high tumour-background contrast; however, significantly higher uptake was observed in the orthotopic tumours compared to the ectopic tumours possibly due to microenvironment which favours tracer uptake in orthotopic tumours [125, 197]. This phenomenon corresponds to the better microenvironment characterised by higher microvascular density [198] and increased perfusion [197] which facilitate tracer penetration and thereby promoting binding to more specific binding sites.

However, the differences in uptake between MDA-MB-HER2+ and MDA-MB-468 cell lines at the same inoculation site, which diminished over time, are likely due to non-specific binding of the tracer. The larger tumour size in the MDA-MB-468 group (Figure 15), leading to increased non-specific uptake [199], is partly responsible for this finding. However, tumour size alone does not explain for the dynamic and clearance of uptake, as aggressive melanoma xenografts, although large, showed lower activity compared to HER2-positive xenografts. Furthermore, melanoma xenografts exhibited a similar uptake pattern to HER2+ xenografts, in contrast, the MDA-MB-468 group, where uptake increased steadily. This disparity can be due to the fact that both MDA-MB-HER2+ and the B16F10 melanoma xenografts exhibit necrotic features [200], resulting in decreased overall xenograft uptake [201]. Conversely, the stroma-rich features of MDA-MB-468 xenografts facilitate tracer retention, resulting in slower clearance rate and increased activity over time [202]. Furthermore, the HER2+ xenograft can show limited tracer uptake due to the binding site barrier as specific binding accumulates in the peripheral parts reducing uptake in the necrotic/hypoxic core located further from the feeding blood vessels [203] as shown in our *in vivo* images (Figure 11). Whereas, MDA-MB-468 tumours with known HER2 phosphorylation at tyrosine Y877 [204], can render the xenografts sensitive to trastuzumab [204, 205].

Our *in vitro* study demonstrates higher tracer uptake in HER2-positive cells, further blocking studies or direct binding assays are required to confirm specific tracer binding. *In vivo,* while the tracer retains some specificity, that can differentiate the HER2 positivity in initial scans, tumour uptake includes a high proportion of non-specific binding which may be responsible for elevated uptake in HER2-negative tumours at later time points. In a study using the same compound labelled with radioactive indium, [^{111}In]In-DOTAGA(anhydride)-trastuzumab, reported a decrease in the tracer immunoreactivity compared to labelling with the parent DOTA chelator [206]. This reduced immunoreactivity may account for the high non-specific binding observed with our tracer.

Our study has several limitations. First, there were only 2 mice in the MDA-MB-468 group, which required the assumption of a normal distribution for the two-way ANOVA analysis. Second, discrepancies between PET/CT and PET/MRI can arise from variations in attenuation correction maps [207, 208]. In our study, we also observed systemic differences between these two modalities (Table 3, Table 4). To address this limitation, we used the tumour-to-background ratio for assessment, aiming to ensure more accurate and reliable results. Using the ratios, such as SUV_{mean} Organ/Muscle, provided reproducible results, as demonstrated by the comparable biodistribution observed in our two breast cancer-bearing groups scanned with different modalities (Figure 12). Lastly, we lacked in vitro binding assays to further investigate the immunoreactivity or receptor binding characteristics of the tracer.

Based on our findings, we conclude that higher antibody tracer uptake is expected in orthotopic tumours compared to ectopic tumours. However, due to the suboptimal specificity of the tracer, this difference may result from either higher HER2 expression or a more favourable microenvironment at the orthotopic inoculation site, and further investigation is needed to confirm our findings. Several non-specific factors, such as tumour size, necrotic or stromal-rich properties, and the tumour microenvironment, influence imaging outcomes. Despite the need for improved specificity towards HER2, [^{52}Mn]Mn-DOTAGA(anhydride)-trastuzumab demonstrates a favourable tumour-to-background ratio and relatively good tracer stability.

3. Evaluation of [^{52}Mn]Mn-BPPA-trastuzumab for Highly Specific HER2 PET Imaging

Addressing the specificity limitations observed in our [^{52}Mn]Mn-DOTAGA(anhydride)-trastuzumab study, our third experimental study introduced a novel Mn(II)-chelator, BPPA, designed for enhanced HER2-antibody imaging. The literature suggests that Mn(II) ions are best complexed with rigid chelators. One such chelator, 3,9-PC2A, is commonly used as a structural motif in bifunctional ligands and Mn(II) based responsive/smart contrast agents [142].

To enhance the physicochemical properties of the Mn(II) chelates we have used an even more rigid platform based on the bispyclen frame during the ligand design. To simplify the synthesis of a suitable BFC chelator, we employed a picolinate pendant arm for metal binding instead of the conventional acetate pendants, resulting in the BPPA ligand. The BPPA chelators designed forms a Mn(II) complex with outstanding stability (log K_{MnL} = 16.14(1) and pMn = 10.98), that includes a metal-bound water molecule, confirmed by relaxometric studies. The inertness of [Mn(BPPA)] is improved compared to the parent [Mn(3,9-PC2A)] complex due to the chelator's rigid backbone and pendant arm design. The given ligand allowed us to use the second macrocyclic N-atom in the ligand for the attachment of a linker group suitable for bioconjugation purposes. Thus the BFC was obtained by the alkylation of the macrocycle with tert-butyl 4-(bromomethyl)benzoate group (BPPA-pBn$^{\mathrm{COOH}}$). After acidic hydrolysis, it was coupled to a maleimide group-containing fragment supporting the bioconjugation with a suitable vector (trastuzumab in our case). BPPA is an ideal chelator for radiolabelling of antibodies with [^{52}Mn]Mn, as [[^{52}Mn]Mn(BPPA)] is formed with high radiochemical purity under mild conditions (room temperature and pH 7) suitable for sensitive proteins. Moreover, BPPA-trastuzumab proves to be more suitable for [^{52}Mn]Mn than DOTAGA-trastuzumab, despite slightly lower stability which can be explained due to the maleimide group used for conjugation.

According to our *in vivo* investigation of free [^{52}Mn]MnCl$_2$, elevated uptake of kidney, pancreas and salivary glands was observed. Additionally, using 90-minutes dynamic study showed high kidney uptake, while minimal signal was detected in the urine, indicating strong renal reabsorption of [^{52}Mn]MnCl$_2$, possibly via transporter located in the apical membrane of proximal tubule cells, including ZIP14, ZIP8, DMT1 [209]. A similar biodistribution can be found in many studies applying either *in vivo* PET imaging or *ex vivo* measurements [195, 196, 210]. The voltage-dependent calcium channels (VDCCs) facilitate Mn(II) uptake in the pancreas [211]. Mn(II) accumulates intracellularly in the pancreas, binding to pro-carboxypeptidase B, contributing to its slow clearance in this organ [212].

In contrast, using [^{52}Mn]Mn(II)-labelled unconjugated DOTAGA and BPPA have a high level of renal clearance as small, hydrophilic molecules are excreted dominantly via kidney. Once the renal clearance had been saturated (24 h), the two chelators showed different uptake patterns. Particularly, [^{52}Mn]Mn-DOTAGA exhibits significant lung uptake, likely due to first-pass effect of the radiotracer, or along with the relatively lower kidney activity compared to radiolabelled BPPA, indicating protein binding properties of the unconjugated DOTAGA [213].

Thus, *in vivo*, [^{52}Mn]Mn-DOTAGA having a distinct biodistribution pattern with free [^{52}Mn]Mn(II), suggesting minimal release of free [^{52}Mn]Mn(II) from the complex. Conversely, [^{52}Mn]Mn-BPPA, showed a similar uptake pattern with free [^{52}Mn]Mn(II) at later time points, possibly suggesting instability of the [^{52}Mn]Mn-BPPA chelator when not conjugated to an antibody (the literature evidence for 3,9-PC2A, for instance, confirms that the conversion of this basic ligand to a bi-functional chelator positively affects the properties of Mn(II) chelate[142]).

Similar to [^{52}Mn]Mn-DOTAGA(anhydride)-trastuzumab, [^{52}Mn]Mn-DOTAGA(pSCN-Bn)-trastuzumab exhibited biodistribution with high uptake in the blood pool, followed by the kidney and liver. This is expected from DOTAGA a DOTA derivative featuring an additional carboxylic arm that reduces liver uptake [188, 214]. Lung uptake was moderate and comparable with other DOTAGA-trastuzumab studies [206]. High liver uptake and moderate blood and lung uptakes were observed using [^{52}Mn]Mn-BPPA-trastuzumab. However, elevated activity in the pancreas and salivary glands at later time points, along with persistent kidney uptake, suggests a minor release of [^{52}Mn]Mn(II) from the radiotracer. Indeed, these organs have been utilized in other studies involving [^{52}Mn]Mn(II)-labelled radiotracers to assess compound stability [210, 215-217]. The accumulation of released [^{52}Mn]Mn(II) in these organs aligns with our findings, and consistent with other [^{52}Mn]MnCl$_2$ biodistribution studies [195, 196, 210]. To investigate the phenomenon further, our serum stability studies showed that the maleimide linker used to conjugate BPPA was unstable. [^{52}Mn]Mn-BPPA-maleimide can bind to plasma proteins via transconjugation, before releasing [^{52}Mn]Mn(II), and evade the kidney clearance, which explains the minimal urinary bladder uptake, in contrary to the dominant urinary bladder uptake observed when using the [[^{52}Mn]Mn(BPPA)] chelate alone. Therefore, our team is working on improving the linker of the BFC.

Despite of these shortcomings, [^{52}Mn]Mn-BPPA-trastuzumab showed outstanding HER2 status differentiating ability. At all the time points after 72 h, the radiotracer can differentiate HER2+ with HER2− with strong confidence, especially at 168 h. This phenomenon is the result of the improved molar activity of [^{52}Mn]Mn-BPPA-trastuzumab due to the enhanced [^{52}Mn]Mn(II) binding capacity of BPPA chelator. In particular, the HER2+ tumour uptake of the [^{52}Mn]Mn-BPPA-trastuzumab is higher than that of [^{52}Mn]Mn-DOTAGA counterpart at all the time points and many folds higher in later time points. Regarding the TBRs, only the [^{52}Mn]Mn-DOTAGA(pSCN-Bn)-trastuzumab HER2+ breast ratios were higher than HER2 negative ratios, and only at the last scan, whereas the difference in ratios of different HER2 levels using [^{52}Mn]Mn-BPPA-trastuzumab was more obvious from earlier time points. Indeed, both the HER2+ tumour/muscle and tumour/liver of [^{52}Mn]Mn-BPPA-trastuzumab were higher than of [^{52}Mn]Mn-DOTAGA(pSCN-Bn)-trastuzumab in all time points despite of higher hepatic uptake in BPPA groups. Despite of lacking block study, the BPPA tracer demonstrated higher specificity than the DOTAGA conjugate. Specifically, similar to the MDA-MB-468 tumours (in the [^{52}Mn]Mn-DOTAGA(anhydride)-trastuzumab study), the 4T1 xenograft is rich in stroma (Figure 30B) and large in size which promote the non-specific uptake of the antibody-based tracer [218], conversely the MDA-MB-HER2+ showed necrotic feature (Figure 30A) limiting the tracer uptake [219]. Consequently, higher uptake was observed in 4T1 tumour using [^{52}Mn]Mn-DOTAGA(pSCN-Bn)-trastuzumab due to non-specific binding whereas [^{52}Mn]Mn-BPPA-trastuzumab demonstrated prominent HER2+ xenograft uptake with high HER2 specificity overcoming the differences in tumour characteristics. Even though orthotopic tumours are believed to have better microenvironment for tumour growth [125] (as suggested in the DOTAGA(anhydride) study), in this BPPA and DOTAGA(pSCN-Bn) study, the tumour activity and tumour-to-background ratio demonstrated inconsistent results when comparing the orthotopic and ectopic tumours (higher uptake in HER2+ back tumours than in the HER2+ breast tumours in the BPPA group (Figure 27)). This discrepancy may be due to one of the MDA-MB-HER2+ cell injections in the BPPA group being inadvertently administered into the subscapular fat pad instead of subcutaneously, leading to markedly elevated tracer uptake in that tumour. Overall, using BPPA chelator in labelling of trastuzumab provides strong HER2 specificity and excellent TBR and allows for differentiating HER2 expression at an earlier time point.

4. Summary and Future Directions

4.1. Summary

Our FDG/RGD study demonstrated that in the 4T1 TNBC model, both [^{18}F]FDG and [^{68}Ga]Ga-NODAGA-c(RGDfK)$_2$ imaging revealed highly heterogeneous tumour structures, with tracer uptake showing linear correlations with tumour growth. 4T1 tumours exhibited higher FDG/RGD ratios compared to MDA-MB-HER2+, reflecting distinct metabolic–angiogenic profiles in aggressive tumours.

Our HER2-targeted imaging study using [^{52}Mn]Mn-DOTAGA(anhydride)-trastuzumab achieved consistently higher TBRs in orthotopic HER2-positive tumours than in ectopic HER2-positive, HER2-negative, and melanoma models across all imaging time points.

Our chelator development study with the novel BPPA ligand significantly outperformed DOTAGA, with [^{52}Mn]Mn-BPPA-trastuzumab demonstrating superior TBRs and 3–4 fold higher HER2+ versus HER2− contrast by day 7. This extended imaging window allows earlier and more specific differentiation of HER2-positive tumours.

In conclusion, integrating metabolic, angiogenic, and receptor-targeted imaging provides a robust approach to assessing breast cancer heterogeneity, enabling more precise characterization and treatment optimization. The combination of [^{18}F]FDG, [^{68}Ga]Ga-NODAGA-c(RGDfK)$_2$, and [^{52}Mn]Mn-based trastuzumab, particularly with the BPPA chelator, shows promise in improving imaging accuracy. [^{18}F]FDG and [^{68}Ga]Ga-NODAGA-c(RGDfK)$_2$ tracers effectively assess tumour heterogeneity, with notable correlations observed between the tracers and tumour growth, particularly in fast-growing TNBC models. This highlights their potential for monitoring aggressive tumour subtypes.

[^{52}Mn]Mn-trastuzumab imaging demonstrates excellent tumour contrast and tracer stability with [^{52}Mn]Mn-DOTAGA-trastuzumab, though improvements in specificity are required. Factors such as inoculation site, tumour characteristics, and microenvironment significantly influence tracer uptake. Meanwhile, [^{52}Mn]Mn-BPPA-trastuzumab shows superior HER2 specificity and tumour contrast, enabling earlier differentiation of HER2-positive tumours. Despite these advancements, the stability of [^{52}Mn]Mn-BPPA-trastuzumab requires further optimization to enhance its clinical utility. Together, these findings demonstrate the potential of integrating advanced radiotracers to improve breast cancer imaging and therapeutic planning.

Despite the limitations of current studies, including the small sample sizes and the absence of dedicated measurements for in vitro immunoreactivity and receptor-binding properties, the research provides crucial insights into breast cancer heterogeneity. These findings hold significant value for the continued development of breast cancer molecular imaging, advancing more precise and effective personalized breast cancer therapies.

4.2. Future Directions

Improvements in HER2-antibody tracer stability and specificity represent an essential area for future research, helping future studies investigate novel tracers. These include dosimetry studies which will be crucial for ensuring imaging safety and laying the framework for future antibody-based radioimmunotherapy. Furthermore, studies on tracers' potential in stratifying varying levels of HER2 expression, including HER2-low subtypes, are essential.

Moreover, exploring their ability to monitor therapeutic responses and predict outcomes for patients undergoing HER2-targeted therapies would further enhance clinical applications.

Antibody-based tracers are highly specific and valuable tools for evaluating antibody biodistribution and supporting radioimmunotherapy dosimetry. However, their extended circulation time and limited tissue penetration present challenges. Alternatively, small molecules targeting HER2 (such as affibodies), with faster clearance rates, improved tissue penetration, and high binding affinity, offer a promising alternative despite drawbacks like high renal uptake.

Therefore, the isotope selection is critical for labelling bioactive molecules. While antibodies benefit from long half-life isotopes like ^{89}Zr, and, especially ^{52}Mn (offers the advantage of manganese(II)'s paramagnetic properties, making it ideal for MRI studies and the hybrid imaging); small molecules require shorter half-life isotopes such as ^{18}F and ^{68}Ga. Ideal isotopes should feature low positron maximum energy and high emission frequency to optimize imaging resolution while maintaining low-energy gamma emissions to ensure radiation safety. Furthermore, the development of advanced chelators and prosthetic groups is essential to improve labelling efficiency and tracer stability without compromising bioactivity.

The transition from preclinical rodent models to human clinical applications presents notable challenges that must be addressed. There are fundamental differences between in vivo antibody studies in rodents, particularly SCID mice, and humans. These differences include faster antibody clearance rates in preclinical mice, which often necessitate increasing antibody doses to match adequate dosing levels observed in clinical studies [220-225]. This accelerated clearance is partially due to the lack of endogenous immunoglobulin G (IgG) in SCID mice, leading to faster non-specific clearance of antibodies [221, 223, 224]. Another factor is the reduced neonatal Fc receptor (FcRn)-mediated recycling of antibodies due to diminished FcRn expression in SCID mice caused by the absence of T and B cells [221]. Furthermore, there are differences in the binding affinity of humanized antibodies, such as trastuzumab, to mouse versus human FcRn receptors. Trastuzumab binds more strongly to mouse FcRn, complicating the recycling pathway and antibody pharmacokinetics [226]. Tumour-bearing mice frequently experience hypoalbuminemia, which can further impact antibody pharmacokinetics [227]. Albumin competes with antibodies for FcRn binding, thereby increasing the clearance rate of antibodies via the FcRn pathway [226, 228]. Additionally, human FcRn has a stronger affinity for both human and mouse serum albumin, particularly at the acidic pH found in lysosomes, further influencing clearance dynamics [226].

Even in human-FcRn transgenic mice, which can project human pharmacokinetics of monoclonal antibodies effectively [225], rapid antibody clearance compared to humans and primates remains an issue [220]. Interaction with Fc gamma receptors (FcγR) on myeloid cells in immunodeficient models, such as SCID and NSG mice, also affects antibody pharmacokinetics, as these mice exhibit a higher frequency of these cells in the bone marrow and spleen [222, 224].

Potential pitfalls such as off-target uptake must be addressed, as they contribute to false positives, increased radiation dose, and reduced tumour contrast. These include the metabolic hepatic pathways for antibody, physiological low HER2 expression of targets in human organs such as liver [229] and ovary [189]. However, these uptake may not present in mouse models due to trastuzumab's lack of cross-reactivity with murine HER2 [190].

These significant discrepancies present considerable challenges in translating preclinical findings to human applications. Therefore, addressing these differences is crucial for ensuring accurate pharmacokinetic profiling and optimizing the therapeutic efficacy of antibody-based radiotracers in breast cancer molecular imaging.

VII. Keywords

FDG, RGD, breast cancer, PET imaging, angiogenesis imaging, PET biomarkers, HER2, trastuzumab, positron emission tomography, ^{52}Mn

VIII. Acknowledgment

I would like to express my heartfelt gratitude to everyone who contributed to the completion of my PhD dissertation and supported me throughout this journey. First and foremost, I would like to express my deepest gratitude to Assoc. Prof. Dr. Ildikó Garai, my supervisor, for her dedicated guidance, continuous support, and invaluable insights throughout this work. Her expertise, dedication, and thoughtful insights have been a cornerstone of this dissertation. My sincere thanks to Dr. György Trencsényi, head of the Department of Nuclear Medicine and Translational Imaging, for his invaluable support, especially in the field of oncology. I am also grateful to Dr. Adrienn Vágner and Dr. Gábor Nagy for sharing their exceptional radiochemistry expertise, and to Prof. Gyula Tircsó and his lab for their contributions in complex chemistry. Special thanks to my lab members Gábor Ország, Tamás Nagy, Csaba Csikós, and Zoltán Szoboszlai, for their assistance, and teamwork. I also extend my sincere appreciation to all the staff members at ScanoMed Ltd. (Debrecen) for their technical support and collaborative spirit throughout this project.

Finally, I wish to thank my parents, and my girlfriend Nguyen Khanh Linh for their unconditional love, patience, and unwavering support throughout this journey. Their belief in me has been a source of strength and motivation.

IX. References

1. Bray F, Laversanne M, Sung H, Ferlay J, Siegel RL, Soerjomataram I, et al. Global cancer statistics 2022: GLOBOCAN estimates of incidence and mortality worldwide for 36 cancers in 185 countries. CA Cancer J Clin. 2024;74(3):229-63.
2. Giaquinto AN, Sung H, Newman LA, Freedman RA, Smith RA, Star J, et al. Breast cancer statistics 2024. CA Cancer J Clin. 2024;74(6):477-95.
3. Arnold M, Morgan E, Rumgay H, Mafra A, Singh D, Laversanne M, et al. Current and future burden of breast cancer: Global statistics for 2020 and 2040. Breast. 2022;66:15-23.
4. Shoemaker ML, White MC, Wu M, Weir HK, Romieu I. Differences in breast cancer incidence among young women aged 20-49 years by stage and tumor characteristics, age, race, and ethnicity, 2004-2013. Breast Cancer Res Treat. 2018;169(3):595-606.
5. Elidrissi Errahhali M, Elidrissi Errahhali M, Ouarzane M, El Harroudi T, Afqir S, Bellaoui M. First report on molecular breast cancer subtypes and their clinico-pathological characteristics in Eastern Morocco: series of 2260 cases. BMC Womens Health. 2017;17(1):3.
6. Clusan L, Ferrière F, Flouriot G, Pakdel F. A Basic Review on Estrogen Receptor Signaling Pathways in Breast Cancer. Int J Mol Sci. 2023;24(7).
7. Davey MG, Hynes SO, Kerin MJ, Miller N, Lowery AJ. Ki-67 as a Prognostic Biomarker in Invasive Breast Cancer. Cancers (Basel). 2021;13(17).
8. Pan L, Li J, Xu Q, Gao Z, Yang M, Wu X, et al. HER2/PI3K/AKT pathway in HER2-positive breast cancer: A review. Medicine (Baltimore). 2024;103(24):e38508.
9. Yin L, Duan JJ, Bian XW, Yu SC. Triple-negative breast cancer molecular subtyping and treatment progress. Breast Cancer Res. 2020;22(1):61.
10. Bethea TN, Rosenberg L, Castro-Webb N, Lunetta KL, Sucheston-Campbell LE, Ruiz-Narváez EA, et al. Family History of Cancer in Relation to Breast Cancer Subtypes in African American Women. Cancer Epidemiol Biomarkers Prev. 2016;25(2):366-73.
11. Larsen MJ, Kruse TA, Tan Q, Lænkholm AV, Bak M, Lykkesfeldt AE, et al. Classifications within molecular subtypes enables identification of BRCA1/BRCA2 mutation carriers by RNA tumor profiling. PLoS One. 2013;8(5):e64268.
12. Mao X, Omeogu C, Karanth S, Joshi A, Meernik C, Wilson L, et al. Association of reproductive risk factors and breast cancer molecular subtypes: a systematic review and meta-analysis. BMC Cancer. 2023;23(1):644.
13. Jung AY, Ahearn TU, Behrens S, Middha P, Bolla MK, Wang Q, et al. Distinct Reproductive Risk Profiles for Intrinsic-Like Breast Cancer Subtypes: Pooled Analysis of Population-Based Studies. J Natl Cancer Inst. 2022;114(12):1706-19.
14. McGuire A, Brown JA, Malone C, McLaughlin R, Kerin MJ. Effects of age on the detection and management of breast cancer. Cancers (Basel). 2015;7(2):908-29.
15. Bai S, Song D, Chen M, Lai X, Xu J, Dong F. The association between mammographic density and breast cancer molecular subtypes: a systematic review and meta-analysis. Clin Radiol. 2023;78(8):622-32.
16. Makki J. Diversity of Breast Carcinoma: Histological Subtypes and Clinical Relevance. Clin Med Insights Pathol. 2015;8:23-31.
17. Zhu JY, He HL, Jiang XC, Bao HW, Chen F. Multimodal ultrasound features of breast cancers: correlation with molecular subtypes. BMC Med Imaging. 2023;23(1):57.
18. Temerik SM, Elwahab SMA, Wahman MM, Ahmed MY, Elwanis MEA. Relation between morphological features of initial breast MRI and breast cancer molecular subtypes. Egyptian Journal of Radiology and Nuclear Medicine. 2023;54(1):147.
19. Abdelbary EAM, Ibrahim AR, Rezk KM, Omar NN. Breast edema score at breast MRI: its value in prediction of molecular subtype of breast cancer and its impact on axillary LN metastasis. Egyptian Journal of Radiology and Nuclear Medicine. 2024;55(1):76.
20. Shokeir FA, Soliman N, Khater A, Bayoumi D. Evaluation of molecular subtypes of breast cancer using MRI BI-RADS Lexicon. Egyptian Journal of Radiology and Nuclear Medicine. 2024;55(1):52.

21. Loibl S, André F, Bachelot T, Barrios CH, Bergh J, Burstein HJ, et al. Early breast cancer: ESMO Clinical Practice Guideline for diagnosis, treatment and follow-up^{☆}. Annals of Oncology. 2024;35(2):159-82.
22. Gennari A, André F, Barrios CH, Cortés J, de Azambuja E, DeMichele A, et al. ESMO Clinical Practice Guideline for the diagnosis, staging and treatment of patients with metastatic breast cancer^{☆}. Annals of Oncology. 2021;32(12):1475-95.
23. Ngô TM, Lê Á, Đinh DPH. The Impact of Chemotherapy on Cardiovascular Mortality across Breast Cancer Subtypes. Curr Oncol. 2024;31(2):649-59.
24. Guo Y, Arciero CA, Jiang R, Behera M, Peng L, Li X. Different Breast Cancer Subtypes Show Different Metastatic Patterns: A Study from A Large Public Database. Asian Pac J Cancer Prev. 2020;21(12):3587-93.
25. Kennecke H, Yerushalmi R, Woods R, Cheang MC, Voduc D, Speers CH, et al. Metastatic behavior of breast cancer subtypes. J Clin Oncol. 2010;28(20):3271-7.
26. Press DJ, Miller ME, Liederbach E, Yao K, Huo D. De novo metastasis in breast cancer: occurrence and overall survival stratified by molecular subtype. Clin Exp Metastasis. 2017;34(8):457-65.
27. Ess SM, Herrmann C, Bouchardy C, Neyroud I, Rapiti E, Konzelmann I, et al. Impact of subtypes and comorbidities on breast cancer relapse and survival in population-based studies. Breast. 2018;41:151-8.
28. Yang SX, Polley EC. Systemic treatment and radiotherapy, breast cancer subtypes, and survival after long-term clinical follow-up. Breast Cancer Res Treat. 2019;175(2):287-95.
29. Lv S, Wang Y, Sun T, Wan D, Sheng L, Li W, et al. Overall Survival Benefit from Trastuzumab-Based Treatment in HER2-Positive Metastatic Breast Cancer: A Retrospective Analysis. Oncol Res Treat. 2018;41(7-8):450-5.
30. Howlader N, Cronin KA, Kurian AW, Andridge R. Differences in Breast Cancer Survival by Molecular Subtypes in the United States. Cancer Epidemiol Biomarkers Prev. 2018;27(6):619-26.
31. Nishikawa Y, Agatsuma N, Utsumi T, Funakoshi T, Mori Y, Nakamura Y, et al. Medical care costs according to the stage and subtype of breast cancer in a municipal setting: a case study of Hachioji City, Japan. Breast Cancer. 2024;31(1):105-15.
32. Visvader JE. Cells of origin in cancer. Nature. 2011;469(7330):314-22.
33. Guo L, Kong D, Liu J, Zhan L, Luo L, Zheng W, et al. Breast cancer heterogeneity and its implication in personalized precision therapy. Exp Hematol Oncol. 2023;12(1):3.
34. Vemuru S, Huang J, Colborn K, Yoon Y, Huynh V, Leonard L, et al. Clinical implications of receptor conversions in breast cancer patients who have undergone neoadjuvant chemotherapy. Breast Cancer Res Treat. 2023;200(2):247-56.
35. Zhao W, Sun L, Dong G, Wang X, Jia Y, Tong Z. Receptor conversion impacts outcomes of different molecular subtypes of primary breast cancer. Ther Adv Med Oncol. 2021;13:17588359211012982.
36. Zhang X, Yang F, Huang Z, Liu X, Xia G, Huang J, et al. Macrophages Promote Subtype Conversion and Endocrine Resistance in Breast Cancer. Cancers (Basel). 2024;16(3).
37. Toàn NM. Novel Molecular Classification of Breast Cancer with PET Imaging. Medicina. 2024;60(12):2099.
38. Shirman Y, Lubovsky S, Shai A. HER2-Low Breast Cancer: Current Landscape and Future Prospects. Breast Cancer (Dove Med Press). 2023;15:605-16.
39. Wei S. Hormone receptors in breast cancer: An update on the uncommon subtypes. Pathol Res Pract. 2023;250:154791.
40. Strimbu K, Tavel JA. What are biomarkers? Curr Opin HIV AIDS. 2010;5(6):463-6.
41. Das S, Dey MK, Devireddy R, Gartia MR. Biomarkers in Cancer Detection, Diagnosis, and Prognosis. Sensors (Basel). 2023;24(1).
42. de Mooij CM, Ploumen RAW, Nelemans PJ, Mottaghy FM, Smidt ML, van Nijnatten TJA. The influence of receptor expression and clinical subtypes on baseline [18F]FDG uptake in breast cancer: systematic review and meta-analysis. EJNMMI Res. 2023;13(1):5.

43. Boers J, Eisses B, Zwager MC, van Geel JJL, Bensch F, de Vries EFJ, et al. Correlation between Histopathological Prognostic Tumor Characteristics and [(18)F]FDG Uptake in Corresponding Metastases in Newly Diagnosed Metastatic Breast Cancer. Diagnostics (Basel). 2024;14(4).
44. Kwon HW, Lee JH, Pahk K, Park KH, Kim S. Clustering subtypes of breast cancer by combining immunohistochemistry profiles and metabolism characteristics measured using FDG PET/CT. Cancer Imaging. 2021;21(1):55.
45. Llombart-Cussac A, Prat A, Pérez-García JM, Mateos J, Pascual T, Escrivà-de-Romani S, et al. Clinicopathological and molecular predictors of [(18)F]FDG-PET disease detection in HER2-positive early breast cancer: RESPONSE, a substudy of the randomized PHERGain trial. Eur J Nucl Med Mol Imaging. 2024;51(9):2733-43.
46. Deng SM, Zhang W, Zhang B, Chen YY, Li JH, Wu YW. Correlation between the Uptake of 18F-Fluorodeoxyglucose (18F-FDG) and the Expression of Proliferation-Associated Antigen Ki-67 in Cancer Patients: A Meta-Analysis. PLoS One. 2015;10(6):e0129028.
47. Chalkidou A, Landau DB, Odell EW, Cornelius VR, O'Doherty MJ, Marsden PK. Correlation between Ki-67 immunohistochemistry and 18F-fluorothymidine uptake in patients with cancer: A systematic review and meta-analysis. Eur J Cancer. 2012;48(18):3499-513.
48. Surov A, Meyer HJ, Wienke A. Associations Between PET Parameters and Expression of Ki-67 in Breast Cancer. Transl Oncol. 2019;12(2):375-80.
49. Oude Munnink TH, Nagengast WB, Brouwers AH, Schröder CP, Hospers GA, Lub-de Hooge MN, et al. Molecular imaging of breast cancer. Breast. 2009;18 Suppl 3:S66-73.
50. Elboga U, Sahin E, Kus T, Cayirli YB, Aktas G, Uzun E, et al. Superiority of (68)Ga-FAPI PET/CT scan in detecting additional lesions compared to (18)FDG PET/CT scan in breast cancer. Ann Nucl Med. 2021;35(12):1321-31.
51. Sahin E, Kus T, Aytekin A, Uzun E, Elboga U, Yilmaz L, et al. (68)Ga-FAPI PET/CT as an Alternative to (18)F-FDG PET/CT in the Imaging of Invasive Lobular Breast Carcinoma. J Nucl Med. 2024;65(4):512-9.
52. Florea A, Mottaghy FM, Bauwens M. Molecular Imaging of Angiogenesis in Oncology: Current Preclinical and Clinical Status. Int J Mol Sci. 2021;22(11).
53. Gu Y, Dong B, He X, Qiu Z, Zhang J, Zhang M, et al. The challenges and opportunities of αvβ3-based therapeutics in cancer: From bench to clinical trials. Pharmacol Res. 2023;189:106694.
54. Liolios C, Sachpekidis C, Kolocouris A, Dimitrakopoulou-Strauss A, Bouziotis P. PET Diagnostic Molecules Utilizing Multimeric Cyclic RGD Peptide Analogs for Imaging Integrin α(v)β(3) Receptors. Molecules. 2021;26(6).
55. Yoon HJ, Kang KW, Chun IK, Cho N, Im SA, Jeong S, et al. Correlation of breast cancer subtypes, based on estrogen receptor, progesterone receptor, and HER2, with functional imaging parameters from ^{68}Ga-RGD PET/CT and ^{18}F-FDG PET/CT. Eur J Nucl Med Mol Imaging. 2014;41(8):1534-43.
56. Wu J, Zhang X, Jia Z, Zhou X, Qi R, Ji H, et al. Combined (18)F-FDG and (18)F-Alfatide II PET May Predict Luminal B (HER2 Negative) Subtype and Nonluminal Subtype of Invasive Breast Cancer. Mol Pharm. 2022;19(9):3405-11.
57. Bensch F, Brouwers AH, Lub-de Hooge MN, de Jong JR, van der Vegt B, Sleijfer S, et al. 89Zr-trastuzumab PET supports clinical decision making in breast cancer patients, when HER2 status cannot be determined by standard work up. European Journal of Nuclear Medicine and Molecular Imaging. 2018;45(13):2300-6.
58. Ulaner GA, Hyman DM, Ross DS, Corben A, Chandarlapaty S, Goldfarb S, et al. Detection of HER2-Positive Metastases in Patients with HER2-Negative Primary Breast Cancer Using 89Zr-Trastuzumab PET/CT. J Nucl Med. 2016;57(10):1523-8.
59. Dehdashti F, Wu N, Bose R, Naughton MJ, Ma CX, Marquez-Nostra BV, et al. Evaluation of [89Zr]trastuzumab-PET/CT in differentiating HER2-positive from HER2-negative breast cancer. Breast Cancer Research and Treatment. 2018;169(3):523-30.
60. Dijkers EC, Oude Munnink TH, Kosterink JG, Brouwers AH, Jager PL, de Jong JR, et al. Biodistribution of 89Zr-trastuzumab and PET Imaging of HER2-Positive Lesions in Patients With Metastatic Breast Cancer. Clinical Pharmacology & Therapeutics. 2010;87(5):586-92.

61. Ulaner GA, Hyman DM, Lyashchenko SK, Lewis JS, Carrasquillo JA. 89Zr-Trastuzumab PET/CT for Detection of Human Epidermal Growth Factor Receptor 2-Positive Metastases in Patients With Human Epidermal Growth Factor Receptor 2-Negative Primary Breast Cancer. Clin Nucl Med. 2017;42(12):912-7.
62. Linders DGJ, Deken MM, van Dam MA, Wasser M, Voormolen EMC, Kroep JR, et al. (89)Zr-Trastuzumab PET/CT Imaging of HER2-Positive Breast Cancer for Predicting Pathological Complete Response after Neoadjuvant Systemic Therapy: A Feasibility Study. Cancers (Basel). 2023;15(20).
63. Gebhart G, Lamberts LE, Wimana Z, Garcia C, Emonts P, Ameye L, et al. Molecular imaging as a tool to investigate heterogeneity of advanced HER2-positive breast cancer and to predict patient outcome under trastuzumab emtansine (T-DM1): the ZEPHIR trial. Ann Oncol. 2016;27(4):619-24.
64. Mileva M, de Vries EGE, Guiot T, Wimana Z, Deleu A-L, Schröder CP, et al. Molecular imaging predicts lack of T-DM1 response in advanced HER2-positive breast cancer (final results of ZEPHIR trial). npj Breast Cancer. 2024;10(1):4.
65. Gaykema SB, Schröder CP, Vitfell-Rasmussen J, Chua S, Oude Munnink TH, Brouwers AH, et al. 89Zr-trastuzumab and 89Zr-bevacizumab PET to evaluate the effect of the HSP90 inhibitor NVP-AUY922 in metastatic breast cancer patients. Clin Cancer Res. 2014;20(15):3945-54.
66. McKnight BN, Viola-Villegas NT. Monitoring Src status after dasatinib treatment in HER2+ breast cancer with (89)Zr-trastuzumab PET imaging. Breast Cancer Res. 2018;20(1):130.
67. Deri MA, Ponnala S, Kozlowski P, Burton-Pye BP, Cicek HT, Hu C, et al. p-SCN-Bn-HOPO: A Superior Bifunctional Chelator for (89)Zr ImmunoPET. Bioconjug Chem. 2015;26(12):2579-91.
68. Chomet M, Schreurs M, Bolijn MJ, Verlaan M, Beaino W, Brown K, et al. Head-to-head comparison of DFO* and DFO chelators: selection of the best candidate for clinical (89)Zr-immuno-PET. Eur J Nucl Med Mol Imaging. 2021;48(3):694-707.
69. Vivier D, Sharma SK, Adumeau P, Rodriguez C, Fung K, Zeglis BM. The Impact of FcγRI Binding on Immuno-PET. J Nucl Med. 2019;60(8):1174-82.
70. Badier L, Quelven I. Zirconium 89 and Copper 64 for ImmunoPET: From Antibody Bioconjugation and Radiolabeling to Molecular Imaging. Pharmaceutics. 2024;16(7):882.
71. Mortimer JE, Bading JR, Colcher DM, Conti PS, Frankel PH, Carroll MI, et al. Functional imaging of human epidermal growth factor receptor 2-positive metastatic breast cancer using (64)Cu-DOTA-trastuzumab PET. J Nucl Med. 2014;55(1):23-9.
72. Carrasquillo JA, Morris PG, Humm JL, Smith-Jones PM, Beylergil V, Akhurst T, et al. Copper-64 trastuzumab PET imaging: a reproducibility study. Q J Nucl Med Mol Imaging. 2019;63(2):191-8.
73. Kurihara H, Hamada A, Yoshida M, Shimma S, Hashimoto J, Yonemori K, et al. (64)Cu-DOTA-trastuzumab PET imaging and HER2 specificity of brain metastases in HER2-positive breast cancer patients. EJNMMI Res. 2015;5:8.
74. Mortimer JE, Bading JR, Frankel PH, Carroll MI, Yuan Y, Park JM, et al. Use of (64)Cu-DOTA-Trastuzumab PET to Predict Response and Outcome of Patients Receiving Trastuzumab Emtansine for Metastatic Breast Cancer: A Pilot Study. J Nucl Med. 2022;63(8):1145-8.
75. Woo SK, Jang SJ, Seo MJ, Park JH, Kim BS, Kim EJ, et al. Development of (64)Cu-NOTA-Trastuzumab for HER2 Targeting: A Radiopharmaceutical with Improved Pharmacokinetics for Human Studies. J Nucl Med. 2019;60(1):26-33.
76. Lee I, Lim I, Byun BH, Kim BI, Choi CW, Woo SK, et al. A preliminary clinical trial to evaluate (64)Cu-NOTA-Trastuzumab as a positron emission tomography imaging agent in patients with breast cancer. EJNMMI Res. 2021;11(1):8.
77. Maisonial-Besset A, Witkowski T, Quintana M, Besse S, Gaumet V, Cordonnier A, et al. Synthesis and In Vitro Comparison of DOTA, NODAGA and 15-5 Macrocycles as Chelators for the (64)Cu-Labelling of Immunoconjugates. Molecules. 2022;28(1).
78. Marquez BV, Ikotun OF, Zheleznyak A, Wright B, Hari-Raj A, Pierce RA, et al. Evaluation of (89)Zr-pertuzumab in Breast cancer xenografts. Mol Pharm. 2014;11(11):3988-95.
79. Ulaner GA, Lyashchenko SK, Riedl C, Ruan S, Zanzonico PB, Lake D, et al. First-in-Human Human Epidermal Growth Factor Receptor 2-Targeted Imaging Using (89)Zr-Pertuzumab

PET/CT: Dosimetry and Clinical Application in Patients with Breast Cancer. J Nucl Med. 2018;59(6):900-6.

80. Massicano AVF, Lee S, Crenshaw BK, Aweda TA, El Sayed R, Super I, et al. Imaging of HER2 with [(89)Zr]pertuzumab in Response to T-DM1 Therapy. Cancer Biother Radiopharm. 2019;34(4):209-17.
81. Kang M, Shin JI, Han S, Kim JY, Park J, Kim KI, et al. Therapeutic Response Monitoring with (89)Zr-DFO-Pertuzumab in HER2-Positive and Trastuzumab-Resistant Breast Cancer Models. Pharmaceutics. 2022;14(7).
82. Lu Y, Li M, Massicano AVF, Song PN, Mansur A, Heinzman KA, et al. [(89)Zr]-Pertuzumab PET Imaging Reveals Paclitaxel Treatment Efficacy Is Positively Correlated with HER2 Expression in Human Breast Cancer Xenograft Mouse Models. Molecules. 2021;26(6).
83. Vivier D, Fung K, Rodriguez C, Adumeau P, Ulaner GA, Lewis JS, et al. The Influence of Glycans-Specific Bioconjugation on the FcγRI Binding and In vivo Performance of (89)Zr-DFO-Pertuzumab. Theranostics. 2020;10(4):1746-57.
84. Yeh R, O'Donoghue JA, Jayaprakasam VS, Mauguen A, Min R, Park S, et al. First-in-Human Evaluation of Site-Specifically Labeled (89)Zr-Pertuzumab in Patients with HER2-Positive Breast Cancer. J Nucl Med. 2024;65(3):386-93.
85. Al-Saden N, Lam K, Chan C, Reilly RM. Positron-Emission Tomography of HER2-Positive Breast Cancer Xenografts in Mice with (89)Zr-Labeled Trastuzumab-DM1: A Comparison with (89)Zr-Labeled Trastuzumab. Mol Pharm. 2018;15(8):3383-93.
86. Al-Saden N, Cai Z, Reilly RM. Tumor uptake and tumor/blood ratios for [(89)Zr]Zr-DFO-trastuzumab-DM1 on microPET/CT images in NOD/SCID mice with human breast cancer xenografts are directly correlated with HER2 expression and response to trastuzumab-DM1. Nucl Med Biol. 2018;67:43-51.
87. Suman SK, Mukherjee A, Pandey U, Chakraborty A, Rakshit S, Tawate M, et al. (68)Ga-Labeled Trastuzumab Fragments for ImmunoPET Imaging of Human Epidermal Growth Factor Receptor 2 Expression in Solid Cancers. Cancer Biother Radiopharm. 2023;38(1):38-50.
88. Moreau M, Poty S, Vrigneaud JM, Walker P, Guillemin M, Raguin O, et al. MANOTA: a promising bifunctional chelating agent for copper-64 immunoPET. Dalton Trans. 2017;46(42):14659-68.
89. Yue TTC, Ge Y, Aprile FA, Ma MT, Pham TT, Long NJ. Site-Specific (68)Ga Radiolabeling of Trastuzumab Fab via Methionine for ImmunoPET Imaging. Bioconjug Chem. 2023;34(10):1802-10.
90. Mendler CT, Gehring T, Wester HJ, Schwaiger M, Skerra A. ^{89}Zr-Labeled Versus ^{124}I-Labeled αHER2 Fab with Optimized Plasma Half-Life for High-Contrast Tumor Imaging In Vivo. J Nucl Med. 2015;56(7):1112-8.
91. Richter A, Knorr K, Schlapschy M, Robu S, Morath V, Mendler C, et al. First In-Human Medical Imaging with a PASylated (89)Zr-Labeled Anti-HER2 Fab-Fragment in a Patient with Metastatic Breast Cancer. Nucl Med Mol Imaging. 2020;54(2):114-9.
92. Zhou Z, McDougald D, Devoogdt N, Zalutsky MR, Vaidyanathan G. Labeling Single Domain Antibody Fragments with Fluorine-18 Using 2,3,5,6-Tetrafluorophenyl 6-[(18)F]Fluoronicotinate Resulting in High Tumor-to-Kidney Ratios. Mol Pharm. 2019;16(1):214-26.
93. Keyaerts M, Xavier C, Heemskerk J, Devoogdt N, Everaert H, Ackaert C, et al. Phase I Study of 68Ga-HER2-Nanobody for PET/CT Assessment of HER2 Expression in Breast Carcinoma. J Nucl Med. 2016;57(1):27-33.
94. Gondry O, Caveliers V, Xavier C, Raes L, Vanhoeij M, Verfaillie G, et al. Phase II Trial Assessing the Repeatability and Tumor Uptake of [(68)Ga]Ga-HER2 Single-Domain Antibody PET/CT in Patients with Breast Carcinoma. J Nucl Med. 2024;65(2):178-84.
95. Ducharme M, Hall L, Eckenroad W, Cingoranelli SJ, Houson HA, Jaskowski L, et al. Evaluation of [(89)Zr]Zr-DFO-2Rs15d Nanobody for Imaging of HER2-Positive Breast Cancer. Mol Pharm. 2023;20(9):4629-39.
96. Luo R, Liu H, Cheng Z. Protein scaffolds: antibody alternatives for cancer diagnosis and therapy. RSC Chem Biol. 2022;3(7):830-47.

97. Ahlgren S, Orlova A, Rosik D, Sandström M, Sjöberg A, Baastrup B, et al. Evaluation of maleimide derivative of DOTA for site-specific labeling of recombinant affibody molecules. Bioconjug Chem. 2008;19(1):235-43.
98. Feldwisch J, Tolmachev V, Lendel C, Herne N, Sjöberg A, Larsson B, et al. Design of an optimized scaffold for affibody molecules. J Mol Biol. 2010;398(2):232-47.
99. Sandström M, Lindskog K, Velikyan I, Wennborg A, Feldwisch J, Sandberg D, et al. Biodistribution and Radiation Dosimetry of the Anti-HER2 Affibody Molecule 68Ga-ABY-025 in Breast Cancer Patients. J Nucl Med. 2016;57(6):867-71.
100. Sandberg D, Tolmachev V, Velikyan I, Olofsson H, Wennborg A, Feldwisch J, et al. Intra-image referencing for simplified assessment of HER2-expression in breast cancer metastases using the Affibody molecule ABY-025 with PET and SPECT. Eur J Nucl Med Mol Imaging. 2017;44(8):1337-46.
101. Sörensen J, Velikyan I, Sandberg D, Wennborg A, Feldwisch J, Tolmachev V, et al. Measuring HER2-Receptor Expression In Metastatic Breast Cancer Using [68Ga]ABY-025 Affibody PET/CT. Theranostics. 2016;6(2):262-71.
102. Altena R, Burén SA, Blomgren A, Karlsson E, Tzortzakakis A, Brun N, et al. Human Epidermal Growth Factor Receptor 2 (HER2) PET Imaging of HER2-Low Breast Cancer with [(68)Ga]Ga-ABY-025: Results from a Pilot Study. J Nucl Med. 2024;65(5):700-7.
103. Alhuseinalkhudhur A, Lindman H, Liss P, Sundin T, Frejd FY, Hartman J, et al. Human Epidermal Growth Factor Receptor 2-Targeting [(68)Ga]Ga-ABY-025 PET/CT Predicts Early Metabolic Response in Metastatic Breast Cancer. J Nucl Med. 2023;64(9):1364-70.
104. Xu Y, Bai Z, Huang Q, Pan Y, Pan D, Wang L, et al. PET of HER2 Expression with a Novel (18)FAl Labeled Affibody. J Cancer. 2017;8(7):1170-8.
105. Xu Y, Wang L, Pan D, Yu C, Mi B, Huang Q, et al. PET imaging of a (68)Ga labeled modified HER2 affibody in breast cancers: from xenografts to patients. Br J Radiol. 2019;92(1104):20190425.
106. Xu Y, Wang L, Pan D, Yan J, Wang X, Yang R, et al. Synthesis of a novel (89)Zr-labeled HER2 affibody and its application study in tumor PET imaging. EJNMMI Res. 2020;10(1):58.
107. Liu Y, Xu T, Vorobyeva A, Loftenius A, Bodenko V, Orlova A, et al. Radionuclide Therapy of HER2-Expressing Xenografts Using [(177)Lu]Lu-ABY-027 Affibody Molecule Alone and in Combination with Trastuzumab. Cancers (Basel). 2023;15(9).
108. Oroujeni M, Rinne SS, Vorobyeva A, Loftenius A, Feldwisch J, Jonasson P, et al. Preclinical Evaluation of 99mTc-ZHER2:41071, a Second-Generation Affibody-Based HER2-Visualizing Imaging Probe with a Low Renal Uptake. International Journal of Molecular Sciences. 2021;22(5):2770.
109. von Witting E, Garousi J, Lindbo S, Vorobyeva A, Altai M, Oroujeni M, et al. Selection of the optimal macrocyclic chelators for labeling with (111)In and (68)Ga improves contrast of HER2 imaging using engineered scaffold protein ADAPT6. Eur J Pharm Biopharm. 2019;140:109-20.
110. Fay R, Törő I, Schinke AL, Simic B, Schaefer JV, Dreier B, et al. Sortase-Mediated Site-Specific Conjugation and (89)Zr-Radiolabeling of Designed Ankyrin Repeat Proteins for PET. Mol Pharm. 2022;19(10):3576-85.
111. Altunay B, Morgenroth A, Beheshti M, Vogg A, Wong NCL, Ting HH, et al. HER2-directed antibodies, affibodies and nanobodies as drug-delivery vehicles in breast cancer with a specific focus on radioimmunotherapy and radioimmunoimaging. Eur J Nucl Med Mol Imaging. 2021;48(5):1371-89.
112. Cavallaro PA, De Santo M, Belsito EL, Longobucco C, Curcio M, Morelli C, et al. Peptides Targeting HER2-Positive Breast Cancer Cells and Applications in Tumor Imaging and Delivery of Chemotherapeutics. Nanomaterials. 2023;13(17):2476.
113. Ducharme M, Lapi SE. Peptide Based Imaging Agents for HER2 Imaging in Oncology. Mol Imaging. 2020;19:1536012120960258.
114. Biabani Ardakani J, Akhlaghi M, Nikkholgh B, Hosseinimehr SJ. Targeting and imaging of HER2 overexpression tumor with a new peptide-based (68)Ga-PET radiotracer. Bioorg Chem. 2021;106:104474.

115. Ducharme M, Houson HA, Fernandez SR, Lapi SE. Evaluation of 68Ga-Radiolabeled Peptides for HER2 PET Imaging. Diagnostics. 2022;12(11):2710.
116. de Roode KE, Joosten L, Behe M. Towards the Magic Radioactive Bullet: Improving Targeted Radionuclide Therapy by Reducing the Renal Retention of Radioligands. Pharmaceuticals. 2024;17(2):256.
117. Kakavand T, Mirzaii M, Eslami M, Valizadeh S. Cyclotron production of 52Mn and Monte Carlo benchmarking. Journal of Radioanalytical and Nuclear Chemistry. 2015;304(2):669-74.
118. Amor-Coarasa A, Kelly JM, Ponnala S, Nikolopoulou A, Williams C, Jr., Babich JW. (66)Ga: A Novelty or a Valuable Preclinical Screening Tool for the Design of Targeted Radiopharmaceuticals? Molecules. 2018;23(10).
119. Aluicio-Sarduy E, Ellison PA, Barnhart TE, Cai W, Nickles RJ, Engle JW. PET radiometals for antibody labeling. J Labelled Comp Radiopharm. 2018;61(9):636-51.
120. Brandt M, Cardinale J, Rausch I, Mindt TL. Manganese in PET imaging: Opportunities and challenges. J Labelled Comp Radiopharm. 2019;62(8):541-51.
121. Daksh S, Kaul A, Deep S, Datta A. Current advancement in the development of manganese complexes as magnetic resonance imaging probes. J Inorg Biochem. 2022;237:112018.
122. Kálmán FK, Tircsó G. Kinetic inertness of the Mn2+ complexes formed with AAZTA and some open-chain EDTA derivatives. Inorg Chem. 2012;51(19):10065-7.
123. Garda Z, Molnár E, Kálmán FK, Botár R, Nagy V, Baranyai Z, et al. Effect of the Nature of Donor Atoms on the Thermodynamic, Kinetic and Relaxation Properties of Mn(II) Complexes Formed With Some Trisubstituted 12-Membered Macrocyclic Ligands. Front Chem. 2018;6:232.
124. Bernhard C, Moreau M, Lhenry D, Goze C, Boschetti F, Rousselin Y, et al. DOTAGA-anhydride: a valuable building block for the preparation of DOTA-like chelating agents. Chemistry. 2012;18(25):7834-41.
125. Okano M, Oshi M, Butash A, Okano I, Saito K, Kawaguchi T, et al. Orthotopic Implantation Achieves Better Engraftment and Faster Growth Than Subcutaneous Implantation in Breast Cancer Patient-Derived Xenografts. J Mammary Gland Biol Neoplasia. 2020;25(1):27-36.
126. Gregório AC, Fonseca NA, Moura V, Lacerda M, Figueiredo P, Simões S, et al. Inoculated Cell Density as a Determinant Factor of the Growth Dynamics and Metastatic Efficiency of a Breast Cancer Murine Model. PLoS One. 2016;11(11):e0165817.
127. Nolting DD, Nickels ML, Guo N, Pham W. Molecular imaging probe development: a chemistry perspective. Am J Nucl Med Mol Imaging. 2012;2(3):273-306.
128. Tomayko MM, Reynolds CP. Determination of subcutaneous tumor size in athymic (nude) mice. Cancer Chemother Pharmacol. 1989;24(3):148-54.
129. Gottlieb HE, Kotlyar V, Nudelman A. NMR Chemical Shifts of Common Laboratory Solvents as Trace Impurities. The Journal of Organic Chemistry. 1997;62(21):7512-5.
130. Irving HM, Miles MG, Pettit LD. A study of some problems in determining the stoicheiometric proton dissociation constants of complexes by potentiometric titrations using a glass electrode. Analytica Chimica Acta. 1967;38:475-88.
131. Zekany L, Nagypal I. PSEQUAD. In: Leggett DJ, editor. Computational Methods for the Determination of Formation Constants. Boston, MA: Springer US; 1985. p. 291-353.
132. Garda Z, Molnár E, Hamon N, Barriada JL, Esteban-Gómez D, Váradi B, et al. Complexation of Mn(II) by Rigid Pyclen Diacetates: Equilibrium, Kinetic, Relaxometric, Density Functional Theory, and Superoxide Dismutase Activity Studies. Inorg Chem. 2021;60(2):1133-48.
133. Gale EM, Atanasova IP, Blasi F, Ay I, Caravan P. A Manganese Alternative to Gadolinium for MRI Contrast. Journal of the American Chemical Society. 2015;137(49):15548-57.
134. Wessel AJ, Schultz JW, Tang F, Duan H, Mirica LM. Improved synthesis of symmetrically & asymmetrically N-substituted pyridinophane derivatives. Org Biomol Chem. 2017;15(46):9923-31.
135. Gracia S, Arrachart G, Marie C, Chapron S, Miguirditchian M, Pellet-Rostaing S. Separation of Am (III) by solvent extraction using water-soluble H4tpaen derivatives. Tetrahedron. 2015;71(33):5321-36.

136. Kim WD, Hrncir DC, Kiefer GE, Sherry AD. Synthesis, Crystal Structure, and Potentiometry of Pyridine-Containing Tetraaza Macrocyclic Ligands with Acetate Pendant Arms. Inorganic Chemistry. 1995;34(8):2225-32.
137. Sharma AK, Schultz JW, Prior JT, Rath NP, Mirica LM. Coordination Chemistry of Bifunctional Chemical Agents Designed for Applications in (64)Cu PET Imaging for Alzheimer's Disease. Inorg Chem. 2017;56(22):13801-14.
138. Takács A, Napolitano R, Purgel M, Bényei AC, Zékány L, Brücher E, et al. Solution structures, stabilities, kinetics, and dynamics of DO3A and DO3A-sulphonamide complexes. Inorg Chem. 2014;53(6):2858-72.
139. Cieslik P, Comba P, Dittmar B, Ndiaye D, Tóth É, Velmurugan G, et al. Exceptional Manganese(II) Stability and Manganese(II)/Zinc(II) Selectivity with Rigid Polydentate Ligands. Angew Chem Int Ed Engl. 2022;61(10):e202115580.
140. Botár R, Molnár E, Trencsényi G, Kiss J, Kálmán FK, Tircsó G. Stable and Inert Mn(II)-Based and pH-Responsive Contrast Agents. J Am Chem Soc. 2020;142(4):1662-6.
141. Botár R, Molnár E, Garda Z, Madarasi E, Trencsényi G, Kiss J, et al. Synthesis and characterization of a stable and inert MnII-based ZnII responsive MRI probe for molecular imaging of glucose stimulated zinc secretion (GSZS). Inorganic Chemistry Frontiers. 2022;9(3):577-83.
142. Váradi B, Brezovcsik K, Garda Z, Madarasi E, Szedlacsek H, Badea R-A, et al. Synthesis and characterization of a novel [52Mn]Mn-labelled affibody based radiotracer for HER2+ targeting. Inorganic Chemistry Frontiers. 2023;10(16):4734-45.
143. Drahoš B, Kotek J, Císařová I, Hermann P, Helm L, Lukeš I, et al. Mn2+ Complexes with 12-Membered Pyridine Based Macrocycles Bearing Carboxylate or Phosphonate Pendant Arm: Crystallographic, Thermodynamic, Kinetic, Redox, and 1H/17O Relaxation Studies. Inorganic Chemistry. 2011;50(24):12785-801.
144. Nishida N, Yano H, Nishida T, Kamura T, Kojiro M. Angiogenesis in cancer. Vasc Health Risk Manag. 2006;2(3):213-9.
145. Porter JC, Ganeshan B, Win T, Fraioli F, Khan S, Rodriguez-Justo M, et al. [(18)F]FDG PET/CT Signal Correlates with Neoangiogenesis Markers in Patients with Fibrotic Interstitial Lung Disease Who Underwent Lung Biopsy: Implication for the Use of PET/CT in Diffuse Lung Diseases. J Nucl Med. 2024;65(4):617-22.
146. Mirus M, Tokalov SV, Abramyuk A, Heinold J, Prochnow V, Zöphel K, et al. Noninvasive assessment and quantification of tumor vascularization using [18F]FDG-PET/CT and CE-CT in a tumor model with modifiable angiogenesis-an animal experimental prospective cohort study. EJNMMI Res. 2019;9(1):55.
147. Groves AM, Shastry M, Rodriguez-Justo M, Malhotra A, Endozo R, Davidson T, et al. ^{18}F-FDG PET and biomarkers for tumour angiogenesis in early breast cancer. Eur J Nucl Med Mol Imaging. 2011;38(1):46-52.
148. Wei YC, Gao Y, Zhang J, Fu Z, Zheng J, Liu N, et al. Stereotactic Comparison Study of (18)F-Alfatide and (18)F-FDG PET Imaging in an LLC Tumor-Bearing C57BL/6 Mouse Model. Sci Rep. 2016;6:28757.
149. Durante S, Dunet V, Gorostidi F, Mitsakis P, Schaefer N, Delage J, et al. Head and neck tumors angiogenesis imaging with (68)Ga-NODAGA-RGD in comparison to (18)F-FDG PET/CT: a pilot study. EJNMMI Res. 2020;10(1):47.
150. Minamimoto R, Karam A, Jamali M, Barkhodari A, Gambhir SS, Dorigo O, et al. Pilot prospective evaluation of (18)F-FPPRGD2 PET/CT in patients with cervical and ovarian cancer. Eur J Nucl Med Mol Imaging. 2016;43(6):1047-55.
151. Dietz M, Dunet V, Mantziari S, Pomoni A, Dias Correia R, Testart Dardel N, et al. Comparison of integrin α(v)β(3) expression with (68)Ga-NODAGA-RGD PET/CT and glucose metabolism with (18)F-FDG PET/CT in esophageal or gastroesophageal junction cancers. Eur J Hybrid Imaging. 2023;7(1):3.
152. Beer AJ, Lorenzen S, Metz S, Herrmann K, Watzlowik P, Wester H-J, et al. Comparison of Integrin α_vβ₃ Expression and Glucose Metabolism in Primary and

Metastatic Lesions in Cancer Patients: A PET Study Using ¹⁸F-Galacto-RGD and ¹⁸F-FDG. Journal of Nuclear Medicine. 2008;49(1):22-9.

153. Chen SH, Wang HM, Lin CY, Chang JT, Hsieh CH, Liao CT, et al. RGD-K5 PET/CT in patients with advanced head and neck cancer treated with concurrent chemoradiotherapy: Results from a pilot study. Eur J Nucl Med Mol Imaging. 2016;43(9):1621-9.
154. Withofs N, Martinive P, Vanderick J, Bletard N, Scagnol I, Mievis F, et al. [(18)F]FPRGD2 PET/CT imaging of integrin αvβ3 levels in patients with locally advanced rectal carcinoma. Eur J Nucl Med Mol Imaging. 2016;43(4):654-62.
155. Ahangari S, Littrup Andersen F, Liv Hansen N, Jakobi Nøttrup T, Berthelsen AK, Folsted Kallehauge J, et al. Multi-parametric PET/MRI for enhanced tumor characterization of patients with cervical cancer. Eur J Hybrid Imaging. 2022;6(1):7.
156. Toriihara A, Duan H, Thompson HM, Park S, Hatami N, Baratto L, et al. (18)F-FPPRGD(2) PET/CT in patients with metastatic renal cell cancer. Eur J Nucl Med Mol Imaging. 2019;46(7):1518-23.
157. Li L, Chen X, Yu J, Yuan S. Preliminary Clinical Application of RGD-Containing Peptides as PET Radiotracers for Imaging Tumors. Front Oncol. 2022;12:837952.
158. Zheng K, Liang N, Zhang J, Lang L, Zhang W, Li S, et al. 68Ga-NOTA-PRGD2 PET/CT for Integrin Imaging in Patients with Lung Cancer. J Nucl Med. 2015;56(12):1823-7.
159. Novy Z, Stepankova J, Hola M, Flasarova D, Popper M, Petrik M. Preclinical Evaluation of Radiolabeled Peptides for PET Imaging of Glioblastoma Multiforme. Molecules. 2019;24(13).
160. Du W, Ren L, Hamblin MH, Fan Y. Endothelial Cell Glucose Metabolism and Angiogenesis. Biomedicines. 2021;9(2).
161. Li XF, Du Y, Ma Y, Postel GC, Civelek AC. (18)F-fluorodeoxyglucose uptake and tumor hypoxia: revisit (18)f-fluorodeoxyglucose in oncology application. Transl Oncol. 2014;7(2):240-7.
162. Kis A, Szabó JP, Dénes N, Vágner A, Nagy G, Garai I, et al. In Vivo Imaging of Hypoxia and Neoangiogenesis in Experimental Syngeneic Hepatocellular Carcinoma Tumor Model Using Positron Emission Tomography. Biomed Res Int. 2020;2020:4952372.
163. Shangguan C, Gan G, Zhang J, Wu J, Miao Y, Zhang M, et al. Cancer-associated fibroblasts enhance tumor (18)F-FDG uptake and contribute to the intratumor heterogeneity of PET-CT. Theranostics. 2018;8(5):1376-88.
164. Tripathi M, Billet S, Bhowmick NA. Understanding the role of stromal fibroblasts in cancer progression. Cell Adh Migr. 2012;6(3):231-5.
165. Tong RT, Boucher Y, Kozin SV, Winkler F, Hicklin DJ, Jain RK. Vascular Normalization by Vascular Endothelial Growth Factor Receptor 2 Blockade Induces a Pressure Gradient Across the Vasculature and Improves Drug Penetration in Tumors. Cancer Research. 2004;64(11):3731-6.
166. Børresen B, Hansen AE, Fliedner FP, Henriksen JR, Elema DR, Brandt-Larsen M, et al. Noninvasive Molecular Imaging of the Enhanced Permeability and Retention Effect by (64)Cu-Liposomes: In vivo Correlations with (68)Ga-RGD, Fluid Pressure, Diffusivity and (18)F-FDG. Int J Nanomedicine. 2020;15:8571-81.
167. Kashkooli FM, Abazari MA, Soltani M, Ghazani MA, Rahmim A. A spatiotemporal multi-scale computational model for FDG PET imaging at different stages of tumor growth and angiogenesis. Scientific Reports. 2022;12(1):10062.
168. Karam MB, Doroudinia A, Behzadi B, Mehrian P, Koma AY. Correlation of quantified metabolic activity in nonsmall cell lung cancer with tumor size and tumor pathological characteristics. Medicine. 2018;97(32):e11628.
169. Wei YC, Hu X, Gao Y, Fu Z, Zhao W, Yu Q, et al. Noninvasive Evaluation of Metabolic Tumor Volume in Lewis Lung Carcinoma Tumor-Bearing C57BL/6 Mice with Micro-PET and the Radiotracers 18F-Alfatide and 18F-FDG: A Comparative Analysis. PLoS One. 2015;10(9):e0136195.
170. Provost C, Rozenblum-Beddok L, Nataf V, Merabtene F, Prignon A, Talbot JN. [(68)Ga]RGD Versus [(18)F]FDG PET Imaging in Monitoring Treatment Response of a Mouse Model of

Human Glioblastoma Tumor with Bevacizumab and/or Temozolomide. Mol Imaging Biol. 2019;21(2):297-305.

171. Cui Y, Liu H, Liang S, Zhang C, Cheng W, Hai W, et al. The feasibility of 18F-AlF-NOTA-PRGD2 PET/CT for monitoring early response of Endostar antiangiogenic therapy in human nasopharyngeal carcinoma xenograft model compared with 18F-FDG. Oncotarget. 2016;7(19):27243-54.
172. Garcia J, Hurwitz HI, Sandler AB, Miles D, Coleman RL, Deurloo R, et al. Bevacizumab (Avastin®) in cancer treatment: A review of 15 years of clinical experience and future outlook. Cancer Treat Rev. 2020;86:102017.
173. Arslan E, Aksoy T, Can Trabulus FD, Kelten Talu C, Yeni B, Çermik TF. The association of 18F-fluorodeoxyglucose PET/computed tomography parameters with tissue gastrin-releasing peptide receptor and integrin αvβ3 receptor levels in patients with breast cancer. Nucl Med Commun. 2020;41(3):260-8.
174. Chen Z, Fu F, Li F, Zhu Z, Yang Y, Chen X, et al. Comparison of [(99m)Tc]3PRGD(2) Imaging and [(18)F]FDG PET/CT in Breast Cancer and Expression of Integrin α(v)β(3) in Breast Cancer Vascular Endothelial Cells. Mol Imaging Biol. 2018;20(5):846-56.
175. Li X, Yang J, Peng L, Sahin AA, Huo L, Ward KC, et al. Triple-negative breast cancer has worse overall survival and cause-specific survival than non-triple-negative breast cancer. Breast Cancer Res Treat. 2017;161(2):279-87.
176. Li Q, Li M, Zheng K, Tang S, Ma S. Expression pattern analysis and drug differential sensitivity of cancer-associated fibroblasts in triple-negative breast cancer. Transl Oncol. 2021;14(1):100891.
177. Bos R, van der Groep P, Greijer AE, Shvarts A, Meijer S, Pinedo HM, et al. Levels of hypoxia-inducible factor-1α independently predict prognosis in patients with lymph node negative breast carcinoma. Cancer. 2003;97(6):1573-81.
178. Kaira K, Murakami H, Endo M, Ohde Y, Naito T, Kondo H, et al. Biological correlation of ^{18}F-FDG uptake on PET in pulmonary neuroendocrine tumors. Anticancer Res. 2013;33(10):4219-28.
179. Jahandideh A, Ståhle M, Virta J, Li X-G, Liljenbäck H, Moisio O, et al. Evaluation of [68Ga]Ga-NODAGA-RGD for PET Imaging of Rat Autoimmune Myocarditis. Frontiers in Medicine. 2021;8.
180. Deleye S, Heylen M, Deiteren A, De Man J, Stroobants S, De Winter B, et al. Continuous flushing of the bladder in rodents reduces artifacts and improves quantification in molecular imaging. Mol Imaging. 2014;13.
181. Cussó L, Desco M. Suppression of 18F-FDG signal in the bladder on small animal PET-CT. PLoS One. 2018;13(10):e0205610.
182. Zhao J, Liu Q, Li C, Song Y, Zhang Y, Chen J-C. Optimization of Spatial Resolution and Image Reconstruction Parameters for the Small-Animal Metis™ PET/CT System. Electronics. 2022;11(10):1542.
183. Mangeat T, Gracia M, Pichard A, Poty S, Martineau P, Robert B, et al. Fc-engineered monoclonal antibodies to reduce off-target liver uptake. EJNMMI Res. 2023;13(1):81.
184. Ryman JT, Meibohm B. Pharmacokinetics of Monoclonal Antibodies. CPT Pharmacometrics Syst Pharmacol. 2017;6(9):576-88.
185. Cataldi M, Vigliotti C, Mosca T, Cammarota M, Capone D. Emerging Role of the Spleen in the Pharmacokinetics of Monoclonal Antibodies, Nanoparticles and Exosomes. Int J Mol Sci. 2017;18(6).
186. Danilov SM, Gavrilyuk VD, Franke FE, Pauls K, Harshaw DW, McDonald TD, et al. Lung uptake of antibodies to endothelial antigens: key determinants of vascular immunotargeting. Am J Physiol Lung Cell Mol Physiol. 2001;280(6):L1335-47.
187. Caironi P, Langer T, Gattinoni L. Albumin in critically ill patients: the ideal colloid? Current Opinion in Critical Care. 2015;21(4):302-8.
188. Westerlund K, Honarvar H, Norrström E, Strand J, Mitran B, Orlova A, et al. Increasing the Net Negative Charge by Replacement of DOTA Chelator with DOTAGA Improves the

Biodistribution of Radiolabeled Second-Generation Synthetic Affibody Molecules. Mol Pharm. 2016;13(5):1668-78.

189. Berchuck A, Kamel A, Whitaker R, Kerns B, Olt G, Kinney R, et al. Overexpression of HER-2/neu is associated with poor survival in advanced epithelial ovarian cancer. Cancer Res. 1990;50(13):4087-91.
190. Lewis Phillips G, Guo J, Kiefer JR, Proctor W, Bumbaca Yadav D, Dybdal N, et al. Trastuzumab does not bind rat or mouse ErbB2/neu: implications for selection of non-clinical safety models for trastuzumab-based therapeutics. Breast Cancer Res Treat. 2022;191(2):303-17.
191. Conrady CD, Joos ZP, Patel BC. Review: The Lacrimal Gland and Its Role in Dry Eye. J Ophthalmol. 2016;2016:7542929.
192. Zhu J, Inomata T, Shih KC, Okumura Y, Fujio K, Huang T, et al. Application of Animal Models in Interpreting Dry Eye Disease. Front Med (Lausanne). 2022;9:830592.
193. Lee H, Kim HK, Shin HS, Han SJ, Yoon S, Seong JK, et al. Evaluation of factors related to Anaesthesia-induced Lens opacity in experimental mice. Lab Anim Res. 2020;36:1.
194. Csikos C, Vágner A, Nagy G, Kálmán-Szabó I, Szabó JP, Ngo MT, et al. In Vivo Preclinical Assessment of the VEGF Targeting Potential of the Newly Synthesized [52Mn]Mn-DOTAGA-Bevacizumab Using Experimental Cervix Carcinoma Mouse Model. Diagnostics. 2023;13(2):236.
195. Hernandez R, Graves SA, Gregg T, VanDeusen HR, Fenske RJ, Wienkes HN, et al. Radiomanganese PET Detects Changes in Functional β-Cell Mass in Mouse Models of Diabetes. Diabetes. 2017;66(8):2163-74.
196. Wooten AL, Aweda TA, Lewis BC, Gross RB, Lapi SE. Biodistribution and PET Imaging of pharmacokinetics of manganese in mice using Manganese-52. PLoS One. 2017;12(3):e0174351.
197. Zhang W, Fan W, Rachagani S, Zhou Z, Lele SM, Batra SK, et al. Comparative Study of Subcutaneous and Orthotopic Mouse Models of Prostate Cancer: Vascular Perfusion, Vasculature Density, Hypoxic Burden and BB2r-Targeting Efficacy. Scientific Reports. 2019;9(1):11117.
198. Ho KS, Poon PC, Owen SC, Shoichet MS. Blood vessel hyperpermeability and pathophysiology in human tumour xenograft models of breast cancer: a comparison of ectopic and orthotopic tumours. BMC Cancer. 2012;12:579.
199. Yoshida K, Rivoire ML, Divgi CR, Niedzwiechi D, Cohen AM, Sigurdson ER. Effect of tumor size on monoclonal antibody uptake in a metastatic model. Journal of Surgical Oncology. 1992;49(4):249-52.
200. Danciu C, Oprean C, Coricovac DE, Andreea C, Cimpean A, Radeke H, et al. Behaviour of four different B16 murine melanoma cell sublines: C57BL/6J skin. Int J Exp Pathol. 2015;96(2):73-80.
201. Thurber GM, Schmidt MM, Wittrup KD. Antibody tumor penetration: Transport opposed by systemic and antigen-mediated clearance. Advanced Drug Delivery Reviews. 2008;60(12):1421-34.
202. Tang Y, Cao Y. Modeling the dynamics of antibody–target binding in living tumors. Scientific Reports. 2020;10(1):16764.
203. Singh AP, Guo L, Verma A, Wong GG-L, Thurber GM, Shah DK. Antibody Coadministration as a Strategy to Overcome Binding-Site Barrier for ADCs: a Quantitative Investigation. The AAPS Journal. 2020;22(2):28.
204. Burguin A, Furrer D, Ouellette G, Jacob S, Diorio C, Durocher F. Trastuzumab effects depend on HER2 phosphorylation in HER2-negative breast cancer cell lines. PLoS One. 2020;15(6):e0234991.
205. Rahmati M, Nikmanesh Y, Abshorshori N, Johari B. Investigating the Cytotoxic and Anti-proliferative Effects of Trastuzumab on MDA-MB-453 and MDA-MB-468 Breast Cell Lines With Different Levels of HER2 Expression. Journal of Applied Biotechnology Reports. 2020;7(2):87-92.
206. Moreau M, Raguin O, Vrigneaud JM, Collin B, Bernhard C, Tizon X, et al. DOTAGA-trastuzumab. A new antibody conjugate targeting HER2/Neu antigen for diagnostic purposes. Bioconjug Chem. 2012;23(6):1181-8.

207. Bini J, Izquierdo-Garcia D, Mateo J, Machac J, Narula J, Fuster V, et al. Preclinical Evaluation of MR Attenuation Correction Versus CT Attenuation Correction on a Sequential Whole-Body MR/PET Scanner. Investigative Radiology. 2013;48(5):313-22.
208. Schäfer JF, Gatidis S, Schmidt H, Gückel B, Bezrukov I, Pfannenberg CA, et al. Simultaneous whole-body PET/MR imaging in comparison to PET/CT in pediatric oncology: initial results. Radiology. 2014;273(1):220-31.
209. Fujishiro H, Yano Y, Takada Y, Tanihara M, Himeno S. Roles of ZIP8, ZIP14, and DMT1 in transport of cadmium and manganese in mouse kidney proximal tubule cells. Metallomics. 2012;4(7):700-8.
210. Graves SA, Hernandez R, Fonslet J, England CG, Valdovinos HF, Ellison PA, et al. Novel Preparation Methods of (52)Mn for ImmunoPET Imaging. Bioconjug Chem. 2015;26(10):2118-24.
211. Graves S, Hernandez R, Valdovinos H, Barnhart T, Cai W, Nickles R. Probing the impact of isoflurane on acute pancreatic function with ⁵²Mn-PET. Journal of Nuclear Medicine. 2016;57(supplement 2):167-.
212. Kodama H, Shimojo N, Suzuki KT. Distribution of manganese in rat pancreas and identification of its primary binding protein as pro-carboxypeptidase B. Biochem J. 1991;278 (Pt 3)(Pt 3):857-62.
213. Prato FS, Wisenberg G, Marshall TP, Uksik P, Zabel P. Comparison of the biodistribution of gadolinium-153 DTPA and technetium-99m DTPA in rats. J Nucl Med. 1988;29(10):1683-7.
214. Rinne SS, Leitao CD, Mitran B, Bass TZ, Andersson KG, Tolmachev V, et al. Optimization of HER3 expression imaging using affibody molecules: Influence of chelator for labeling with indium-111. Scientific Reports. 2019;9(1):655.
215. Gawne P, Man F, Fonslet J, Radia R, Bordoloi J, Cleveland M, et al. Manganese-52: applications in cell radiolabelling and liposomal nanomedicine PET imaging using oxine (8-hydroxyquinoline) as an ionophore. Dalton Trans. 2018;47(28):9283-93.
216. Ferreira CA, Kang L, Li C, Kamkaew A, Barrett KE, Aluicio-Sarduy E, et al. ImmunoPET of the differential expression of CD146 in breast cancer. Am J Cancer Res. 2021;11(4):1586-99.
217. Jensen AI, Severin GW, Hansen AE, Fliedner FP, Eliasen R, Parhamifar L, et al. Remote-loading of liposomes with manganese-52 and in vivo evaluation of the stabilities of (52)Mn-DOTA and (64)Cu-DOTA using radiolabelled liposomes and PET imaging. J Control Release. 2018;269:100-9.
218. Tang Y, Cao Y. Modeling the dynamics of antibody-target binding in living tumors. Sci Rep. 2020;10(1):16764.
219. Thurber GM, Schmidt MM, Wittrup KD. Antibody tumor penetration: transport opposed by systemic and antigen-mediated clearance. Adv Drug Deliv Rev. 2008;60(12):1421-34.
220. Betts A, Keunecke A, van Steeg TJ, van der Graaf PH, Avery LB, Jones H, et al. Linear pharmacokinetic parameters for monoclonal antibodies are similar within a species and across different pharmacological targets: A comparison between human, cynomolgus monkey and hFcRn Tg32 transgenic mouse using a population-modeling approach. MAbs. 2018;10(5):751-64.
221. Fuhrmann S, Kloft C, Huisinga W. Impact of altered endogenous IgG on unspecific mAb clearance. J Pharmacokinet Pharmacodyn. 2017;44(4):351-74.
222. Li F, Ulrich ML, Shih VF, Cochran JH, Hunter JH, Westendorf L, et al. Mouse Strains Influence Clearance and Efficacy of Antibody and Antibody-Drug Conjugate Via Fc-FcγR Interaction. Mol Cancer Ther. 2019;18(4):780-7.
223. Reddy N, Ong GL, Behr TM, Sharkey RM, Goldenberg DM, Mattes MJ. Rapid blood clearance of mouse IgG2a and human IgG1 in many nude and nu/+ mouse strains is due to low IgG2a serum concentrations. Cancer Immunol Immunother. 1998;46(1):25-33.
224. Michel RB, Ochakovskaya R, Mattes MJ. Rapid blood clearance of injected mouse IgG2a in SCID mice. Cancer Immunol Immunother. 2002;51(10):547-56.
225. Avery LB, Wang M, Kavosi MS, Joyce A, Kurz JC, Fan YY, et al. Utility of a human FcRn transgenic mouse model in drug discovery for early assessment and prediction of human pharmacokinetics of monoclonal antibodies. MAbs. 2016;8(6):1064-78.

226. Andersen JT, Daba MB, Berntzen G, Michaelsen TE, Sandlie I. Cross-species binding analyses of mouse and human neonatal Fc receptor show dramatic differences in immunoglobulin G and albumin binding. J Biol Chem. 2010;285(7):4826-36.
227. Swiercz R, Mo M, Khare P, Schneider Z, Ober RJ, Ward ES. Loss of expression of the recycling receptor, FcRn, promotes tumor cell growth by increasing albumin consumption. Oncotarget. 2017;8(2):3528-41.
228. Zheng M. Serum albumin: a pharmacokinetic marker for optimizing treatment outcome of immune checkpoint blockade. J Immunother Cancer. 2022;10(12).
229. Yan H, Endo Y, Shen Y, Rotstein D, Dokmanovic M, Mohan N, et al. Ado-Trastuzumab Emtansine Targets Hepatocytes Via Human Epidermal Growth Factor Receptor 2 to Induce Hepatotoxicity. Mol Cancer Ther. 2016;15(3):480-90.

X. Publications list

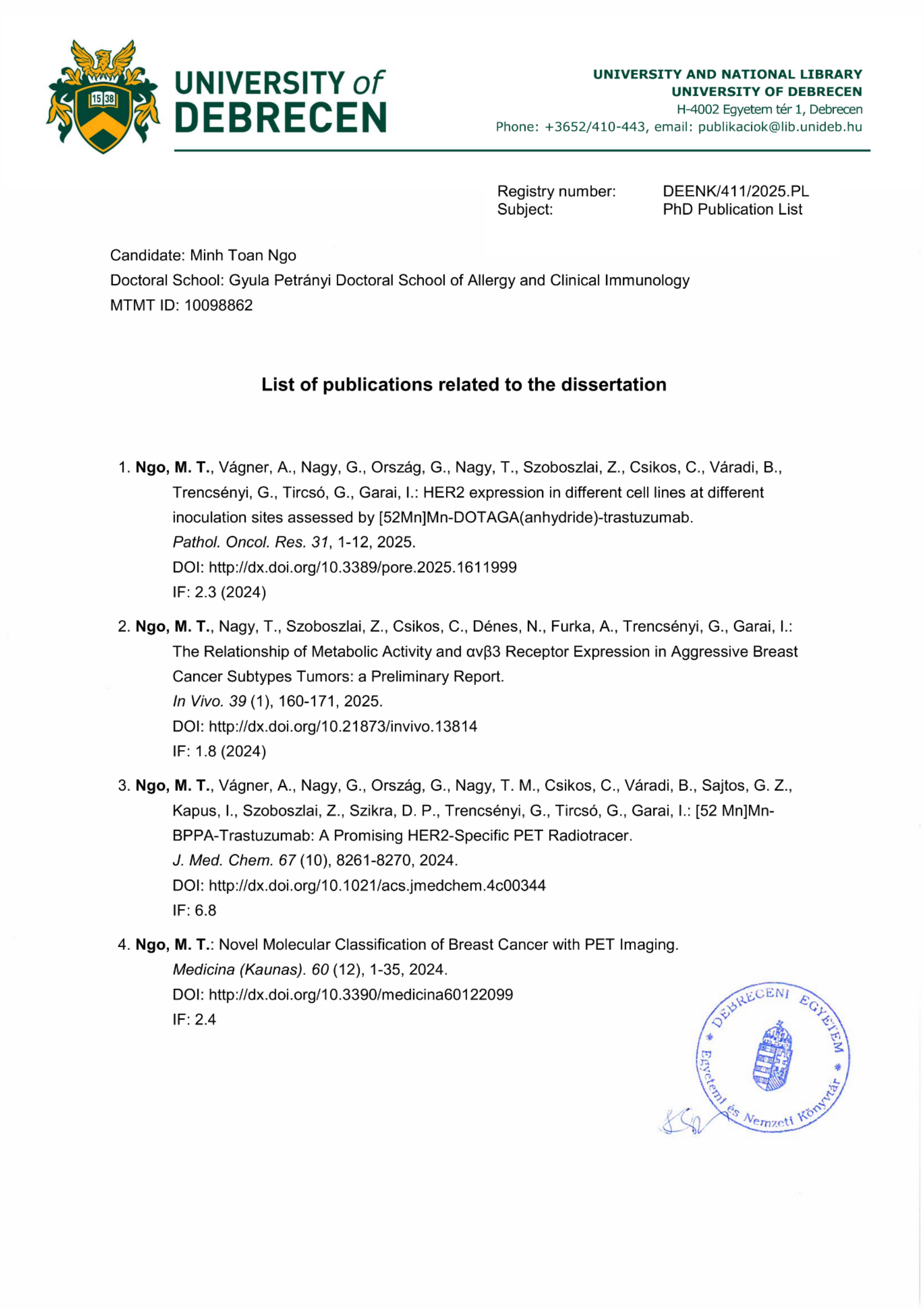

UNIVERSITY of DEBRECEN

UNIVERSITY AND NATIONAL LIBRARY
UNIVERSITY OF DEBRECEN
H-4002 Egyetem tér 1, Debrecen
Phone: +3652/410-443, email: publikaciok@lib.unideb.hu

Registry number: DEENK/411/2025.PL
Subject: PhD Publication List

Candidate: Minh Toan Ngo
Doctoral School: Gyula Petrányi Doctoral School of Allergy and Clinical Immunology
MTMT ID: 10098862

List of publications related to the dissertation

1. **Ngo, M. T.**, Vágner, A., Nagy, G., Ország, G., Nagy, T., Szoboszlai, Z., Csikos, C., Váradi, B., Trencsényi, G., Tircsó, G., Garai, I.: HER2 expression in different cell lines at different inoculation sites assessed by [52Mn]Mn-DOTAGA(anhydride)-trastuzumab.
   Pathol. Oncol. Res. 31, 1-12, 2025.
   DOI: http://dx.doi.org/10.3389/pore.2025.1611999
   IF: 2.3 (2024)
2. **Ngo, M. T.**, Nagy, T., Szoboszlai, Z., Csikos, C., Dénes, N., Furka, A., Trencsényi, G., Garai, I.: The Relationship of Metabolic Activity and αvβ3 Receptor Expression in Aggressive Breast Cancer Subtypes Tumors: a Preliminary Report.
   In Vivo. 39 (1), 160-171, 2025.
   DOI: http://dx.doi.org/10.21873/invivo.13814
   IF: 1.8 (2024)
3. **Ngo, M. T.**, Vágner, A., Nagy, G., Ország, G., Nagy, T. M., Csikos, C., Váradi, B., Sajtos, G. Z., Kapus, I., Szoboszlai, Z., Szikra, D. P., Trencsényi, G., Tircsó, G., Garai, I.: [52 Mn]Mn-BPPA-Trastuzumab: A Promising HER2-Specific PET Radiotracer.
   J. Med. Chem. 67 (10), 8261-8270, 2024.
   DOI: http://dx.doi.org/10.1021/acs.jmedchem.4c00344
   IF: 6.8
4. **Ngo, M. T.**: Novel Molecular Classification of Breast Cancer with PET Imaging.
   Medicina (Kaunas). 60 (12), 1-35, 2024.
   DOI: http://dx.doi.org/10.3390/medicina60122099
   IF: 2.4

UNIVERSITY of DEBRECEN

UNIVERSITY AND NATIONAL LIBRARY
UNIVERSITY OF DEBRECEN
H-4002 Egyetem tér 1, Debrecen
Phone: +3652/410-443, email: publikaciok@lib.unideb.hu

List of other publications

5. **Ngo, M. T.**, Lê, Á. N., Đinh, D. P. H.: The Impact of Chemotherapy on Cardiovascular Mortality across Breast Cancer Subtypes.
   Current Oncology. 31 (2), 649-659, 2024.
   DOI: http://dx.doi.org/10.3390/curroncol31020047
   IF: 3.4
6. Csikos, C., Vágner, A., Nagy, G., Kálmán-Szabó, I., Péli-Szabó, J., **Ngo, M. T.**, Szoboszlai, Z., Szikra, D. P., Krasznai, Z. T., Trencsényi, G., Garai, I.: In Vivo Preclinical Assessment of the VEGF Targeting Potential of the Newly Synthesized [52Mn]Mn-DOTAGA-Bevacizumab Using Experimental Cervix Carcinoma Mouse Model.
   Diagnostics. 13 (2), 236-, 2023.
   DOI: http://dx.doi.org/10.3390/diagnostics13020236
   IF: 3
7. Váradi, B., Brezovcsik, K., Garda, Z., Madarasi, E., Szedlacsek, H., Badea, R. A., Vasilescu, A. M., Puiu, A. G., Ionescu, A. E., Sima, L. E., Munteanu, C. V. A., Călăraş, S., Vágner, A., Szikra, D. P., **Ngo, M. T.**, Nagy, T., Szűcs, Z., Szedlacsek, S. E., Nagy, G., Tircsó, G.: Synthesis and characterization of a novel [52Mn]Mn-labelled affibody based radiotracer for HER2+ targeting.
   Inorg. Chem. Front. 10 (16), 4734-4745, 2023.
   DOI: https://doi.org/10.1039/D3QI00356F
   IF: 6.1

Total IF of journals (all publications): 25,8
Total IF of journals (publications related to the dissertation): 13,3

The Candidate's publication data submitted to the Tudóstér have been validated by DEENK on the basis of the Journal Citation Report (Impact Factor) database.

18 June, 2025